Universidad Autónoma de Madrid

Facultad de Ciencias

Nanostructured ZnO films obtained by Electrophoretic Deposition of tailored ZnO nanoparticles

Memoria presentada por:

María Verde Lozano

Para optar al título de Doctor Internacional en Ciencias Químicas

Directores:

Dr. Amador Caballero Cuesta

Dra. Begoña Ferrari Fernández

Instituto de Cerámica y Vidrio

Consejo Superior de Investigaciones Científicas

Madrid, 2013

Esta Tesis Doctoral ha sido realizada en el Instituto de Cerámica y Vidrio (CSIC) y ha sido financiada por los proyectos CICYT MAT-2009-14448-C02-01 “Processing by association of colloid-chemical and power-metallurgical techniques of metal-ceramic nanocomposite structures", MAT-2010-16614 “Eco-friendly soft processing of electroceramics”, MAT-2012-38650C02-02 “Design of the Microstructure and the Microarchitecture of metal-ceramic materials using colloidal and powder metallurgy technologies” y por una Beca JAE-PreDoc 2009 del Consejo Superior de Investigaciones Científicas (CSIC).

Esta memoria de tesis cumple los requisitos necesarios para obtener la Mención Internacional en el Título de Doctor que se describen en la normativa de enseñanzas universitarias de doctorado de la Universidad Autónoma de Madrid y que han sido establecidos en el artículo 15 del Real Decreto 99/2011 que establece la Ordenación de las Enseñanzas Universitarias Oficiales (B.O.E nº 35 del 28 de Enero de 2011, Págs. 13909-13926. Dicha Memoria de tesis ha sido informada por dos doctores que pertenecen a instituciones de educación superior de Estados miembros de la Unión Europea distintos de España:

Dr. Raúl Bermejo
Institut für Struktur- und Funktionskeramik
Montanuniversität Leoben
Austria

Dr. Sandra Cabañas Polo
Department of Materials Science and Engineering
University of Erlangen-Nuremberg
Alemania

RESUMEN

Planteamiento y objetivos de la tesis

El trabajo que se describe en la presente memoria de tesis lleva por título "Obtención de láminas de ZnO mediante deposición electroforética de nanoparticulas de ZnO modificadas ad hoc" (*Nanostructured ZnO films obtained by electrophoretic deposition of tailored Z*nO nanoparticles). Tal y como resume el título, el trabajo se plantea como una aproximación al problema de la obtención de capas o láminas de ZnO con morfología controlada mediante el uso de una técnica con elevado potencial de escalado.

Los materiales basados en ZnO y en particular las láminas de ZnO con morfología controlada han sido objeto en los últimos años de numerosas investigaciones. El renovado interés por el ZnO surge por su elevado potencial para su uso en múltiples aplicaciones y en particular en algunas aplicaciones emergentes. A modo de ejemplo y muy brevemente, algunos materiales dopados de ZnO se postulan como conductor transparente potencialmente sustituto del excesivamente costoso ITO, otros para su aplicación en las celdas solares de última generación mejorando su rendimiento, también se proponen para la fabricación de dispositivos espintrónicos, como generadores piezoeléctricos a escala submicrónica para dispositivos electrónicos, fotocatalizadores, sensores de gases, etc. Las razones de esta explosión son básicamente dos: por un lado las propiedades únicas del ZnO y por otro el aumento de nuestra capacidad de procesado del material controlando su hábito de crecimiento cristalino y por tanto su morfología. Desde el punto de vista del ZnO cabe decir que es un óxido anfótero, semiconductor de banda ancha, especialmente adecuado para la ingeniería de band gap mediante dopado y que tiene carácter piezoeléctrico. Presenta hábitos de crecimiento cristalino diferenciados que dan lugar a una multitud de morfologías con diferentes ratios superficie/volumen que a su vez modifican las propiedades del material. Este punto es uno de los que más interés recaba actualmente y genera muchos trabajos enfocados en el uso de técnicas diferentes para obtener morfologías concretas.

El uso de la técnica de deposición electroforética se plantea debido a su fácil escalabilidad. Esta técnica es usada en la industria para realizar recubrimientos sobre superficies prácticamente de cualquier dimensión, con formas que pueden llegar a presentar gran complejidad (desde tornillería a frontales de automóvil). Además

permite procesar en agua con un bajo consumo energético y poco contaminante, es decir es un proceso que puede realizarse en condiciones de sostenibilidad minimizando su impacto medioambiental. Hasta la fecha, la inmensa mayoría de los trabajos en los que obtienen láminas de ZnO con morfologías controladas sobre superficies muy pequeñas usan técnicas evaporativas como PVD, CVD, MOCVD, PLD, etc. Estas técnicas tienen un alto impacto energético y su escalabilidad es más difícil que la del EPD.

Otra aproximación emergente con gran potencial para el control morfológico del ZnO consiste en la utilización de un proceso de crecimiento hidrotermal combinado con la utilización de sustratos y el semillado adecuado. Esta aproximación entraría igualmente dentro del concepto de sostenibilidad, i.e., bajo consumo energético y bajo impacto medioambiental y también se ha abordado su uso en la tesis.

En este marco conceptual, los objetivos que se plantean en la tesis se pueden resumir de la manera siguiente:

- Seleccionar y optimizar una ruta de síntesis de ZnO en medio acuoso que permita obtener nanopartículas modificadas a conveniencia. Obtención de partículas inferiores a 100 nm con morfología laminar y diferentes tamaños.
- Preparación de láminas de ZnO mediante EPD en medio acuoso de las nanopartículas sintetizadas. Obtención de láminas con las partículas orientadas.
- Obtención de láminas por EPD sobre diferentes sustratos variando de manera controlada su morfología.
- Crecimiento de láminas con morfología controlada mediante tratamientos hidrotermales sobre láminas semilladas mediante EPD.

Desarrollo de la tesis

La memoria de tesis está estructurada en 5 capítulos y unas conclusiones generales: un primer capítulo de revisión, el capítulo segundo con los detalles de las técnicas usadas y procedimientos experimentales, el tercer capítulo dedicado a la síntesis de las nanopartículas de ZnO, el capítulo cuarto que describe todo el estudio de deposición electroforética realizado sobre estas partículas, el quinto capítulo en el que se presentan los resultados obtenidos utilizando diferentes aproximaciones de EPD y crecimiento hidrotermal sobre sustratos semillados, y por último un resumen de las conclusiones generales.

En el primer capítulo, la revisión bibliográfica se centra en resumir y comentar de una manera crítica la información disponible en la bibliografía para abordar los problemas objeto de la tesis. Tras un breve resumen de las principales características y propiedades del ZnO, se realiza un trabajo más extenso en lo referente a la síntesis en medio acuoso y la posibilidad de controlar la morfología de los cristales. Con respecto a la preparación de láminas, se evalúan las diferentes técnicas y morfologías obtenidas con las publicadas en los últimos años. Posteriormente se presentan los principios básicos de la EPD y se discute la naturaleza de las superficies del ZnO de cara al papel que puedan jugar en el comportamiento coloidal del ZnO en agua, y frente a la adsorción de dispersantes. Finalmente se revisa la información publicada sobre EPD de partículas de ZnO.

En el capítulo segundo se detallan los procedimientos generales utilizados en la síntesis de las nanopartículas, en los procesos de EPD y en los experimentos de crecimiento hidrotermal. Aquellos detalles relevantes para la discusión o específicos de ciertos experimentos se detallan en su capítulo correspondiente. También se detalla la preparación de las muestras para las diferentes técnicas de medida. Se especifican las metodologías utilizadas, así como las capacidades técnicas de los equipos y su aplicabilidad a una medida concreta, cuando es relevante para su correcta interpretación.

El tercer capítulo presenta los resultados obtenidos en cuanto a la síntesis de las nanopartículas de ZnO. Mediante una ruta de precipitación en agua, partiendo de acetato de Zn y usando sosa como precipitante, se obtiene un precipitado que tras diferentes ciclos de lavado en agua y etanol, deja un precursor formado por compuestos laminares basados en acetato de Zn. Este precursor puede transformarse en nanoparticulas de ZnO mediante tratamientos de calentamiento y enfriamiento brusco entre 200 y 300 ºC (ciclos frío-frío de 10 minutos). Cambiando las condiciones de lavado así como la temperatura del tratamiento se pueden obtener partículas en el rango 10 nm - 100 nm con forma de copo o placa. Al aumentar el tamaño de la partícula se acentúa la forma y aumenta la cristalinidad. El estado de agregación es mucho mayor para las partículas de mayor tamaño debido a su elevado factor de forma. La síntesis puede realizarse también coprecipitando Zn y Co manteniendo las características de las partículas obtenidas. La transformación a ZnO no es completa, quedando algunos restos de precursor.

La obtención de láminas por EPD se presenta en el capítulo 4. En la primera parte del capítulo se estudia el comportamiento coloidal de las partículas sintetizadas en agua de cara a la preparación de suspensiones estables para EPD. Se optimizan los

parámetros de dispersión y se ha utilizado un polielectrolito catódico de cadena larga (PEI con peso molecular de 25000 g/mol) como dispersante. El PEI de elevado peso molecular es capaz de protonarse en un amplio rango de pH (2 < pH < 11), lo que permite mantener la estabilidad coloidal en el rango de estabilidad química del ZnO (6 < pH < 11), y propiciar la deposición catódica, necesaria para evitar problemas de corrosión si se usa un metal como substrato en un medio acuoso. Este polielectrolito se adsorbe preferencialmente en algunas superficies de las nanopartículas de ZnO. Esto es debido a la diferente naturaleza eléctrica de las caras basales de los copos/placas de ZnO. Como consecuencia de ello, el conjunto nanopartícula-polielectrolito conforman un sistema que puede ejemplificarse gráficamente como "con forma de medusa" que facilita que las partículas se depositen en el sustrato de forma ordenada con sus planos basales paralelos al sustrato. Este efecto es mayor cuanto mayor es el factor de forma de las nanoparticulas. El resultado es que se pueden obtener láminas de ZnO con una anormalmente elevada densidad de empaquetamiento que les permite ser transparentes y flexibles. Tanto sobre sustratos de ITO como de acero AISI304 electropulido, el proceso de EPD conforma esta lámina en un tiempo muy corto, tras el cual se para la deposición. El espesor de lámina que se alcanza sobre el acero está en el entorno de 50 nm mientras que sobre el ITO parece menor, si bien en este caso la deposición es más heterogénea, apareciendo islas o pequeños aglomerados sobre la capa depositada. La razón del bloqueo del proceso parece hallarse precisamente en la elevada densidad de esta primera capa ordenada, que puede llegar a bloquear el campo eléctrico en las condiciones de trabajo que se están utilizando. La densidad y orden de la capa se ha verificado mediante técnicas de medida en masa, como la elipsometría, y mediante rastreo de superficies por microscopia electrónica de barrido, de transmisión de alta resolución y microscopia de fuerzas atómicas. Por otro lado, aumentando la concentración de la suspensión, la rugosidad y la conductividad eléctrica del sustrato (en este caso utilizando Ni) pueden obtenerse capas con un mayor espesor, si bien, la nanoestructura ordenada de las partículas paralelas al sustrato se pierde de forma parcial, al aparecer zonas en las que se aglomeran las partículas. Precisamente, el parcial desorden que acompaña a este tipo de capas menos densas limita el efecto bloqueante y permite que la deposición prosiga.

En el capítulo quinto y a la vista de los resultados obtenidos se describen diferentes aproximaciones para intentar el crecimiento controlado de láminas de ZnO sobre diferentes sustratos. Se estudió la posibilidad de crecer capa a capa mediante el uso de EPD pulsada. Si se considera que la capa que se deposita sobre el sustrato tiene

un efecto capacitivo de bloqueo (como hace un condensador en un circuito eléctrico sometido a una señal dc), esta técnica podría permitir la descarga de esa capacidad de intercara y propiciar la deposición de una nueva capa. No se pudo observar un efecto de crecimiento capa a capa, ni con pulsos de corriente ni de voltaje. En los ensayos en corriente continua o pulsada, al trabajar en agua, el voltaje está limitado por el efecto/deterioro que provoca la hidrólisis en la capa, por lo que se ha considerado el estudio de un sistema no acuoso para poder utilizar campos muy superiores. La EPD en etanol a voltajes superiores en dos órdenes de magnitud propicia el crecimiento de las capas, obteniéndose espesores superiores a la micra, pero perdiendo la nanoestructura ordenada y perfectamente empaquetada. La razón para que esto suceda puede deberse al efecto combinado de un voltaje alto junto con el hecho de que en etanol no se utiliza PEI, con lo que no se tiene el conjunto "con forma de medusa" que posibilita la ordenación de las nanopartículas al llegar al sustrato. En otro tipo de aproximación, se usaron sustratos semillados por EPD de nanopartículas de ZnO para explora las posibilidades de crecimiento hidrotermal. Se obtuvieron varios tipos de comportamiento bien diferenciados. Cuando el semillado conforma una capa muy densa y compacta, obtenida con las nanopartículas de mayor tamaño (50 nm), se favorece la nucleación frente al crecimiento y crecen nanoestructuras sobre el semillado con forma de estrella, en una estructura conocida como "multipod". Cuando el semillado conforma una capa compacta pero se realiza con las nanopartículas de menor tamaño y mayor reactividad (10 nm), se favorece el crecimiento apareciendo una estructura prismas ordenados alineados verticalmente a lo largo de toda la superficie. Las partículas de la capa semillada recristalizan y se constituyen en núcleos que crecen en la dirección libre, ya que el crecimiento lateral esta constreñido por la propia naturaleza compacta de la lámina. Cuando el crecimiento lateral está permitido, como es el caso de los sustratos de ITO semillados que presentan una estructura de pequeñas islas, en lugar de prismas ordenados y alineados entre sí se obtiene un crecimiento en forma de pétalos agrupados a modo de flores.

Finalmente esta memoria recoge las conclusiones generales a modo de resumen de las que se han ido obteniendo en los diferentes capítulos, donde se describen los fenómenos más relevantes observados y su demostrada o posible causa según el caso.

ABSTRACT

The present thesis is structured into 5 chapters, each of which has its own conclusions: a first chapter reviewing the topics of ZnO and EPD, a second chapter with the details of the experimental procedures characterization techniques used, a third chapter reporting the synthesis of ZnO nanoparticles, a fourth chapter describing the study carried out for the electrophoretic deposition on these particles, a fifth chapter presenting the results obtained using different approaches to EPD and using seeded substrates for hydrothermal growth, and finally a summary of the overall conclusions.

In the first chapter, the bibliographic review focuses on summarizing and critically commenting the information available in the literature to address the problems tackled in the present thesis. After a brief summary of the main characteristics and properties of ZnO, an extensive research is performed regarding the synthesis in aqueous medium and the ability to control the morphology of the crystals. With respect to the preparation of films, various techniques published in recent years and the morphologies of the ZnO structures obtained using them are evaluated. The basic principles of EPD are then presented and the nature of ZnO surfaces are discussed with respect to the role they can play in the colloidal behavior of ZnO in water and to the adsorption of dispersants. Finally, the published information on EPD of ZnO particles is reviewed.

The second chapter details the general procedures used in the synthesis of nanoparticles, in the deposition by EPD, and in the subsequent hydrothermal growth experiments. Those details relevant for the discussion or specific of certain experiments are detailed in their corresponding chapters. The preparation of samples for different measuring techniques is also described. The different methodologies used and the technical characteristics of the equipment are specified, as well as its applicability to a particular kind of measure whenever it is relevant for its correct interpretation.

The third chapter presents the results obtained from the synthesis of ZnO nanoparticles. Following a direct precipitation route from aqueous suspensions of zinc acetate and using sodium hydroxide as precipitant agent, a precipitate is obtained which after several washing cycles in water and ethanol, rendered a layered precursor consisting of compounds based on Zn acetate. This precursor can be converted into ZnO nanoparticles by heat treatments and quenching between 200 and 300 ° C.

Changing both the washing conditions and the temperature of the thermal treatment particles in the range of 10 – 100 nm with plate or flake morphologies can be obtained. Increasing the particle size, shape is emphasized and crystallinity increased. The agglomeration state is much higher for larger particles due to their high shape factor. The synthesis can also be carried out coprecipitating Zn and Co, maintaining the characteristics of the obtained particles. In this case the transformation of the precursors to ZnO is not complete, leaving some remnants.

The obtaining of films by EPD is presented in Chapter 4. In the first part of the chapter the behavior of the colloidal synthesized particles in water is studied, with the aim of preparing stable suspensions for EPD. Dispersion parameters are optimized using a long chain cathodic polyelectrolyte (PEI, Mw= 25000 g/mol) as dispersant. PEI with a high molecular weight can stay protonated over a broad pH range ($2 < pH < 11$), maintaining the colloidal stability in the range of chemical stability of ZnO ($6 < pH < 11$) and promoting the cathodic deposition, necessary to avoid corrosion problems when using metal substrates in aqueous media. This polyelectrolyte is preferentially adsorbed on certain surfaces of ZnO nanoparticles, due to the different electric nature of the basal facets of the ZnO flakes. Consequently, the nanoparticle-polyelectrolyte set up a system that can be graphically exemplified as “jellyfish-like” and which enables particles to be deposited on the substrate in an ordered way, with their basal planes parallel to the substrate. It must be noted that this effect acquires more relevance with increasing shape factor of the nanoparticles. In this way, the result is that ZnO films with abnormally high packing densities (which make them transparent and flexible) are obtained. Either on ITO or on electropolished AISI304 stainless steel substrates, the EPD process shapes the ZnO thin film in a very short time, after which deposition stops. The thickness of the film deposited on steel is of about 50 nm, whereas on ITO it seems lower, although in this case the deposition is more heterogeneous, appearing small islands or agglomerates on the deposited layer. The reason for the blocking of the deposition process seems to be precisely in the high density of this first ordered layer, which might block the electric field in the applied working conditions. Density and ordering of the films have been verified by mass measurement techniques such as ellipsometry, and by surface scanning methods, such as scanning electron microscopy high resolution transmission electron microscopy and atomic force microscopy. Furthermore, increasing the concentration of the suspension and the roughness and electrical conductivity of the substrates (using Ni foils as substrates) films with higher thicknesses can be obtained, although the ordered nanostructure of the particles parallel to the substrate is partially lost, as areas appear where the particles are

agglomerated. In fact, the partial disorder present in these less dense layers limits the blocking effect and allows the deposition to resume.

In the fifth chapter and in view of the results different approaches to attempt the controlled growth of ZnO films on different substrates are described. The possibility of growing layer by layer films using pulsed EPD is studied. Considering that the layer deposited on the substrate has a capacitive locking effect (as does a capacitor in an electrical circuit under dc signal), this technique could allow the discharge of that capacity, promoting the deposition of a new layer. However, no layer by layer growth effect was observed, neither with current nor voltage pulses. In tests in continuous or pulsed current working in aqueous media, the voltage is limited by the effect / deterioration caused by water hydrolysis on the layer, and thus a non-aqueous system were considered so as to be able to use much higher fields. The EPD in ethanol, using voltages two orders of magnitude higher, promotes the growth of the layers, yielding thickness in the range of microns, but losing the perfectly packed and ordered nanostructure. This can be ascribed to the combined effect of the high voltages used, together with the fact that PEI is not used when working in ethanol, and thus the “jellyfish” conformation which enabled the orientation of the particles is not present. In a different approach, substrates seeded with ZnO nanoparticles by EPD were used so as to explore the potential of hydrothermal growth. Several well differentiated behaviors were observed. When the seeding forms a very dense and compact layer obtained with larger nanoparticles (50 nm), nucleation is favored vs. growth and nanostructures are grown on top of the seed layer, with star-like shapes in a structure known as "multipod". When the seeding forms a compact layer composed of smaller nanoparticles with higher reactivity (10 nm), growth is favored vs. nucleation and an array of vertically aligned prisms/rods arranged along the entire surface appears. In this case the particles in the seed layer recrystallize, constituting nuclei which grow in the free direction (i.e. vertically), as the lateral growth is constrained by the compact nature of the film. When the lateral growth is allowed, as is the case of ITO substrates seeded with heterogeneous ZnO seed layers forming small islands, growth in the shape of grouped petals is obtained instead of the array of nanorods.

Finally, this report contains a summary in Spanish of the overall conclusions- which have been presented in English in each chapter.

Presentation and Objectives of the Thesis

As summarized in the title, the work described in the present thesis is set out as an approximation to the issue of obtaining of ZnO films with tailored/controlled morphology by using a method with a high scaling potential.

ZnO-based materials, and in particular ZnO films with controlled morphology have been subjected to extensive research in the past few years. The renewed interest in ZnO arises from its potential use in different areas of technology and in particular prospective applications. Some of the applications for which (doped) ZnO materials have been postdated include as feasible potential transparent conductors to substitute Indium tin oxide (ITO), to improve the performance of solar cells, as submicronic piezoelectric generators for espintronic devices, as photocatalysts or gas sensors, etc. The main reasons for this substantial interest are two. First, the intrinsic properties of ZnO (amphoteric oxide, wide bandgap semiconductor with piezoelectric character), which make it especially suitable for its use in bandgap engineering through doping. The second reason for the regained interest in ZnO consists on the improvements made in materials processing, which allow the control of the crystal growth habit and thus of its morphology. In this sense, ZnO presents several growth habits that give rise to a multitude of morphologies with different surface/volume ratios which, in turn, modify the properties of the material. This topic focuses most of the current interest in ZnO and generates a great number of publications dealing with different techniques for the obtaining of specific morphologies.

Amongst the great variety of methods for the preparation of ZnO thin filmsElectrophoretic Deposition (EPD) is gaining increasing interest, due to its versatility and high potential for scaling up to large volumes. Actually, it might even become an alternative to the evaporative coating processes to tailor ceramic nanostructures and nanoparticles assembly.

The use of electrophoretic deposition is suggested in this thesis due to its high potential for scaling up to large volumes. This technique is widely used in the industry for the obtaining of coatings of practically any dimensions, complex shapes (from fasteners to car bodyworks). In addition, it allows processing in aqueous media with low energy consumption and low contamination, i.e. it is a sustainable process with a minimal environmental impact. Up to date, most of the methods for the preparation of ZnO films with controlled morphologies include evaporative techniques, such as PVD,

CVD, MOCVD, PLD, etc. These techniques, however, require high energy consumptions and are not as easily scalable as EPD.

Another emerging approximation to the morphological control of ZnO consists on the use of a hydrothermal growth process combined with the used of adequately seeded substrates. As EPD, this method is low energy-consuming and sustainable, and its use has also been cosidered in this thesis.

In this context, the main objectives of this thesis can be summarized as follows:

- Select and optimize an aqueous synthesis route for the preparation of ZnO nanoparticles with tailored morphology. Obtaining of particles with different sizes below 100 nm and laminar morphologies.
- Preparation of ZnO films by EPD of the synthesized particles in aqueous media. Deposition of ZnO films with oriented particles.
- Obtaining of ZnO films by EPD on different substrates, varying their morphology in a controlled way.
- Growth of films with controlled morphology by hydrothermal growth on seed layers preprared by EPD.

Chapter 1

Chapter 1: Introduction

Zinc oxide is a semiconductor material which has been subject to periods of intensive study in the past, starting in first quarter of the past century and reaching its "peak" in the late 70s and beginning of the 80s [1-4]. At that moment, the requirement for new materials in the nanoscale and the impossibility of ambipolar p-n doping it made the interest in ZnO as bulk material decrease. However, there has been a resurgence of the interest on ZnO in the past decade, fueled and fanned by the vast amount of prospects that functional, nanostructured ZnO films present for a wide range of applications, such as chemical sensors, transparent semiconductors or high speed electronic and optoelectronic devices [5-8].

Chemically speaking, ZnO is a semiconductor material which appears in nature as the mineral zincite, with impurities that give it a yellow-to-red color, whereas pure ZnO is a white powder. Nevertheless, its color can change from white to pale yellow due to oxygen losses, forming non-stoichiometric $Zn_{1+x}O$, which reverts to ZnO by oxidation.

ZnO is at the border between covalent and ionic semiconductors, as the ZnO bond presents 59% ionic character (according to the equation of the fraction of ionic character) due to the great difference in polarities between Zn and O (3.5 and 1.6 in the Pauling scale, respectively)[9].

$$\text{Fraction of ionic character} = 1 - \exp[-0.25 * (X_M - X_X)^2]$$

Therefore, Zn and O can be considered to be as their Zn^{2+} and O^{2-} ions, with ionic crystal radii (in tetrahedral coordination) of 0.74 and 1.40 Å, respectively[10].
Moreover, the binding in the ZnO crystal lattice presents sp^3 hybridization between the $4s^2$ orbitals of Zn and the $2p^4$ orbitals of O, and therefore a tetrahedral geometry. This geometry, in which each Zn atom has four O neighbor atoms in a tetrahedral configuration and vice versa, forms Zn and O layers that can give place to the two main crystalline structures of ZnO, hexagonal wurtzite and cubic zinc-blende. Both structures are non-centrosymmetric, and their difference consists on the stacking sequence of the Zn and O planes along the c axis: *AaBbAaBb* for wurtzite and *AaBbCcAaBbCc* for zinc-blende (The small and large letters stand for the two different kinds of constituents)[11].

Even though zinc oxide can have three different crystalline structures- wurtzite, zinc-blende and rocksalt-, the high polarity of the Zn-O bond accounts for the preferential formation of wurtzite rather than zinc-blende, which is metastable, or rocksalt, which can only be obtained at high pressures.

Wurtzite shows a hexagonal unit cell, which contains two ZnO units, belongs to the space group or $P6_3mc$, and presents two lattice parameters, a=b with values ranging from 3.2475 to 3.2501 Å, and c,from 5.2042 to 5.2075 Å [12] (Figure 1.1). The density of the ZnO is 5.606 g/cm^3. In it, the hexagonal-close-packed (hcp) Zn^{2+} and O^{2-} planes interpenetrate alternatively, with the c-axis directed along the direction of one of the sp^3 hybrid orbitals, [0001], giving rise to ending facets with different atoms and charges: positively charged Zn-(0001) and negatively charged O-(000) surfaces.

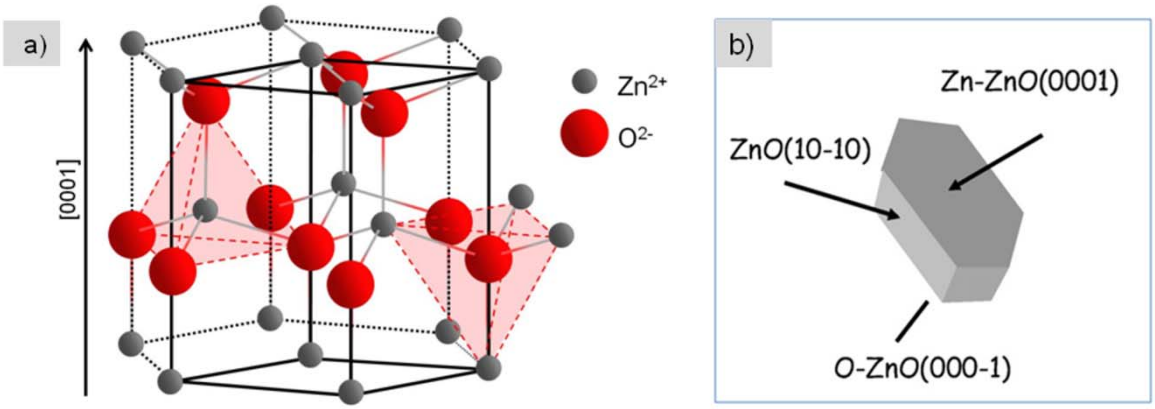

Figure 1.1: a) Representation of the crystallographice structure of wurtzite structure. b) schematical sketch showing the typical shape of ZnO powder particles, a hexagonal column with the top-face corresponding to the Zn-terminated Zn–ZnO surface and the bottom to the O-terminated O–ZnO surface. (borrowed from [13]).

This results in a normal dipole moment and a spontaneous polarization along the c-axis, as well as a divergence in surface energy. This divergence in surface energy between the different surfaces is extremely relevant to explain the reactivity of zinc oxide [13-15]:

The (1010) and (11 0) mixed-terminated surfaces of zinc oxide correspond to what Tasker [16] defined as type I: layers of mixed stoichiometry, with both anions and cations and no polar moment (see Figure 1.2). These are the energetically most favorable ones, and therefore the predominant ones, forming the sides of the hexagonal columns. They have no instabilities, and their (low) reactivity is mainly due to defects and to the fact that the Zn and O atoms in them are threefold coordinated, and thus have a free site for adsorption of molecules.

On the other hand, the polar Zn-ZnO (0001) and O-ZnO (000) surfaces correspond to Tasker's type III. These are charged, highly unstable surfaces (with very large surface energies for finite crystals), with a high density of defects in them and a perpendicular dipolar moment, which produces a polarizing electric field in the bulk. Even though an electrostatic argument states that such surfaces cannot exist, and in all

other polar surfaces of metal oxides this instability is removed by a structural rearrangement of the surface, no reconstruction is observed for ZnO, and the stabilization mechanism remains a controversial issue [17, 18].

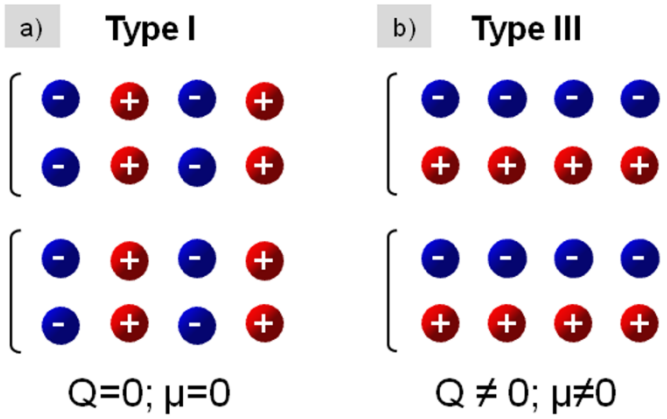

Figure 1.2.: Surfaces classification according to Tasker: a) Type I, each plane contains an equal number of cations and anions (the net dipole moment is zero; μ = 0) b) Type III, charged planes and dipole moment normal to the surface (μ≠0). Q is the layer charge density in the repeat unit perpendicular to the surface.

This structure with different ending facets not only accounts for the surface reactivity and the multiple growth morphologies that ZnO can adopt, but it also is determinant for some of the various properties of ZnO, the most important of which are briefly described here:

- *Direct and wide band gap.* The band gap of ZnO is 3.37 eV at room temperature. As mentioned above, this enables applications in optoelectronics in the blue/UV region, including light-emitting diodes, laser diodes and photodetectors.

- *Large exciton binding energy.* The free-exciton binding energy in ZnO is 60 meV, which indicates that efficient excitonic emission in ZnO can persist at room and higher temperatures, and makes ZnO a promising material for optical devices that are based on excitonic effects.

- *Large piezoelectric constant.* The lack of centrosymmetry of the wurtzite crystal *structure,* combined with a large electromechanical coupling in ZnO, gives rise to strong piezoelectric and pyroelectric properties.

- *Strong luminescence* in the green–white region of the spectrum, ZnO is also a suitable material for phosphor applications, whereas the n-type conductivity makes it appropriate for applications in vacuum fluorescent displays and field emission displays.

- *Strong sensitivity of surface conductivity to the presence of adsorbed species.* The conductivity of ZnO thin films is very sensitive to the exposure of the surface to various gases due to its structure with polar, reactive facets.

- *Large non-linear optical coefficients.* ZnO thin films exhibit second- and third-order non-linear optical behavior, suitable for non-linear optical devices.

- *High thermal conductivity,* which translates into high efficiency of heat removal during device operation. ZnO also presents a very *high thermal stability* (with a high melting temperature, Tm= 2242 K), due to the high cohesive energy per bond, as high as 7.52 eV.

- *Availability of large single crystals.* One of the most attractive features of ZnO as a semiconductor is that large area single crystals are available. Moreover, the epitaxial growth of ZnO on native substrates can potentially lead to high quality thin films with reduced concentrations of extended defects, which could surpass the efficiencies obtained with GaN.

- *Amenability to wet chemical etching.* Due to its amphoteric nature, (dissolves at pH values below 6 and over 12), ZnO thin films can be etched both with acidic and alkaline solutions. This makes the processing, designing and integration of electronic and optoelectronic devices based on ZnO extremely flexible.

- *Exceptionally high radiation hardness,* which makes it a feasible material for applications at high altitude or in space.

1.1. Synthesis of ZnO nanostructures.

There is a very large variety of techniques that can be used for the synthesis of zinc oxide nanostructures. These techniques can be divided into two groups, bulk industrial methods and laboratory or pilot-plant scale methods, which mainly differ in the scale at which they are carried out, as well as in the used precursors, process temperature, and equipment [7].

Industrially, the largest proportion of ZnO is produced by the indirect (French) process. In this method zinc metal is vaporized at high temperature (1230–1270 ºC) in a crucible, and let out into the atmosphere with a calculated nozzle speed. This results in a rapid oxidation of the Zn vapor, producing a greenish-white flame, and the ZnO

powder formed by combustion is then aspired by a suction hood, led to a cooling duct and finally collected in the bag-house at a temperature below 100 ºC.

Other industrial methods are the direct process or hydrometallurgical methods. However, industrial methods are well understood and thus have less scientific interest, which is driven by the prospect of many exciting new technological functionalities for ZnO. In this sense, the methods used for the synthesis of ZnO in a scientific laboratory scale can also be divided into two major classes: (thermo) physical decomposition/evaporation and chemical soft solution based methods. We will now briefly discuss these two classes.

1.1.1. Evaporative techniques.

Methods in this first class typically convert zinc precursors into crystalline zinc oxide through gas-phase reactions at high temperatures and/or pressures. The most commonly used methods are chemical vapor deposition (CVD) and physical vapor deposition (PVD). CVD is a chemical procedure in which volatile precursors of the desired material are adsorbed onto the surface of a substrate, where they react and/or decompose to produce the desired deposit. PVD, on the other hand involves purely physical processes, such as high temperature vacuum evaporation or plasma sputter bombardment, rather than involving chemical reactions as in the case of CVD. In this sense, PVD compiles a variety of vacuum deposition methods, which differ in the way the precursors are transformed into the gas state. Some examples are thermal evaporation, in which the material to be deposited is heated to a high vapor pressure by electrically resistive heating in "low" vacuum, pulsed laser deposition (PLD), in which a high power laser ablates target material into vapor, or sputtering, in which a glow plasma discharge (usually localized around the "target" by a magnet) bombards the material sputtering some away as a vapor for subsequent deposition. Moreover, of each of these techniques there are also variations, e.g. thermal evaporation with the use of a liquid catalyst is known as the vapour–liquid–solid (VLS) approach, in which a droplet of a metal catalyst serves as a preferential site for absorption of gas phase reactant and, when supersaturated, a nucleation site for crystallization.

The synthesis of ZnO nanostructures with different morphologies using these techniques is being widely reported: ZnO nanorods/nanowires are typically obtained by vapor−liquid−solid (VLS) growth mechanisms [19-21], as the catalyst droplet defines the diameter of the nanorods/nanowires and directs their growth direction. Moreover, when neighbouring, these nanorods can coalesce and lead to single-crystalline ZnO

hollow microtubes, as reported by Jeong et al. [22]. Thermal evaporation without the presence of a catalyst, on the other hand, typically leads to the formation of ZnO nanobelts [23], which can spontaneously coil into nanorings so as to minimize the energy contributed by polar charges, surface area, and elastic deformation [24]. However, when lower temperatures and pressures were used, ZnO nanocolumns were obtained [25].

CVD can also render different morphologies depending on the conditions in which it is carried out. Umar et al. [26, 27] reported the obtaining of flower-like structures when using cyclic feeding in the CVD, as ZnO nuclei grow onto the firstly formed ZnO droplets, whereas Zhang et al. [28] obtained different hierarchical structures under different temperature and pressure conditions.

Some of the mentioned examples of the variety of the nanostructures grown by these evaporative techniques are shown in Figure 1.3, whereas reviews on the topic can be found in the literature, such as those by Hahn [6] or Wang et al. [29, 30].

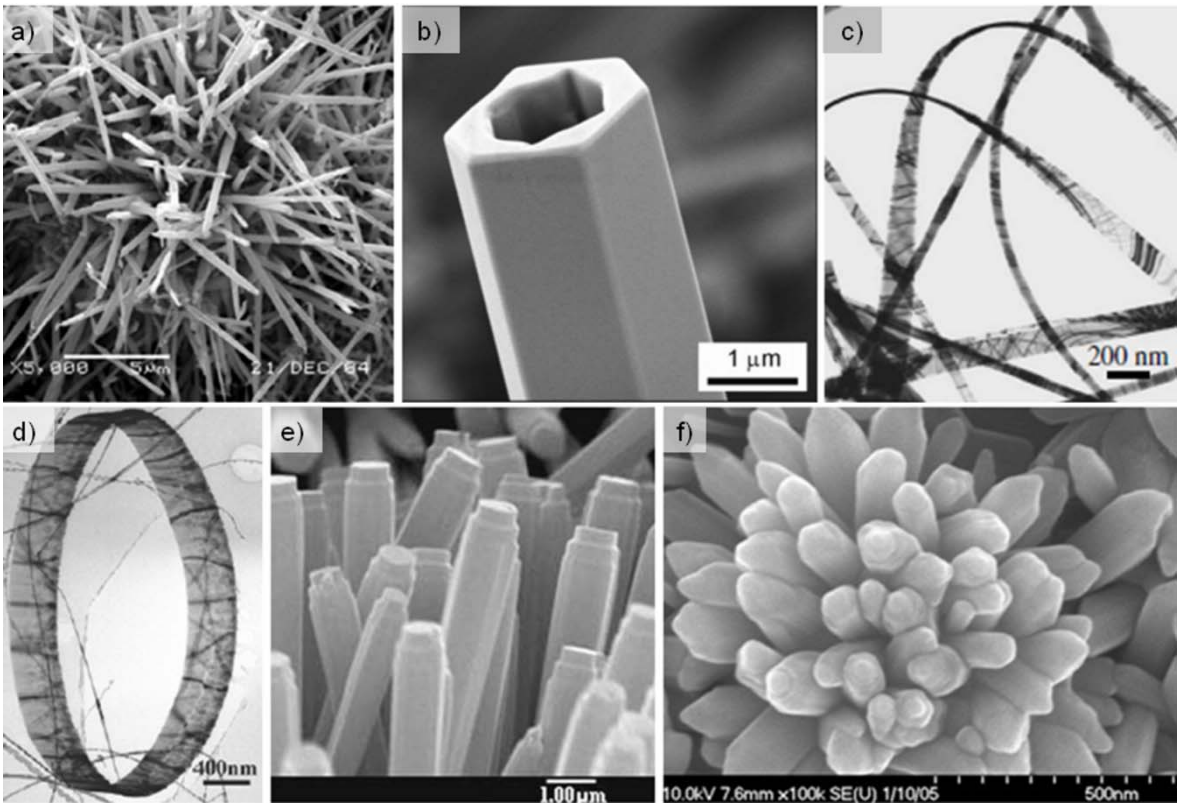

Figure 1.3: ZnO nanostructures grown by several evaporative techniques. a,b) nanowires and microtubes grown by VLS [20, 22]; c-e) nanobelts, nanorings and nanocolumns grown by thermal evaporation without catalyst [23-25]; f) flower-like structures grown by CVD [26, 27]

However, the obtaining of different ZnO morphologies by all these techniques is problematic, as they all have in common the use of highly energy consuming methods

(such as lasers, particle bombing, high temperatures/pressures, etc.) and sophisticated instrumentation for the transformation of the Zn precursors to the gas state. Moreover, they also result expensive, hardly scalable and quite often highly contaminant, due to the formation of corrosive gases.

1.1.2. Chemical soft solution processing.

Chemical soft solution processes stand out as feasible substitutes of the evaporative processes described in the previous section, and are increasingly focusing interest over other methods as powerful low-energy consumption routes to successfully control the crystallization engineering of ZnO. These solution methods are based on the hydrolysis of zinc salts which form intermediate species that generally transform to zinc oxide after a thermal treatment.

The term “soft solution processing’’ (SSP) was a term first used by Yoshimura et al. [31] which encompasses a wide range of methods used to prepare advanced solid state materials using a solution treatment at a low temperature. In this term “soft” implies less environmental charge, minimized energy and material consumption and no complicated instrumentation. The schematic representation of the energy and pressure vs. temperature maps of different growth methods are shown in Figure 1.4.

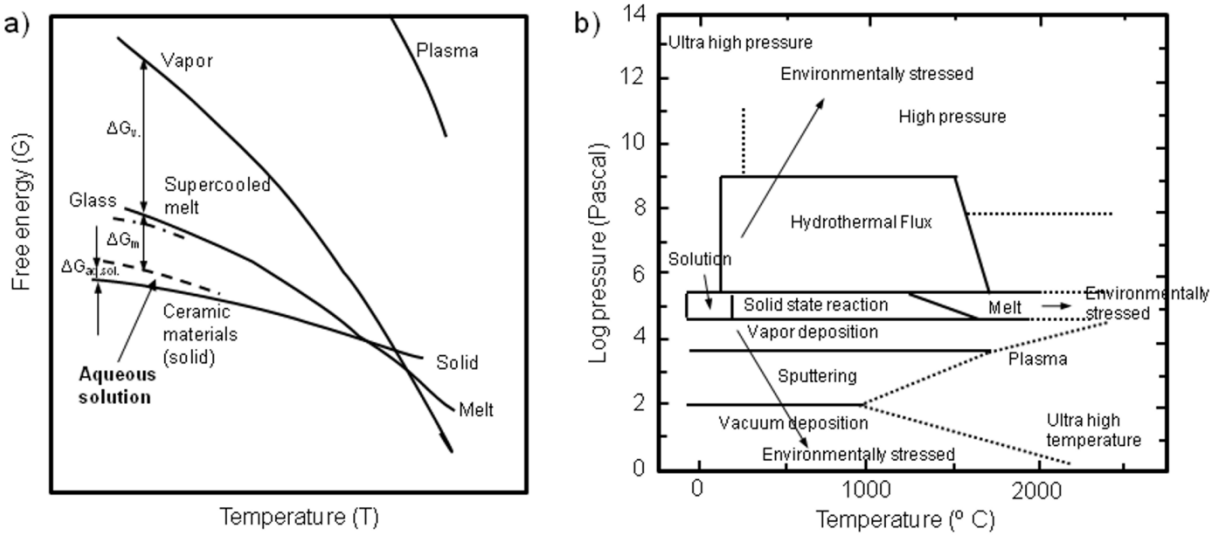

Figure 1.4: a) Schematic energy diagram (G-T) in a single component system, and b) schematic P-T diagram for growth techniques. From [32].

The solution treatment of the starting products can be carried out by different activation methods, such as chemical or electrochemical reactions, photochemical

excitation, application of microwaves or ultrasonics, hydrothermal reactions at a low temperature, etc., so as to prepare the desired materials. Some examples are direct precipitation, hydro/solvothermal synthesis, chemical bath deposition (CBD), sol–gel synthesis, electrochemical deposition, etc. These procedures, with low growth temperatures, allow large scale production of nanostructures in a simple, cost effective way, enabling a relative control of the obtained morphology and particle size at the same time. This is extremely relevant for the synthesis of zinc oxide, as it presents a wide range of morphologies due to the different surfaces in the ZnO structure: even though, under thermodynamic equilibrium conditions the highest growth rate is along the c-axis and elongated shapes are favored, described morphologies vary from nanowires and nanorods to dumbbell bipods, sheets, flakes, or hierarchical flower-like complex structures. Moreover, the properties of the ZnO nanostructures, and therefore their subsequent applications, heavily depend on morphology, crystal size, particle size distribution, degree of agglomeration, and porosity. Thus, these specific chemical, surface and microstructural properties of ZnO can be tuned by introducing changes into the procedure of its chemical synthesis.

1.1.3. Synthesis by precipitation.

For the first goal, direct precipitation/coprecipitation was chosen as synthesis method, as it provides a facile way for low cost and large-scale production, which does not need expensive raw materials and complicated equipments [33] and at the same time can be carried out in an ecologically sustainable environment, ideally water.

Precipitation occurs in three steps: supersaturation, nucleation and growth.

The *supersaturation* region can be reached by means of physical transformations (change in temperature or solvent evaporation) or chemical processes (addition of bases or acids, use of complex forming agents) (Figure 1.5). Within this region the system possesses a high Gibbs free energy, i.e, it is unstable, and precipitation occurs as a result of any small perturbation, reducing the overall energy of the system by segregating solute from the solution [34].

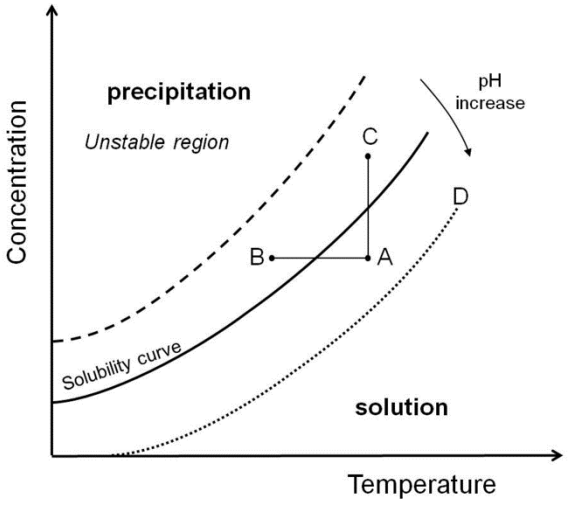

Figure 1.5: Solubility curves as a function of temperature and pH. Supersaturation can be achieved through solvent evaporation (A to C), temperature decrease (A to B) or pH increase (which moves the solubility curve to D and A into the supersaturation region) [35].

Formation of the precipitate within this region takes place in two steps, both driven by the reduction of Gibbs free energy: (i) nucleation, i.e, formation of the smallest elementary particles of the new phase which are stable under the precipitation conditions, and (ii) growth or agglomeration of the particles.

In the first step, *nucleation*, the reduction of the system's Gibbs free energy by forming a solid phase and maintaining an equilibrium concentration in the solution is counter balanced with the formation of new energetic surfaces. Therefore only those nucleation processes with enough energy to overcome the energy barrier, ΔG*, formed by the convergence of this two opposite phenomena will take place and develop into stable nuclei which are beyond a critical size r*. This energy barrier is described by the following equation [34]:

$$\Delta G^* = \frac{16\pi\gamma}{(3\Delta G_v)^2} \qquad \text{(Eq.1.1)}$$

where γ is the interfacial energy per unit area and ΔG_v is the change of Gibbs free energy per unit volume of the precipitate. This equation corresponds to homogeneous nucleation, this is, that which proceeds spontaneously. In the case of heterogeneous nucleation, that which is initiated by seed materials or surfaces, the equation presents a wetting factor:

$$\Delta G^* = \left[\frac{16\pi\gamma}{(3\Delta G_v)^2}\right]\left[\frac{2-3\cos\theta+\cos^3\theta}{4}\right] \qquad \text{(Eq.1.2)}$$

However, when the contact angle is 180º, i.e. the precipitate does not wet on the seed material or substrate at all, this wetting factor equals to 1 and the critical energy barrier becomes the same as that of homogeneous nucleation. Moreover, for contact angles less than 180º, the energy barrier for heterogeneous nucleation is smaller than that of homogeneous nucleation, which explains the fact that heterogeneous nucleation is much more common than homogeneous nucleation.

In this sense, nucleation can be controlled, to some extent, by modulating the critical size, which is in turn a function of the interfacial energy: the smaller the interfacial energy, the smaller the critical size and the more likely nucleation becomes for any given supersaturation [36].

Above the minimum concentration, nucleation and growth are inseparable processes, even though they take place at different speeds. However, after the initial nucleation, the concentration (supersaturation) of the growth species decreases, the change of Gibbs free energy reduces down to a value below the critical energy, and no more nucleation takes place, but growth proceeds (Figure 1.6).

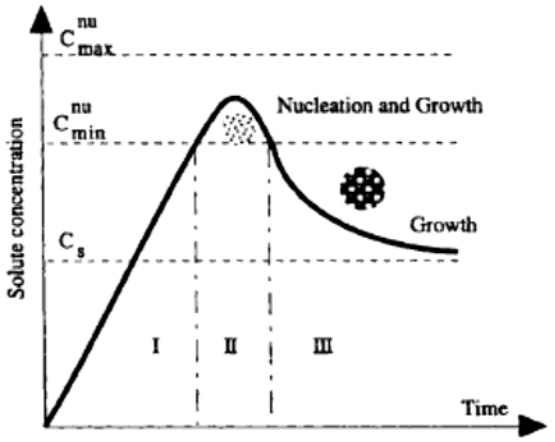

Figure 1.6: Schematic illustration of the processes of nucleation and subsequent growth, from [37].

Growth of the formed nuclei can be divided into two main processes: (i) diffusion, which compiles generation, diffusion and adsorption of species onto the growth surface, and (ii) growth itself, consisting on surface growth due to irreversible adsorption of growth species onto the solid surface. Diffusion-controlled growth promotes the formation of uniformly sized particles, whereas surface process-controlled growth can either promote uniform or non-uniform formation, depending on the type of growth (either mononuclear or polynuclear). Williams et al. [38] suggested that the growth of nanoparticles involves all three mechanisms: when the nuclei are small, mononuclear growth mechanisms may dominate, poly-nuclear growth becomes

predominant as the nuclei become bigger, and finally diffusion is predominant for the growth of relatively large particles.

However, even though the topic has been extensively studied, the mechanisms that define the final particle morphology remain unclear [39]. This is a major issue in the case of zinc oxide, as it is well known that the wide variety of ZnO particle shapes depends on the synthesis conditions, which alter the kinetics of both nucleation and crystal growth [40-44]. Basically, all process parameters influence the morphology of the final precipitation products, and fine tuning of the parameters is necessary in order to produce the required material.

1.1.3.1. Precipitation of Zinc Hidroxide.

In solution, the zinc salts acting as precursors undergo hydrolysis/dissolution processes, dissociating into their ions in the aqueous medium and forming intermediate species (which are considered to be in a reversible equilibrium) [45]. Nucleation is then induced by addition of a precipitant (tipically an alkaline reagent), and zinc hydroxide nuclei are formed and developed, which transform into ZnO after a subsequent thermal treatment. In aqueous solution, the following reactions are the main contributors to the formation of zinc oxide [46]:

$$Zn^{2+}_{(aq)} + OH^-_{(aq)} \leftrightarrow Zn(OH)^+_{(aq)} \quad \text{(Eq.1.3)}$$

$$Zn(OH)^+_{(aq)} + OH^-_{(aq)} \leftrightarrow Zn(OH)_{2\,(s)} \quad \text{(Eq.1.4)}$$

$$Zn(OH)_{2\,(s)} \leftrightarrow Zn(OH)_{2\,(aq)} \quad \text{(Eq.1.5)}$$

$$Zn(OH)_{2\,(aq)} + OH^-_{(aq)} \leftrightarrow [Zn(OH)_3]^-_{(aq)} \quad \text{(Eq.1.6)}$$

$$[Zn(OH)_3]^-_{(aq)} + OH^-_{(aq)} \leftrightarrow [Zn(OH)_4]^{2-}_{(aq)} \quad \text{(Eq.1.7)}$$

$$Zn(OH)_{2\,(aq)} \leftrightarrow ZnO_{(s)} + H_2O_{(l)} \quad \text{(Eq.1.8)}$$

$$Zn(OH)_{2\,(s)} \leftrightarrow ZnO_{(s)} + H_2O_{(l)} \quad \text{(Eq.1.9)}$$

$$[Zn(OH)_3]^-_{(aq)} \leftrightarrow ZnO_{(s)} + H_2O_{(l)} + OH^-_{(aq)} \quad \text{(Eq.1.10)}$$

$$[Zn(OH)_4]^{2-}_{(aq)} \leftrightarrow ZnO_{(s)} + H_2O_{(l)} + 2OH^-_{(aq)} \quad \text{(Eq.1.11)}$$

These reactions are mainly controlled by the pH of the system. $Zn(OH)_2$ will be formed when the OH^-:Zn^{2+} molar ratio is 2:1 (Eq. 1.4), and if more hydroxide is added soluble higher-order hydroxo-complexes of zinc may be formed (Eq. 1.6 and 1.7), which can decompose to ZnO (Eq. 1.10 and 1.11). Influence of these different reaction

intermediates, which are strongly pH dependent, on ZnO morphology has been described as extremely relevant in the literature [47], and several solution growth mechanisms have been suggested (see [48]).

At this point, the different parameters that affect the morphology of the ZnO products obtained by precipitation will be discussed.

- Zinc precursor.

It is generally assumed that the counter-ions of the zinc precursor present in the aqueous phase are eliminated during the subsequent heat treatments applied to obtain ZnO, and thus, their influence is often disregarded. However, it has been reported that variations in the counter-ion can result in changes in crystallinity, morphology and even chemical composition, since their complexes in solution act as precursors and thus condition the solid phase formation (nucleation) [49]. In this sense, the most commonly used precursors for the precipitation of ZnO are zinc chlorides, sulfates, nitrates and acetates, though the use of chlorides is gradually decreasing, as it may produce unwanted and contaminant Cl_2 species. The particular precursor is typically chosen as a function of the media in which the precipitation will take place: sulfates and especially nitrates are commonly used for the precipitation in organic media, given the amount of ammonium-derived complexes that can be formed in aqueous media. Acetate precursors, on the other hand, are more commonly used in aqueous solutions.

Srikanth and Jeevanandnam [50], and more recently, Giraldi et al. [51] reported the effect of each of these anions (Cl^-, SO_4^{2-}, NO_3^-, and CH_3COO^-) on the morphology of ZnO prepared by homogeneous precipitation, e.g. $ZnCl_2$ led to plate-like morphologies, whereas $Zn(NO_3)_2$, and $ZnSO_4$ rendered semi-spherical particles or $Zn(CH_3COO)_2{\cdot}2H_2O$ produced irregular shaped ZnO agglomerates. The different morphologies have been ascribed to the crystal growth inhibition caused by the adsorption of the different counter-ions to certain faces of ZnO. As an example, Govender et al. [52] reported the obtaining of millimetric ZnO platelets from zinc sulfate solutions, due to a considerable crystal growth inhibition of the polar *c* faces by sorption of the sulfate anions. Moreover, Giraldi et al. [53] also reported how the strong adsorption of carboxylate species derived from the use of zinc acetate stood rinsing and thermal treatments at temperatures as high as 300ºC. However, it is generally believed that the behavior of different counter-ions cannot be solely ascribed to their behavior as surface modifiers, but also to the nature and structure of their precursors, which play a key role in the determination of the size and morphology of the ZnO products. Along this line, Distaso et al. [54] reported the formation of primary ZnO

crystallites organized in the linear and three-dimensional structures typical of the acetate and nitrate precursors, respectively. This behavior is especially relevant for zinc acetate, as the morphology of the products obtained from it are determined by the formation of layered basic zinc acetate (LBZA), $Zn_5(OH)_8(CH_3COO)_2 \cdot nH_2O$, when immersed in water [55]. The structure of this product consists of a stacking of complex hydroxyl layers, $[Zn_5(OH)_8(H_2O)_2]^{2+}$, in which three fifths of zinc ions are octahedrally coordinated to six OH^- groups, and two fifths of them are located above and below the octahedrons, forming tetrahedra composed of three OH^- groups and one water molecule, as shown in Figure 1.7a [56, 57]. In this structure acetate molecules are located in between layers, balancing the charge.

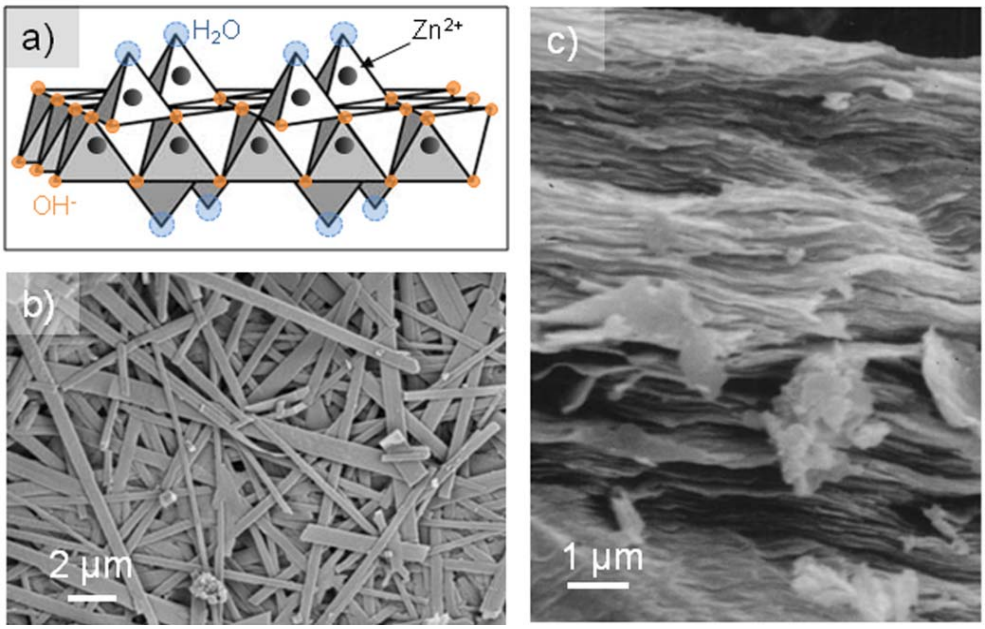

Figure 1.7: a) complex layer of $[Zn_5(OH)_8(H_2O)_2]^{2+}$ present in the LBZA structure; b and c) SEM micrographs of typical LBZA morphologies (from [56, 58]) .

This structure is responsible for the typical layered crystallization morphologies of LBZA, e.g. flakes, needles or thin, elongated plates (see Figure 1.7b and c). Moreover, it is also responsible for these morphologies in ZnO, since, as reported by Golgotiu et al. [59] the decomposition of LBZA leads to the formation of a mixture of zinc oxide and a second phase identified as a zinc oxoacetate, which undergoes a transformation at higher temperature that leads to zinc oxide.

- Precipitant agent.

Another parameter to take into account during precipitation is the choice of the precipitant agent, which can also have a notorious influence on morphology. It has been

reported that hydrolysis does not take place readily for divalent metal ions, and thus addition of a base is crucial for the precipitation of the hydroxide [60]. In this sense, the most commonly used bases are NH_4OH/NH_3 and different alkalis. The use of ammonia/ammonium hydroxide as base for the precipitation of ZnO, however, can result problematic, as several zinc-ammonia complexes can form, which are not easily removed. On the other hand, the use of the different alkalis and their role on ZnO morphology and size is still a controvesial topic. In this sense, Chittofrati et al. [49] reported that, even though both produced large crystals, ZnO crystals grown with NaOH had a worse aspect ratio than those grown with KOH. However, these results were opposed to those of Uekawa et al. [61], who observed that as the cation (Na^+, K^+, Cs^+) became larger the resultant ZnO crystals became more irregular, but in general there appeared to be a decrease in crystal size. Moreover, Uekawa et al. also reported that the rate of zinc oxide precipitation from the $Zn(OH)_4^{2-}$ aqueous solution also depended on the ionic radius of the cation ($Li^+<Na^+<K^+<Cs^+$) which was adsorbed onto the ZnO nuclei. In aggrement with this, in a more recent work, Viswanatha et al. [62] reported the virtual capping effect of Na^+ ions from NaOH, which migrate to the nanocrystal surface and act as counterions to the OH^- species attached to it, thereby hindering the approach of Zn^{2+} ions necessary for further growth. This fact coincides with another method for controlling morphology during precipitation: the use of surfactants, polymers and different organic additives that can act as promoters or inhibitors of the nucleation and growth processes [63-67]. This procedure is quite extended for the preparation of ZnO nanostructures, as the characteristic structure of ZnO-wurtizte allows somewhat predicting the preferential binding of the molecules to certain facets according to their charge. Although the precise mechanism of each particular additive is different and characteristic, these molecules usually tune the surface energy of the synthesized nuclei by blocking/hampering the growth in one or more faces, hence letting the crystal develop only in certain directions/morphologies [68-70].

- Solution media.

As mentioned preciously, the choice of the zinc precursor is closely related to the media in which precipitation will take place, e. g. as water is a dipolar, amphiprotic solvent with a high dielectric constant most salts are readily dissolved in it. On the other hand, most alcohols are dipolar, amphiprotic solvents whose dielectric constants and viscosities dependent on the chains lengths. Moreover, the kinetics of nucleation and growth, as well as processes such as coarsening and aggregation are strongly dependent on the properties of the solvent. In this sense, Hu et al. [71] described the influence of solvent on the synthesis of ZnO nanoparticles by precipitation from zinc

acetate, as a means to achieve control over their size and particle size distribution. In any case, even though hystorically organic media were more common, the trend nowadays is towards the use of a more sustainable and ecofriendly chemistry, and thus the use of aqueous solution, which present the adddtional advantage of their low cost.

- Subsequent thermal treatment.

Finally, as mentioned previously, the precipitated zinc hydroxide has to undergo a subsequent thermal treatment in order to obtain the desired ZnO nanostructures. Some authors have handled the issue of the thermal treatment step by increasing the temperature precipitation process to prepare uniform ZnO particles without a further thermal decomposition process [72].

1.1.3.2. Coprecipitation of doped ZnO.

Doping of ZnO with selective elements stands out as an effective method to adjust its electrical, optical, and magnetic properties, necessary for many of its innovative applications, such as electronics, optoelectronics, and magnetic devices [5, 7, 73]. The issue of which dopant to use in order to enhance certain properties has been extensively studied, e.g. doping with group-III elements (Ga, Al, In) is commonly used for the obtaining of n- type ZnO-based semiconductors, whereas doping with transition metals, rich in electron states, is described as a way to develop ferromagnetic properties in ZnO [11, 74, 75]. However, the introduction of dopants during growth often results in the change of morphology.

In this sense, it has been reported that doping with Cobalt can tune both optical and magnetic properties without changing the morphology of the ZnO powders, which depends on the synthesis parameters, but might slightly reduce the particle size. More specifically, Wang et al. [76] reported that the incorporation of up to 10 mol % of Co in the ZnO lattice leads to a slight contraction of the unit cell, so as to accommodate the smaller Co^{2+} ions (ionic radius in tetrahedral coordination T_d= 0.058 nm) which replaced Zn^{2+} ions (ionic radius T_d=0.060 nm [10]. In this work, the authors suggested that the dopant atoms might add a thermodynamical barrier to the phase transformation from the precursor precipitate to ZnO nanocrystals, which would result in a slowdown of the whole process and thus a decrease in particle size.

$Zn_{1-x}Co_xO$ materials raise high expectations as potentially exhibiting room temperature ferromagnetism for application in magnetic semiconductors [77]. Still, different studies have proven that magnetism is very sensitive to preparation conditions

and shape of the samples (bulk, thin films and particles), and ever since the first report on ferromagnetism in Co:ZnO was published [78], sample quality and reproducibility have been issues that arise huge controversy [79]. Along these lines, and among the range of methods for the synthesis of Co-doped ZnO [33, 80-83], coprecipitation allows the mixing/mixture of the reagents at molecular levels and thus the easy incorporation of the Co^{2+} ions into the ZnO lattice by inclusion mechanism, [76] in what Kolthoff [84] described as mixed crystal formation.

1.1.4. Hydrothermal processing of ZnO nanostructures.

Yoshimura et al. defined hydrothermal processing as "any homogeneous (nanoparticles) or heterogeneous (bulk materials) reaction in the presence of aqueous solvents or mineralizers under high pressure and temperature conditions to dissolve and recrystallize (recover) materials that are relatively insoluble under ordinary conditions" [85]. Amongst the soft solution processing methods for the processing of advanced materials, hydrothermal processing allows the obtaining on highly crystalline products with a good nucleation control, high dispersion, high rate of reaction and a good control of their morphology. Moreover, as it allows tailoring of the chemical environment and accelerates interactions between solid and fluid species, mass transport and powder dissolution are facilitated and thus phase pure and homogeneous materials can be achieved.

This kind of processing consists of two different stages: hydrothermal synthesis and hydrothermal growth.

The hydrothermal synthesis stage of ZnO is ruled by dissolution-reprecipitation processes, and in situ crystallization transformation, which involve dehydration and internal atomic rearrangements [86-88]. Therefore, hydrothermal synthesis, as opposed to precipitation, allows obtaining of ZnO structures directly, without need of a subsequent thermal treatment, as the conditions of high temperature and pressure inside the reactor are enough for $Zn(OH)_2$ to transform into ZnO.

The hydrothermal growth stage, on the other hand, is ruled by nucleation and growth processes. In the case of ZnO, given its characteristic surface chemistry these processes –and thus the resulting morphology of the ZnO nanostructures- can be tailored in different ways. The most commonly used method for the control of the morphology of ZnO nanostructures during hydrothermal growth is the use of capping agents, i.e surfactants, polymers and different organic additives that can act as

promoters or inhibitors of the nucleation and growth processes. However, the use of this kind of additives, somehow reduces the “eco-friendliness” of the process.

Hence, an alternative way of controlling the morphology of ZnO structures during hydrothermal growth is the use of substrates, known as heterogeneous hydrothermal growth. It has been reported that the incorporation of substrates to the hydrothermal growth processing, specially seeded or pretreated ones, not only allows the obtaining of coated architectures with intended properties, but it may also represent a handy way of controlling the morphology, texture and orientation of the grown ZnO structures [89-91]. This is due to the intrinsic competition between homogeneous and heterogeneous nucleation that takes place in solution processes: the interfacial energy between crystals and substrates is typically lower than that between crystals and solution [92], as the molecules in the crystal can form bonds with those in the substrate that are stronger than the bonds of solvation. This, together with the fact that heterogeneous nucleation generally has a lower activation energy barrier than homogeneous nucleation favors that the first one will occur more readily onto a foreign surface. In other words, the presence of energetically favorable sites on the rough surface of the substrate may enable heterogeneous nucleation and this could lead, under certain specific conditions, to the creation of a hierarchical structure.

The use of ZnO-seeded substrates allows the obtaining of specific morphologies, depending on the substrates and on the seed layer nature. In this sense, Guo et al. [93] and Weng et al. [94] reported how the morphology of ZnO nanostructures varied as a result of the different preparation of the seed-layer after the same solution growth, whereas Yang et al. [95] described the hydrothermal growth of pencil-like, well aligned and oriented 1D ZnO nanorods, on Si wafers, Cu substrates and ZnO seeded Si substrates. Even though these two last references were published during the development of this thesis, they did not take into account the influence of the nature of the seed layer itself (in terms of crystallinity and composition), but only considered the preparation method and nature of the substrate. This fact, in contrast, has been considered in this thesis and will be discussed in following chapters.

1.2. ZnO thin films by colloidal processing.

Ceramic materials can be shaped into very different conformations (from bulk to films). However, in this work we will just focus on the preparation of thin films, which are the research topic of our interest.

Thin films are defined as microscopic two dimensional layers (with a high area/volume ratio) with thicknesses in the nanometric or submicronic range, which are deposited on a supporting material (e.g. substrate).

As for the powders, there is a vast number of methods available for the preparation of ZnO thin films, most of which are physical methods that start from a gaseous phase. Some examples of these methods are physical vapor deposition (PVD) [96], RF magnetron sputtering [97], spray pyrolisis [98], metal organic chemical vapor deposition (MOCVD) [99] or pulsed laser deposition (PLD) [100]. However, colloidal, i.e. solution-based methods are slowly taking over interest, as they allow the economical, reliable production of films with complex shapes, small defect size/numbers, good phase dispersion and homogeneous compositions. This is achieved through a careful control of the starting suspension, that has to be stable, and the different types of interparticle forces in it.

1.2.1. ZnO in aqueous media.

When a ceramic particle is immersed in a polar liquid medium, i.e. water, there is a build-up of charge at the solid liquid interface, due to different charging mechanisms [101, 102]. This surface charge influences the distribution of nearby ions in the polar medium, which rearrange in order to neutralize it, forming an electric double layer. This consists of an inner layer, known as Stern layer, formed by a monolayer of counter-ions attached to the particles surface, and a diffuse layer, in which a neutralizing excess of ions and counter ions distributed in a diffuse manner in the polar medium form an “ionic atmosphere” around the particle [103]. The resulting potential at the shear layer formed between the stern and the diffuse layer when the particle moves in the liquid is known as electrokinetic or zeta potential (ζ), and its value is proportional to the surface charge of the particle. Moreover, the pH value at which the zeta potential of a powder is zero is known as isoelectric point (IEP) [1], and its characteristic of every particle-solvent system.

In the case of metal oxides formation of hydroxide layers (≡M-OH) on their surface due to hydrolysis is a very common phenomenon, as water molecules can be both physically and chemically adsorbed onto the surface of the dispersed oxide particles. It

[1] The IEP shouldn’t be confused with the point of zero charge (PZC), where net charge on the surface is zero. The IEP and the PZC will be the same only if there is no adsorption of other ions rather than the potential determining H^+/OH^- at the surface.

is these hydroxide layers that become charged by reacting with H^+ or OH^- species due to surface amphoteric reactions [104], giving place to positively charged surfaces at low pH values, by proton H^+ adsorptions, or negatively charged surfaces at high pH values, due to proton losses.

$$\equiv M\text{-}OH + H^+ \leftrightarrow \equiv M\text{-}OH^{2+} \qquad pH < 7 \qquad \text{(Eq.1.12)}$$

$$\equiv M\text{-}OH + OH^- \leftrightarrow \equiv M\text{-}O^- + H_2O \qquad pH > 7 \qquad \text{(Eq. 1.13)}$$

For ZnO in aqueous media, the surface zinc hydroxide layer, ≡Zn-OH or $Zn(OH)_{2(S)}$, is in equilibrium with different species in solution, whose fraction varies over a range of pH (see Figure 1.8).

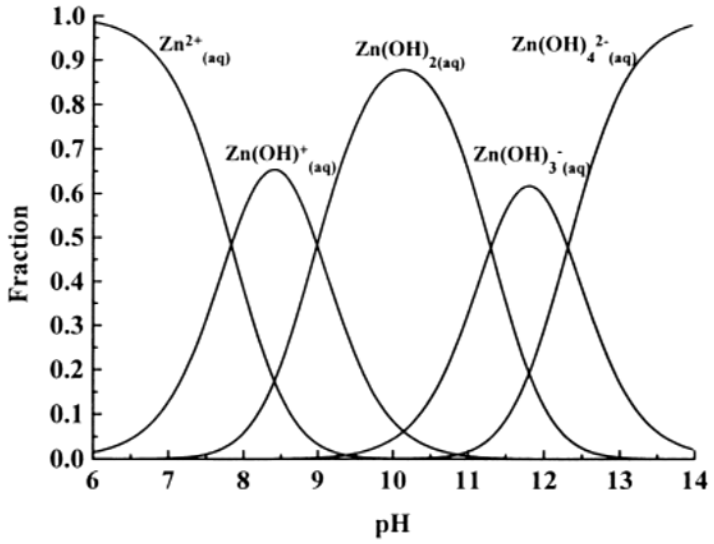

Figure 1.8: Fraction of Zn (II) ions species existing as $Zn^{2+}_{(aq)}$, $Zn(OH)^+_{(aq)}$, $Zn(OH)_{2\,(aq)}$, $Zn(OH)_3^-{}_{(aq)}$ and $Zn(OH)_4^{2-}{}_{(aq)}$ over a range of pH at 25ºC [104, 105].

In this case, the mechanism of surface charge consists mainly on the formation of hydroxylated metal species in solution, according to the following reactions,

$$\equiv Zn\text{-}OH^+ + H^+ \leftrightarrow \equiv Zn\text{-}OH_2 \qquad pH < 7 \qquad \text{(Eq. 1.14)}$$

$$\equiv Zn(OH)_2 + H^+ \leftrightarrow Zn(OH)^+ + H_2O \qquad \text{(Eq. 1.15)}$$

$$\equiv Zn\text{-}OH^+ + OH^- \leftrightarrow \equiv Zn\text{-}O + H_2O \qquad pH > 7 \qquad \text{(Eq. 1.16)}$$

$$\equiv Zn(OH)_2 + OH^- \leftrightarrow [Zn(OH)_3]^- \qquad \text{(Eq. 1.17)}$$

When, as in this case, H^+ and OH^- are the potential determining ions, the number of charge sites and the surface charge of the oxide particles are determined by the pH of the solution. In this sense, one of the most useful “tools” to tailor stabilization is zeta potential measurements. By measuring the zeta potential vs. pH of a suspension a

graphical representation of the surface charge behavior as a function of pH will be obtained. According to the literature, ZnO presents its IEP at a pH ≈ 8.5 [106, 107], which implies that it will be positively charged at pH < 8.5 and negatively charged at pH > 8.5 (Figure 1.9a). Therefore, considering its zeta potential, ZnO can (theoretically) be stabilized by just a pH adjustment, locating the suspension at a pH far from its isoelectric point. However, the useful pH range will need to be limited to 7 < pH < 12 in order to avoid ZnO dissolution (see Figure 1.9b).

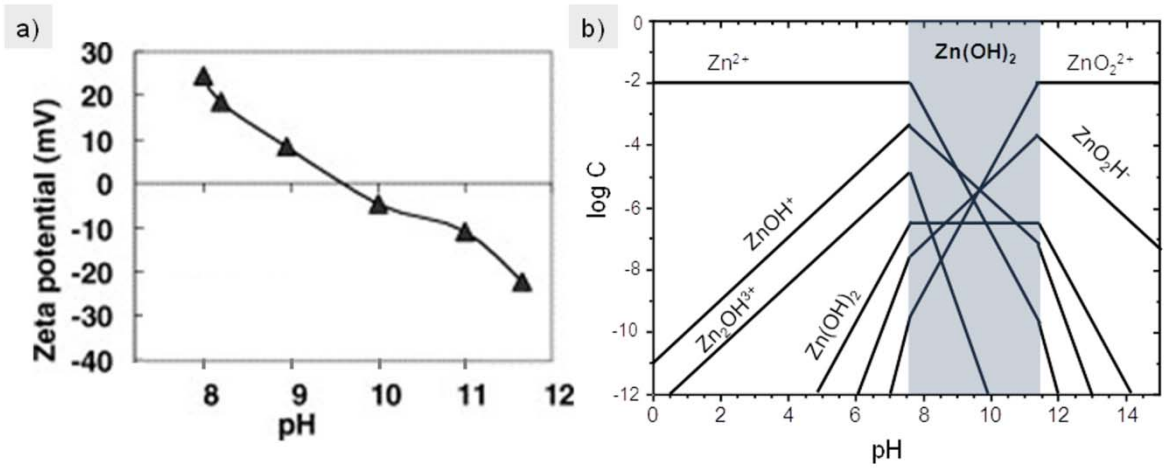

Figure 1.9: a) zeta potential vs. pH curve of ZnO (from [108]) and b) log [Zn^{2+}] vs. pH diagram. The area lighted in blue corresponds to the predominance pH range of $Zn(OH)_2$.

In practice, the effective design of stable suspensions based only on electrostatic stabilization is not trivial, and when it comes to ZnO, the influence of the reactivity of the different kind of surfaces also plays a key role in its stabilization, as will be discussed in the following section.

1.2.2. Influence of the kind of surfaces in the colloidal chemistry of ZnO.

It has been repeatedly reported in the literature how the surface chemistry of ceramic particles in aqueous suspension highly influences their dispersion and stabilization. One of the first reported examples was the clay–water system, the first colloidal system to be extensively studied. [109-111]. Clay particles generally have a plate-like morphology, which shows a differential surface charge when suspended in a polar solvent (typically due to isomorphic substitutions or adsorption-desorption reactions): the basal facets are negatively charged, whereas the edges appear positively charged. This surface charge is responsible for their tendency to form the house of cards structure in solution, as well as for the formation of ion-electrostatic

interactions and hence their capacity to swell [112-114]. Kelso et al. reported a similar behavior for aqueous suspensions of alumina [115]. They observed how different surface chemistries of alumina powders lead to differences in pH, magnitude and sign of the dispersions mobility (zeta potential). This, in turn, lead to differences in the amount of dispersant required to stabilize the system. Franks and Gan [116] also studied the charging behavior of alumina surfaces, putting special interest in the structure of the different surfaces: when immersed in water, hydroxyl group (OH^-) terminated surfaces are formed, that can be singly, doubly or triply coordinated. These are preferentially formed on certain facets: basal planes of Al_2O_3 and $Al_2(OH)_3$ are composed of doubly coordinated surface hydroxyl groups, whereas singly coordinated ones occur in greater proportion on prismatic and high index planes, as well as on the edge of the basal plane. These different types of surface hydroxyl groups have different reactivity (pKa values), and thus different charging behavior. The overall charge of the particle results from the combination of contributions from the basal plane and the edge faces. On the other hand, colloidal sized particles (from powder) have surfaces composed of plane edges, steps, vacancies and other defects, and therefore, mainly show singly coordinated surface hydroxyl groups which have much higher pKa values.

Something similar occurs for ZnO. As we described in section 1.1., ZnO presents a hexagonal, non centrosymmetric structure which is polarized along the c-axis, and this gives rise to polar and non polar facets with different reactivity. In a review published in 2007, Woll [13] described the structure of these different facets and their distinct reactivities towards several adsorbates. In this way, he reported how for the ZnO $(010\bar{1})$ nonpolar surface with no electrostatic instabilities and truncated bulk structure, the adsorption of CO_2, CO, H_2O and H atoms gives place to ordered adlayers. However, the situation differed for polar surfaces: for the Zn-ZnO surface, the general consensus states that it essentially presents a (1x1) structure, terminated by Zn atoms and exhibits a high density of steps forming triangular terraces, which make it specially reactive to small molecules, such as H and CO and provide active sites for the dissociation of Brønsted acids [18] (see Figure 1.10a). Nevertheless, the most interesting surface of ZnO from a chemical point of view is the oxygen terminated polar surface, O–ZnO. In this case, there is still no convincing mechanism proposed for the removal of its electrostatic instability. There are experimental evidences that a hydrogen-terminated (1×1) O-ZnO is formed whenever ZnO is not in vaccum (though theoretically unstable) and a (1x3) reconstruction mechanism has been suggested for the clean, hydroxyl-free O-ZnO surface (although this mechanism has remained controversial). The model for this reconstruction basically consists of an ordered array of O-vacancies which renders the surface a very high reactivity (Figure 1.10d).

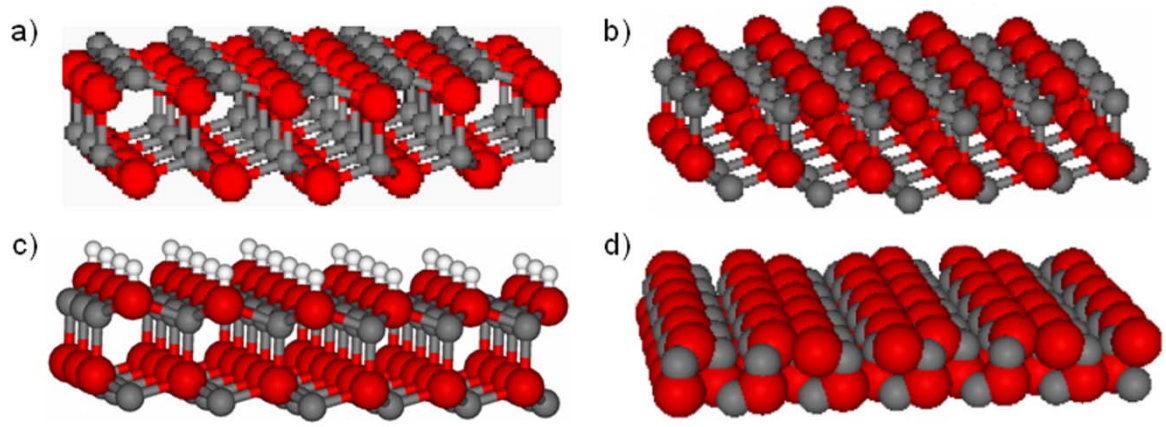

Figure 1.10: Structures of (a) an ideal, unreconstructed Zn–ZnO surface (b) an ideal oxygen-terminated polar surface, (c) the H-saturated (1x1) O–ZnO surface, and (d) model proposed for the (1x3)-reconstructed surface of the O–surface. Note, that all four models are electrostatically instable. Zn atoms are represented by the grey, small balls, O atoms by the red balls and H atoms by the white ones.

In any case, it is clear that these different surface reconstruction/stabilization mechanisms dramatically affect the surface behavior [101, 102] and thus the reactivity of the polar ZnO surfaces [117], and this will have a relevant effect on the different methods used to enhance stabilization and dispersion.

1.2.3. Colloidal Stabilization.

Colloidal stability is given by the total interparticle potential energy, V_{total}, which is determined by the balance between attractive Van der Waals forces (V_{vdW}), and repulsive ones, mainly double-layer (electrostatic, V_{elect}) and/or steric (V_{steric}) interactions:

$$V_{total} = V_{vdW} + V_{elect} + V_{steric}$$

There are three main stabilization mechanisms based on these repulsive interactions [118]:

- Electrostatic mechanism: due to double-layer repulsion between particles. Its extent is controlled by the thickness of the electrical double layers (commonly identified with the Debye length).
- Steric mechanism: based on the adsorption of polymers onto the surface of the particle, stabilization is due to the physical impediment created by the organic chains.

- Electrosteric mechanism: based on a combination of the both previous mechanisms, polyelectrolytes or charged dispersants are adsorbed onto the surface of the particles.

A theory for the overall net interaction energy between charged spherical particles as a function of interparticle separation was developed (independently) by Deryagin and Landau and Verwey and Overbeek (known as DLVO theory). This theory suggests that the total interparticle potential (V_{total}) is obtained by the addition of the electrostatic repulsion (V_{elect}) and the van der Waals attraction (V_{vdW}). This is represented in Figure 1.11.

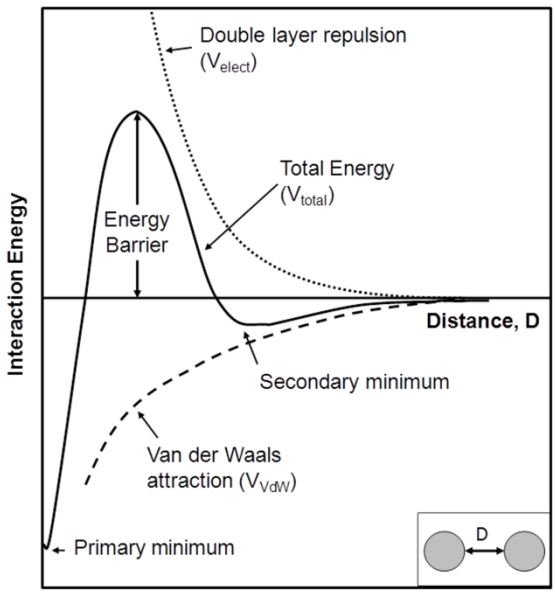

Figure 1.11: Representation of the interaction energy as a function of separation between two particles in suspension [119].

The graphical representation of V_{total} presents two minimums, in which attractive forces overcome repulsive ones: in the first one, known as primary minimum, particles are in touch, forming hard agglomerates and leading to coagulation. On the other hand, in the secondary minimum, particles are separated and only soft agglomerates are formed, leading to flocculation, which can be reversed. Thus the optimal stabilization and dispersion point is the maximum in the V_t curve, where repulsive interactions overcome attractive ones, (V_t < 0) forming an energy barrier which prevents coagulation. The position of the energy barrier and the depth of the secondary minimum depend on the nature of the particles surface and the conditions of the medium surrounding it (such as pH, dielectric constant, etc.). In addition, it has been reported that the barrier height diminishes with decreasing particle size, therefore

nanoparticles are more susceptible to coalescence [120]. However, this theory, though widely accepted, disregards the effect of non electrostatic interactions.

Experimentally, the total repulsive interaction is measured through the zeta potential of the suspensions and the determination of their IEP, which corresponds to the maximum instability of the suspension. These parameters mainly depend on the surface chemistry of the particle in the specific media, which can be tuned by modifying the surface charge of the particles.

1.2.4. Surface charge modifiers.

There are four main mechanisms through which a particle can acquire surface charge: (a) Preferential adsorption of ions, (b) Differential Solution of Surface Ions, (c) Isomorphic Substitution of ions, or (d) Physical adsorption of charged species onto the surface [34]. Mechanisms (a) and (b) have already been described somehow previously (see section 1.2.2) and mechanism (c) is most common for clay materials, hence we will basically focus on mechanism (d), which refers to steric or electrosteric stabilization, i.e the use of dispersants.

Dispersants are generally organic molecules (often polymeric in nature) adsorbed onto the particles surface to induce repulsion. In order to be effective, dispersants need to fulfill some requirements: the adsorbed layers must be of sufficient thickness to overcome van der Waals attraction, dense enough to avoid bridging flocculation between particles and anchored firmly enough to avoid desorption during particle collisions. Moreover, these dispersants/polymers can present ionizable groups (such as carboxylic or amine groups), case in which they are known as polyelectrolites, and the stabilization mechanism is considered to be electrosteric. Polyelectrolytes can be cationic (with organic groups that ionize positively at low pH), stabilizing suspensions at positive zeta potentials (pH < PIE) or anionic (with organic groups that become negatively charged with pH), stabilizing suspensions at negative zeta potentials (pH > PIE).

The adsorbed polymers (both charged and uncharged) can present different conformations for their anchoring (as depicted on Figure 1.12), depending on various parameters such as pH, ionic strength, used solvent, molecular architecture, etc. [114].

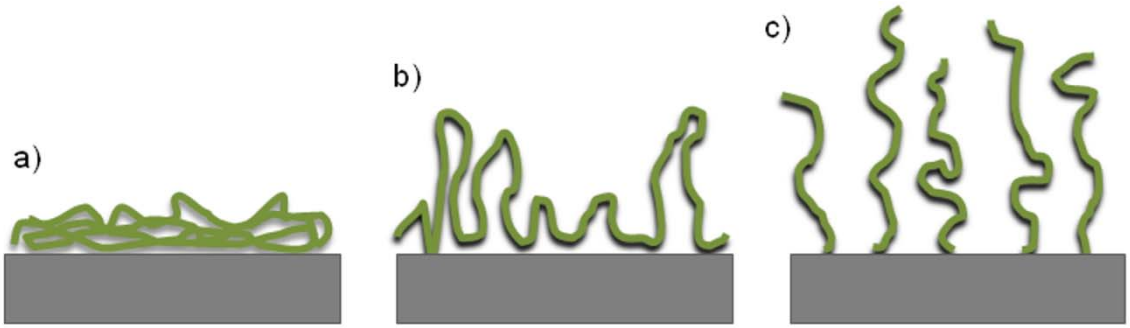

Figure 1.12: Possible adsorption conformations of a polymer: a) train, b) loop and c) tail.

In this sense, polyelectrolyte adsorption is strongly influenced by the chemical and physical properties of the solid surfaces and solvent medium. As an example, due to the different nature of their surfaces (described in the previous section), single crystal alumina and alumina powders present different IEPs and therefore the adsorption behavior of solution species will be significantly different on the two different types of surfaces, e.g. anionic polymers, adsorb to alumina particles over a wide range of pH while they would not be expected to adsorb to single crystal sapphire except at pH below 4 or 5 [116]. In this type of stabilization the relative importance of the respective contributions (steric and electrostatic) is closely related to the conformation acquired by the polyelectrolyte: if it presents a train conformation, the polymeric repulsion is short range, and the stabilization mechanism is mainly electrostatic (typical for highly charged polyelectrolytes with an extended conformation attached to oppositely charged particles). However for a tail conformation, with chains “dangling” into the solution, the steric mechanism gains importance.

The conformation acquired by polyelectrolytes depends on whether they are strong polyelectrolytes, for which the degree of ionization is independent of the solution pH, or weak polyelectrolytes, for which the degree of ionization is determined by the solution pH [121]. An example of a weak polyelectrolyte is polyethylenimine (PEI), a widely used cationic electrolyte, with amines as polarization group (see structure in Figure 1.13).

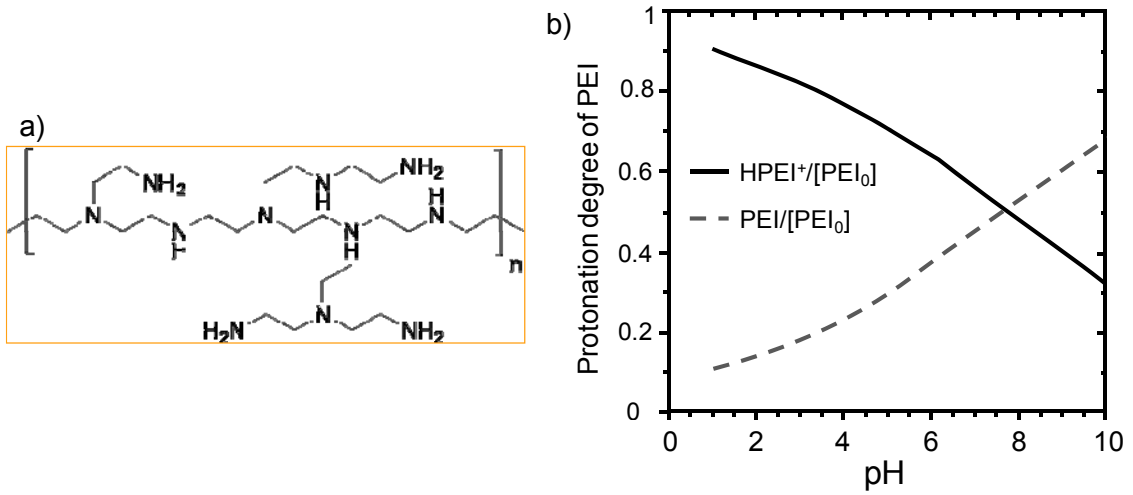

Figure 1.13: a) structure of polyethylenimine, and b) graph representing the effect of pH on the protonation of PEI.

At low pH values almost all the amine groups become positively charged as they acquire protons, and the PEI molecules are in a fully extended state with maximum repulsion. These protons are gradually lost as pH increases, e.g. only half of all amine groups in the PEI are still charged at pH≈6.5 at 0.05 M NaCl, and all are completely uncharged at pH≈11 [122, 123]. Avadiar et al. [124] reported that the use of PEI with different molecular weights did not have an influence on their dissociation. However, in another work, Verde et al. [125] showed that the molecular weight of the used PEI does have an effect on dispersion.

1.3. Electrophoretic deposition.

Amongst thin film preparation techniques, Electrophoretic deposition (EPD) stands out for its cost-effectiveness, versatility and high potential for scaling up to large volumes. Moreover, and in contrast to other colloidal processing methods, it allows direct shaping of dense ceramic bodies from stable colloidal suspensions with low solid contents (< 10 g/L). Actually EPD might become an alternative to evaporative coating processes used to tailor ceramic nanostructures and assembly of nanoparticles.

EPD consists of the application of field to a suspension containing surface-charged particles, so that these particles migrate towards an oppositely charged electrode (electrophoresis), and subsequently “accumulate” on it, forming a coherent,

homogeneous deposit. Generally, in order to densify the deposit, which is no more than a powder compact, a subsequent thermal treatment is required.

The main parameters that determine the effectiveness of EPD are those related to the suspensions and their stability: suspensions must be stable and well dispersed for particles to migrate and deposit independently. So as to be able to migrate particles must present a high electrophoretic velocity, *v*, which is related to the applied electrical conditions, E, and to the electrophoretic mobility of the particles, μ_e.

$$v = E \cdot \mu_e \qquad \text{(Eq.1.18)}$$

The electrophoretic mobility, μ_e., in turn, is related to their zeta potential (ζ) through Henry's equation:

$$\mu_e = \frac{\zeta \cdot \varepsilon}{\eta} f(\chi \cdot r_p) \qquad \text{(Eq.1.19)}$$

where ε is the dielectric constant of the medium, η its viscosity and $f(\chi r_p)$ a parameter dependent on the inverse of Debye's length(χ) and the particle radio (r_p).In this sense, solid content of the suspensions is also determinant, as the deposition speed depends on the solid loading: for low solid contents particles will deposit at a speed proportional to their μ, but for high solid loadings (specially for multicomponent particles) speeds of the different particles balance.

Moreover, suspensions also need to have an adequate conductivity (determined by the number of charge carriers (ions and/or particles), which determines the viability and the efficiency of the process [126, 127].

Historically, EPD has been carried out in organic, non-aqueous media so as to avoid unwanted reactions such as the hydrolysis of water or oxidation of metallic electrodes [128, 129]. However, the use of aqueous systems is gaining increasing interest, due to its lower cost and sustainability. In this sense several methods based on the discontinuity of the electric field, such as the use of AC current [130] and/or pulsed DC current [131, 132] have been suggested to tackle with the mentioned problems of aqueous EPD.

1.3.1. Kinetic models of EPD.

The first model describing EPD kinetics was developed by Hamaker [133] in 1940, relating the deposited, *m* (g) with suspensions parameters, such as concentration, C_s

($g \cdot cm^{-3}$), and electrophoretic mobility, μ_e ($cm^2 \cdot V^{-1} \cdot s^{-1}$), and external electrical parameters, as the electric field, E ($V \cdot cm^{-1}$), deposition area, S (cm^2), and deposition time, t (s):

$$m = C_s \mu_e S E t \qquad \text{(Eq. 1.20)}$$

This model was very simple and only valid for short deposition times, as the variation of deposited mass with deposition time is linearly dependent and thus requires that the parameters of Eq. (1) remain unchanged with time. Nevertheless, it set the basis for further models which took into consideration other aspects, e.g considering particles as the unique charge carriers in the suspension [134] or the variation of suspensions concentration with deposition time suggested by Zhang et al. [135] in 1994. In this sense, Sarkar and Nicholson [119] introduced an efficiency factor or "sticking parameter", $f \leq 1$ (i.e. $f = 1$ when all the particles reaching the electrode are a part of the deposit) to quantify the effect of the undetermined process of deposition. Moreover, they considered the effect of the variation of particle concentration with time on the EPD kinetics by defining a characteristic time scale (τ):

$$\tau = Vf\mu SE \qquad \text{(Eq. 1.21)}$$

where V is the volume of suspension, which remains unchanged with time. The inverse value of this characteristic time scale was defined as a universal parameter, k, named the "kinetics parameter". Thus, the equation defined by Sarkar and Nicholson was:

$$m(t) = m_0(1 - e^{-t/\tau}) \qquad \text{(Eq. 1.22)}$$

This equation has been widely accepted and applied in the literature, as it can be reduced to the Hamaker model for short times and predicts deviations from linearity (occurring when EPD is carried out under constant-voltage conditions and the deposit resistivity is higher than that of the suspension). Further kinetic models for EPD are extensively described in the recent review by Ferrari et al. [136].

1.3.2. Mechanisms of EPD.

Even though the principles of EPD and its kinetics have been subject to many studies in the literature, controversy on the mechanisms during particle arrangement into coherent deposits remains nowadays. This is a key issue, as effectiveness of EPD in producing homogeneous and reliable films not only depends on particle surface

chemistry or behavior of surface–liquid interfaces behavior, but also on the particle–particle and particle–substrate interactions during assembly. In order for aggregation/ deposition to take place, some kind of attractive interaction strong enough has to be developed in order to overcome electrostatic interparticle repulsion (see Figure 1.5). “Traditional” approaches proposed to explain this fact included flocculation by particle accumulation, particle charge neutralization, electrochemical particle coagulation, and electrical double layer (EDL) distortion and thinning mechanism. This latter is the most widely, suggested by Sarkar and Nicholson [119] and consists on the EDL distortion on application of an electric field: when a particle is moving towards an electrode due to an applied field, the double layer around it distorts, due to fluid dynamics and the field itself, becoming thinner ahead and wider behind the particle and favoring deposition/agglomeration. However, this model was considered incomplete later on, by De and Nicholson [137], who suggested that there is a decrease of the concentration of H^+ at the cathode due to particle discharge or other chemical reactions, which rises the local pH towards the isoelectric point (IEP), zeta potential decreases and the particles coagulate.

Nevertheless, novel theories and modeling studies are still being developed in order to clarify the mechanisms of particles aggregation/packing in the electrode. These new models also provide an explanation for the “lateral attraction” phenomenon first observed by Richetti et al. [138] , and which consists on migration of particles towards one another across the surface of the electrode, transversely to the applied electric field, forming stable two-dimensional colloidal crystals. This seemed to be a general phenomenon that operates for any colloidal material that remains stable at the electrode-solution interface during EPD, but a detailed theory had not been provided.

In any case, it must be noted that most models have only taken into consideration particles with controlled morphology, i.e. mainly spherical particles such as SiO_2 and Polystyrene, and they have not been tested with materials with several particle sizes or high-shape factor morphologies.

- Electrohydrodynamics and Electroosmosis.

As an example of these novel theories, Trau et al. [128] ascribed particles (lateral) agglomeration to electrohydrodynamic (EHD) effects, which arise from perturbations on the electrode polarization charge layer: Lateral variations in the concentration of the polarization layer (due to the presence of particles near the electrode) induce a spatially varying " free charge", and the action of the electric field on the free charge

induces fluid motion. This electro-hydrodynamic motion and the associated pressure field cause the particles to move toward one another (see Figure 1.14).

Alternatively, (though with great similarity) Böhmer et al. [139] suggested that the aggregation of particles was due to an electroosmotic effect around each particle, which causes hydrodynamic flow: liquid in the *lyosphere* around the particles follows their motion towards the electrode with a certain time lapse, and when reaching the electrodes surface, it flows along it towards the particle, dragging any nearby particles with it. Based on these works, Solomentsev et al. [140] proposed the model for particle aggregation on an electrode during EPD under a DC electric field depicted in Figure 1.14b and defined the electroosmotic velocity. The authors in this work observed systematic deviations from the model suggested by Bohmer, especially at higher field strengths, and therefore hypothesized that the EHD flow proposed by Trau et al. might also be involved in the process.

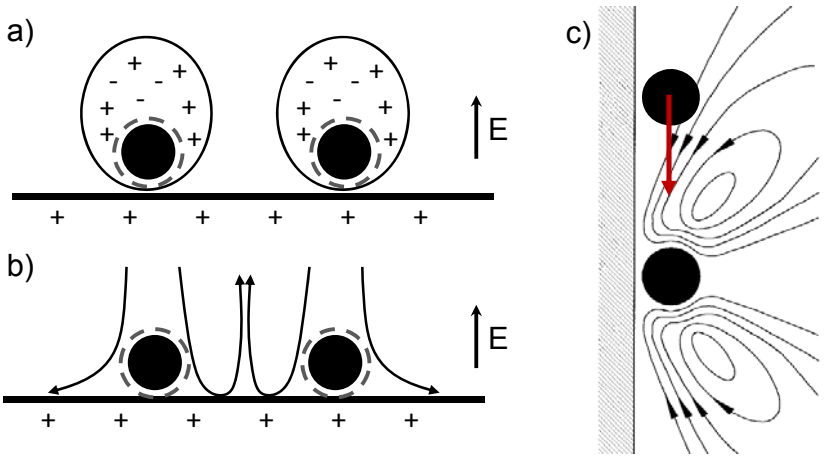

Figure 1.14: a) polarization of the double layer of the particles, (b) flow pattern expected to give rise to particle attraction. c) Streamlines for electroosmotic flow about a deposited particle. A second particle on the electrode would be drawn toward particle 1 and vice versa, resulting in aggregation.

However, even though both phenomena (electrohydrodynamics and electroosmosis) have been extensively described in relation to EPD later on, discussing topics such as their kinetics [141], scaling analysis [142], influence of the electrode [143, 144] or of the electric field [145, 146], the literature on the topic regarding the influence of particles morphology is quite scarce, and only a short number of papers consider non-spherical particles: Solomentsev *et.al* [147] modeled the electrophoretic motion of slender particles with zeta potentials that varied with position along their length; Yamamoto et al. [148] developed a simulation to analyze the dynamics of platelike particle dispersed systems, modeling the platelike particles as arrays of spheres connected by three types of springs and considering intraparticle and interparticle hydrodynamic

interactions. Finally, Yariv et al. [149] analyzed the dependence of the electrophoretic motion upon particle shape and concluded that arbitrary non-spherical particles may translate and/or rotate in response to the imposed field, even if their net electric charge vanishes.

Still, these articles only considered theoretical modellings of EPD. In this sense, Zhang et al. [150] carried out a thorough experimental study of the orientation mechanisms of platelet-shaped alumina particles during EPD, assessing the influence of the electric field force, gravity and fluid flow. In this work they observed that alignment due to the electric field can take place either during electrophoresis or deposition, and is influenced by different phenomena:

- The initial orientation of the particles and polarization of their EDL: when the platelets are oriented parallel to the electric field, the positive ions above the basal plane in between the platelet and the electrode will try to counteract the electric force on the platelet, resulting in reduced platelet mobility in the electric field. However, if the basal plane of the platelet is initially perpendicularly positioned with respect to the electric field, polarization of the diffuse ion cloud is easier resulting in more net charge and preferred deposition.
- Actual hydrodynamics of the liquid media surrounding them (which can give place to rotational flip-over movements of the particles [151]: when particles are moving towards the electrode during EPD, there is a hydrodynamic force in the opposite direction due to the fact that the solvent has to move in the opposite direction of particle movement.
- Reorientation of platelets once they make contact with the deposit or the deposition electrode. According to the model by Harnau et al. [152], plate-like particles in a fluid in the vicinity of a hard wall will adopt nearly a fully parallel alignment due to interactions with the wall. Thus, in EPD the plate-like particles will align themselves parallel to the deposition electrode no matter their orientation in the suspension. However, the surface charge influence is ignored in this model.

Moreover, Zhang et al. also analyzed the influence of the hydrodynamic force in the surroundings of the electrode (generated by stirring) on deposition, observing that the basal plane of the platelets gets aligned along the fluid direction so as to minimize the drag force. The shear force applied by the fluid flow is almost parallel to the electrode surface, as illustrated in Figure 1.15. In this case, the hydrodynamic force assists in aligning the basal plane of the platelets parallel to the deposition electrode surface.

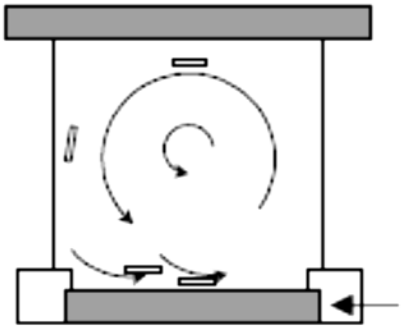

Figure 1.15: Top view of the flow pattern during EPD in a vertical cell with magnetic stirring.

1.3.3. EPD of ZnO thin films.

Even though the number of publications on Electrophoretic Deposition of ZnO is not very high, it has been exponentially increasing in the past few years. These cover different topics, such as particles stabilization and surface charge, kinetic studies, or the use of templates. Here we will briefly summarize the most relevant ones.

As we described in previous sections, understanding the colloidal behavior of ZnO nanopowders is a key point in order to prepare stable suspensions suitable for EPD. However, and surprisingly, only a few works focused on the stabilization of ZnO suspensions. In this sense, Tang et al. analyzed the use of cationic and anionic polyelectrolytes, Polyethylenimine (PEI) [153] and ammonium polyacrylate (PAA) [108], as surfactants to disperse zinc oxide nanopowder (nano-ZnO) suspensions and modify the particles to become positively or negatively charged, respectively. For both cases they reported the obtaining of well-dispersed ZnO suspensions from which uniform and bubble-free nano-ZnO films were deposited. Based on the work of Tang et al., Verde et al. studied the dispersion of ZnO nanoflakes with PEI addition [154]. Moreover, they analyzed the influence of the molecular weight of PEI on its dispersion effect, and suggested that a preferential adsorption of PEI onto negatively charged O-ZnO surfaces takes place [125].

On the other hand, several authors studied the kinetics of the process, in order to obtain films with different thicknesses. Wong et al. [155] described the electrophoretic deposition of ZnO quantum dots in their (organic) synthesis media, and determined the deposition kinetics from the change in the optical absorbance of the films, relating this with the Zn^{2+} concentration. They observed a semilogarithmic relationship of deposition mass with deposition time, stating that the EPD of quantum particles follows the rate

law derived for micrometer-sized particles. This behavior has been reported by several other authors: Wang [156] et al. analyzed the critical transition time, which can be defined as the deposition time at which deposition kinetics change from a linear ($t < t_c$) to a parabolic behavior ($t > t_c$), i.e. the deposition rate increases quickly at the initial stage and then approaches a steady state. They obtained ZnO films with varying thicknesses by varying the applied voltage and deposition times. Taking into account these results, the authors stated that kinetics of the deposition process are directly determined by the deposit layer thickness, and considered the voltage drop and suspension concentrations to be responsible for the deposition kinetics deviation from linear growth. Something similar was observed by Lommens et al. [157] when depositing thin layers of ZnO quantum dots. They analyzed the influence of the applied voltage, deposition time and quantum dot concentration on the final layer thickness, and obtained ZnO layers with thicknesses ranging from a few QD monolayers to 250 nm by applying voltages ranging from 20 to 60 V. However they reported that for layers thicker than a few monolayers, the deposition rate was considerably smaller than the theoretically calculated value, which points towards a strong screening of the electric field by the deposited ZnO layer. This was confirmed by Balaji et al. [158], who reported a sharp decrease of the current density for deposition times higher than 50 seconds. Miao et al. [159] studied the influence of other parameters, such as aging treatment of ZnO nanocrystallites and suspension concentration on the deposit weight. When the applied voltage and deposition time were kept constant, the deposit weight increased almost linearly with an increase in suspension concentration, but decreased for aging times above 3 days-due to agglomeration.

On the other hand, Lee et al. [160] reported the “production” of ZnO nanoparticles with different surface charge states by adjusting their zeta potential values, in order to demonstrate the role of surface charge coupling during the EPD process. In this way, and combining nanosphere lithography (NSL) and EPD processes, they described the fabrication of 2D ordered arrays of ZnO hierarchical structures with micro and nanopores. Moreover, they successfully tailored the effect of charge balance between the colloidal particles and the polystyrene sphere-coated template to prepare arrays of ordered solid or hollow dots/network structures, and have determined the mechanism governing the filling characteristics by the coupling effect of the surface charge.

This leads us to another of the topics covered in the bibliography on EPD of ZnO: the use of templates. Many of the works published on EPD of ZnO describe the use of different kinds of templates in order to obtain specific shapes. Wang et al. [161] reported the deposition of uniform and aligned ZnO nanowire arrays embedded in

anodic alumina membranes (AAM). The morphology of ZnO nanowire arrays and the deposition rate are influenced by the pH of the suspension (which affects particle size and surface chemistry) and the applied voltage-which changes the deposition morphology. Moreover, it was observed that, under a given electric field, the zeta-potential effect is higher than that of the particle size in determining the deposition rate of ZnO nanowire arrays.

On the other hand, and as opposed to the results reported by Miao et al. [162] for films, these authors observed that with an increase in the colloidal concentration the growth rate of ZnO arrays embedded in AAM will be decreased, while the crystallite size will be enhanced. This is ascribed to the higher viscosity of concentrated suspensions, which inhibits particle transportation in the solution, and to the fact that the equilibrium speed of the particles will increase with decreasing coloidal concentration. The annealing effects on microstructure and dielectric breakdown of amorphous AAM templates, and the related characteristics of the ZnO deposits were also studied [163]. They observed that the morphologies of ZnO nanowire arrays and current-time curves during EPD are determined by the breakdown behaviors of AAM templates and the applied voltages. Moreover, three different morphologies due to the voltage dependent filling characteristics of AAM were obtained: fibrils, tubules, and the mixed product [164, 165].

In addition, Chung et al. [166, 167] reported the use of EPD as nanochannel filling process of colloidal crystal templates, in order to obtain high quality ZnO inverse opal. Accurate control of the kinetics in the interstitial spaces of the colloidal template becomes a key issue, in order to fill the colloidal template completely, avoiding jamming of the nano-channel.

However, recent literature tends to focus on the applications of these films, rather than on the deposition process itself. The number of works on this topic is much higher than that for the other parameters we have described, and the described applications vary from “traditional” ones of ZnO, such as gas sensors, [168-172] or photoluminiscent materials [173-175], to innovative applications, such as catalysts [176] or dye-sensitized solar cells (DSSC) [176-182].

Chapter 2

Chapter 2: Experimental Procedure and Characterization Techniques

In this chapter the experimental methods used for the development of this thesis are described, including the experimental conditions of the different tests carried out and the characterization techniques of the obtained products.

2.1. Experimental Procedures.

2.1.1. Synthesis of ZnO nanopowders.

Synthesis of the ZnO nanopowders was carried out by a direct precipitation process. For this purpose, a 0.3 M aqueous solution of zinc acetate dyhydrate, ($Zn(CH_3COO)_2 \cdot 2H_2O$) (Sigma Aldrich Co., EEUU) was prepared, to which 2 M solution of NaOH (Merck, Germany) was added dropwise, under constant magnetic stirring. The addition of NaOH was continued until supersaturation was reached by pH increase (pH > 8), after the addition of aprox. 400 mL. The obtained white powders were filtered under vacuum and rinsed several times with distilled water and ethanol, so as to remove possible rests of starting reagents. Finally, a subsequent mild thermal treatment in a stove with an automatic programmer (Nabertherm, Germany) was applied, so as to transform the precipitated $Zn(OH)_2$ into pure nano-sized ZnO particles. For this thermal treatment the powders were introduced in the stove when the temperature reached that of the desired thermal treatment, and taken out after it in quenching.

Two different ZnO powders were obtained following this procedure, by changing the washing protocols. Further details will be described in Chapter 3.

The same procedure was followed for the preparation of 5 wt % Co-doped ZnO powders. In this case, coprecipitation took place by dropwise addition of 2 M NaOH to an aqueous solution of zinc acetate dyhydrate, ($Zn(CH_3COO)_2 \cdot 2H_2O$) and cobalt nitrate hexahydrate ($Co(NO_3)_2 \cdot 6H_2O$).

2.1.2. Study of the colloidal behavior of the powders.

The study of the colloidal behavior of the different synthesized powders was carried out in aqueous suspension. Suspensions were prepared so as to fit the requirements of the experimental technique used for the determination of the powders properties, i.e.

particle size and zeta potential determination. These techniques will be discussed in detail in subsequent sections.

Suspensions of the synthesized powders were prepared following different protocols, depending on the purpose they would be used for. In any case, it must be noted that those here exposed are general protocols that might suffer variations as a function of the specific characteristics of each powder-solvent-dispersant system.

- Suspensions used for zeta potential determination were prepared with concentrations of 0.1 g/L using 10^{-2} M KCl as solvent and inert electrolyte, so as to maintain the ionic strength of the medium. pH adjustment of the suspensions was carried out by addition of small quantities of 0.1 M HCl or KOH and controlled with a pH probe (Metrohm AG, Germany). Subsequently, homogenization was achieved by sonication, using a UP 400S Ultrasonication Probe (Hielscher, Germany) for an optimized period of time. Finally, the pH and zeta potential of the suspensions were determined.
- Suspensions used for particle size determination require the optimization of their solid contents in order to obtain a stable measurement. Thus the first step was the dilution of the suspensions to the optimal measurement concentration, followed by pH adjustment and sonication, and finally, pH and particle size determination.

In addition, the influence of different quantities of Polyethylenimine (up to 2 wt%) with different molecular weights as cationic dispersant was also evaluated. In this sense, the three different PEIs used were (from Sigma Aldrich):

- Polyethylenimine branched, average Mw ~25.000
- Polyethylenimine low molecular weight, average Mw ~2000
- Polyethylenimine low molecular weight, average Mw ~1300

The protocol followed for suspensions containing dispersant was the same, adding the PEI previously to powder addition. In this way, adsorption of the additive was favored, and the subsequent pH adjustment affected its polarization state (see details in Chapter 4).

2.1.3. Preparation of ZnO films by Electrophoretic Deposition.

In the first place, and taking into account that stable, well dispersed suspensions are one of the main requirements of EPD, suspensions of the synthesized powders used for EPD were prepared according to the following general protocol:

- Addition of the optimized amount of dispersant to the solvent.
- Preparation of the suspension by powder addition, with solid contents adjusted to those necessary for deposition (from 1 to 0.1 g/L).
- pH adjustment to the optimized pH range (details in Chapter 4).
- Sonication.
- pH and conductivity determination.
- Shaping by EPD.

The EPD itself was carried out in a home-made setup, consisting of an electrophoretic cell, a Keithley 2611 System SourceMeter (Keithley Instruments Inc., USA)[183] and an elevator (Figure 2.1).

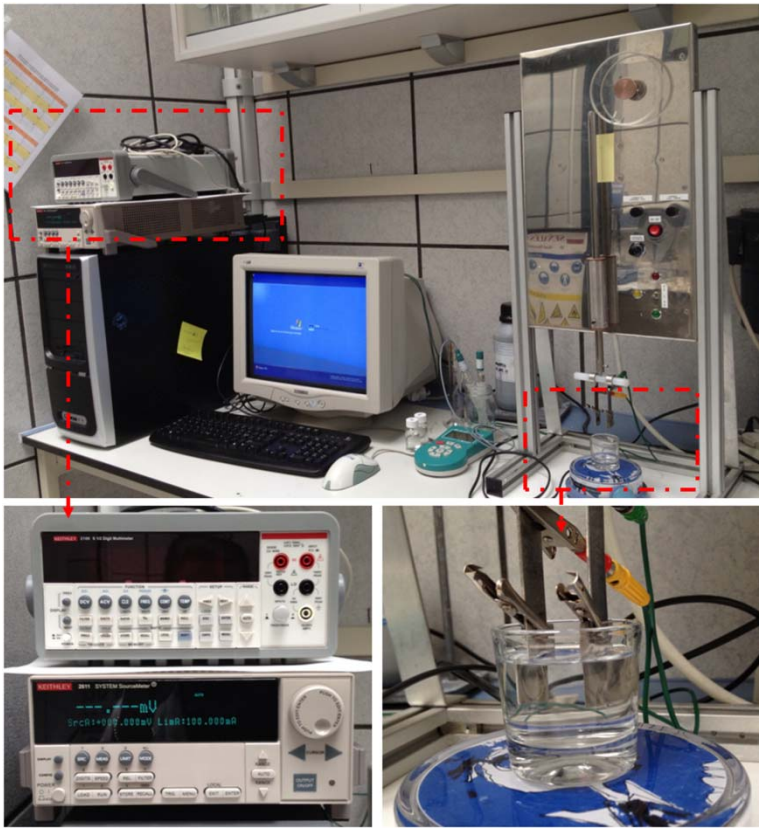

Figure 2.1: Photographs of the EPD setup.

The electrophoretic cell was composed of a small beaker, containing 30 mL of suspension in which the electrodes, which were 2 cm apart from each other, were

immersed. These electrodes were in turn attached to the elevator, which allowed immersing and lifting the electrodes at a controlled speed/rate.

Different substrates were used as deposition cathodes: electropolished stainless steel substrates (AISI 304) with areas of 25 x 15 x 0.5 mm, ITO-Coated Float Glass Polished Slides of 25 x 25 mm (SPI Supplies, Structure Probe Inc., USA), and Nickel foils of 25 x 25 x 0.5 mm (Goodfellow, USA). The electropolishing of the stainless steel substrates was carried out in an Electromet 4 electropolisher (Buehler, USA) with an electrolyte composed of perchloric acid, ethanol and DI water, applying a voltage of 38 V for 1 min. In all cases the counter-electrode was a platinum foil of dimensions similar to those of the cathode.

For the deposition of ZnO thin films, EPD was carried out in galvanostatic conditions, applying (optimized) current densities between 20 to 31.2 $\mu A/cm^2$ for times between 1 and 10 minutes. In contrast, in the experiments carried out for the obtaining of thicker films, both continuous and pulsed galvanostatic and potentiostatic conditions were applied (see Chapter 5 for details).

Low rhythm magnetic stirring was used in all experiments in order to avoid charge concentration gradients on the surroundings of the work electrode.

The obtained films were left to dry in ambient conditions and ready for characterization.

2.1.4. Hydrothermal growth of ZnO nanostructures.

Hydrothermal growth of ZnO nanostructures onto ZnO films shaped by EPD was studied as a way to obtain ZnO films with controlled morphology. For this purpose, several different cases of hydrothermal growth of ZnO nanostructures were studied: in the absence of substrates, with presence of unseeded stainless steel substrates, and in presence of ZnO films prepared by EPD that will act as seed layers.

All hydrothermal experiments were carried out using as received analytical reagent-grade chemicals from Sigma–Aldrich, without further purification. In a typical procedure 0.02 mol of zinc acetate dihydrate ($Zn(CH_3COO)_2 \cdot 2H_2O$) were dissolved in 140 mL of distilled water and then 40 mL of 1 M KOH were added dropwise to the solution under vigorous magnetic stirring at room temperature [184]. Subsequently the precipitate-containing solution was transferred to a 200 ml BR100 Teflon-lined stainless steel

autoclave provided with a single-loop temperature controller/programmer (Berghof, Germany) [185] (Figure 2.2). In those experiments involving substrates, the substrate was introduced in the autoclave at this point.

Figure 2.2: Photograph of the Teflon-lined stainless steel autoclave used for the hydrothermal growth procedure.

The sealed autoclave was then sealed tightly, heated up to 200 ºC and maintained at this temperature for 4 h. Autogenous pressure (< 5 bar) gradually increased as the temperature rose during the hydrothermal procedure. The system was allowed to cool down to room temperature naturally. The resulting precipitate powder was retrieved from the solution by filtration, washed several times first with ethanol and then with distilled water and finally dried in air at 60 ºC, whereas the resulting films on the substrates were rinsed with distilled water to remove the residual reactants or products from their surface and dried at room temperature. The samples obtained by this procedure were morphologically characterized by Field Emission Scanning Electron Microscopy (FE-SEM).

2.2. Characterization techniques.

2.2.1. Powder Characterization.

2.2.1.1. X-Ray Diffraction.

The identification of the crystal phase of the synthesized powders was carried out by X-ray diffraction (XRD). For this purpose an *X'Pert PRO* diffractometer (*Panalytical,* EEUU) was used, with CuKα (λ=1.540598 Å) radiation [186]. Analysis conditions were

of 40 KV and 30 mA intensity for all samples, which were mounted on plastic sample holders. The diffractograms were recorded in a 2θ range from 20 to 60 º, with a step size of 0.05 º and continuous register. Moreover, the assignment of the diffraction peaks was carried out using the EVA application of the Diffrac.Suite^{TM} software (Bruker Corporation, Germany), by comparison with the the PDF main data base and ICDD (*International Centre for Diffraction Data)* cards of ZnO-wurtzite. In addition, FullProf 2k program [187] was used for Rietveld adjustment and estimation of the lattice parameters.

2.2.1.2. Thermogravimetric and Differential Thermal Analysis (TG-DTA).

Differential Thermal Analysis is based on the analysis of the variations in temperature of a sample, compared to a reference material, in a constant heating and cooling cycle. The differences in temperature are due to endotermic or exotermic processes that take place in the sample, and this technique, together with thermogravimetry, (which detects variations in samples weight) allows ascribing them to desorption of specific molecules or decomposition processes. In this work, these techniques were used to follow the transformation of the precursors into ZnO.

The analyses were carried out in air, with constant heating rates of 3 ºC/min up to temperatures of 500 ºC, in a TG-DTA 7 equipment (Perkin Elmer, USA)[188].

2.2.1.3. Specific surface Area (SS_A).

The specific surface area of the synthesized powders was determined in a ASAP 2020 Physisorption Analyzer (Micromeritics, USA)[189], by the Brunauer, Emmett, and Teller (BET) method. This method (derived from the Langmuir theory) consists on the measurement of the quantity of inert gas (typically N_2) adsorbed onto the surface of a solid material, forming multilayers. Knowing the amount of gas necessary to form a monolayer and the area of the gas molecule, the specific surface area of the solid can be calculated by applying the following equation,

$$SS_A = \frac{V_m \cdot S_0}{P} \qquad \text{(Eq. 2.1)}$$

where V_m is the volume of the monolayer (calculated applying the BET isotherm), S_0 is the surface occupied by 1 mL of gas and P is the weight of the sample. This technique presents a ± 3 % of experimental uncertainty.

2.2.1.4. Density (ρ).

Density of the synthesized powders was characterized by Helium Pycnometry (Multipycnometer, Quantachrome Co. EEUU). True densities are usually measured using helium gas since it will penetrate very fine pores down to about two Angstroms (0.2 nm), thereby enabling the measurement of true volumes with great accuracy. This technique determines the volume of powder by calculating the difference between the pressure applied by a certain amount of Helium (P_1) in a reference cell of known volume (V_R), and the pressure applied by the same amount of He (P_2) in a cell of volume V_C which contains the powder sample. The volume of powder is calculated by applying the law of ideal gases:

$$V_P = (V_C - V_R) \cdot \left(\frac{P_1}{P_2} - 1\right) \qquad \text{(Eq. 2.2)}$$

Knowing the volume of the powder and the mass of the sample its density can be calculated. The experimental uncertainty of this technique is ± 10 % (in this equipment).

2.2.1.5. Field-Emission Scanning Electron Microscopy (FE-SEM).

This kind of microscopy was used for the general observation of the morphology of the powders. For this purpose a field emission scanning electron microscope S-4700 (Hitachi, Japan) equipped with an energy dispersive X-ray spectroscopy (EDX) system was used, with a resolution of 1.5 nm, working at 20 kV with a current intensity of 10 μA [190].

Powder samples were prepared suspending some powder in DI water, homogenizing with 1 min sonication and depositing a droplet of the suspension on a SEM sample holder which was left to dry in air. In all cases samples were coated with a thin layer (nm) of gold by sputtering, in order to avoid charging of their surfaces due to electron accumulation.

2.2.1.6. Transmission Electron Microscopy (TEM and HRTEM).

Transmission electron microscopy (TEM) and high resolution transmission electron microscopy (HRTEM) were used to examine the particle size of the powders and carry out their morphological characterization, as the available scanning electron microscope did not have enough resolution for the observation of such small particles.

Three different equipments were used: a Hitachi H7100 TEM microscope (Hitachi Ltd. Japan) working at 125 KV [191], a JEM-2011 high resolution TEM (JEOL Ltd., Japan) working at 200 KV [192], and a second TEM microscope with a high resolution (JEM 2000FX, JEOL Ltd., Japan) [193] used in a short stay in collaboration with the department of Synthesis of materials (K8) in the Jozef Stefan Institute in Ljubljana (Slovenia) under the supervision of Prof. Dr. Darja Lisjak. All three microscopes were also equipped with EDX systems.

In all cases, samples were prepared by depositing a droplet of an aqueous suspension of the powders (homogenized in a sonication bath) onto a Lacey carbon TEM grid (LC200-Cu, Aname, USA) with a polymeric film on it.

2.2.1.7. Particle size.

Particle size and particle size distribution of the powders have been evaluated by different methods: direct observation in the TEM, estimation of the BET diameter from the powder characteristics and analysis of the particle size distribution in suspension by DLS. We will now briefly describe each of these methods.

- TEM: particle size of the particles was examined by direct observation in the TEM microscope described in section 2.2.1.6.

- BET diameter:

The primary particle size was initially calculated from the powder characteristics by applying the equation of the BET diameter [194]:

$$d_{BET}=\frac{6}{(SS_A\cdot\rho)} \qquad \text{(Eq. 2.3)}$$

However, this approximation assumes spherical, monodisperse particles, with the same specific surface area as the powder, so it should only be considered as a first estimation [195].

- Dynamic Lights Sctattering (DLS):

The mean particle size (d_{V50}) and particle size distributions of the different powders were measured using a Zetasizer Nano ZS equipment (Malvern S, UK) with a 633 nm laser (Figure 2.3a) [196]. This equipment is based on Dynamic light scattering (DLS), which is a non-invasive, well-established technique for measuring size distributions of

populations of molecules and particles typically in the submicron and nanometric range (from 6 μm to 0.6 nm).

DLS measures the speed at which the particles are diffusing due to Brownian motion (defined by the translational diffusion coefficient, D) and relates it to the size of the particles. When a cuvette containing a suspension is illuminated by a laser, a classical speckle pattern is obtained, due to constructive and destructive interferences of the light scattered by the particles (see Figure 2.3b). Due to brownian movement of the particles, this pattern is reflected as fluctuations of the detected scattered light, and the rate at which these intensity fluctuations occur will depend on the size of the particles, as larger particles have slower brownian motion (Figure 2.3b) [196]. Therefore, the size of a particle can be calculated considering its translational diffusion coefficient by using the Stokes-Einstein equation,

$$d(H) \quad \text{——} \qquad \text{(Eq. 2.4)}$$

where d(H) is the hydrodynamic diameter, k is Boltzmann's constant, T is the absolute temperature, η is the viscosity and D is the translational diffusion coefficient. However, it must be noted that the diameter that is measured in DLS is the hydrodynamic diameter, i.e. the diameter of a sphere that has the same translational diffusion coefficient as the particle.

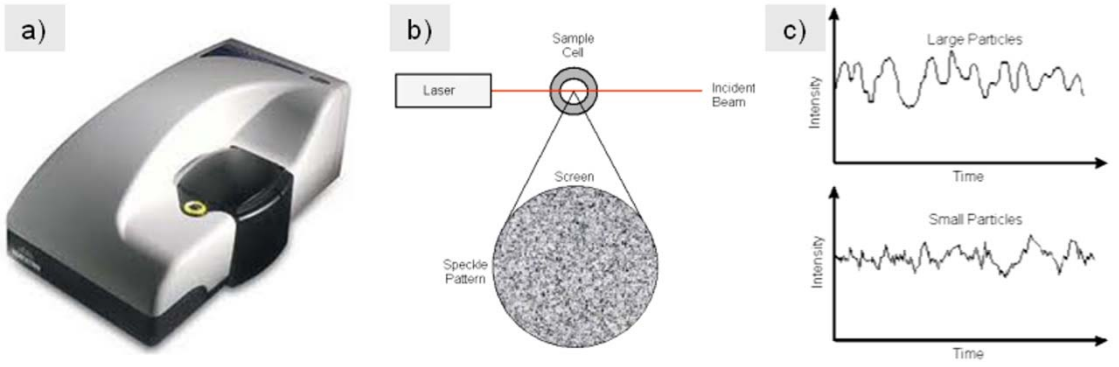

Figure 2.3: a) Photograph of the Zetasizer nano ZS equipment; b) schematic representation of the patter formed by light interferences and c) representation of the intensity fluctuations which are correlated to particle size.

Given the small size of the powders, measurement in this equipment is quite delicate, and a perfect preparation of the samples is required. Suspensions must be stable and well dispersed and the solids loading should be adequated to the optical

parameters. The attenuator and measurement position of the equipment are automatically optimized (see section 2.1.2 for the protocol of suspensions preparation).

The agglomeration factor is defined as the relation between the primary particle size (d_{BET}) and the mean particle size in volume, dV50, measured by DLS, and it points out the degree of agglomeration of the particles in the powder [194].

$$A_f = \frac{d_{V50}}{d_{BET}} \quad \text{(Eq. 2.5)}$$

2.2.2. Characterization of the suspensions.

2.2.2.1. Zeta potential (ζ).

Zeta potential measurements were carried out in the same equipment as particle size measurements, a Zetasizer Nano ZS (Malvern S, UK). However, the principles on which this measurement is based are laser Doppler velocimetry and phase analysis light scattering (PALS), instead of DLS. To be precise, the equipment determines the fluctuations on the intensity of an incident laser beam caused by the movement of suspended particles under an applied alternating electric field (electrophoresis). The frequency of these fluctuations is proportional to the speed at which the particles move, i.e. the electrophoretic mobility, μ_e, and this is then converted to zeta potential values by applying the Henry equation [197],

$$\mu_e = \frac{2\varepsilon\zeta f(Ka)}{3\eta} \quad \text{(Eq. 2.6)}$$

where ε is the dielectric constant of the suspensions media, η its viscosity, ζ the zeta potential of the particles and f(κa) is Henry's function. This last parameter depends on the ratio of the particle radius (a) to the electrical double layer thickness (κ^{-1}), which in turn depends on the media and electrolyte concentration: for polar media and moderate electrolyte concentrations, the value of f(κa) is 1.5, and this is referred to as the Smoluchowski approximation. On the other hand, for small particles in low dielectric constant media (e.g. non-aqueous media), f(κa) becomes 1.0 and this is known as the Hückel approximation [197].

The protocol for the preparation of the suspensions for zeta potential determination was already detailed in section 2.1.2.

2.2.2.2. Conductivity (σ).

Besides good stability and dispersion, electrical conductivity of the suspensions is also a very relevant parameter for EPD, as it determines the viability and development of the deposition process [136]. Conductivity of a suspension is determined by the number of charge carriers (ions and/or particles) and thus is directly related to the deposition yield (see Chapter 4).

In our experiments, conductivity of all suspensions was measured before and after EPD with a LF320 conductimeter (WTW, Xylem Inc., Germany)[198], so as to determine the variation caused by the decrease in the number of chargers after deposition.

2.2.2.3. Ultraviolet–Visible spectroscopy (UV-Vis).

UV-Vis spectroscopy is based on the absorption by the sample molecules of UV or visible light, which produces the excitation of π or n electrons to higher anti-bonding molecular orbitals. The analysis of the obtained spectra provides information about the structure of the compound, and for nanometric or sub-nanometric particles the shift of the signal provides information about the size of the crystals in our sample. In this sense, this technique has been extensively reported as a method for the estimation of particle size distributions (PSD) of quantum sized semiconductor powders, as their optical properties depend on their disperse properties, namely, size and shape [199, 200]. The overall absorbance, *A*, of a sample is dependent on several parameters in Lambert-Beer's law (Eq 2.7),: the absolute particle concentration, *C*, the pathlength, *,l,* i.e distance that the light beam travels through the solution, and the molar absorption coefficient, ε, which is also a function of particle size.

$$A = \varepsilon \cdot C \cdot l \qquad \text{(Eq.2.7)}$$

In this work, UV-Vis spectroscopy was used for several purposes. In the first place, and together with DLS measurements, it was used for the determination of the dispersion state of the powder suspensions after sonication. Second, it allowed determining the experimental variability in the preparation of the suspensions by comparing the measured absorbances with those of a calibration curve. Finally, UV-Vis spectroscopy was also used as an indirect method for the calculation of the mass deposited by EPD, as the variation of intensity in the absorbance spectra of the suspensions recorded previously and after the deposition process was considered to be due to a variation in the concentration, which decreased as the powder was

deposited, and thus removed from the suspension. Therefore, this variation in the absorbance was transformed into a variation in the concentration of the suspensions by applying Eq. 2.7, and this, in turn was transformed into a variation in mass by multiplying by the volume of suspension.

The UV-Vis spectra of the powder suspensions were recorded in direct absorption mode, using a Lambda 950 spectrophotometer (Perkin-Elmer Inc. Estados Unidos), working in the range from 2000 to 200nm, with a step of 1 nm and integration time of 0.5 s [201].

2.2.3. Characterization of the deposited films.

2.2.3.1. Roughness determination.

The roughness of the substrates in which the films were deposited was characterized prior to the deposition, using a Surtronic 3+ roughness-meter (Taylor Hobson Ltd, Ametek Inc., USA). The measurement is based on the scanning of the surface with a pickup with a stylus tip that touches the surface. The movements of this pickup are detected and turned into electric signals, which are registered in the electronics. The maximum scanning length is of 25 mm and height of 500 μm, with resolutions of 1 and 10 nm, respectively [202].

2.2.3.2. Field-Emission Scanning Electron Microscopy (FE-SEM).

In this case, the SEM equipment described in section 2.2.1.5 was used to characterize the films shaped by electrophoretic deposition both in surface and cross section. The samples were directly mounted onto the sample holders. Films deposited onto stainless steel substrates were characterized in surface and by bending them, as the nature of the substrate hampered a neat cutting for their observation in cross section. On the other hand, films deposited onto ITO substrates were characterized both in surface and cross section by SEM, by mounting them in parallel and perpendicularly to the substrate surface (respectively). As in the case of powder samples, films were coated with a thin layer (nm) of gold by sputtering so as to avoid charging of their surfaces due to electron accumulation.

2.2.3.3. High resolution transmission electron microscopy (HRTEM).

In order to study the organization of the ZnO powders within the films, 0.1 and 1 g/L suspensions were deposited directly onto Lacey carbon TEM grids (LC200-Cu, Aname, USA) with polymeric film on them. For this purpose the grids were attached to a Si wafer with a platinum wire, and constant currents of 100 μA were applied for times of 10 min. These films were characterized using a JEM 2000FX equipment (JEOL Ltd., Japan) working at 200 KV.

2.2.3.4. Atomic Force Microscopy (AFM).

Atomic force microscopy (AFM) is a very high-resolution type of scanning probe microscopy, with demonstrated resolution on the order of fractions of a nanometer, which is typically used for imaging, measuring, and characterizing samples at the nanoscale. The equipment, in this case a Cervantes model (Nanotec Electrónica, Spain) consists of a laser, a cantilever with a sharp tip (probe) at its end that is used to scan the specimen surface, a photodetector and a piezoelectric component (Figure 2.4) [203].

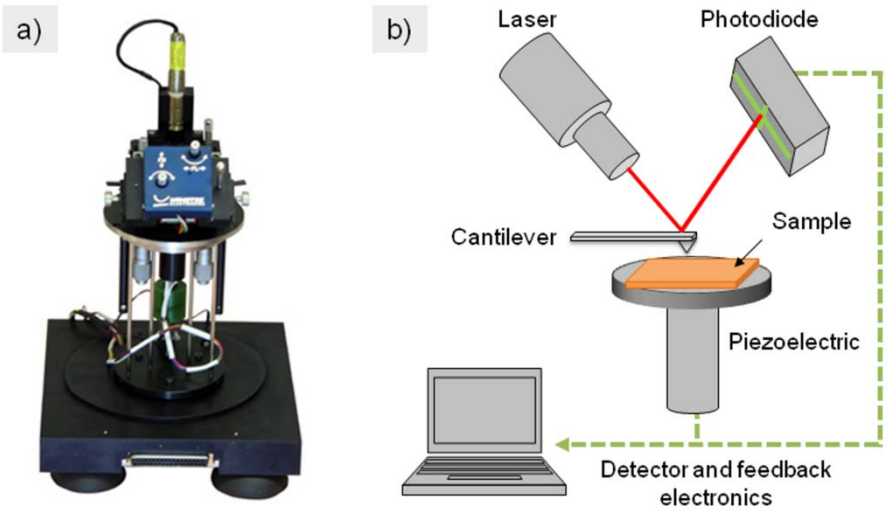

Figure 2.4: a) Photograph of the AFM measurement equipment and b) scheme of the components configuration in it.

This equipment can carry out two kinds of measurements: image and force. In the image kind, the measurement is based on the continuous register of the topography of the sample in the (x, y) plane with the tip of the cantilever, which, when brought into proximity of a sample surface, is deflected due to the interatomic forces between the tip and the sample. This deflection is measured using a laser spot reflected from the top

surface of the cantilever into an array of photodiodes, and a feedback mechanism automatically adjusts the tip-to-sample distance (z) with the piezoelectric component, so as to maintain a constant force between the tip and the sample. The maximum scanning range of the equipment is of 10 μm in the (x, y) plane and of 15 μm in z. In this way, the resulting map of the area $z=f(x,y)$ represents the topography of the sample. On the other hand, in force measurements, the tip is vertically vibrated and the deflection is registered.

In addition, the AFM can be operated in different imaging modes, which are generally divided into static (also called *contact*) modes and a variety of dynamic (non-contact or "tapping") modes where the cantilever is vibrated. The use of one or other imaging mode depends on the application: in our case, and given the fact that the samples are in green (non syntherized powder) the measurements were carried out in a dynamic mode, using Nanosensor PPP- NCH silicon tips, which have a radius of curvature < 10 nm.

Chapter 3

Chapter 3: Synthesis of ZnO nanopowders

In the present chapter the results obtained from the synthesis of ZnO nanoparticles are described. According to the objectives of this thesis, a synthesis route has been sought which enabled controlling variable sizes and morphologies. ZnO nanoparticles have been obtained by a direct precipitation process from aqueous solutions and crystallization of zinc acetate. The role of the anion in the Zn^{2+} starting precursor has been already recognized as a factor capable of influencing the morphology and size of nanoparticles [52, 204]. The relation between these two parameters is reflected through the crystallinity of the ZnO precursor itself. In this sense, the reasons for choosing zinc acetate dihydrate (shortened as ZA) as the precursor amongst the compounds available for the precipitation of ZnO or $Zn(OH)_2$ were various. First, due to its nature (a salt of amphoteric zinc oxide and a weak acid) ZA is partially hydrolyzed and mostly ionized [55], being the product of the partial hydrolysis mainly layered basic zinc acetate (LBZA), $Zn_5(OH)_8(CH_3COO)_2 \cdot nH_2O$). The structure of this product (shown in Figure 1.5) is responsible for the typical layered crystallization morphologies of LBZA, e.g. flakes, needles or thin, elongated plates, which are maintained after calcinations. In addition, ZA is a low cost commercially available precursor that has been widely used in the literature for the precipitation of ZnO, which corresponds to a highly sustainable and eco-friendly synthesis route.

3.1. Synthesis of ZnO nanocrystals (< 10 nm): ZnO-NC.

Zinc oxide nanoparticles with sizes below 10 nm were synthesized by direct precipitation from an aqueous solution of zinc acetate dihydrate. The conditions in which the precipitation was carried out were determined from the equilibrium diagram (log C vs pH) of the Zn^{2+} cation (see figure 1.7): pH of the aqueous solution of zinc acetate (pH ~ 5) was raised by dropwise addition of NaOH 2M. During addition of the NaOH formation of a white precipitate was observed, which subsequently dissolved as additional base was added. This precipitate has been identified in the literature as aggregates of semi-crystalline hydrated ZnO [42], and thus NaOH addition was prolonged up to pH=9, so as to ensure the precipitation of zinc hydroxide. Subsequently, the precipitated powders were washed by putting them into 3.5 l of deionized (DI) water under stirring, step that was repeated in order to favor the removal of both starting reagents and precipitant. The washed powders were then filtered under vacuum and rinsed with a 1:1 ethanol:DI water mixture, which lowered the pH, and

ethanol, which also lowered the pH and boosted the drying of the powders. This whole protocol favored the smaller size of the particles, due to dissolution/reprecipitation processes of the hydroxide in the washing step, together with the decrease in pH (to values of 6-5) in the rinsing with ethanol. Moreover, these processes might induce precipitation of the oxide [42].

Characterization of the as-synthesized powders by XRD (Figure 3.1) showed that their composition corresponded mainly to zinc oxide, together with residues from the synthetic procedure that were not washed away with the rinsing. These species, such as oxy or hydroxy acetates, are inherent to the synthesis procedure, due to hydrolysis of ZA in the basic aqueous medium in which precipitation takes place [53].

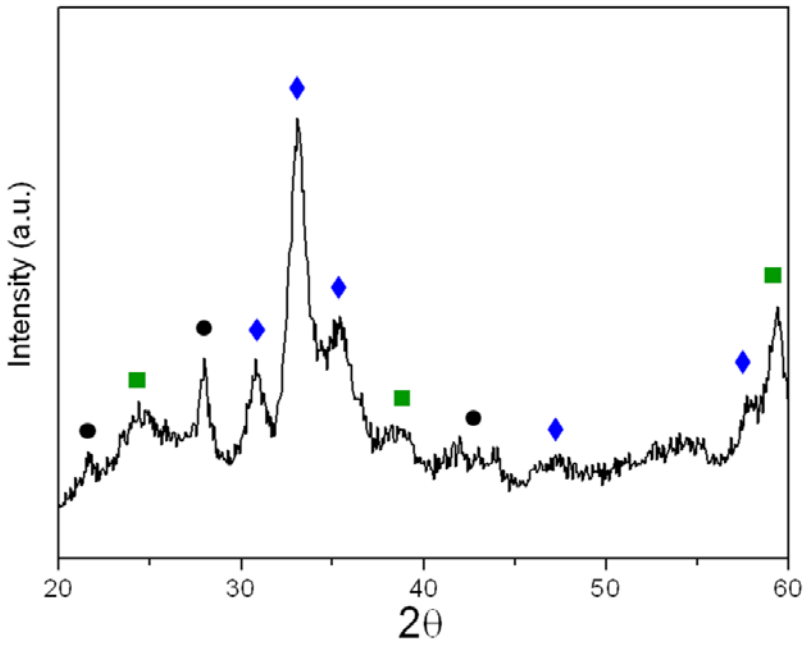

Figure 3.1.XRD diffractogram of the as synthesized powders. ♦ ZnO (ICDD nº 36-1451); ■ hydrated zinc acetate (ICDD nº 14-0902); ● hydrozincite, zinc hydroxicarbonate, $Zn_5(CO_3)_2(OH)_6$ (ICDD nº 19-1458).

In order to determine the optimal thermal treatment required for the transformation of these precursors into zinc oxide, thermal evolution of the precipitate powder in air was studied by Thermogravimetric and Differential Thermal Analysis (TG-DTA). Results of this analysis, presented in Figure 3.2, show three events related to a total weight loss of about 27 % during the heating procedure. The first one, at about 100 ºC, can be ascribed to free water elimination, with a weight loss of about 3 %, whereas the second one, with a mass loss of 1.2 % at 130 ºC may be associated to the dehydration of zinc hydroxide in order to form zinc oxide (which takes place at 125 ºC)[205] and the departure of water from the dehydroxilation of LBZA [57]. The last weight loss, which is also the largest, presents a maximum at about 225 ºC in which most of the mass is lost

(about 18 %). This 18 % can be related to decomposition of LBZA and removal of the major part of carboxylate groups, which are lost as $CO_{2\ (g)}$ [206]. However, a slight gradual decrease of mass (about 3 %) can still be observed up to 500 ºC, which can be due to remaining structural water molecules and hydroxyl groups.

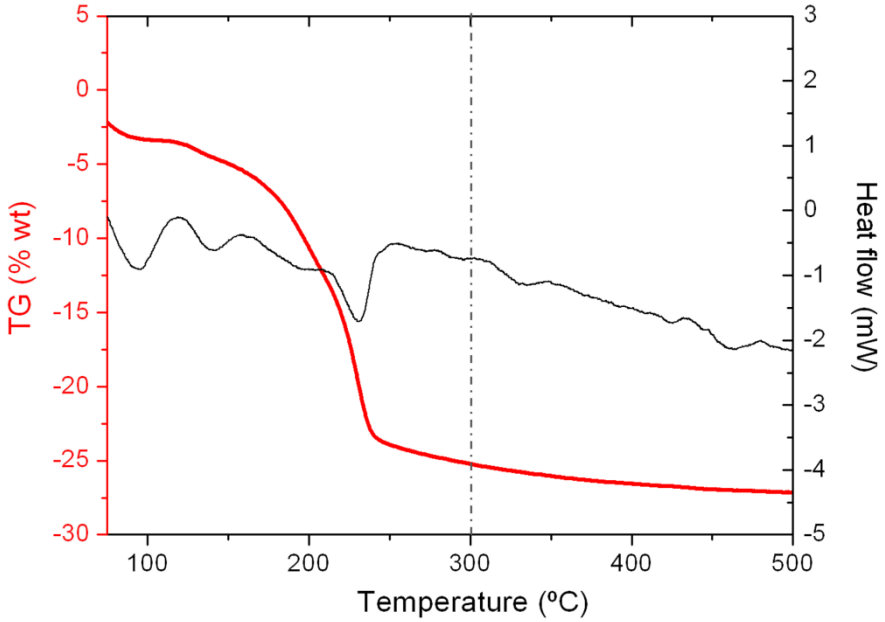

Figure 3.2: TG-DTA analysis of the as-synthesized ZnO-NC powders. The dotted line represents the temperature of the subsequent thermal treatment.

Taking into account the results of the TG-DTA analysis, a thermal treatment of 300ºC was used to transform most of the different species in the powder (zinc hydroxides, hydrated zinc acetates and zinc hydroxicarbonates) into zinc oxide without increasing the particle size. For this purpose, the furnace was preheated up to the required temperature at a heating rate of 5 ºC/min. When the desired temperature was reached, the powders were put inside the furnace, were they were left for 10 minutes. After this time they were taken out and the empty furnace was allowed to cool down naturally. The resulting powders after calcinations will be named ZnO-NC from now on (where NC stands for nano crystals).

Effectiveness of this mild thermal treatment was verified by XRD studies. As can be observed in the diffractogram in Figure 3.3, all diffraction peaks were well defined and in good agreement with the ICDD card no. 36-1451 for a typical wurtzite-type ZnO structure, and no evidence of secondary phases or impurities was detected. The peak broadening is commonly to a very small crystallite size with poor crystallinity. The average crystallite size along the hkl direction, D_{hkl} (nm), was calculated using the Warren modification of the Scherrer equation,

$$D_{hkl} = \frac{K\lambda}{\beta \cos(\theta)}$$

where λ is the wavelength of the radiation (in Å), θ is half the diffraction angle (2θ) in radians, β is the full width at half maximum of a given [hkl] peak (in radians too), and *K* is the Scherrer constant, which takes into account the asymmetry of the particles: *K* is equal to 0.94 for [00l] directions and 1.84 for the [hk0] ones [207]. Results showed that, as expected, the powders had a very small crystallite size, of 6.5 nm. The estimated lattice parameters calculated and refined using the least square method in the FullProf 2k program, (shown in the inset), were larger than those reported for the ZnO wurtzite pattern (a ranging from 3.2475 to 3.2501 Å and c ranging from 5.2042 to 5.2075 Å) [11]. This points out to a defective structure in the ZnO-NC powders, with a high presence of vacancies distorting the unit cell.

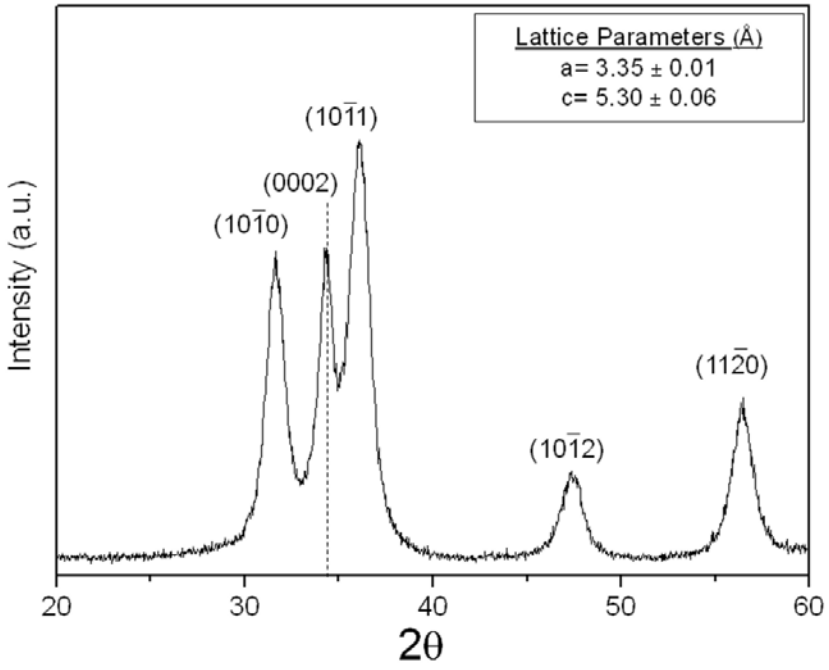

Figure 3.3: XRD diffractogram of ZnO-NC powders treated at 300 ºC for 10 min.

Even though the thermal treatment was enough to transform most of the zinc acetates and hydroxides into ZnO, it was too fast and not high enough to eliminate all residues. Thus, in order to verify the amount of residues remaining, the ZnO-NC powders were studied by analysis of their thermal evolution. As can be observed in Figure 3.4, the DTA curve of the calcined powders still showed a main exothermic effect with its maximum at 250 ºC, with a corresponding weight loss of about 16% in the TG. Therefore, the presence of some intermediate zinc acetate species which

resisted the calcinations was confirmed, even though they were not observed in the XRD, since they did not form a crystalline structure for themselves.

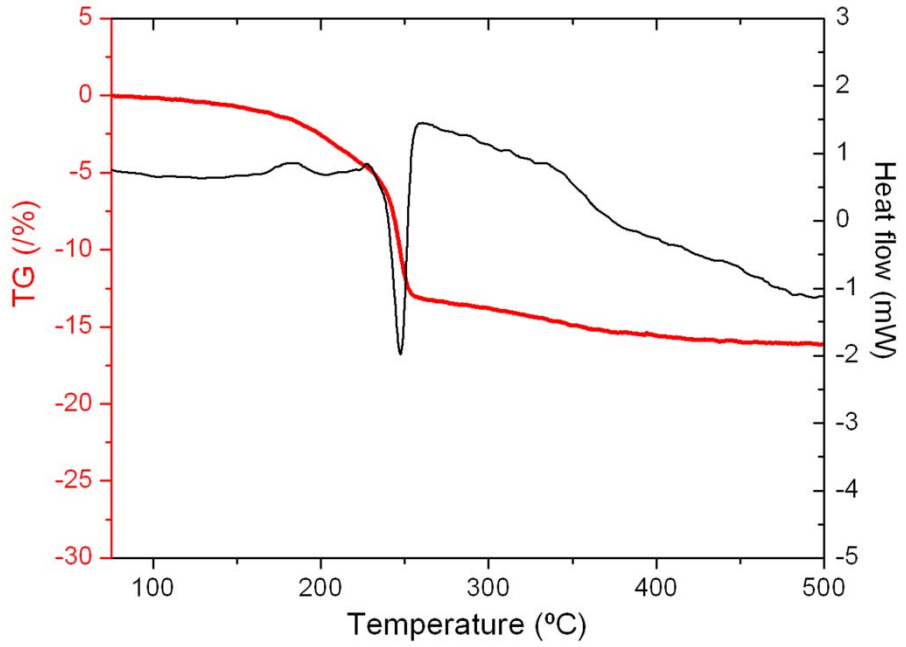

Figure 3.4: TG-DTA analysis of ZnO-NC powders treated at 300ºC for 10 min.

Several thermal treatments at higher temperatures (up to 500 ºC) and longer times were carried out in order to try to eliminate the remains of zinc acetates and derived phases from the ZnO-NC samples. However, these thermal treatments led to unwanted particle growth due to coarsening and interparticle neck growth, and the nano-size of the particles was lost. Thus, despite the presence of some remains of starting reagents in the resulting powders, no other thermal treatment was applied, as the main desired parameter was the small size of the particles, valued over their purity or crystallinity.

Morphology of the powders was studied by means of scanning electron microscopy. SEM micrographs in Figure 3.5 show how the mild thermal treatment prevented particles from growing, as the particle size is still well below 100nm. Micrographs taken at higher magnifications (Figure 3.5b) allowed observation of a homogeneous population of small ZnO-NC particles, as expected from the XRD analysis. However, these small particles appeared highly agglomerated, as both large agglomerates (~500 nm) and the aggregates in them (> 100 nm) can be observed in the micrographs.

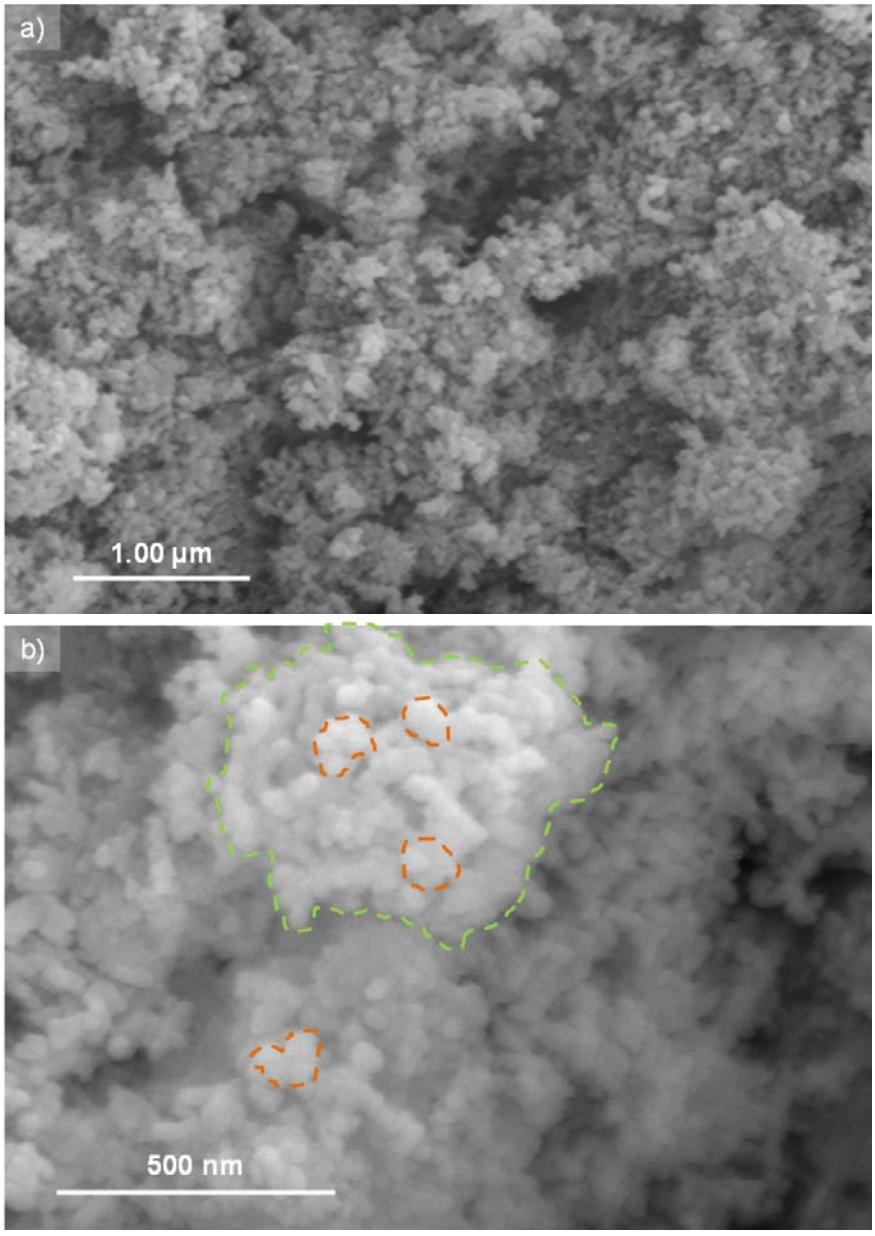

Figure 3.5: SEM micrographs of the ZnO-NC powders. Some agglomerates (in green) and aggregates (in orange) are indicated for their easy observation.

This agglomeration, especially relevant for nanoparticles upon drying, was also confirmed through particle size measurements by DLS. The graph in Figure 3.6 shows the particle size distribution of a ZnO-NC suspension at its natural pH after 15 s sonication. It must be noted than the measured hydrodynamic diameter is much larger than both the crystal size calculated from the XRD and the particle size observed in the SEM micrographs. Hence, it can be assumed that this particle size distribution does not correspond to dispersed particles but to the strong aggregates that were not broken during sample preparation with US sonication. In fact, the size observed in the particle

size distribution curve is in close agreement with that of the aggregates in the SEM micrograph in Figure 3.5b).

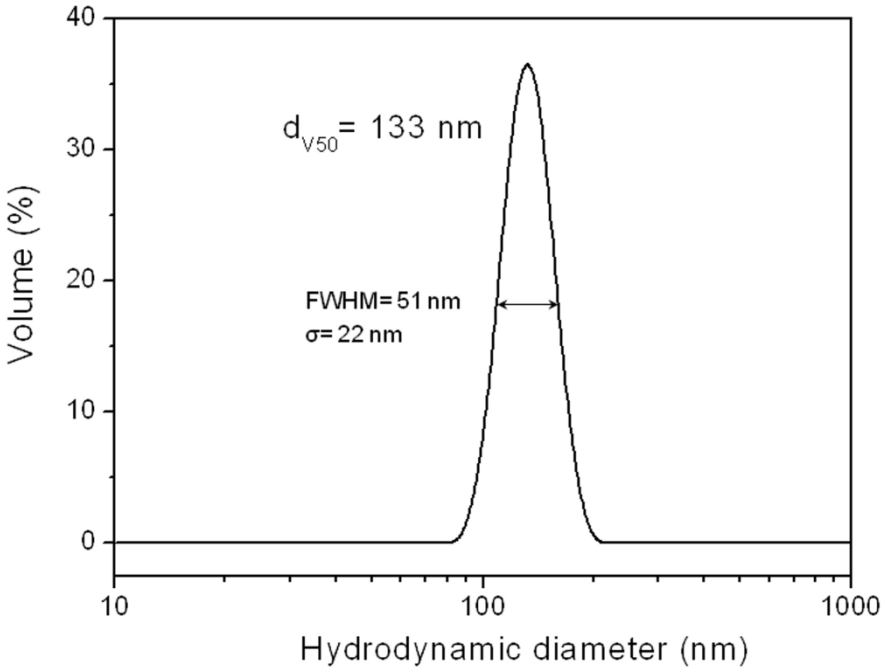

Figure 3.6: Particle size distribution of a ZnO-NC suspension. The standard deviation of the measurement (σ) was calculated applying the following equation [208], FWHM=2·√(2·ln 2)·σ, where FWHM is the full width at half maximum of the Gaussian curve.

The presence of these agglomerates and aggregates is responsible for the value of specific surface area, of 77 m^2/g. Even though the ZnO-NC particles seem to be very small, and therefore should have a very high specific surface area, they are strongly aggregated. On the other hand, the density of the powders measured by Helium Pycnometry was 3.3 g/cm^3. Divergence of this density value from that of pure ZnO (5.2 g/cm^3) was consistent with the amount of secondary phases, with lower densities, observed in the TG-DTA analysis. From these data the value of the BET diameter (calculated applying Eq. 2.3) was estimated to be of 24 nm. However, this was just considered as an approximation, since this model assumes a spherical morphology of the particles. In addition, dividing the value of the d_{V50} from the particle size distribution in Figure 3.6 (133 nm) and dividing it by the BET diameter the agglomeration factor was calculated (see Eq. 2.5). The obtained value was A_f=5.5, which corroborates the results of the DLS measurements and SEM observations, confirming both agglomeration and aggregation of the powders.

Following with the characterization it was noticed that, even though the presence of secondary phases had been verified in the TG-DTA analysis, these could not be observed in the SEM micrographs. For this reason the samples were also studied by

transmission electron microscopy, which allowed higher magnification with good resolution. The TEM micrograph of the ZnO-NC sample in Figure 3.7 confirmed how some rests of starting reagents remained after the thermal treatment, as expected from the TG-DTA analysis. These remains presented needle morphologies, consistent with the presence of LBZA species, which usually present needle-like structures (as shown in Figure 1.7). In between these needles small, rounded and slightly hexagonal particles of the ZnO-NC could be observed.

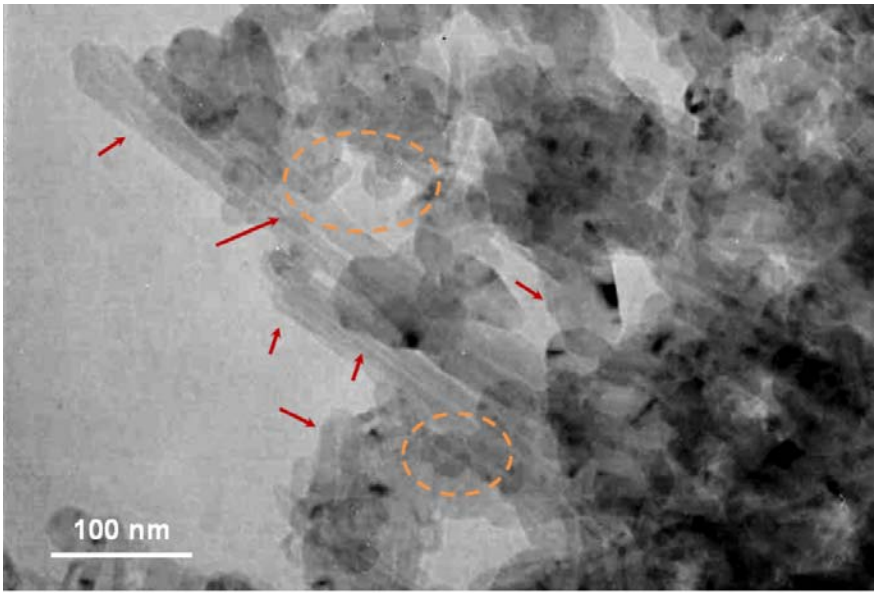

Figure 3.7: TEM micrographs of the ZnO-NC sample. LBZA remains are indicated with red arrows, whereas the orange circles show small ZnO-NC particles.

When these samples were taken to the HRTEM, it was observed that the powders presented a thread-like morphology (Figure 3.8a), which, at higher magnifications, was seen to be composed of very small particles (~ 5 nm) assembled in line (figure 3.8b). This can be ascribed to the washing protocol, which left some rests of intermediate LBZA species, which were partially dissolved, forming threads. These threads evolved with the thermal treatment into small crystalline particles (5 – 8 nm) that stayed aligned. The lattice fringes corresponding to the (0 0 0 2) plane of ZnO (indexed using Gatan Digital micrograph) can be seen in the HRTEM micrograph. In addition, the selected area electron diffraction (SAED) results shown in Figure 3.8c show the presence of spots and concentric rings, which indicate the polycrystalline nature of the analyzed area. However, the spots point out to the fact that, in the ZnO-NC powder each nanoparticle is in fact, a nanocrystal.

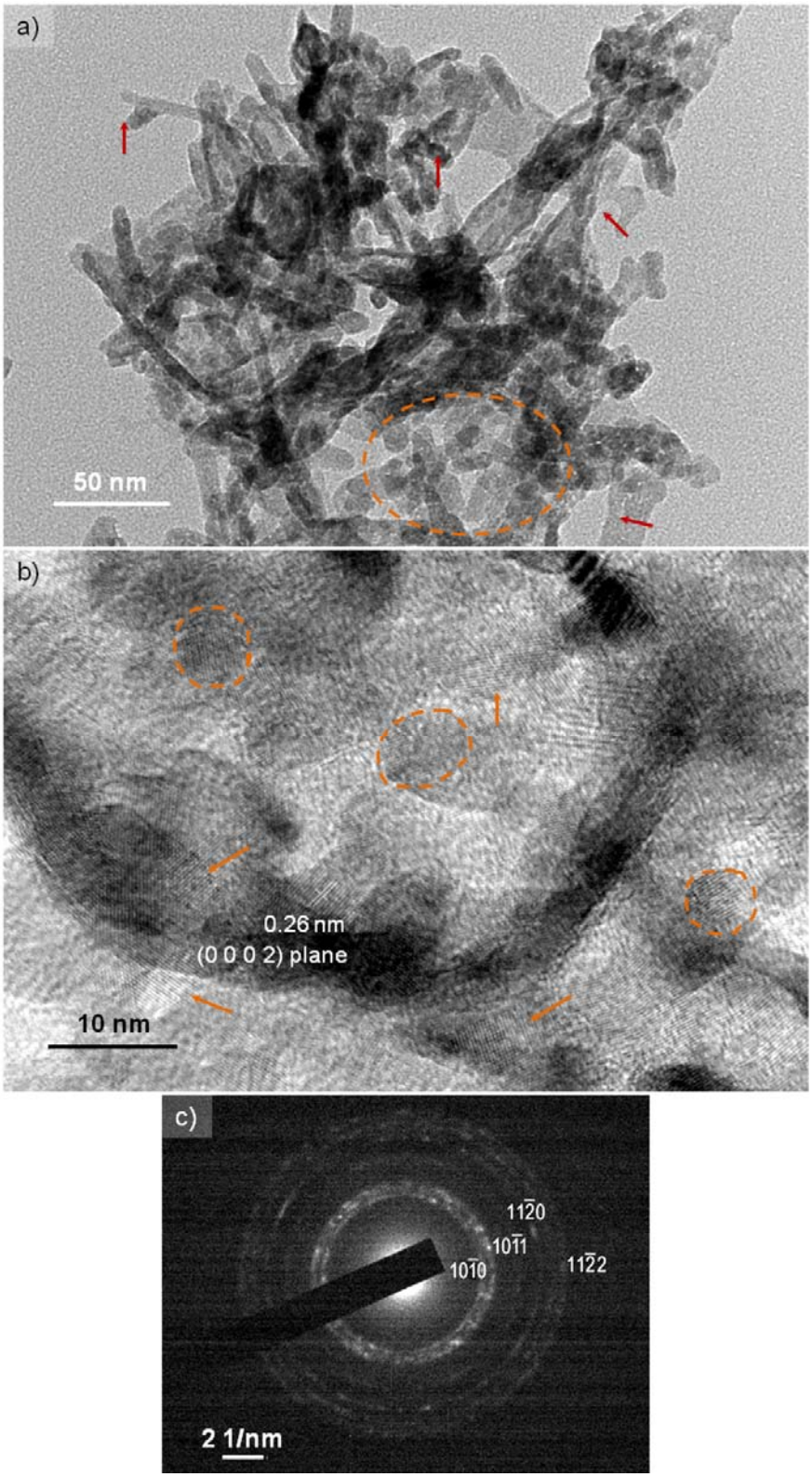

Figure 3.8: a and b) HRTEM micrographs and c) SAED diffraction pattern of the ZnO-NC powders indexed to several ZnO planes. Red arrows in a) indicate the presence of acetate remains, whereas the orange circle shows an area with small ZnO-NC particles. Circles and arrows in b) indicate some particles and areas in which lattice fringes can be observed. The scale in c) corresponds to the reciprocal space used for the calculation of the d-spacing and assignment of the diffraction indexes.

3.2. Synthesis of Co-doped ZnO nanocrystals (< 10 nm): ZnO-DNC.

ZnO nanoparticles doped with a 3 % wt of Cobalt and sizes below 10 nm were synthesized by coprecipitation. According to the literature, doping with such a small amount of Co should not change the morphology or size of the ZnO powders, since Zn^{2+} ions in tetrahedral coordination (noted as T_d) are replaced by Co^{2+} ions in the same coordination and therefore no charge difference nor extra vacancies are introduced [209]. A slight contraction of the ZnO unit cell could be expected, due to the smaller ionic radius of Co^{2+} ions (ionic radius in tetrahedral coordination T_d= 0.058 nm) compared to that of Zn^{2+} ions (ionic radius T_d=0.060 nm) [10, 210].

Coprecipitation was carried by dropwise addition of NaOH 2M up to pH=9 to an aqueous solution of the precursors. Considering the results obtained in the previous section, in this case cobalt nitrate hexahydrate, $Co(NO_3)_2 \cdot 6H_2O$, was chosen as Co^{2+} precursor so as not to introduce more carboxylates, but instead introduce nitrates which are easily removed in the washing and drying steps [51]. During NaOH addition formation of a light pink precipitate was observed, which was retrieved after the thorough washing procedure, i.e. washing in 3.5 l of DI water under stirring (twice), filtering and rinsing with a 1:1 ethanol:DI water mixture and ethanol. This light pink color of the powders points out to the presence of cobalt hydroxide: Co^{2+} ions in aqueous solution become hydrated forming the octahedral complex $Co(H_2O)_6^{2+}$. This complex precipitates as $Co(OH)_2$ with NaOH addition, showing this light pink color [211]. After the thermal treatment (300º-10min), the color of the powders changed from light pink to moss green, which is indicative of the loss of water molecules attached to the Co, and the incorporation of Co^{2+} ions into the ZnO structure. This procedure involving a Co(II) precursor and a low crystallization temperature inhibits the formation of CoO and promotes the diffusion Co^{2+} ions with a four-fold coordination and ionic radius of 0.58 Å inside the wurtzite structure [212].

The calcined powders (which from now on will be referred to as ZnO-DNC, short for doped nanocrystals) were characterized by means of XRD and TG-TDA analysis.

Figure 3.9 shows the XRD diffractogram of the DNC-ZnO sample, which presents wide, broad peaks which correspond to a typical wurtzite structure, with traces of a secondary phase that was identified as hydrozincite, which was already observed in the synthesis of the ZnO-NC (see Figure 3.1) As in the previous case, the broadness of the diffraction peaks points out to a very small particle size. Crystallite size of this sample, calculated using the Warren modification of the Scherrer equation, was of 5.4 nm, confirming the small size of the particles. This decrease in particle size might be

due to the incorporation of Co^{2+} ions, smaller than Zn^{2+} ions, into the crystal structure of ZnO [76], or a capping effect produced by the acetates and nitrates adsorbed onto the ZnO. On the other hand, the estimated lattice parameters (shown in the inset) were even larger than those of the undoped powders. This divergence from the lattice parameters of ZnO wurtzite pattern might be ascribed to the poor crystallinity of the nanosized particles and the lattice defects in them.

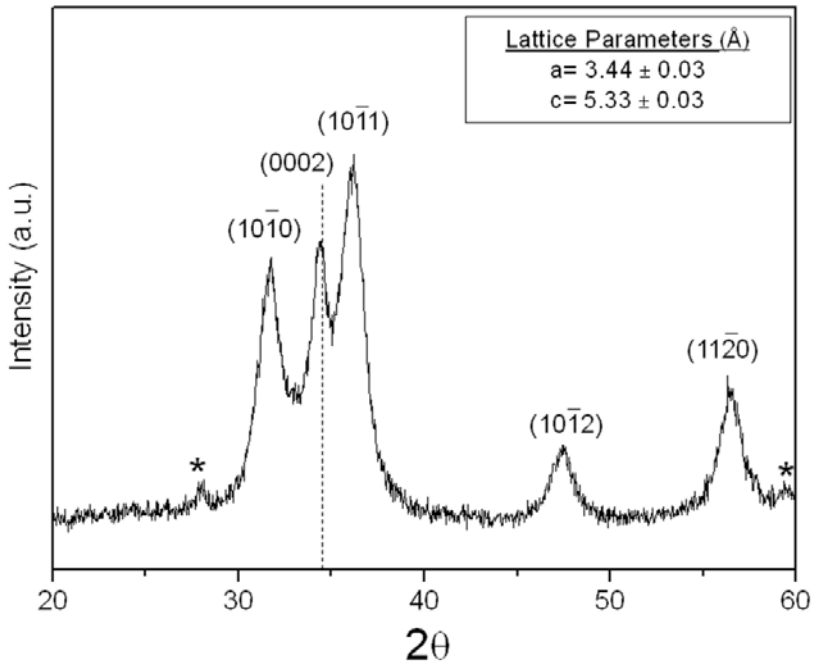

Figure 3.9: XRD diffractogram of ZnO-DNC powders treated at 300ºC for 10 min. The * peaks in the diffractogram correspond to hydrozincite, $Zn_5(CO_3)_2(OH)_6$, (ICDD nº 00-019-1458).

However, as in the case of the undoped ZnO-NC, TGA of the sample confirmed the presence of remaining acetates from the synthesis, which decomposed at 225 ºC, with a corresponding mass loss of 24 % wt (Figure 3.10). In this case the amount of remaining reagents was higher than that of the pure ZnO-NC (mass loss of 16 % wt), as could be inferred from the presence of peaks of secondary phases in the XRD diffractogram, which were not observed for ZnO-NC powders.

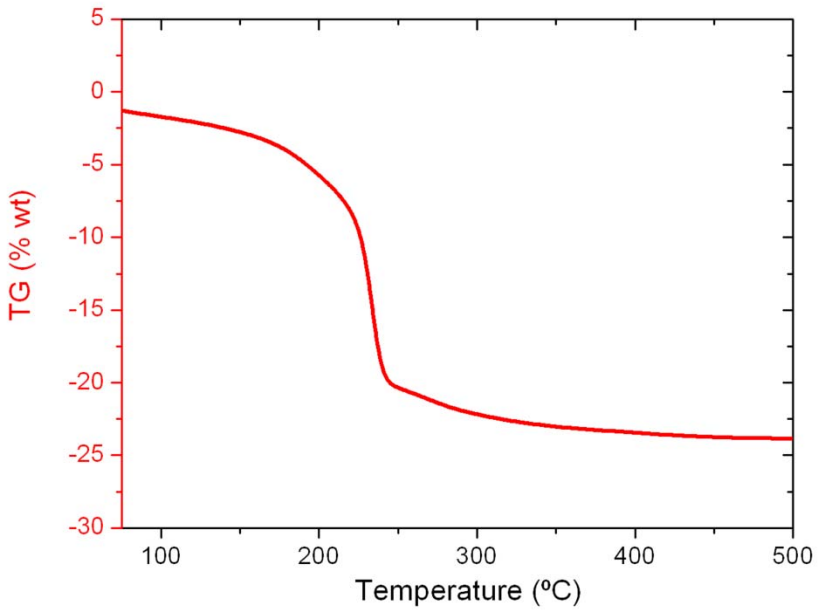

Figure 3.10: TG analysis of the ZnO-DNC powders treated at 300ºC for 10 min.

Morphological characterization of the DNC-ZnO powders by means of SEM showed that the small particles were forming aggregates of about 100 nm (Figure 3.11). In this case the presence of larger agglomerates was not as high/visible as for the undoped ZnO-NC.

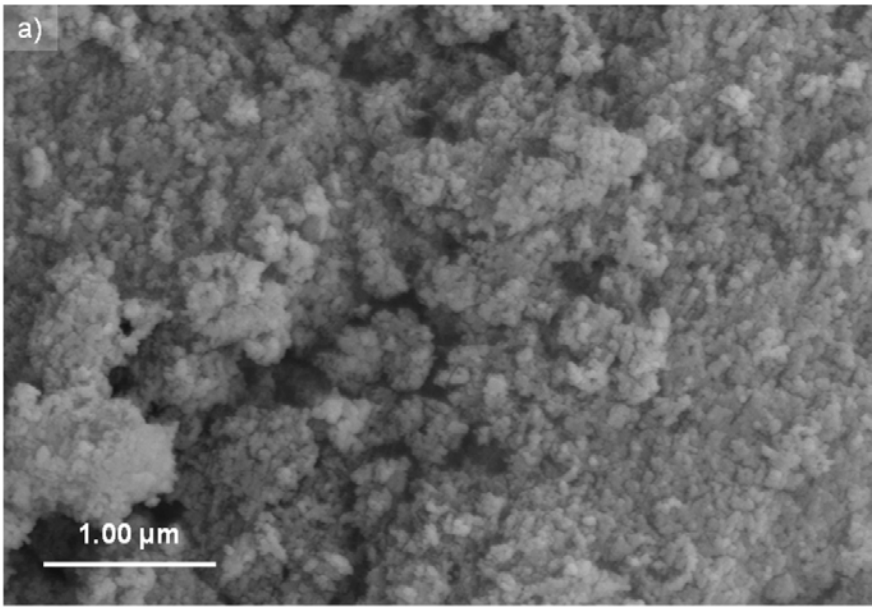

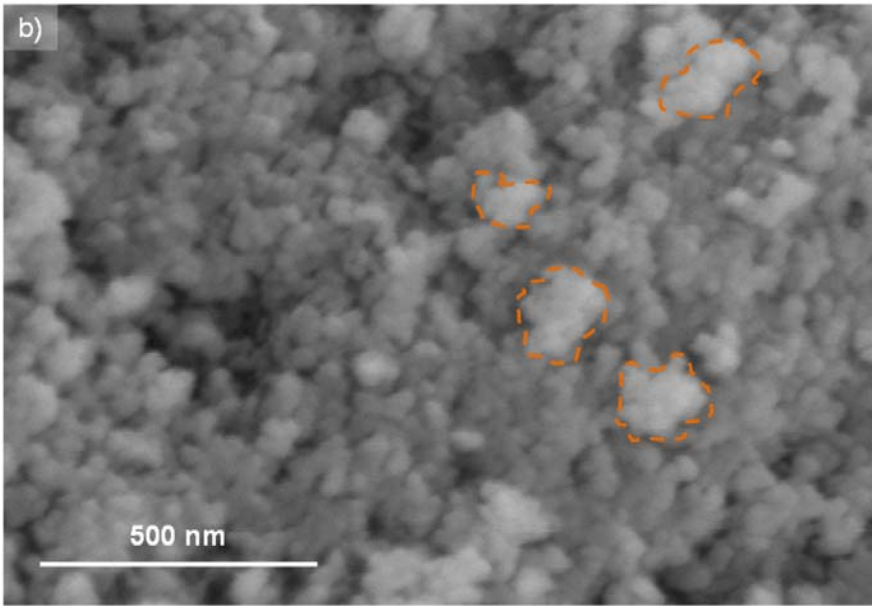

Figure 3.11: SEM micrographs of the ZnO-DNC powders. Some aggregates are signaled in orange, for their easy observation.

The size of these aggregates was determined by DLS measurements. Figure 3.12 shows the particle size distribution of a ZnO-DNC suspension (at natural pH and after 15 s sonication), from which it can be inferred that the aggregates formed by these powders are slightly larger than those of the ZnO-NC powders. This is consistent with the high trend of nanoparticles towards aggregation (which increases with decreasing particle size), as the ZnO-DNC particles seem to be smaller than the ZnO-NC ones.

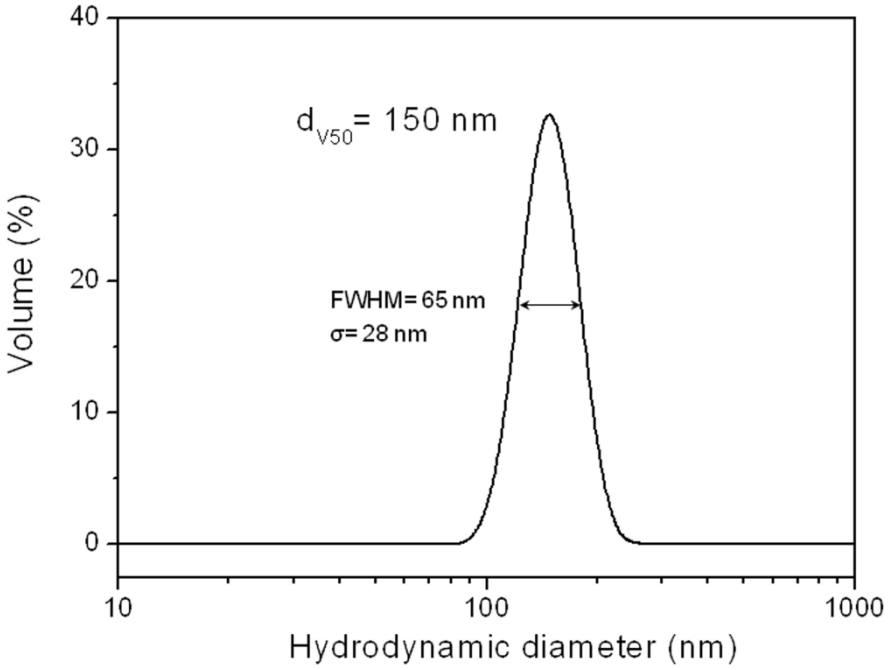

Figure 3.12: Particle size distribution of a ZnO-DNC suspension. The standard deviation of the measurement (σ) was calculated applying the following equation [208] , FWHM=2·√(2·ln 2)·σ, where

FWHM is the full width at half maximum of the Gaussian curve.

Specific surface area and density values of the ZnO-DNC powders were of 85 m^2/g and 2.5 g/cm^3, respectively. These results are in agreement with those previously observed: the higher specific surface of the ZnO-DNC compared to the undoped ones confirms the smaller crystal size of the doped particles calculated from the XRD, whereas the lower density is consequence of the higher amount of remaining species in the powders, detected in the TGA, and their poor crystallinity. For these powders the calculated BET diameter was of 28 nm, higher than that of ZnO-NC. This increase in the BET diameter is easily explained by the decrease in density. In addition, the calculated agglomeration factor was of 5.3, in agreement with the agglomeration of the powders observed in the SEM micrographs in Figure 3.11.

The TEM micrograph in Figure 3.13 confirms the smaller particle size of ZnO-DNC powders compared to that of ZnO-NC. In this case, and even though the amount of remaining species was higher for this sample, these are not as easily observed in the micrograph. This might be due to the presence of nitrate species, which may facilitate the dissolution of the bigger acetate needles into smaller particles.

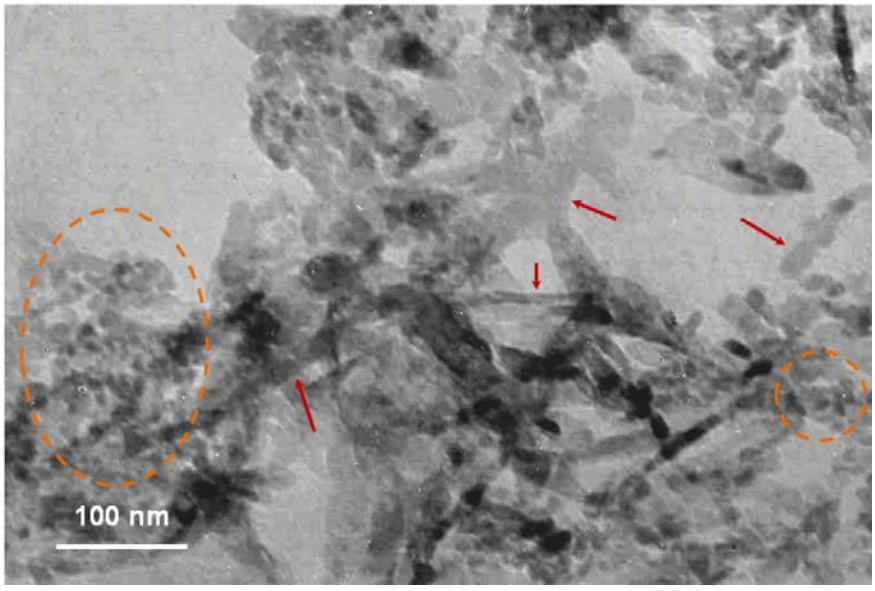

Figure 3.13: TEM micrograph of the ZnO-DNC sample. Red arrows point out the presence of secondary acetate phases, whereas orange circles show the small ZnO-DNC particles.

From the HRTEM micrographs of the ZnO-DNC powders (Figure 3.14) it can be noted that even though they present the same thread-like arrangement, the size of the doped particles is slightly smaller than that of ZnO-NC, which is consistent with the results obtained from the XRD crystal size calculations and the Ss_a values. ZnO-DNC

particles are crystalline, as inferred from the fact that lattice fringes can be observed in the micrograph in Figure 3.14b (indicated with orange arrows). In addition, SAED diffraction patterns show both spots (which correspond to bigger crystalline particles) and diffuse concentric rings, due to very small nanoparticles. As in the previous case, each ZnO-DNC nanoparticle seems to be a nanocrystal.

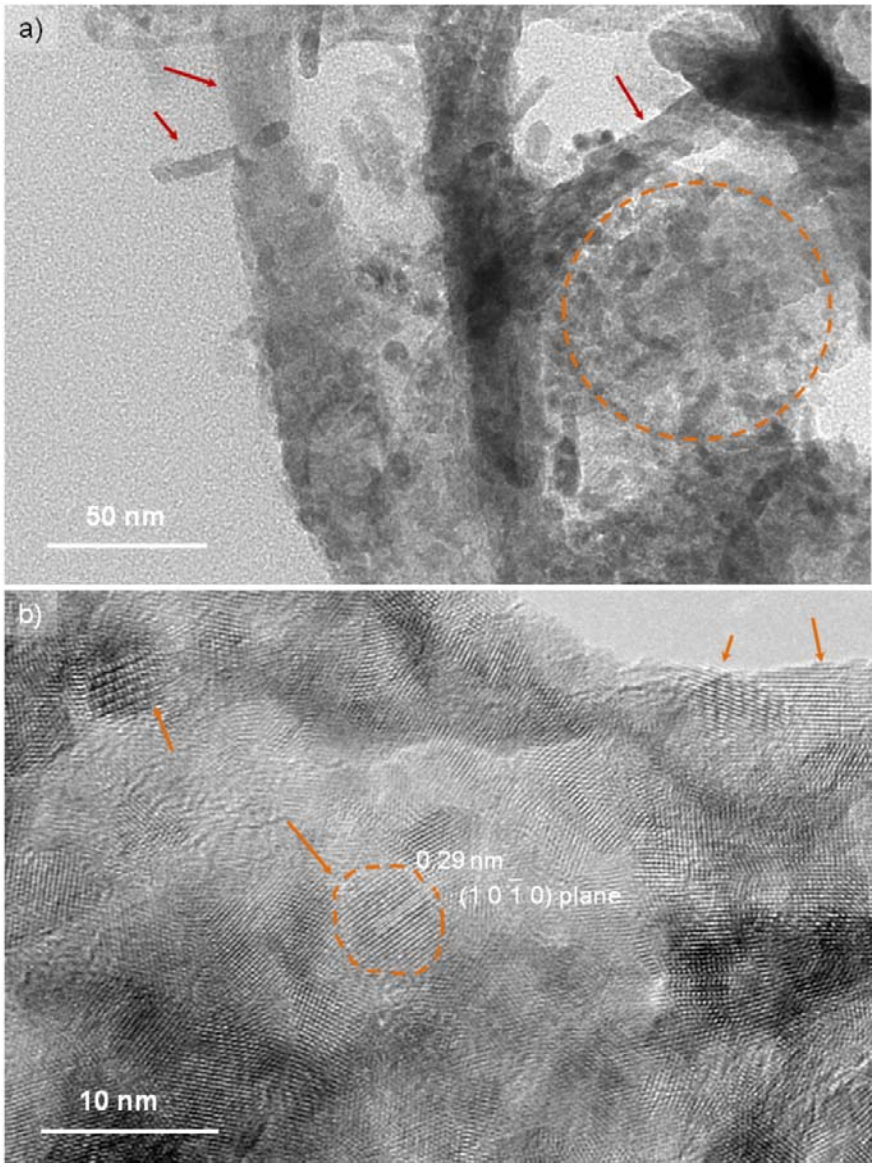

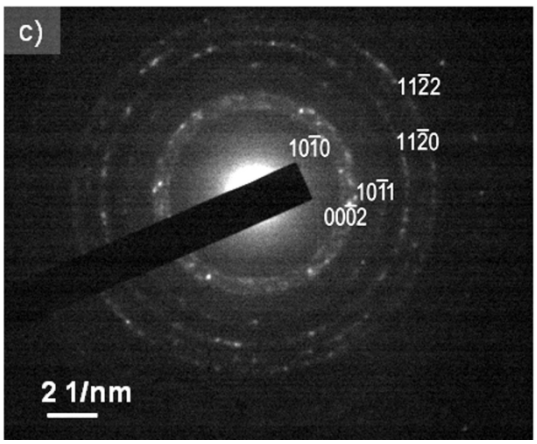

Figure 3.14: a and b) HRTEM micrographs and c) SAED diffraction pattern of the ZnO-NC powders indexed to several planes of the wurtzite structure. Red arrows and orange circles in a) indicate the presence of impurities and ZnO-DNC nanoparticles, respectively. Circles and arrows in b) indicate some particles and areas in which lattice fringes can be observed.

3.3. Synthesis of ZnO nanoparticles with tailored morphology (ZnO-F).

In the procedures reported in the previous sections the small size of the ZnO nanoparticles was valued over their purity and crystallinity. However, in order to try to decrease the amount of secondary acetate phases and promote their transformation into crystalline ZnO, a second procedure was carried out. In this second protocol, precipitation was produced in the same conditions as in the previous case (dropwise addition of NaOH 2M up to pH=9), but the rinsing protocol was much more thorough: a washing cycle in which the precipitate powders were washed with 5 l of DI water and subsequently rinsed with ethanol was repeated until, after seven cycles, the presence of LBZA is minimized. The SEM micrographs in Figure 3.15 show how, in addition to minimizing the amount of LBZA and remaining species, the washing procedure also had an effect on the morphology and particle size of the powder: before the washing step (Figure 3.15 a and b) the powders showed a plate-like morphology, which was gradually lost with the washing. In this sense, the washing step was stopped after seven cycles, so as to avoid a further change of the morphology and particle coarsening due to recrystallization.

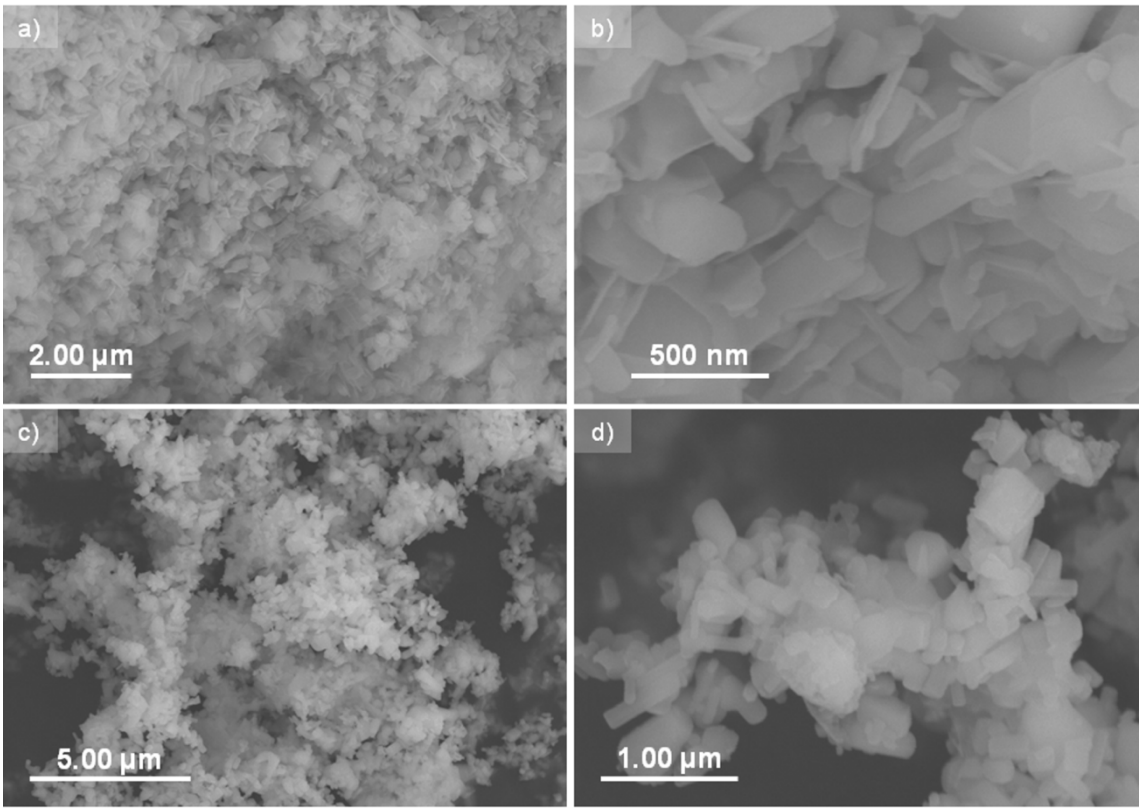

Figure 3.15: SEM micrographs of the ZnO powders a,b) as synthesized and c,d) after 7 washing cycles.

Results of the TG-DTA analysis, presented in Figure 3.16, show a large exothermic peak at about 175 ºC, with a corresponding mass loss of 70 wt%, which can be ascribed to the dehydration of zinc hydroxide to form zinc oxide. Another two effects can be observed in the DTA curve, which can be ascribed to the decomposition of zinc acetate, which starts at 237 ºC, leading to the formation of basic zinc acetate, and to the decarboxylation of this into ZnO above 350 ºC [213-216].

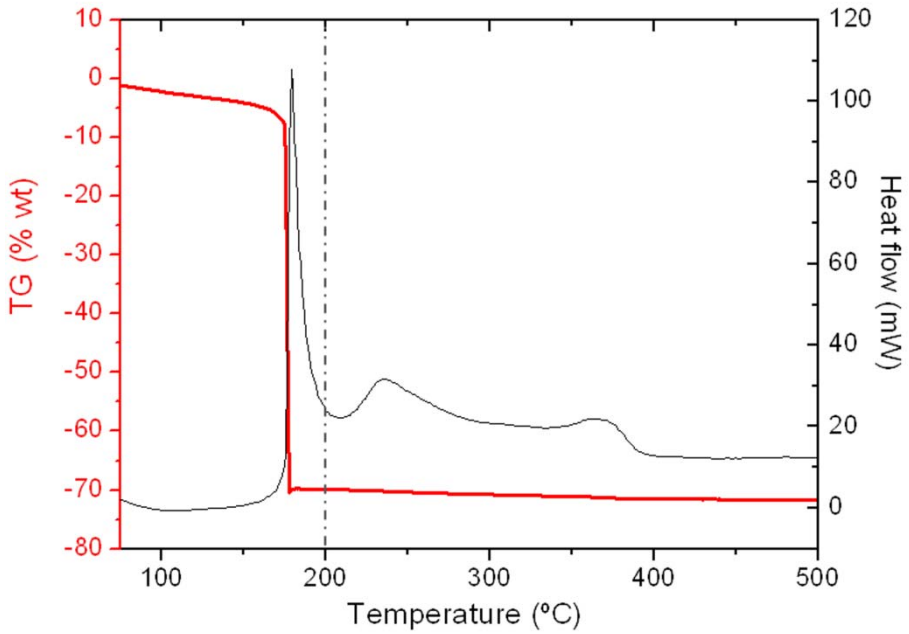

Figure 3.16: TG-DTA analysis of the synthesized ZnO powders after 7 washing cycles. The dotted line indicates the temperature of the subsequent thermal treatment.

From these results it can be inferred that this protocol allowed a better removal of acetate species which, as has been reported, may promote a pinning effect on grain boundaries, reducing the boundary mobility of as-formed particles and minimizing mass diffusion effects during calcinations, thus preventing particle growth [53]. Thus, given the confirmed absence of impurities, the applied thermal treatment was milder, 200 ºC for 4 min, in order to boost crystallization of the ZnO particles but not particle growth. The obtained powders will be named F-ZnO (where F stands for flakes).

Effectiveness of the exhaustive washing procedure and thermal treatment was verified by means of XRD and TGA analysis of the calcined powders. The XRD diffractogram of the powder after calcination (Figure 3.17) presents sharp peaks which can be indexed to pure ZnO together with a small background signal and no trace of secondary phases. Moreover, estimated lattice parameters match those of ZnO wurtzite pattern much more closely than in the previous cases. This result, in addition to the narrowness of the peaks in the XRD diffractogram, tends to confirm the expected increase in crystallinity of the powders.

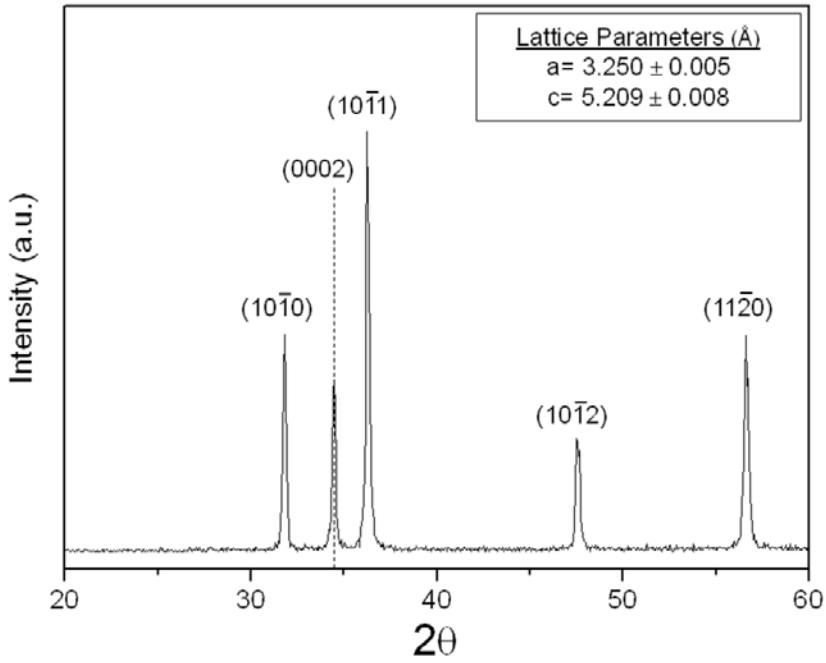

Figure 3.17: XRD diffractogram of the ZnO-F powders treated at 200ºC for 4 min.

Calculations from the XRD diffractogram rendered an average crystallite size of 29.4 nm, which indicates that there was some crystal growth during the washing and calcination steps. Moreover the I(0 0 2)/I(1 0 0)<1 ratio suggests that morphology of the ZnO-F particles differs from that of a sphere [217]. On the other hand, the TGA analysis of the calcined powders (Figure 3.18) shows a mass loss of about 20 wt %, half of which takes place at about 150 ºC and can be ascribed once more to the dehydration of zinc hydroxide to form zinc oxide. On the other hand, the other half of the mass loss takes place gradually between 200 and 350 ºC and can be associated to the elimination of remaining structural water molecules and hydroxyl groups.

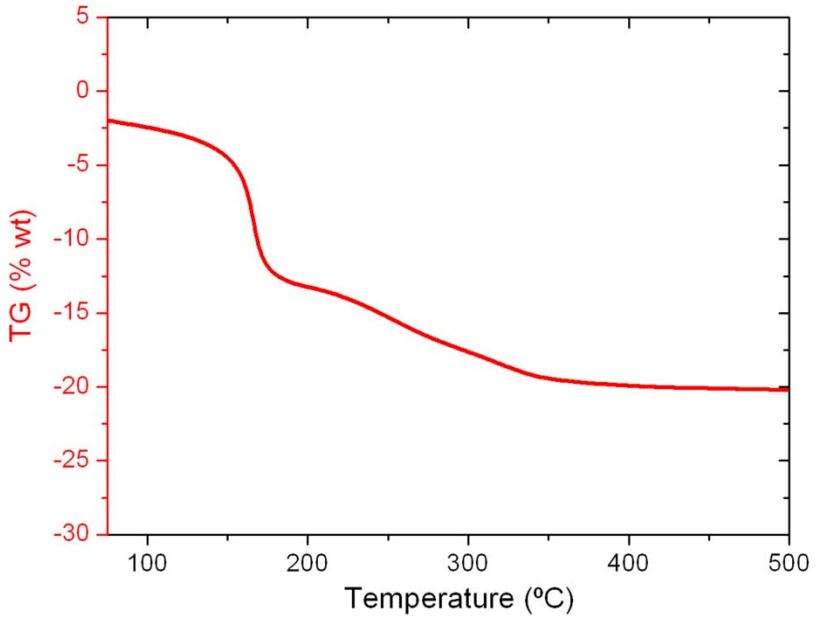

Figure 3.18: TG analysis of ZnO-F powders treated at 200 ºC for 4 min.

This mass loss suggests the presence of some remains of zinc hydroxide, which did not have the time to transform into ZnO, given the short length of the thermal treatment. Therefore, in order to verify the presence of zinc hydroxide in the sample, and observe their morphology, the powders were characterized by electron microscopies.

From a quick look at the SEM micrographs of the ZnO-F powders in Figure 3.19 it is immediately obvious that the ZnO-F powders are much more heavily agglomerated than the powders prepared following the first protocol. In addition, both particle size and shape factor of these powders seemed larger than that of the NC-ZnO samples.

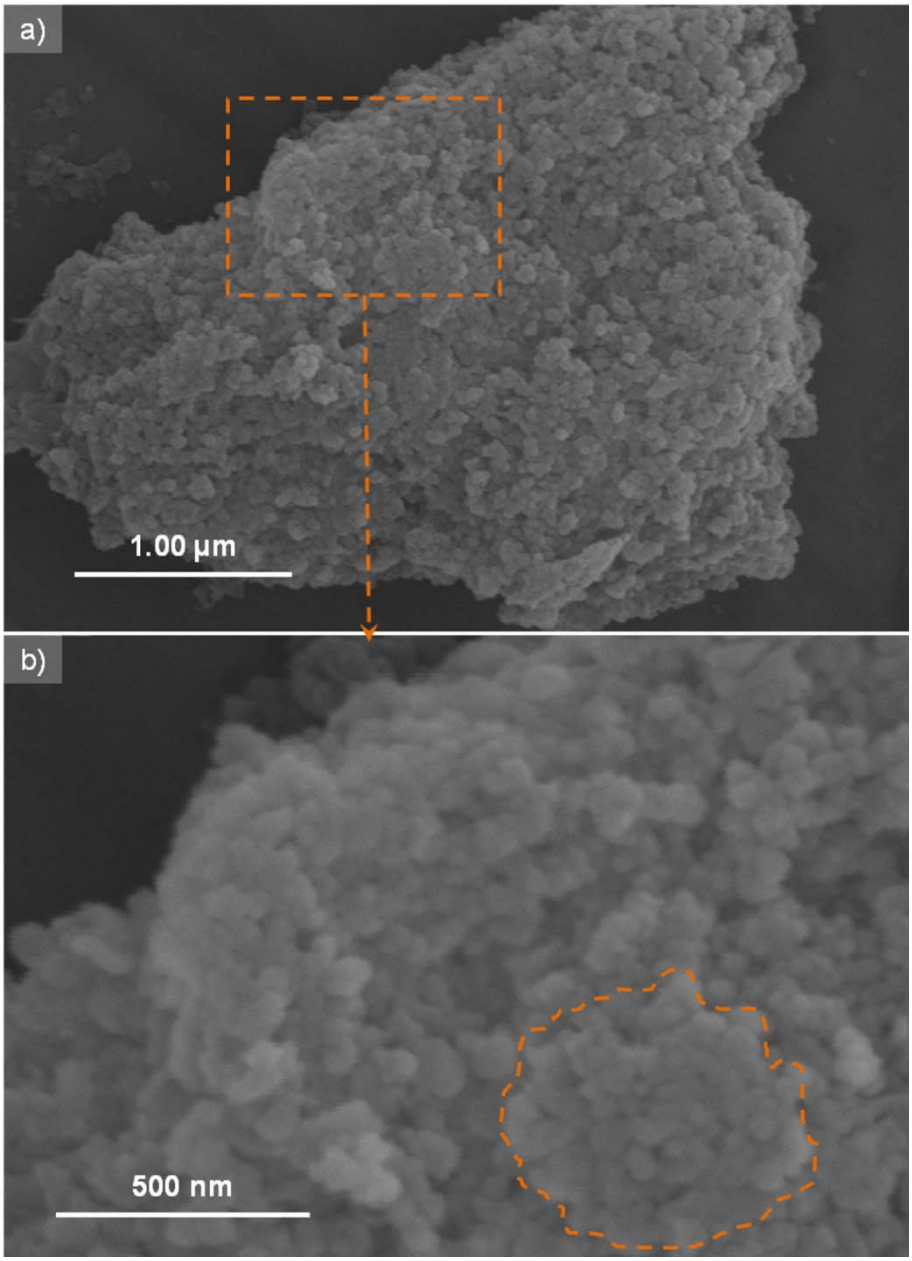

Figure 3.19: SEM micrographs of the ZnO-F powders. An example of large aggregate is circled in orange.

Heavy agglomeration of the particles was confirmed by DLS measurements. As represented in the graph in Figure 3.20, the agglomerate sizes of ZnO-F suspensions are almost four times bigger than in the previous cases.

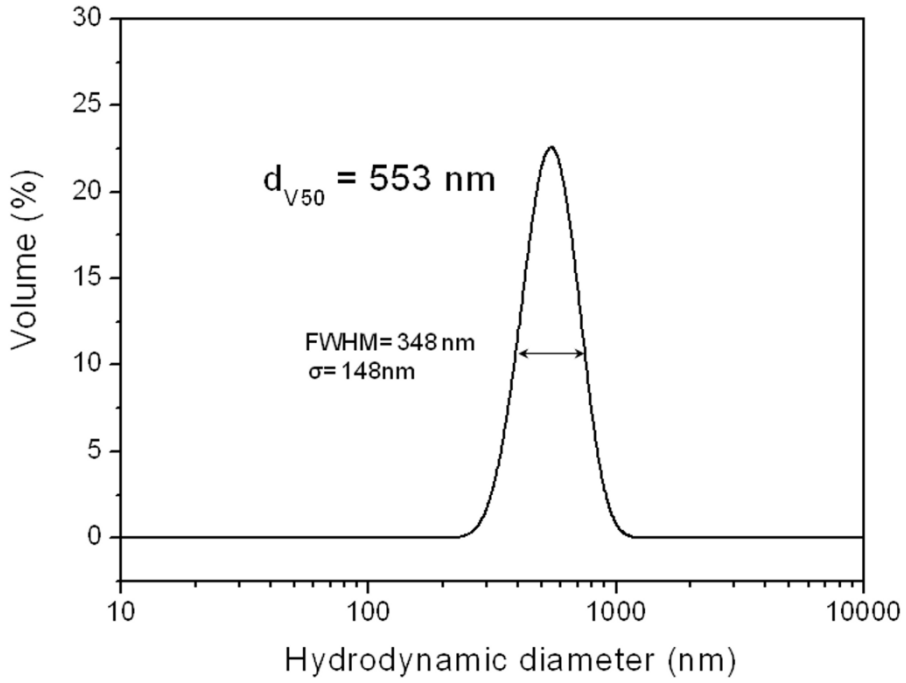

Figure 3.20: Particle size distributions of a ZnO-F suspension. The standard deviation of the measurement (σ) was calculated applying the following equation [208] , FWHM=2·√(2·ln 2)·σ, where FWHM is the full width at half maximum of the Gaussian curve.

Specific surface area and density of the ZnO-F powders were determined by N_2 adsorption and helium pycnometry, respectively. The high density of the ZnO-F powders, ρ = 4.4 g/cm^3, relatively close to that of pure ZnO, confirms the low amount of impurities, and is in agreement with the presence of large aggregates, which hamper higher densities. However, the high specific surface, Ss_a = 170 m^2/g, was very unexpected given the nature of the powders, bigger and forming larger aggregates than in previous cases. Taking into account this value of Ss_a, the resulting BET diameter was of 10 nm, which is extremely small, and was only considered to calculate the agglomeration factor. The high value obtained for the calculation of this parameter, A_f = 56, confirmed the massive agglomeration of the particles.

In order to better examine the morphology and agglomeration state of the powders, ZnO-F powders were characterized by TEM microscopy. The TEM micrograph in Figure 3.21 clearly shows the presence of two different particle populations: a homogeneous population of hexagonal-like flake-shaped particles with diameters of 20-30nm (in agreement with those calculated from the XRD diffractogram), and a second, dense population of very small particles in the background of the micrograph.

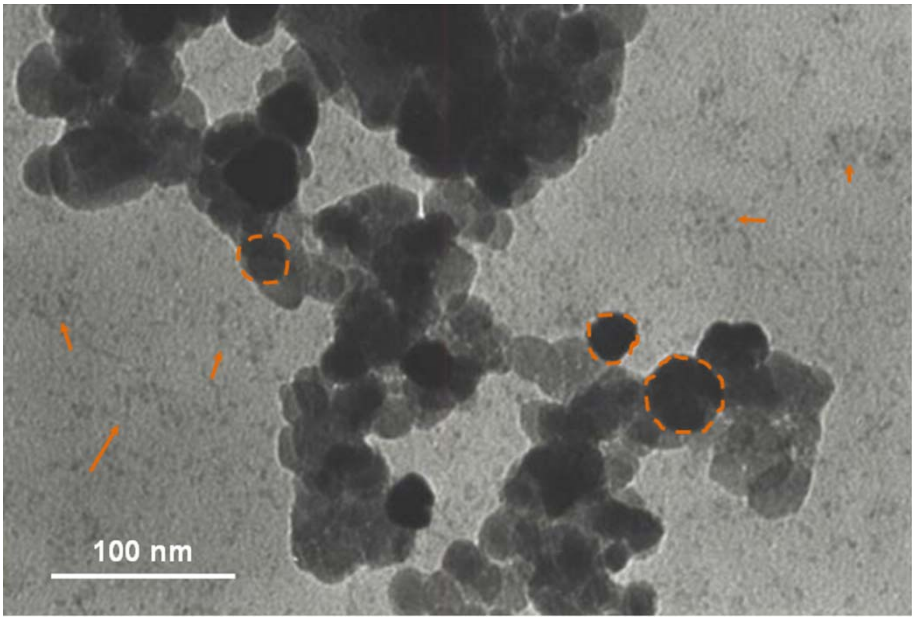

Figure 3.21: TEM micrograph of the ZnO-F sample. Some examples of larger ZnO particles are circled in orange; arrows indicate the large population of smaller particles in the background.

This second smaller population is probably responsible for the high Ss_a of the powders, and thus, in order to verify this, the curve of N_2 adsorption of the powder was studied, together with those of the previously synthesized powders, ZnO-NC and ZnO-DNC. Results in Figure 3.22 show that the porosity of the ZnO-F powders is of about 200 nm, much larger than those of the ZnO-NC and ZnO-DNC powders, of about 3 nm.

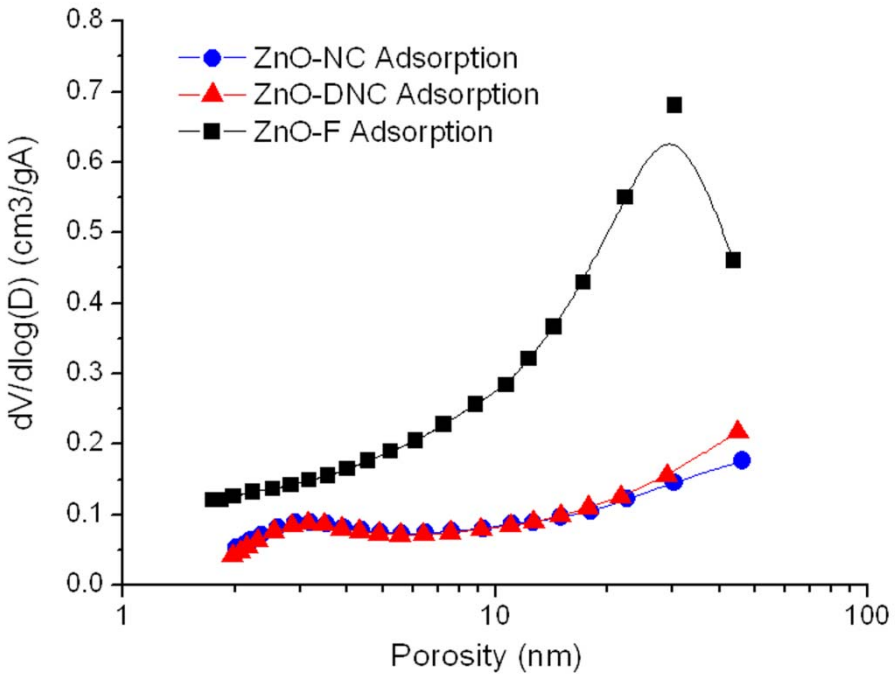

Figure 3.22: N_2 adsorption curves of the three synthesized powders.

These results are in agreement with the observations carried out in the TEM. In the ZnO-NC and ZnO-DNC powders the nanocrystals are forming small agglomerates which present a small amount of micropores. The ZnO-F powder, in contrast, is constituted by larger flakes (of about 30 nm) which agglomerate leaving a representative amount of mesopores in between them. Therefore this mesoporosity is the responsible of the high value of the specific surface area, and not the smaller population of ZnO-F particles.

The high resolution TEM was then used to verify the nature of this smaller population of ZnO-F particles. HRTEM micrographs (Figure 3.23) showed that these smaller particles had sizes of ~3 nm and a less defined morphology (almost spherical) than that of the bigger flake-shaped nanoparticles. What is more, it could be observed that in some cases, what seemed to be larger flakes were in fact aggregates of these smaller particles (Figure 3.23a).

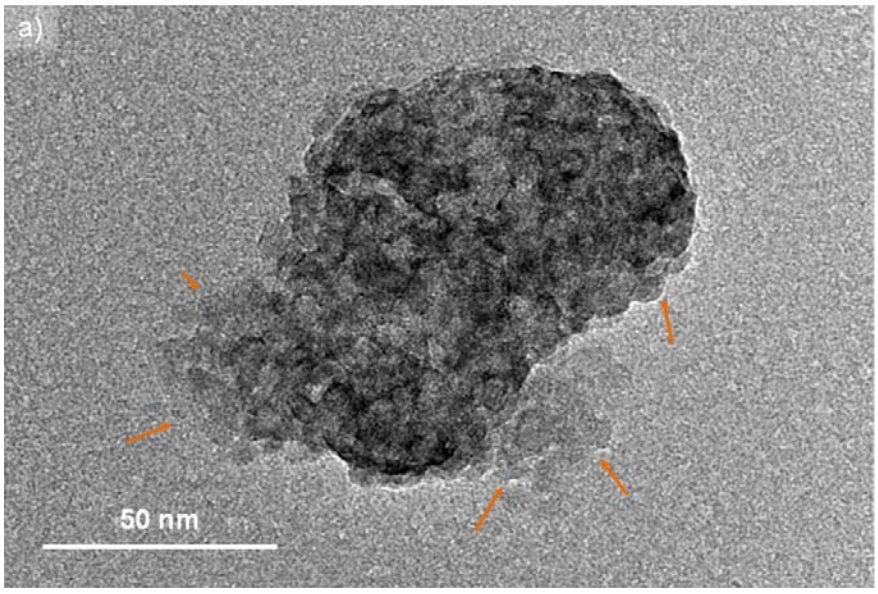

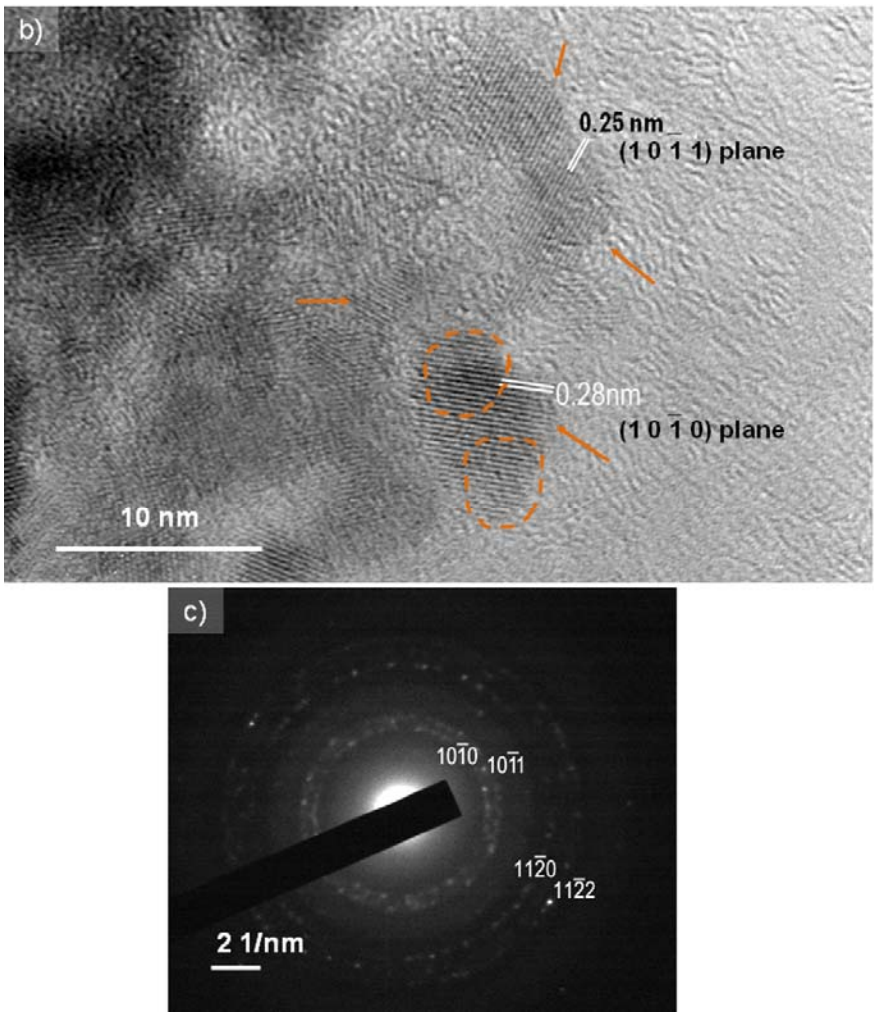

Figure 3.23: a and b) HRTEM micrographs and c) SAED diffraction pattern of the ZnO-F powders indexed to several planes of the wurtzite structure. Arrows in a) point areas in which the small particles that form the aggregate can be observed. Circles and arrows in b) indicate some particles and areas in which lattice fringes can be clearly observed, respectively.

Lattice fringes can easily be seen in the HRTEM micrograph in Figure 3.23b, which points out to a high crystallinity of the particles. However, not all the interplanar distances calculated from these fringes could be assigned to a ZnO wurtzite structure. Moreover, when selected area electron diffraction (SAED) analysis was performed on these samples, some inconvenient arose: on the one hand, the small size of the particles lead to wide, blurry diffraction rings which could not be easily assigned, and on the other hand it seemed that not all of these rings could be assigned to a ZnO wurtzite structure. These results, together with the size and the two types of particles observed in the sample, can be ascribed to the synthesis procedure. During the precipitation procedure, a large number of zinc hydroxide nuclei were generated, which, during the thorough and prolonged rinsing step, overcame two opposite phenomena. On the one hand, and as in the previous cases, the rinsing led to a slight

re-dissolution of the nuclei. On the other hand, and as there was no additional input of Zn^{2+}, growth was favored vs. nucleation and only those nuclei above the certain critical size developed to form larger particles with tailored, hexagonal flake morphology, whereas the rest stayed as very small hydroxide nuclei. Moreover, the subsequent thermal treatment was so fast that the bigger, more crystalline particles, which constituted crystalline nuclei, grew at the expense of the smaller particles and transformed into ZnO. This result is in agreement with the TGA analysis, in which we observed the transformation of first, the larger and then the smaller particles from zinc hydroxide into the oxide.

3.4. Summary and brief comparison of the synthesized powders.

The synthesis and characterization of three different ZnO powders has been described. In all three cases the synthesis was carried out by direct precipitation from aqueous solutions of zinc acetate, and two different protocols for washing were followed:

The first protocol, in which small particle size was valued over purity and crystallinity, rendered powders with significant amounts of acetate phases, which strongly adsorbed onto the ZnO surface, hindering particle growth and thus leading to small particle sizes. For the co-precipitation of co-doped nanoparticles (ZnO-DNC), Cobalt nitrate was used instead of cobalt acetate. However this change in the counterion did not have a dramatic effect on the amount of secondary phases, nor in the particle size and morphology.

The second protocol focused on decreasing the amount of acetate remains and promoting their transformation into ZnO. For this purpose, several washing cycles were carried out until the presence of acetates was minimized. This protocol favored particle growth vs. nucleation. However, when characterized, two particle size populations were observed: large hexagonal ZnO flakes (30 nm) and smaller (3 nm) particles of $Zn(OH)_2$.

Table 3.1 summarizes the main parameters of the three synthesized powders, for their facile comparison.

Table 3.1.: experimental conditions and calculated parameters of F-ZnO, NC-ZnO and DNC-ZnO powders.

	NC-ZnO	**DNC-ZnO**	**F-ZnO**	**Reference Pure ZnO**
Rinsing volume (l)	3.5 x 2	3.5 x 2	5 x 7	-
Thermal treatment	300 ºC- 10 min	300 ºC- 10 min	200 ºC - 4 min	-
Cell parameters (Å)	a = 3.35 ± 0.01 c = 5.30 ± 0.06	a = 3.44 ± 0.03 c = 5.33 ± 0.03	a= 3.250 ± 0.005 c = 5.208 ± 0.008	a = 3.2488 ± 0.001 c = 5.2059 ± 0.001
Crystal size (nm)	6.5	5.4	29.4	-
S_{Se} (m^2/g) (± 3 %)	77	85	170	-
ρ (g/cm^3) (± 10 %)	3.3	2.5	4.4	5.2
$d_{BET\ (nm)}$	24	28	10	-
d_{V50} (nm)*	133 ± 22	150 ± 28	553 ± 148	-
A_F	5.5	5.1	55	-

*at natural pH

Chapter 4

Chapter 4: Electrophoretic deposition from ZnO suspensions

A necessary requirement for the shaping of films and coatings by Electrophoretic Deposition is the use of stable, well dispersed colloidal systems. This implies that suspensions must be optimized in order to achieve the maximum dispersion of the powders, i.e. minimum aggregate size, and maximum stability: dispersion of powders into their minimum aggregate sizes must last in time for them to move towards the electrode independently, and prevent them from sedimenting or agglomerating. This is not as trivial a matter as it might seem, as dry powders (especially those of nanometric sizes) present a high trend towards agglomeration, forming aggregates that are not easily re-dispersed.

This is the case in the present work, in which there are three clearly different ZnO nanometric powders: on the one hand two powders, ZnO-NC and ZnO-DNC, with low crystallinity, presence of impurities (acetates) which result in low densities (3.3 and 2.5 g/cm^3 respectively), crystal sizes of about 5-8 nm with relatively high agglomeration factors (5.5 and 5.3 determined by DLS), and a 3 wt % of Co-doping (in the case of the ZnO-DNC powders). On the other hand a pure, well crystallized ZnO-F powder, with a relatively high density (4.4 g/cm^3) and flake-like polycrystalline particles of 50 nm which appear heavily agglomerated (A_f = 56). The different nature of the three powders will determine their surface reactivity and thus their behavior when suspended in a liquid medium. In this sense, ZnO-F powders present well crystallized flake-like particles where the two differentiated polar surfaces in the structure of ZnO (described in the Introduction) are expected [218]. Therefore it can also be expected that these surfaces will suffer the hydroxilation reactions that typically take place for metal oxides in the presence of water to form hydroxide layers at the surface. On the other hand, the presence of polar surfaces in the ZnO-NC and ZnO-DNC powders is not clear due to their low crystallinity and small size. Moreover, the impurities in these powders might affect their colloidal behavior, as they might adhere to their surfaces.

Therefore, in this chapter the study of the superficial behavior of each of the different powders when immersed in water will be described, together with their stabilization in aqueous suspensions and their assembly into thin films by electrophoretic deposition.

4.1. Optimization and stabilization of ZnO suspensions.

4.1.1. ZnO-NC and DNC suspensions.

4.1.1.1. Superficial behavior in aqueous media.

The study of the superficial behavior of the particles is determinant to understand the surface chemistry of the powders. In this case, given the fact that both powders were synthesized and washed following the same protocols (described in the previous chapter) a similar colloidal behavior could be expected. Moreover, colloidal characterization of the powders will help determine whether the diffusion of Co^{2+} ions present in the ZnO-DNC powder affects the surface stabilization mechanisms or not.

The first step consisted on the determination of the zeta potential of aqueous suspensions of the powders, which is directly related to the species on the surface of the powders. The suspensions for zeta potential (ζ) measurements were prepared in 10^{-2} KCl solutions, so as to keep the ionic concentration constant, with solid contents of 0.1 g/L. These suspensions were adjusted to different pH values by addition of HCl/KOH in order to determine the variation of the zeta potential with pH, and dispersion was carried out by applying US sonication for 1 min. The resulting zeta potential vs. pH curves are shown in Figure 4.1.

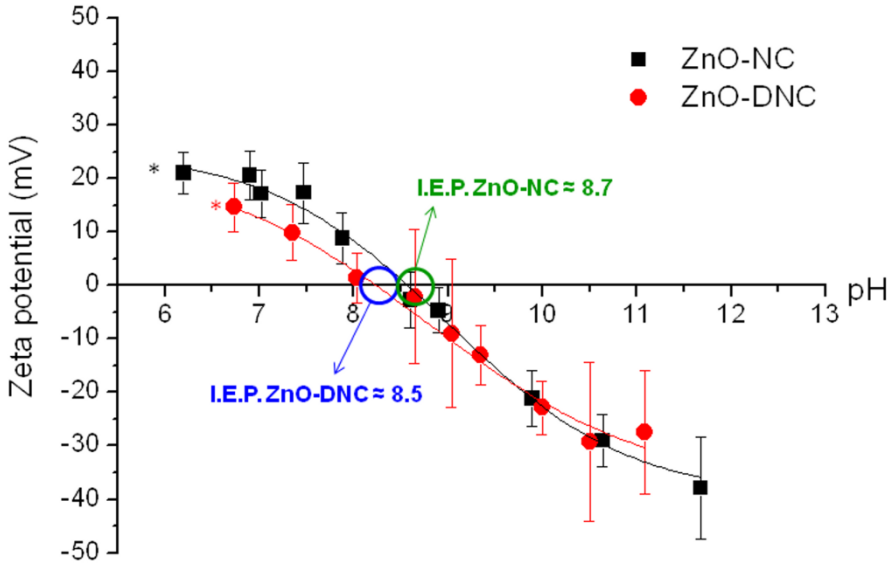

Figure 4.1: Evolution of the zeta potential of ZnO-N and ZnO-DNC suspensions with pH. The * indicate that those ζ-potential values correspond to the natural pH of the powders.

The similarity in the colloidal behavior of both powders is reflected in the similar trend of their ζ-pH curves. Nevertheless, slight differences between them can be observed. The curve of the ZnO-NC powder shows an isoelectric point (IEP) of about

8.5, whereas the doped ZnO-DNC presents a lower IEP powder, and its ζ-pH curve appears slightly tilted towards lower ζ values. Both IEP data are consistent with those reported in the literature for ZnO (between 8.5 and 9.3) [104, 107]. However, their differences should be ascribed to the nature of the surface of both powders. From their characterization we know that the ZnO-DNC powders presented a lower crystallinity than that of the undoped powders (see the XRD diffractograms in Figures 3.3 and 3.9 and density values in Table 3.1). This lower crystallinity might be the reason for the tilting of its ζ-pH curve: the less crystalline powders are prone to forming a higher amount of superficial hydroxides, thus rendering a lower ζ value [219]. In addition, the slight shift in the IEP towards more acidic pH values can be ascribed to the specific adsorption of negatively charged acetate anions (CH_3COO^-) onto the surface of the powders, which modify their surface charge [220]; even though both powders presented secondary phases (acetates) the amount of these determined by TG-DTA analysis (see Figures 3.4 and 3.10) was higher for the ZnO-DNC than for the ZnO-NC powders (24 and 16 wt %, respectively).

Nevertheless, and despite their differences, the ζ-pH curves in Fig. 4.1 show that at pH values below the IEP both powders are positively charged in their surfaces, thus fulfilling the main requirement for their the cathodic electrophoretic deposition. However, the working pH must be above 6 so as to avoid the dissolution of ZnO (see Figure 1.7) [221]. Hence, for this reason, suspensions prepared from this point on were adjusted to 6 < pH < IEP, range in which the surfaces of both powders are positively charged and dissolution is prevented.

In addition to zeta potential measurements, the stability and dispersion of the suspensions is also evaluated by means of particle size measurements by DLS. In this sense, and due to the small size of these particles, several tests have been aimed at establishing the guidelines for the preparation of suspensions susceptible of being measured by DLS for the determination of their average particle size and dispersion degrees. In the first place, suspensions with solid contents from 10^{-4} to 0.1 g/L were prepared, so as to determine the range of solid contents in which particle size measurements were stable. These suspensions were prepared at natural pH (≈7), and applying optimized US sonication times of up to 30 s to disperse the powders. The protocol for the preparation of the suspensions is schematized in the following diagram:

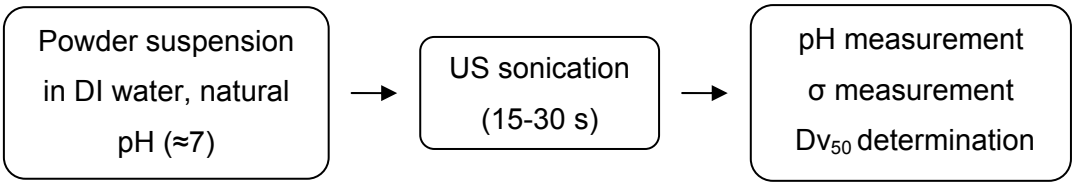

The obtained average aggregate sizes as a function of the number of nanoparticles are shown in Figure 4.2.

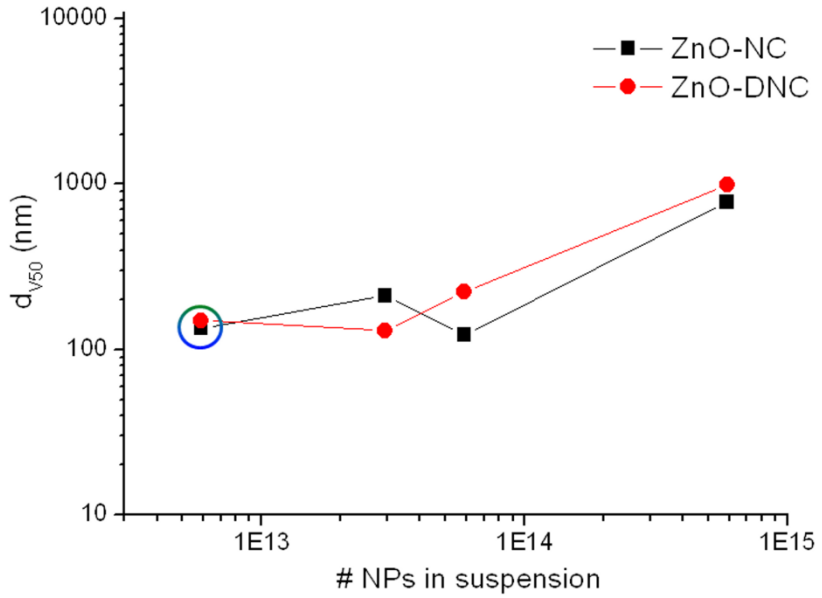

Figure 4.2: Variation of the mean aggregate size of ZnO-NC and ZnO-DNC suspensions as a function of the number of particles in suspension.

As can be observed in the graph, dispersion was improved and the size of the agglomerates remained relatively stable when the number of particles in suspension was below 10^{14} (i,.e., solid contents ≤ 0.1 g/L). Moreover, below the 10^{13} (10^{-3} g/L) range, the parameters in the equipment (such as polidisperisty, correlation curve, attenuator and measuring position) were automatically adjusted to their optimal values. Thus, solid contents ≤ 10^{-3} g/L were chosen as the optimal concentrations for the subsequent size determinations. For these determinations, the protocol for the preparation of the suspensions was as follows:

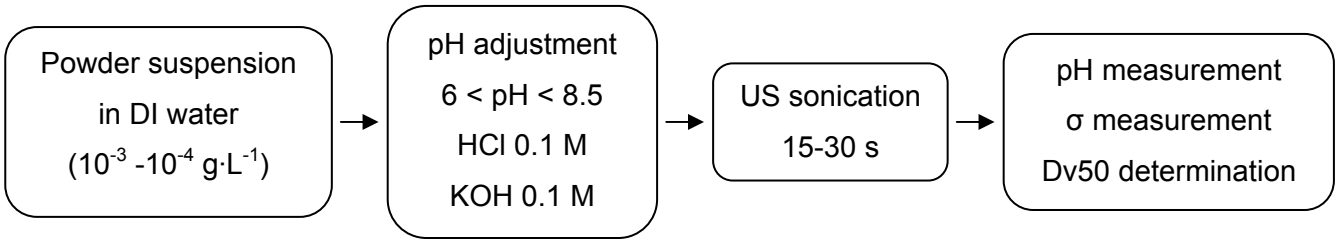

The optimal results of these measurements were already shown in the graphs in Figures 3.6 and 3.12: aggregate sizes of 133 nm and 150 nm were obtained for ZnO-NC and ZnO-DNC suspensions, respectively. In any case, it must be noted that all particle size values were > 100 nm for pH < IEP, which implies that, despite the optimization of the dispersion conditions, the particle size observed by TEM is never reached, and there is still a certain degree of agglomeration.

4.1.1.2. Surface modification: stability and dispersion of the suspensions.

In the light of the obtained results, the use of a weak polyelectrolyte named Polyethylenimine (PEI- Mw=25000 a.u.) was studied in order to first improve and extend dispersion and stabilization of the particles, and second, favor their deposition by electrophoresis. The choice of this specific dispersant in its branched structure was based on several facts: in the first place, as a polyelectrolyte it provided stabilization through two different mechanisms, electrostatic and steric. Second, its high molecular weight granted a great steric contribution to the dispersion and stabilization of the small ZnO-NC and ZnO-DNC particles. Third, its adsorption onto ZnO particles enabled and promoted their cathodic deposition, since it is a cationic polyelectrolyte, i.e, it is positively charged. Finally, as a weak electrolyte, the degree of ionization and thus its conformation can be tailored by controlling the pH of the solution [121]. The structure of branched PEI, shown in Figure 4.3, contains primary, secondary, and tertiary amino groups in the ratio 1:2:1 [222]. At low pH values almost all the amine groups become positively charged as they acquire protons, and the PEI molecules are in a fully extended state with maximum repulsion. These protons are gradually lost as pH increases, e.g. only half of all amine groups in the PEI are still charged at pH≈6.5 at 0.05 M NaCl, and all are completely uncharged at pH≈11 [122, 123].

Figure 4.3: structure of branched Polyethylenimine and its speciation curves as a function of pH [223].

The modification of the ZnO surfaces can be tailored by controlling the protocol used for the preparation of the suspensions, which was as follows:

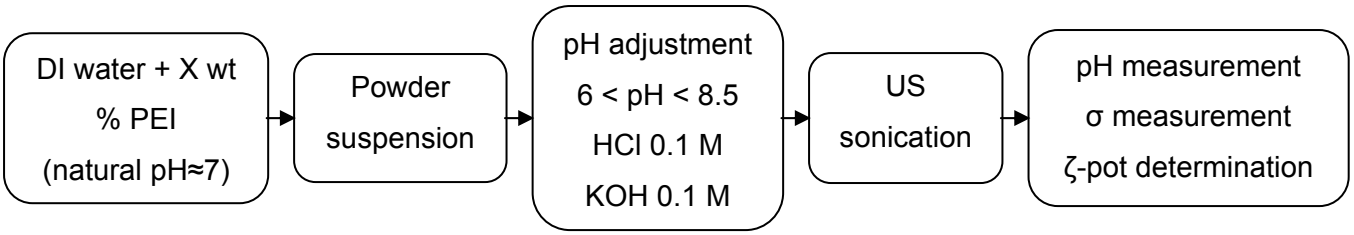

ZnO-NC and ZnO-DNC powders were suspended in DI water at their natural pH values, at which both presented moderately positive surface charges (21 mV at pH=6.2 for ZnO-NC and 15 mV at pH=6.7 for ZnO-DNC)(See Figure 4.1). This implied that at natural pH there was a predominance of positive charges on the surface of the powders, though there still were a certain (smaller) number of attractive negative sites too. In this sense, when the powders were suspended in DI water containing a certain amount of PEI, the electrostatic repulsion between the powders and the additive was not enough to promote depletion and some of the PEI chains could anchor onto the negatively charged sites. Therefore, the subsequent pH adjustment did not directly alter the superficial charge of the particles, but that of the PEI adsorbed onto them. This protocol ensured the adsorption of PEI onto ZnO surfaces and its subsequent protonation/deprotonation with pH. Otherwise, if pH was adjusted prior to powder addition, PEI would be in its larger conformation, and not as much amount would be adsorbed, due to steric hindrance between the PEI chains and the surface charges of the particles. This protocol was followed for the preparation of all suspensions containing PEI.

The dispersion capability of PEI (Mw= 25000 a.u.) was evaluated by measuring the zeta potential vs. wt % PEI saturation curves of the powders (Figure 4.4), which, as reported by Hegelson et al. [224] enables the estimation of the adsorbed amount of dispersant. For this purpose suspensions with 0.1 g/L solid contents and increasing PEI wt % (up to 2 wt %) were prepared following the designed protocol, though in this case the pH was adjusted to a constant value of 7.5. Sonication times of 30 s were applied so as to break soft agglomerates and facilitate the adsorption of PEI onto the newly formed surfaces.

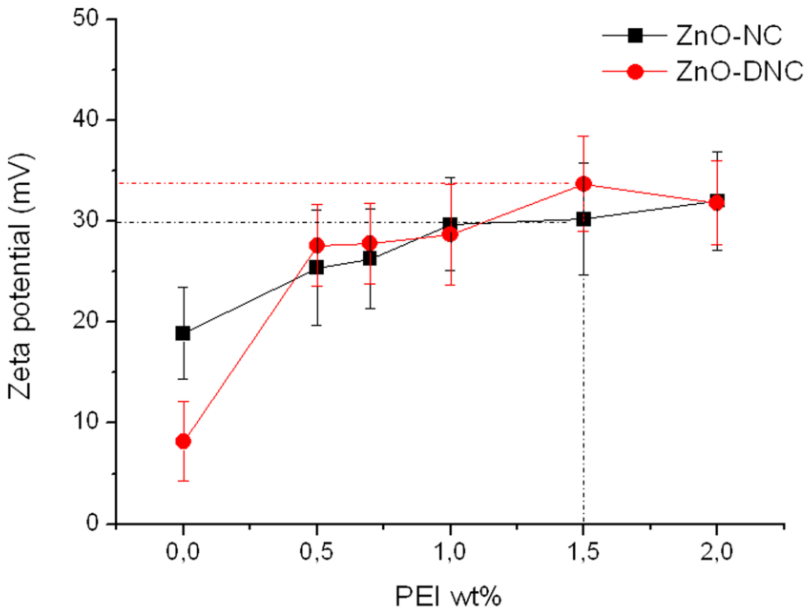

Figure 4.4: zeta potential vs. wt % PEI (Mw= 25000) saturation curves of the ZnO-NC and ZnO-DNC powders.

As can be observed in the graph in Figure 4.4, the saturation curves of both powders presented the same shape. This result implied that adsorption of PEI onto their surfaces was very similar. However, slight differences in the superficial behavior of both powders (already observed in Figure 4.1) could be noticed: for 0 wt % PEI the ZnO-DNC powders presented a lower zeta potential value than the undoped ones, which pointed out to the presence of a higher number of negative surface charges. This higher number of negative surface sites favored the anchoring of a slightly higher amount of adsorbed PEI, which was reflected in higher zeta potential values for the ZnO-DNC powders compared to the ZnO-NC ones. From this graph the chosen optimal amount of PEI for both powders was 1.5 wt %.

Improvement of the stabilization and dispersion of the particles by addition of a 1.5 wt % PEI was verified by measuring the zeta potential vs. pH curve of a ZnO-NC suspension with this PEI content (Figure 4.5).

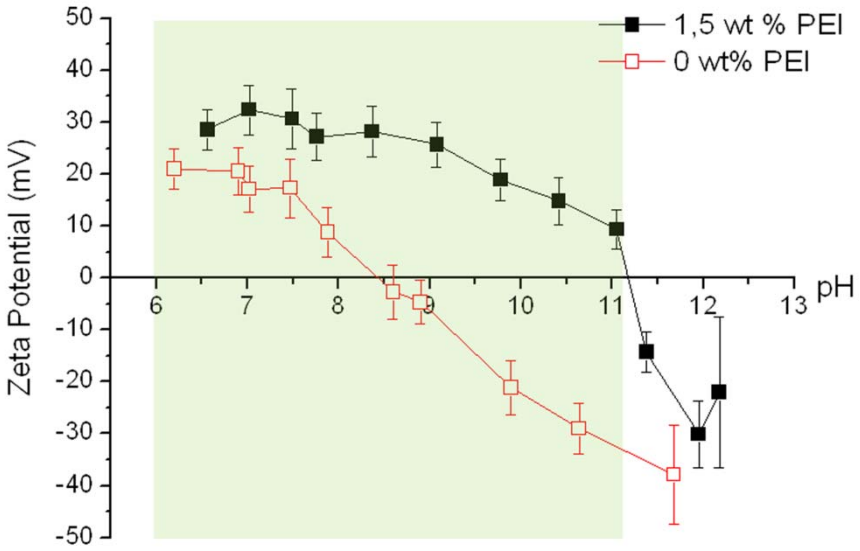

Figure 4.5: Evolution of zeta potential of a ZnO-NC suspension without and with 1.5 wt% PEI as a function of pH. The area in green corresponds to the increased pH working range.

Results shown in Figure 4.5 confirmed the improvement in stabilization due to PEI addition. The IEP of the ZnO-NC powders shifted from 8.5 to > 11 with PEI addition, due to the larger electrostatic repulsion potentials developed with PEI molecules adsorbed onto their surfaces. This provided a wider pH range in which to work, limited on the acid region to pH > 6 so as to prevent ZnO from dissolving.

On the other hand, results of PEI adsorption were not as significant for aggregate size measurements, as shown in Figure 4.6. The minimum aggregate size achieved using PEI was only slightly smaller than without PEI, probably due to the large size of the PEI molecule, which promoted a large area of water exclusion around the ZnO particles. In any case, the aggregate size was in all cases below 100 nm, and in agreement with the aggregates sizes observed in the SEM micrographs of the powders (see Figures 3.6 and 3.12).

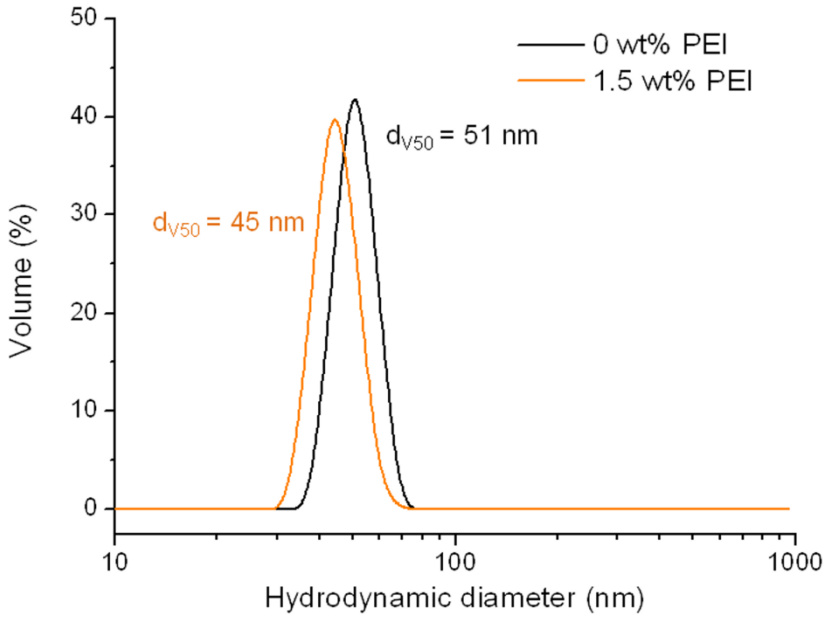

Figure 4.6: Particle size distributions of ZnO-NC suspensions at pH 7 with and without PEI.

4.1.2. ZnO-F suspensions.

4.1.2.1. Superficial behavior in aqueous media.

Colloidal behavior of the ZnO-F powders, characterized by means of zeta potential vs. pH measurements, is shown in Figure 4.7. The protocol for the preparation of these suspensions is detailed in the Figure caption. As expected from their characterization in the previous chapter, the surface of the powders presented no impurities that altered their stabilization, and the IEP was in agreement with those reported in the literature. As in the previous case, the working pH range was chosen to be between 6.5 and 8.5 so as to avoid ZnO dissolution and have positively charged surfaces.

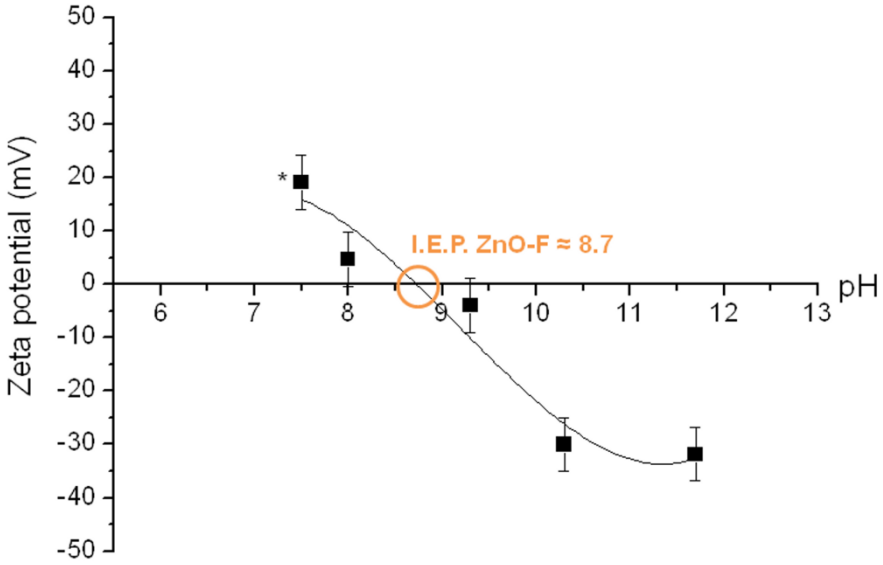

Figure 4.7: Evolution of the zeta potential of ZnO-F suspensions as a function of pH. Suspensions were prepared in 10^{-2} KCl solutions, with solid contents of 0.1 g/L. pH was adjusted by HCl/KOH addition, and US sonication was applied for 15 s. The * indicates that that value corresponds to the natural pH of the powder.

Under optimized conditions (solid contents of 10^{-2} g/L and sonication times of 30 s) the maximum possible dispersion for the ZnO-F powders was achieved, and suspensions were prepared to analyze the evolution of particle size with pH. As can be observed in the graph in Figure 4.8, the increase in pH to values above 8 decreased the size of the aggregates, which remained stable with higher pH values. However, it must be noted that the aggregate sizes were in the range of 200-300 nm, which corresponded to approximately half the size of the agglomerates observed by SEM (see Figure 3.20), and thus implied that a good dispersion was not being achieved.

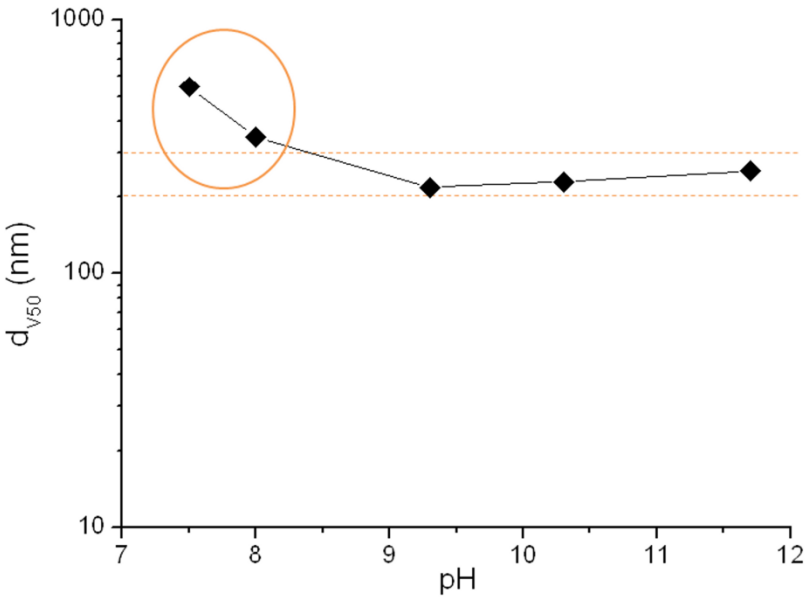

Figure 4.8: Evolution of the mean volumetric particle size (determined by DLS) as a function of pH. Suspensions were prepared following the protocol: powder suspension → pH adjustment → US sonication→ pH and Dv_{50} measurement. The points circled in orange correspond to the particle size distributions depicted in Figure 3.21.

Comparing these results to those obtained for ZnO-NC powders (of about 50 nm, see the black curve in Figure 4.6,) it can be noticed that the final agglomerate size was closely related to the shape factor of the particles: the resulting agglomerate was much smaller for smaller, more rounded particles (5-8 nm) than for the bigger ZnO-F flakes (of about 30x5 nm), as reflected in their agglomeration factors (5.5 and 56, respectively).

4.1.2.2. Surface modification: stability and dispersion of the suspensions.

In order to try and improve both dispersion and stability of the suspensions, the use of PEI as surfactant and stabilizer was analyzed. Due to the large of the polycrystalline ZnO-F particles, in this case a shorter PEI chain (Mw= 2000 a.u.) was selected to improve stabilization. As in the previous case, modification of the ZnO-F surface by PEI adsorption was tailored by using the following protocol for the preparation of the suspensions:

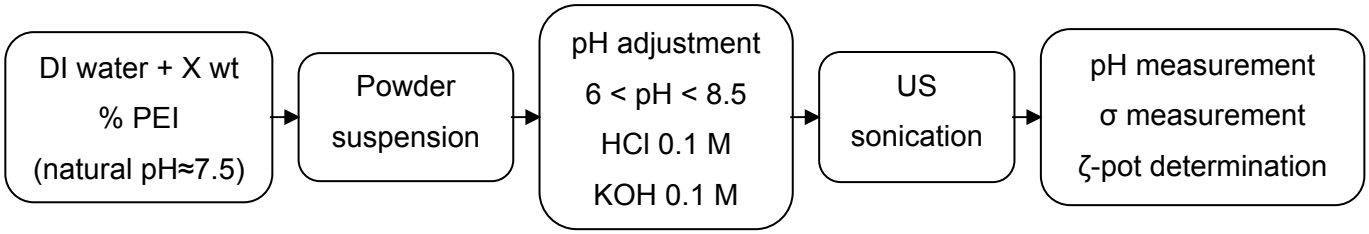

The saturation curve of ZnO-F powders was determined using suspensions with 0.1 g/L solid contents and increasing PEI wt % (up to 2 wt %). Sonication times of 30 s were applied so as to break soft agglomerates. In addition, the variation of the agglomerate size with the different wt % of PEI was also determined. In this sense, suspensions were diluted so as to meet the requirements for the measurement by DLS. Results of both measurements are shown in Figure 4.9. From the graph in Figure 4.9a) it can be noted that zeta potential, and thus stabilization, increased slightly with increasing amounts of PEI, up to 0.7-1 wt %. On the other hand, when dispersant addition was increased above 0.3 wt % bimodal particle size distributions were obtained (Figure 4.9b). Moreover, addition of higher amounts of PEI (2 wt %) seemed to favor reagglomeration, as the fraction of large agglomerates increased. The bimodality can be ascribed to the presence of two different particle populations, already verified by HRTEM in the previous chapter (see Figure 3.23).

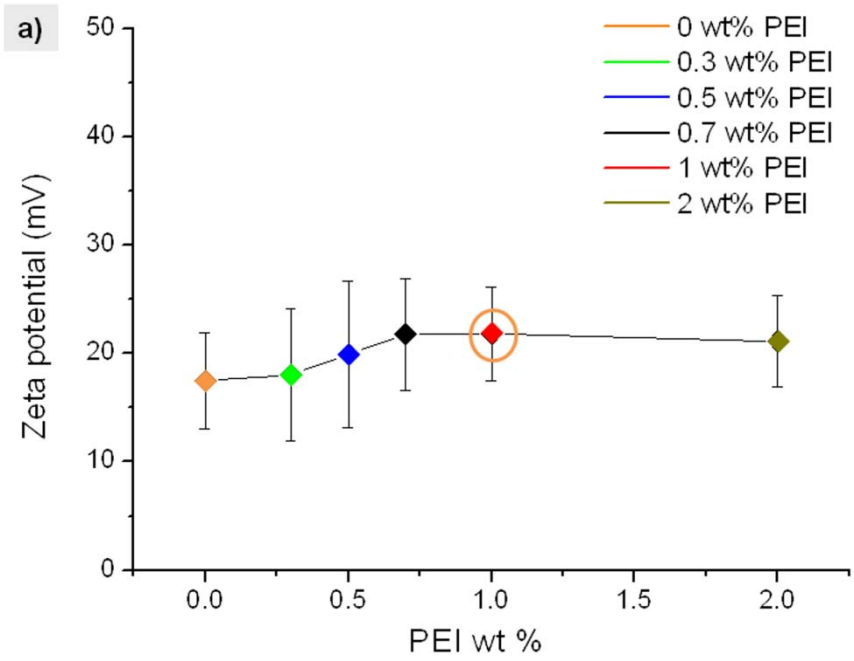

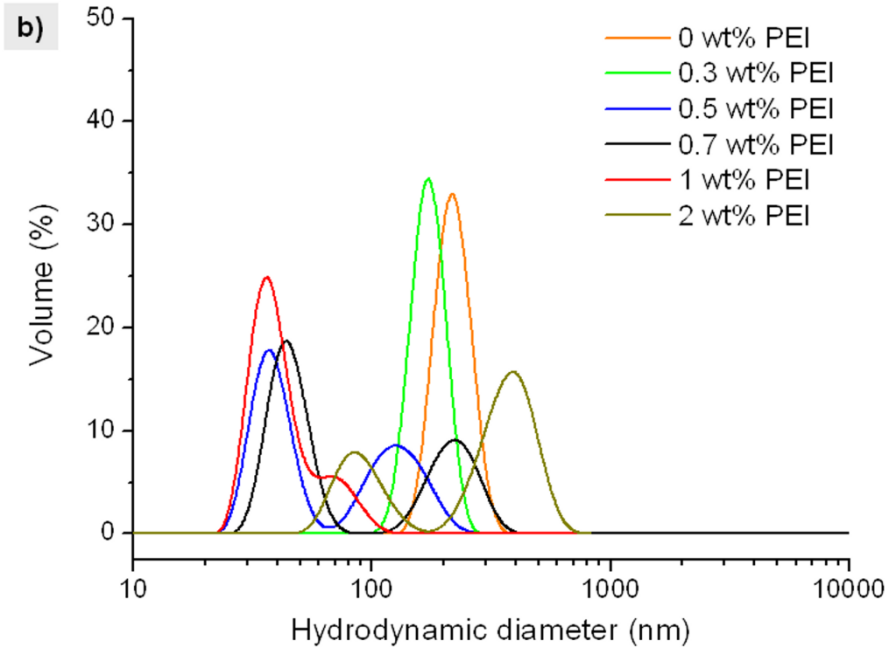

Figure 4.9: a) zeta potential saturation curve and b) particle size distributions of ZnO-F suspensions vs. wt % PEI (Mw= 2000 a.u.).

Taking into account the results of both measurements, a 1 wt % was considered as the optimal amount of dispersant necessary to improve stabilization and dispersion without promoting reagglomeration.

At this point, and given the larger size of the ZnO-F particles compared to the ZnO-NC and ZnO-DNC ones, the use of an additive with such a large steric contribution was not strictly necessary, and thus Polyethylenimines with different molecular weights were used in order to determine the influence of the molecular weight of the additive on dispersion, which has barely been reported [124]. For this purpose, 0.1 g/L suspensions with 1 wt % of polyethylenimines with molecular weights of 1300, 2000 and 250000 a.u. were prepared, and their different effects on dispersion were determined by means of zeta potential and particle size versus pH measurements. By following this procedure, and according to previous zeta potential measurements (Figure 4.7), in the chosen working pH range (6 < pH < 8.5) ZnO particles had a slightly positive surface charge, and thus certain number of negative sites on their surface. The number of adsorption sites on the particles surface is always the same, as well as the charges per monomer of organic chain, regardless of which PEI is used. However, the number of polymeric chains that adsorb onto the particles surface depends on the size, and thus on the molecular weight of the organic chain. Therefore, it could be expected that the percentage of adsorbed PEI would be smaller for the one with higher molecular weight and higher for the one with smaller molecular weight. On the other hand, and

besides the stability of the suspension, the key parameter of the electrophoretic process is the electrophoretic mobility, directly proportional to the zeta potential, which depends on the protonation of the PEI at the working pH value once it is anchored to the particle surface. In this way, the ζ-pH curves in Figure 4.10 show how all Polyethylenimines shifted the isoelectric point of the ZnO-F powders to higher pH values, pointing out to an effective adsorption of the additives onto the particles surfaces, which promoted an electrostatic stabilization. Moreover, results showed that the PEI with the highest molecular weight (Mw = 25000 a.u.) provided the greatest repulsive electrostatic interaction of all three, shifting the isoelectric point to pH > 12.

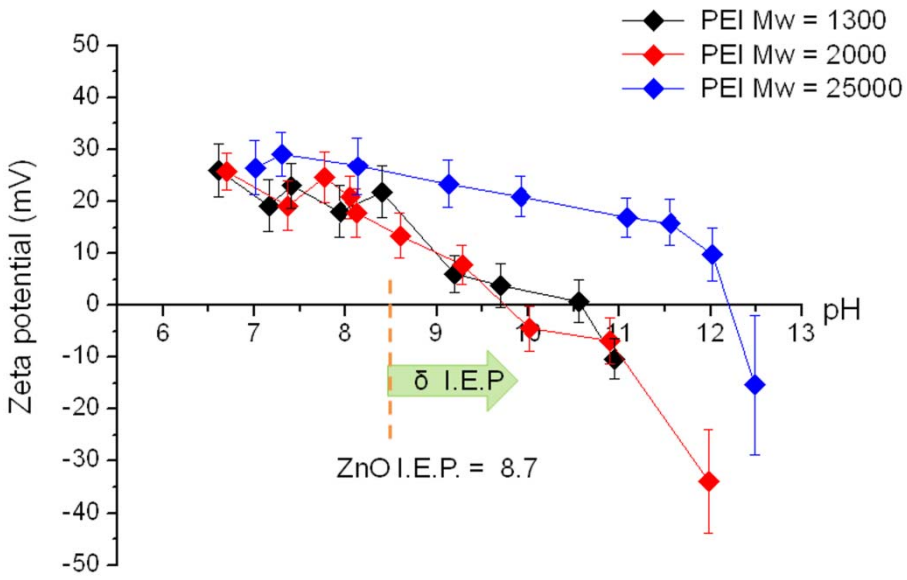

Figure 4.10: Variation of zeta potential of ZnO-F suspensions as a function of the molecular weight of the Polyethylenimine used as dispersant.

This larger repulsive electrostatic interaction provided by the PEI with the highest molecular might be ascribed to its large size: even though a smaller number of chains of this PEI were able to anchor to the surface of the ZnO-F particles, these were much larger than those of the other two PEIs, and therefore, provided much more charges. This implied not only a better stabilization (with higher zeta potential values) but a wider stabilization range, as the shorter PEIs became fully deprotonated at lower pH values than the larger one.

The effective adsorption of PEI and its effects on stabilization due to both the electrostatic and steric components were also clear in the equivalent-sphere size distribution measurement versus pH values shown in Figure 4.11. In the graph it can be observed how at the pH values where the zeta potential was increased with the shorter PEI chains, the particle size measurements were around 100 nm. On the other

hand, the larger electro-steric effect favored by the highest molecular weight PEI maintained ZnO nanoparticles dispersion after sonication, i.e. the new surfaces generated by the breakdown of agglomerates by sonication became covered by PEI, which prevented re-agglomeration, keeping the agglomerates size below 100 nm. Results verified the efficiency of the sonication as dispersing technique and remarked the role of the PEI as surface modifier and stabilizer at neutral to basic pH values.

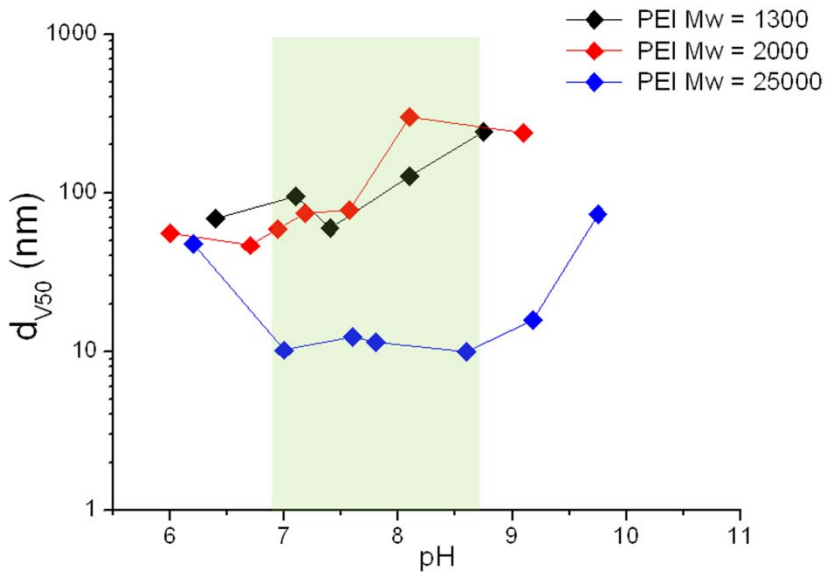

Figure 4.11: Variation of agglomerate size of ZnO-F suspensions as a function of the molecular weight of the Polyethylenimine used as dispersant.

4.2. Electrophoretic Deposition.

The EPD process is based on the migration and later deposition of charged particles in a stable suspension, induced by the application of an electric field between two electrodes. Even though the principles of electrophoresis have been known since the last century, particle arrangement in cohesive deposits is still not well-understood, [102, 225, 226] and several theories and models have been suggested to explain it. One of the reasons why this topic raises such controversy is the large number of parameters that can affect deposition: deposit yield and particle packing in electrophoresis not only depend on the stability and the solids content of the suspension, but also on the aggregation and the arrangement of the particles on the electrode surface

These parameters can be divided in three main groups: those related to the suspensions, those related to the substrates and those related to the electrical conditions. In this section we will study each of these groups in detail.

4.2.1. Parameters related to the suspensions.

From the number of parameters that are key for the EPD process, this work focuses on the study of the solid contents and the conductivity of the suspensions. These two parameters are intrinsically related to each other, as conductivity is determined by the number of charge carriers (ions and/or particles), and together with the electrophoretic mobility, they determine the viability and the development of the deposition process [126, 127]. Moreover, the solids content is directly related to the dispersion and stability of the suspensions, key requirements for EPD. Hence, in order to successfully achieve EPD of a suspension, a compromise between high particle mobility and low particle charge per unit weight must be reached [136].

4.2.1.1. Influence of the solids contents and their dispersion.

In the first place the study of the dispersion was readjusted to the solid contents necessary for EPD, higher than those used for minimum aggregate size determination. For this purpose, suspensions with solid contents, 0.1 and 1 g/L were prepared with the optimized conditions of PEI content and sonication times, and their particle size distributions were measured by DLS. From the results shown in Figure 4.12 it can be observed how, despite the increase in solid contents, the dispersion technique was still effective, measuring particle sizes (d_{V50}) around 20 nm for 1 g/L ZnO-F suspensions.

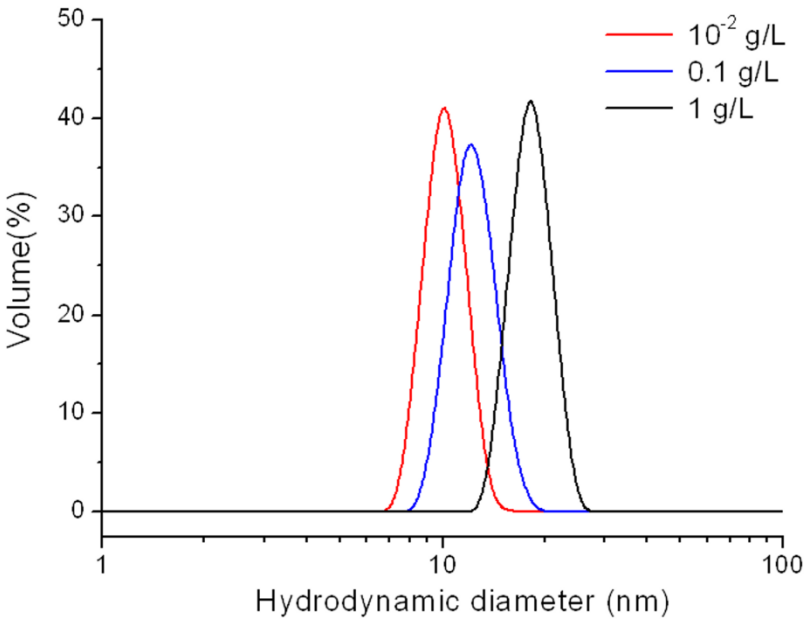

Figure 4.12: Particle size measurements as a function of solid contents. 0.01, 0.1 and 1 g/L suspensions were prepared following the protocol described in the previous section: powder suspension in water with 1 wt % PEI (Mw = 25000), pH adjustment, US sonication and pH and d_{v50} measurement. Dispersion technique is effective in all the solid contents range.

Dispersion was also evaluated by using UV-Visible Spectroscopy. This technique has been extensively reported as a method for the estimation of particle size distributions (PSD) of quantum sized semiconductor powders, as their optical properties depend on their disperse properties, namely, size and shape [199, 200]. This is not as trivial a matter as might seem, as the overall absorbance of a sample, *A,* is not only dependent on the absolute particle concentration, *C,* in Lambert-Beer's law (see Eq. 2.7), but also on the pathlength, *l*, and most important, on the molar absorption coefficient, ε, which is also a function of particle size. Interestingly, and despite this fact, only few authors have considered dispersion as a relevant parameter to take into account [227-230]. Amongst these latter, Li et al. [229] reported the influence of dispersion of multi-walled Carbon nanotubes (MWCNT) suspensions on their molar absorption coefficient, and Zhang *et al.* [230] described the variation of absorbance of colloidal Au nanoparticles suspensions with agglomeration.

In this sense, following the experiences of these authors we studied the variation of the intensity of the UV–Vis absorption band of ZnO-F suspensions (located at 365 nm) with US sonication time (Figure 4.13). As can be observed, suspensions with no sonication were too turbid and unstable, and showed very low absorbances. In addition, results show how this absorbance of the suspensions increased with longer sonication times, and from the particle size distributions on the inset it can be confirmed that this increase in absorbance corresponded to an increase in dispersion,

as the agglomerate size measured by DLS decreased from 600 to 120 with 45 s US, and further on to 12 nm with another 45s. In other words, changes of one order of magnitude in particle size, and thus in the dispersion of the suspension, resulted in changes of a 43 % of the intensity of the absorption band.

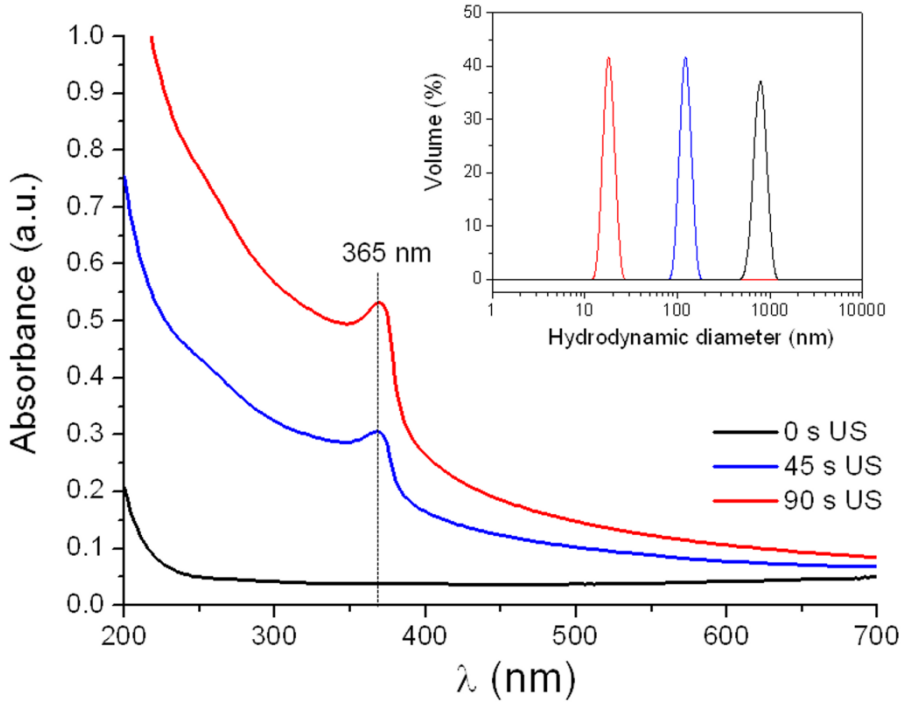

Figure 4.13: variation of the absorbance of the UV-Vis spectra of 0.1 g/L ZnO-F suspensions as a function of sonication time. Note that further sonication times resulted in re-agglomeration of the particles due to local warming of the suspensions.

Moreover, UV-Visible spectroscopy was also used to determine the experimental variability in the preparation of the suspensions. For this purpose, a calibration curve (represented in Figure 4.14) was prepared by measuring the absorbance of ZnO-F standardized suspensions with concentrations ranging from 10^{-3} to 0.1 g/L. Next, the absorbance of several suspensions prepared different days for different tests was measured, and the experimental variability in the preparation of the suspensions was then evaluated by comparison of their absorbances with those of the calibration curve. The concentration of the different suspensions was calculated by applying the definition of absorbance in the Lambert-Beer law (Eq. 2.7). In this sense results shown in Figure 4.14 showed that the variability in the preparation of the suspensions caused a deviation of 14 % in absorbance. This implied that the preparation of the suspensions had a lack of reproducibility due to changes in the solid contents (± 15 % in graph) or in the dispersion.

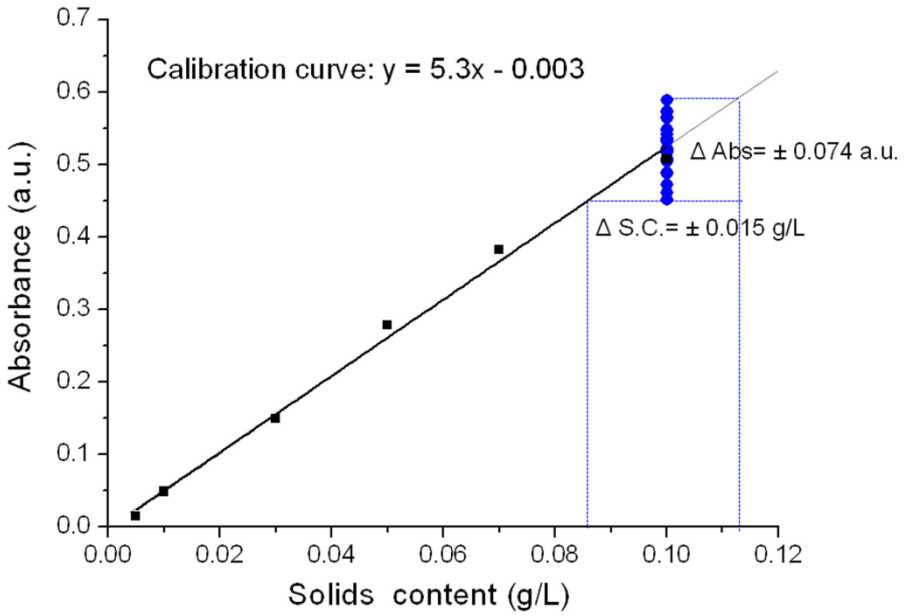

Figure 4.14: Experimental variability in the preparation of ZnO-F suspensions. Note that these calculations exclusively correspond to 0.1 g/L suspensions. This is due to the fact that 1 g/L suspensions were too concentrated for the UV-Vis spectrophotometer detector, which became saturated when trying to measure them and dilutions gave place to an experimental variability that could not be controlled.

4.2.1.2. Influence of the conductivity, σ:

Once dispersion conditions for each solid contents considered for EPD were studied, the next step consisted in the determination of the range of conductivities associated to their stability conditions. For this purpose, conductivity of all suspensions was measured after sonication (see diagram in section 4.1.2). Results are shown in Figure 4.15. From the graph it can be seen that conductivity increased when the solid content of the suspensions was increased from 0.1 to 1 g/L, due to the increase in the number of charge carriers, mainly ZnO-F particles. The increase in conductivity, however, was not linear, as the slope, m, of both lines was not exactly the same (m varied from 0.8 for 0.1 g/L suspensions to 2.7 for 1 g/L suspensions). This divergence can be explained considering the dispersion of the suspensions: even though the increase in solid contents was linear, the increase in the number of agglomerates was not, as the degree of dispersion of both suspensions was different (see Figure 4.12). Suspensions with higher solid contents had a higher number of agglomerates, which were larger, and this implied not only a higher number of carriers (though this was not proportional to the increase in solid contents) but also a higher charge per carrier. On the other hand, it can also be observed that for both concentrations conductivity increased linearly with temperature: suspensions with 1 g/L solid contents had conductivities ranging from 97 to 133 μS/cm (± 11 %) at temperatures between 16.5 to

30 ºC, whereas 0.1 g/L suspensions presented conductivities from 33 to 39 µS/cm (± 24 %) at temperatures between 19 and 26 ºC. This behavior (linear increaser of conductivity with temperature) is coherent with the semiconductor nature of the suspension. In addition, it must be noted that, even though higher solid contents promoted both a larger variability in the conductivity and a larger range vs. test temperature, the experimental errors were lower with higher solid contents. This can be ascribed to the fact that the effect of the experimental error in the preparation of the suspensions decreased with the increase in solids content. It is important to note that changes in dispersion and concentration during the preparation of 0.1 g/L suspensions produced a variability of about 24 % in the conductivity.

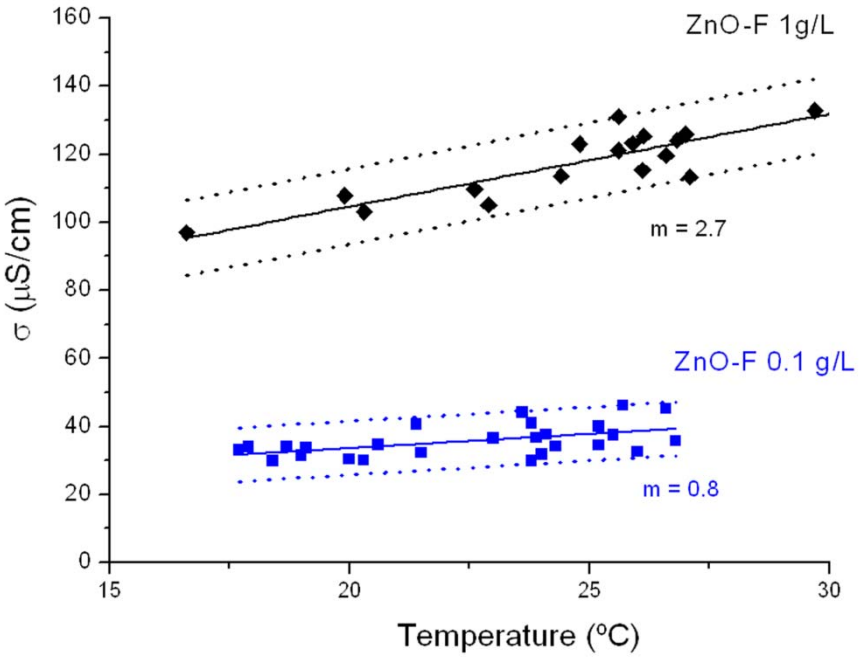

Figure 4.15: Variation of the conductivity of 1 and 0.1 g/L suspensions as a function of temperature. The slopes of the lines are named as m.

However, from the absorbance vs. conductivity graph, depicted in Figure 4.16, it can be inferred that absorbance of the 0.1 g/L suspensions similarly dispersed and stabilized is practically unaffected by their conductivities and temperatures. Therefore, in subsequent UV-Vis measurements the only two variables to be taken into account will be the dispersion and the concentration of the suspensions.

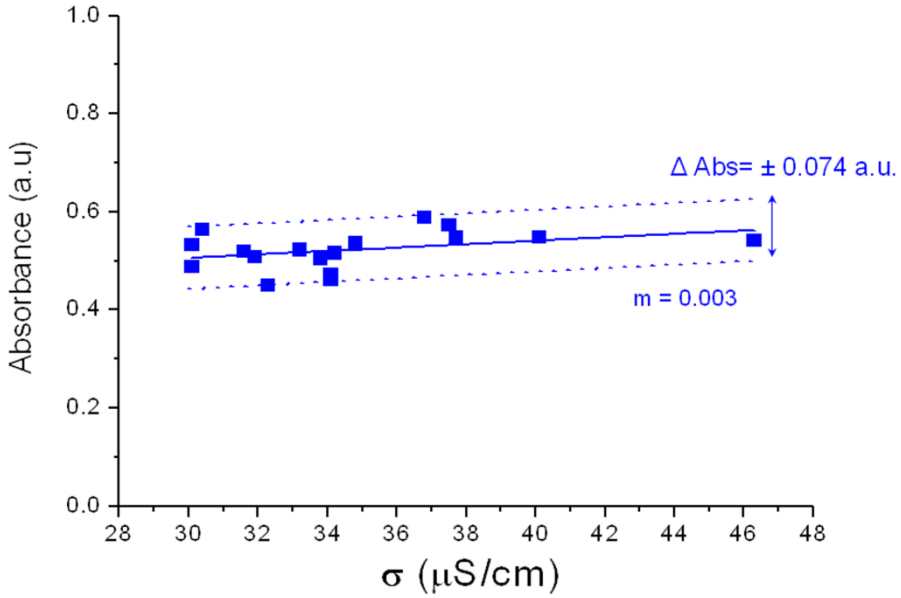

Figure 4.16: Variation of the absorbance of 0.1 g/L suspensions as a function of conductivity.

Taking into consideration the results described in this section (see Figures 4.12, 4.14 and 4.15), the experimental uncertainty in the preparation of the suspensions for EPD stability is summarized in Table 4.1.

Table 4.1: Experimental uncertainties in the conditions of the prepared suspensions.

Solid Contents:	0.100 ± 15 %	1 ± 0.015 %
Agglomerate size	12 ± 3 nm	18 ± 4 nm
Conductivity:	33 - 39 μS/cm ± 24 %*	97 - 133 μS/cm ± 11 %*
Absorbance max.	0.53 ± 14%	-**

* Ranges of σ are a function of the temperature of the suspensions.

** The absorbance of 1 g/L suspensions could not be determined unless they were diluted, as they were too concentrated for the UV-Vis spectrophotometer detector, which became saturated when trying to measure them.

4.2.2. Parameters related to the substrates.

The substrates chosen as electrodes also play a determinant role in the EPD process, as their surfaces determine the final arrangement of the particles and can alter the local electrical conditions. Moreover, electrochemical reactions produced during current flow through the electrode can seriously decrease the efficiency of the process and uniformity of the deposits. This is the case of aqueous suspensions, in which the electrolysis of water can take place and produce unwanted bubbling in the suspensions.

In this work, three different types of conducting substrates were used for the EPD of ZnO-F: ITO-coated glass substrates, electropolished AISI 304 stainless steel foils (shortened as ESS) and Nickel foils (Figure 4.17).

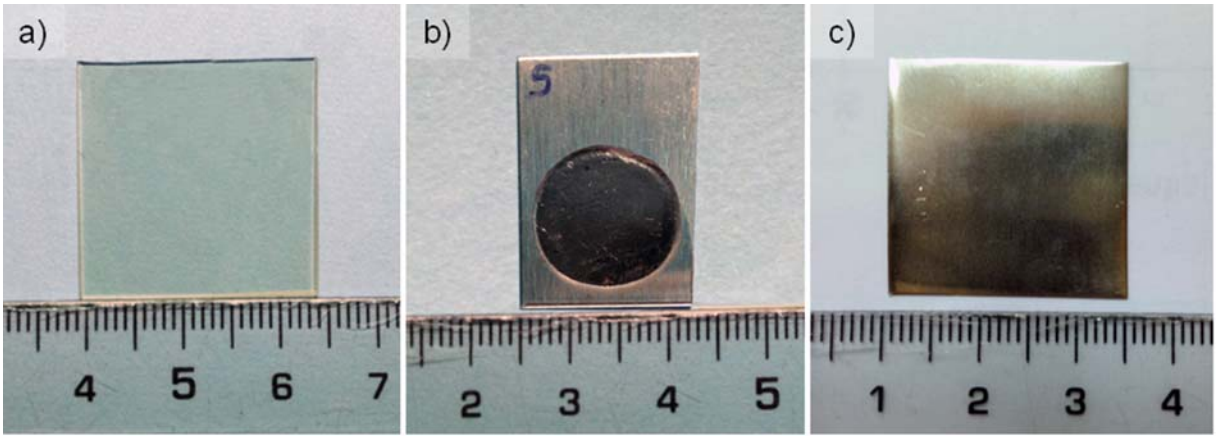

Figure 4.17: Photographs of the three kinds of substrates used: a) ITO-coated glass b) electropolished stainless steel and c) nickel foils. The rounded area in the stainless steel substrate corresponds to the electropolished area.

These substrates were chosen according to their increasing roughnesses: the ITO substrate was considered to have a null roughness, and the other two substrates were characterized using a surface roughness-meter. The parameters used for the evaluation of the roughness of the substrates were the mean profile height, R_c, the roughness average, R_a, (i.e. main height as calculated over the entire measured length), and the kurtosis factor, $R_{ku,}$ which is a measure of the distribution of spikes above and below the mean line: for spiky surfaces, $R_{ku} > 3$; for bumpy surfaces, $R_{ku} < 3$. The results of these measurements, shown in Figure 4.18, show that the surface of the ESS substrate had an undulating appearance (probably due to the electropolishing procedure), confirmed by its R_{ku} value = 2.4. However, the roughness within these undulations was very low, with R_c and R_a values of 80 and 0.04 nm, respectively. The Ni foil showed a bumpy surface too, R_{ku} = 2.8 nm, though in this case the “”bumps” had a spiky nature, with R_c = 266 nm and R_a = 79 nm.

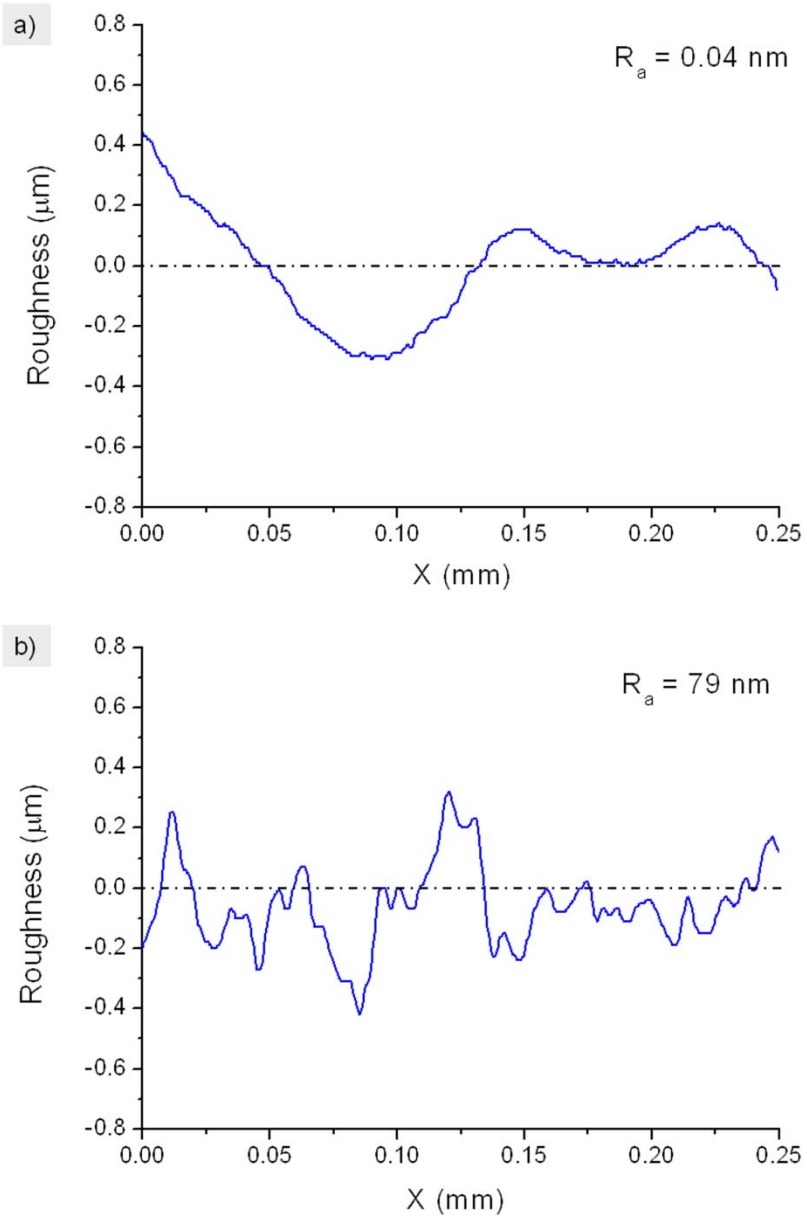

Figure 4.18: Roughness profiles of the a) electropolished stainless steel and b) nickel substrates.

These results were completed by analyzing the topography of the substrates surfaces by AFM (Figure 4.19), which allowed a closer study of the nanometric roughness. The topography image of the ITO substrate presented an extremely planar and homogeneous surface, with an AFM profile with R_c of 5.2 nm and R_a = 1.1 nm (Figure 4.19b), whereas that of the ESS substrate showed some aligned scratches and pores, and a profile with a relatively low roughness, with R_c and R_a values of 11.6 nm and 2.7 nm, respectively (Figure 4.19d). In addition, the kurtosis factor of these ESS substrates, R_{ku} = 11.2 nm, pointed out to a spiky nanometric texture, already suspected from the roughness measurements (Figure 4.18). These results point out to the fact that, even though the electropolishing procedure decreased the roughness of the

substrate, some defects remained. Finally, the topography and profile of the Ni substrate showed a very defective surface, with wide creases and folds of about 30 nm (Figures 4.19e and f). The roughness analysis of this surface rendered values of R_c= 26.5 nm, R_a = 6.0 and R_{ku}=2.8. Therefore, the higher roughness (both nanometric, by AFM, and submicronic, by roughness determination) of the Ni substrates compared to the ESS and ITO ones was confirmed.

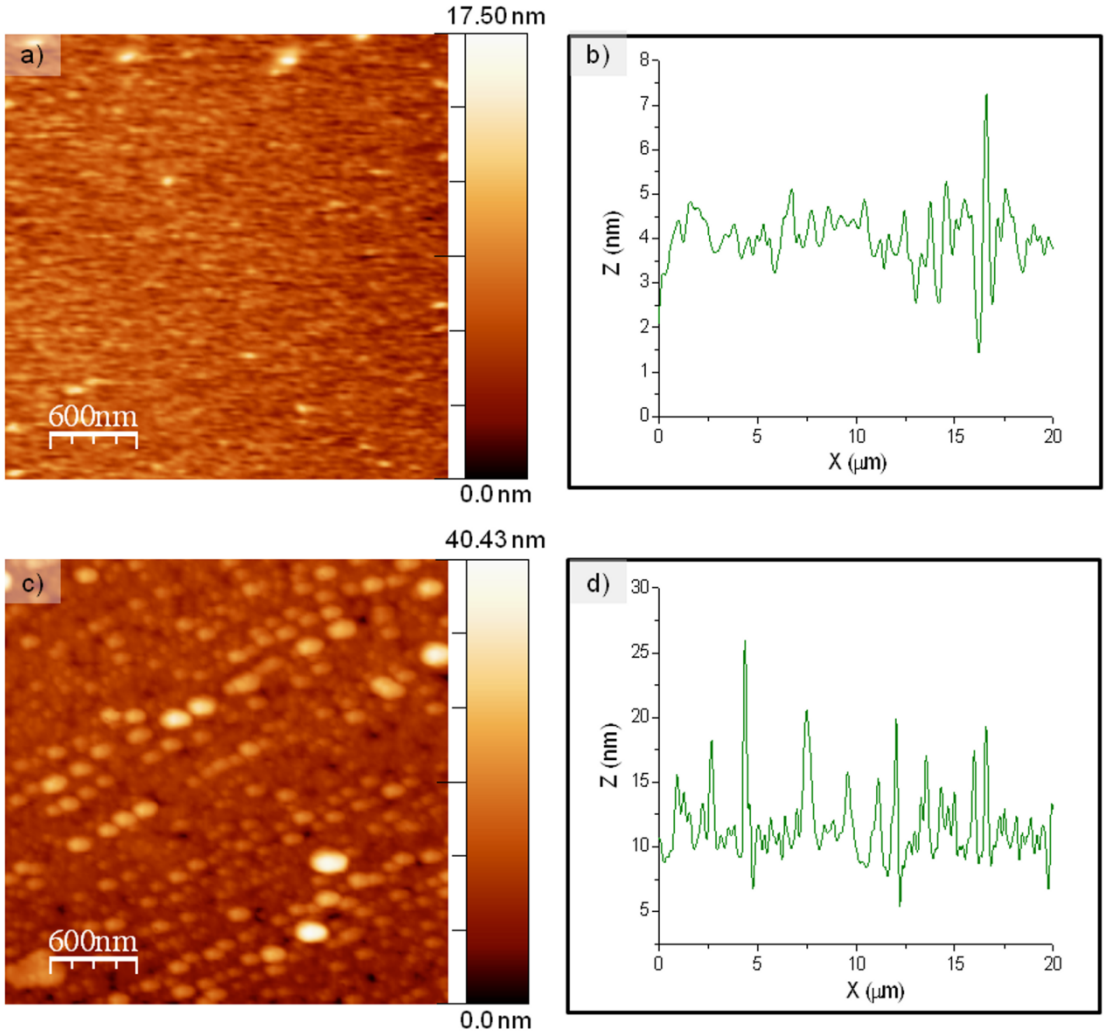

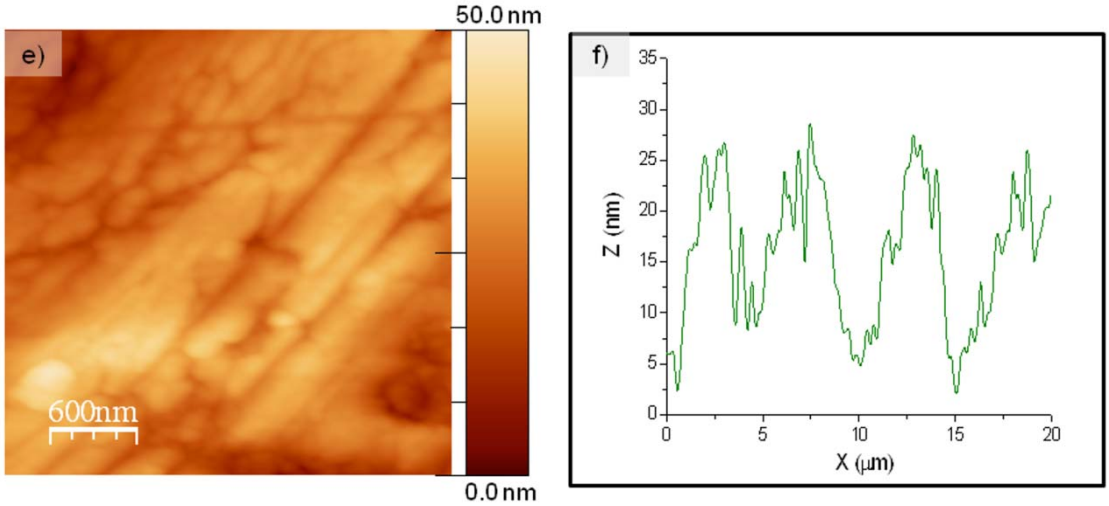

Figure 4.19: AFM topographies (a, c, e) and profiles (b, d, f) of the ITO, electropolished stainless steel and nickel substrates, respectively.

The surface of the substrates was also characterized by scanning electron microscopy. The FE-SEM micrographs of the substrates are in agreement with the previous results. FE-SEM micrographs of the substrates in Figure 4.20 showed a textured surface in the ITO substrate, in which the grains could be observed, in contrast with the electropolished steel substrate, in which no texture could be observed, but only the scratches on its surface, or with the highly defective surface of the nickel foil.

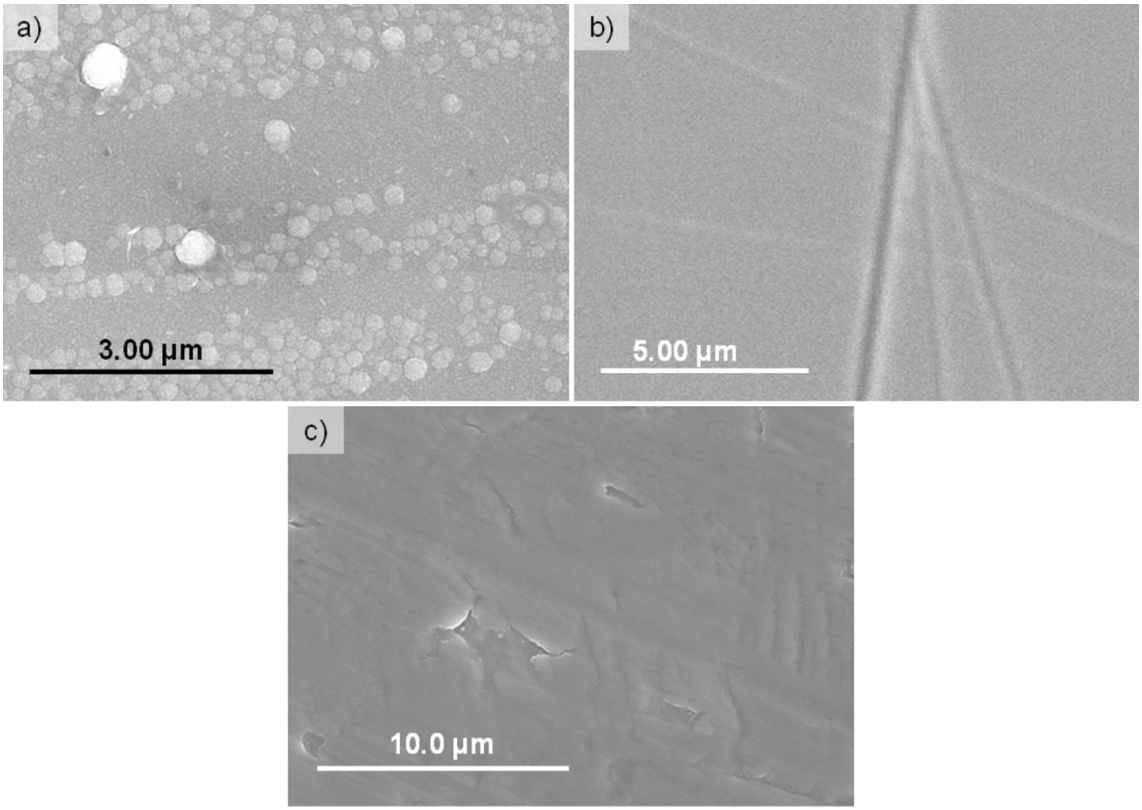

Figure 4.20: SEM micrographs of the surface of the a) ITO, b) stainless steel and c) nickel substrates.

Finally, resistivity of the substrates was determined by the four-point probe method, obtaining values of 30, $1.5 \cdot 10^{-3}$ and $2.0 \cdot 10^{-4}$ Ω/cm for the ITO, ESS and Ni substrates, respectively.

4.2.3. Electrophoretic deposition of ZnO-F powders.

ZnO-F suspensions for EPD were prepared applying the optimized parameters for particles dispersion and stabilization described above. The conditions of these suspensions are summarized in Table 4.2.

Table 4.2: ZnO-F EPD suspensions conditions

Powder / Medium	Cc (g/L)	Dispersant	pH	d_{V50}	μ_e ($cm^2/V \cdot s$)
ZnO-F / H_2O	0.1-1	PEI (Mw = 25000) 1 wt.%	6 < pH < 8	12-18 nm	$2.28 \cdot 10^{-4}$

In all cases EPD was performed under galvanostatic conditions, i.e. applying constant current, so as to avoid the effect of the deposit resistivity increase on the effective electrical force acting on particles. By using this method, first suggested by Sarkar and Nicholson [119], the voltage/unit distance in the suspension remains

constant, despite the increase of the voltage drop across the two electrodes with time. In this sense, working under these conditions allows a more effective modeling and controlling of the process [231]. In addition, a low current intensity of 100 μA was applied for dipped surfaces ranging from 3.2 to 4.9 cm^2 (which corresponded to current densities of 20 to 31.2 $\mu A/cm^2$), so as to avoid H_2 bubbling (due to water electrolysis at voltages above 2.5 V). Moreover, all substrates were weighed prior to the deposition.

4.2.3.1. Growth of ZnO thin films and ordering in aqueous EPD under mild conditions

Films deposited from 0.1 and 1 g/L suspensions were first prepared on ITO-coated glass substrates, applying increasing deposition times, from 60 to 6000 s. All suspensions were fresh, prepared right before each EPD process, and with conductivities within the ranges established for both solids contents. The parameters fixed for all depositions are summarized in Table 4.3 whereas Figure 4.21 shows the E vs. time curves.

Table 4.3: Fixed parameters for the deposition of 0.1 and 1 g/L suspensions on ITO substrates

	0.1 g/L	**1 g/L**
Volume, V (mL)	30	30
Initial mass, m_0 (mg)	3	30
pH (t=0)	7.5	7.5
Electrophoretic mobility, μ_e ($cm^2/V \cdot s$)	$2.28 \cdot 10^{-4}$	$2.28 \cdot 10^{-4}$
Conduction Area, (cm^2)	3.9	3.2
Intensity, I (μA)	100	100
Distance between electrodes, L (cm)	2	2

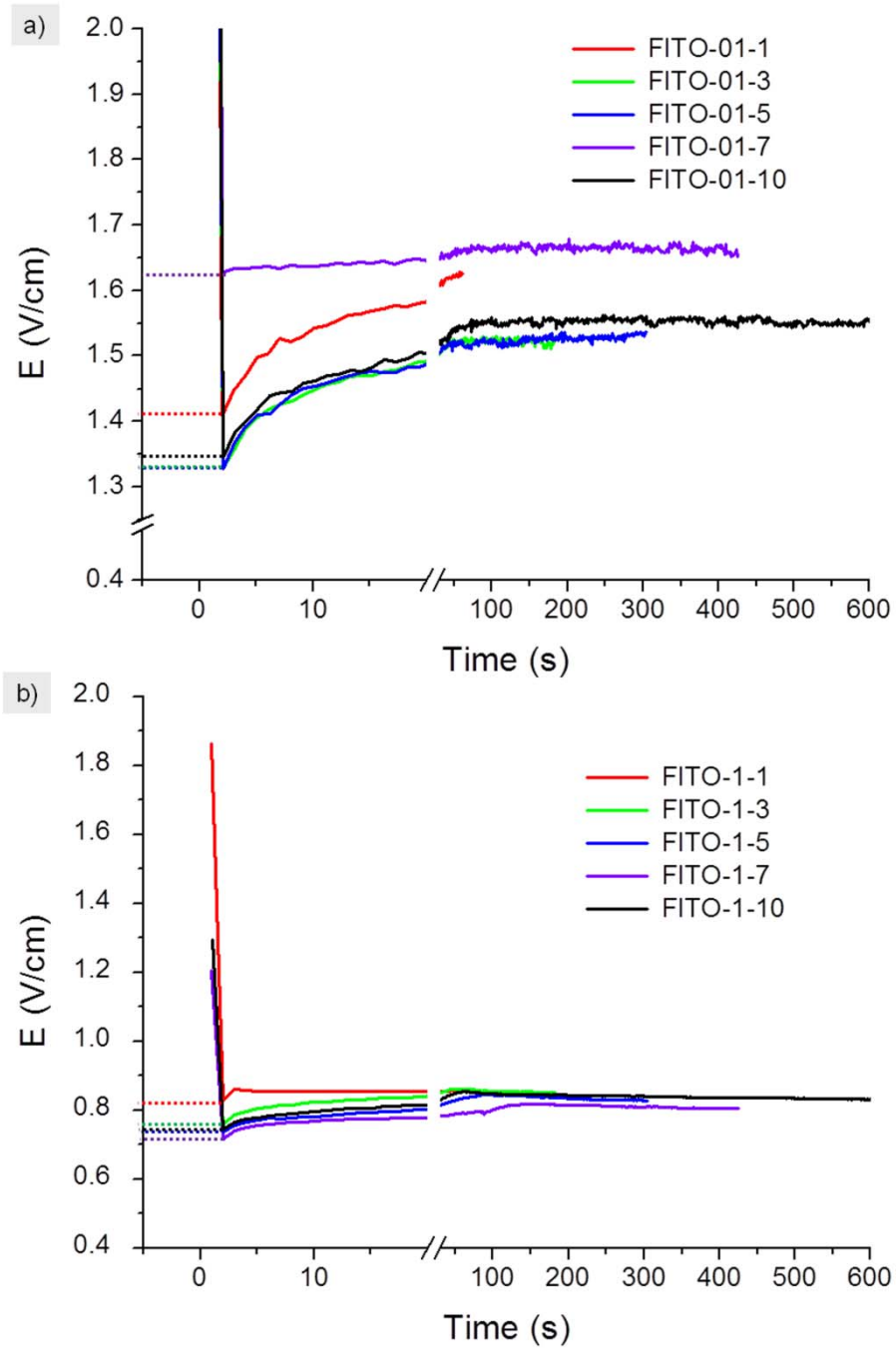

Figure 4.21: Electric field vs. deposition time curves for a) 0.1 and b) 1 g/L ZnO-F suspensions.

Several facts must be noted from the graphs in Fig.4.20. First, in both cases the electric field did not remain constant, but varied with the earliest deposition. Moreover, the fact that the field was not exactly the same for all samples was due to the experimental variability in the preparation of the suspensions, already described in previous sections. The variations in the electric field were of approximately a 9 % for 0.1 g/L suspensions and 11 % for 1 g/L suspensions and thus were within the range of errors in the conductivity (see Figure 4.15). Finally, and most important, it can be

observed that there was a relevant decrease in the electric field with the increase in solid contents, with average initial values of $E_{t=0}$ = 1.41 and 0.76 V/cm for 0.1 and 1 g/L respectively. This decrease in the electric field can be ascribed to the increase in the conductivity of the suspensions, as the applied electric field is inversely proportional to the conductivity of the system σ (S/cm), according to the following equation [232]:

$$E = \frac{I}{S \cdot \sigma} \qquad \text{(Eq. 4.8)}$$

where I is the applied intensity (A) and S the conduction area (cm^2), which in this case corresponds only to the side of the substrate coated with the ITO layer. This effect of the solid contents suggests that, oppositely to what was expected, an increase in the solids content of the suspension does not imply a higher deposition yield within the applied conditions.

However, while films deposited from 0.1 g/L suspensions were transparent and could not be detected by visual inspection, films obtained from 1 g/L suspensions were translucent, i.e. visible to the naked eye, as can be observed in the photographs in Figure 4.22.

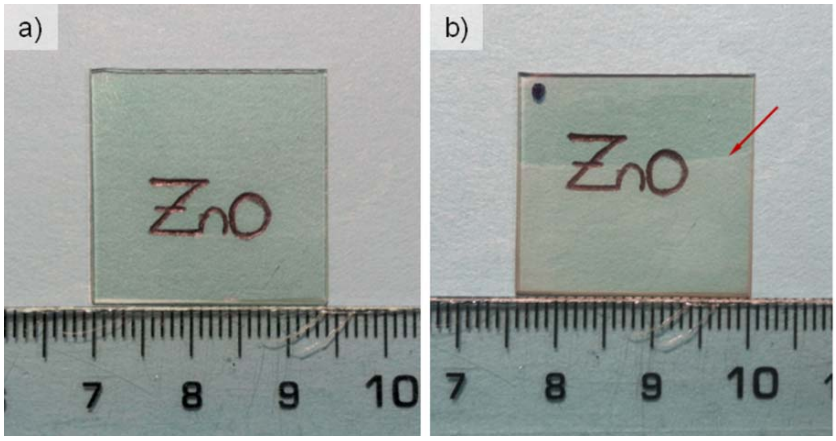

Figure 4.22: Photographs of ITO substrates coated with ZnO-F films deposited from a) 0.1 and b) 1 g/L suspensions and deposition conditions of 100 μA for of 10 min. The red arrow points to the upper limit of the ZnO-F film.

Therefore, in order to verify the effect of the increase in solid contents of the suspensions, the deposited films were characterized by several methods.

In the first place, the deposited mass was determined by weighing the substrates with the films on a 6-decimal digit microbalance. Films deposited from high solids content suspensions were characterized in this way. However, films deposited from 0.1

g/L suspensions showed no mass increase. Results of the weighing are shown in Table 4.4.

Table 4.4: results obtained from weighing the films deposited on ITO substrates on the microbalance.

1 g/L samples	Weighed mass (µg/cm^2)
FITO-1-1	9.7
FITO-1-3	-
FITO-1-5	17.2
FITO-1-7	18.4
FITO-1-10	31.6

Thus, taking into account these results, the deposited mass was estimated by two indirect methods: measuring the UV- Vis absorbance of the suspensions and characterizing the films by ellipsometry.

The first method considered the sensibility of UV-Vis spectroscopy to variations in the concentration of the suspensions. In this method the variation of intensity in the UV-Vis absorbance spectra of the suspensions recorded previously and after the deposition process, shown in Figure 4.23, was considered to be due to a variation in the concentration, which decreased as the powder was deposited, and thus removed from the suspension.

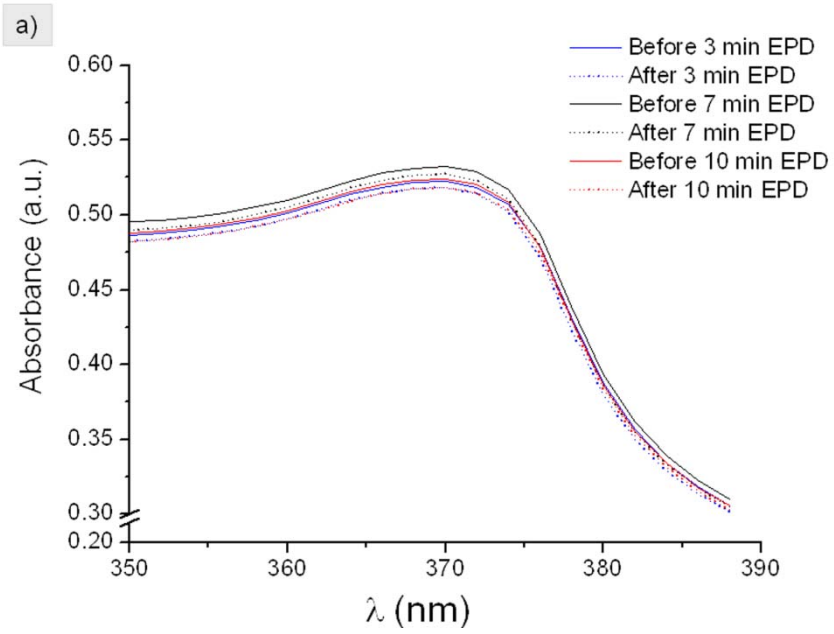

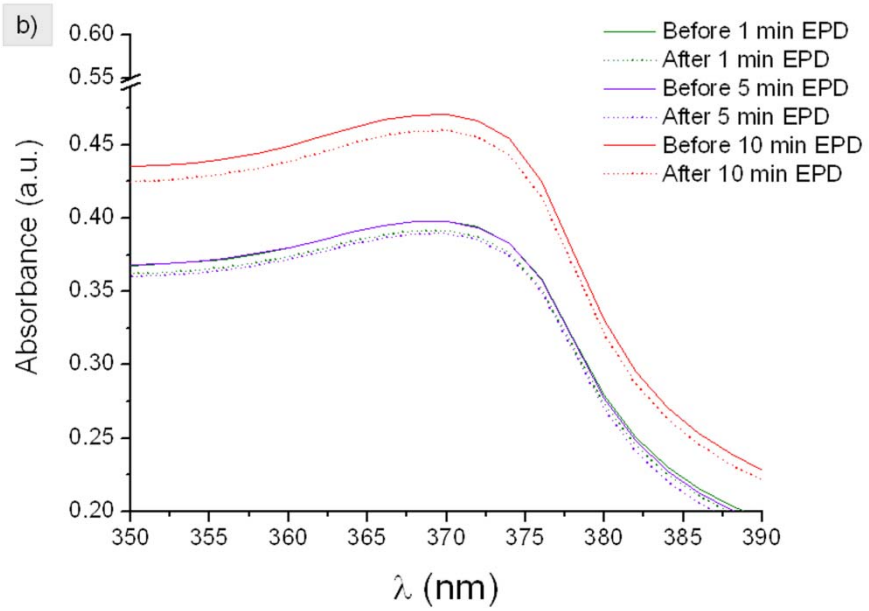

Figure 4.23: UV-Vis absorbance spectra of a) 0.1 and b) 1 g/L ZnO-F suspensions recorded before and after EPD. It must be noted that the variation in the absorbance of the different suspensions is due to the experimental variation in the preparation of the suspensions. This was especially relevant for 1 g/L suspensions, which had to be diluted to 0.1 g/L in order for the detector not to saturate and thus be able to carry out the UV-Vis measurement

Therefore, this variation in the absorbance was transformed into a variation in the concentration of the suspensions by applying Lamber-Beer's law (Eq. 2.7), and this, in turn was transformed into a variation in mass by multiplying by the volume of suspension, which remained constant (see Table 4.3). From the spectra in the figure it can be expected that the amount of mass deposited will be higher for 1 g/L suspensions than for 0.1 g/L ones, as the variation in their intensity previously and after deposition is much larger. Results obtained from the calculations, shown in Table 4.5, confirmed this, and showed that, despite the decrease in the electric field when the solids content was increased, the amount of deposited mass was increased one order of magnitude, from tens to hundreds of micrograms. It must be noted that in this case the absorbance of the concentrated suspensions could not be directly measured and the different dilutions (before and after EPD) increased the experimental error. Therefore, this method was considered to be reliable only for low solid content suspensions.

Table 4.5: results obtained from the analysis of the UV-spectra of the suspensions before and after EPD.

0.1 g/L samples	Δ Abs. ($\cdot 10^{-3}$)	Calculated Mass (µg/cm^2)	1 g/L samples	Δ Abs. ($\cdot 10^{-3}$)	Calculated Mass (µg/cm^2)
FITO-01-1	-	-	FITO-1-1	6.41	113.7
FITO-01-3	3.98	5.8	FITO-1-3	-	-
FITO-01-5	-	-	FITO-1-5	8.27	146.9
FITO-01-7	5.02	7.3	FITO-1-7	-	-
FITO-01-10	5.86	8.5	FITO-1-10	11.2	198.1

The second indirect method for the determination of the deposited mass consisted on the characterization of the films by ellipsometry, which, as described in Chapter 2, determines the change in the polarization state of a beam of light after its reflection on the surface of a sample, and relates this change to the physical properties of the sample. For this purpose, a theoretical model of the film as the one shown in Figure 4.24 is simulated, in which some structural assumptions (e.g. homogeneity of the film) are made taking into account several parameters, such as concentration of the material, approximate thickness of the film, which dispersion law is used, etc.

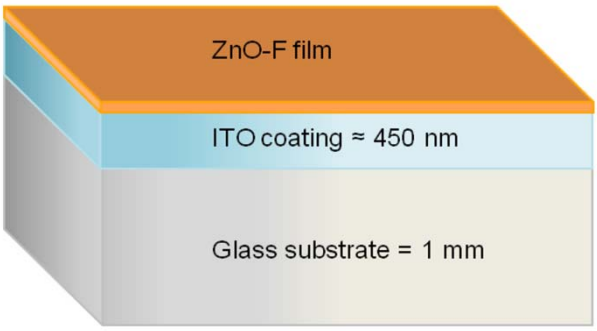

Figure 4.24: simulated model used for ellipsometry measurements. The ZnO-F film was simulated using the law of Cauchy for light dispersion.

In this way, from the adjustment of the model to the experimental results, ellipsometry measurements of our samples provided information about the thickness and refraction index of the films, shown in Figure 4.25 and summarized in Table 4.6.

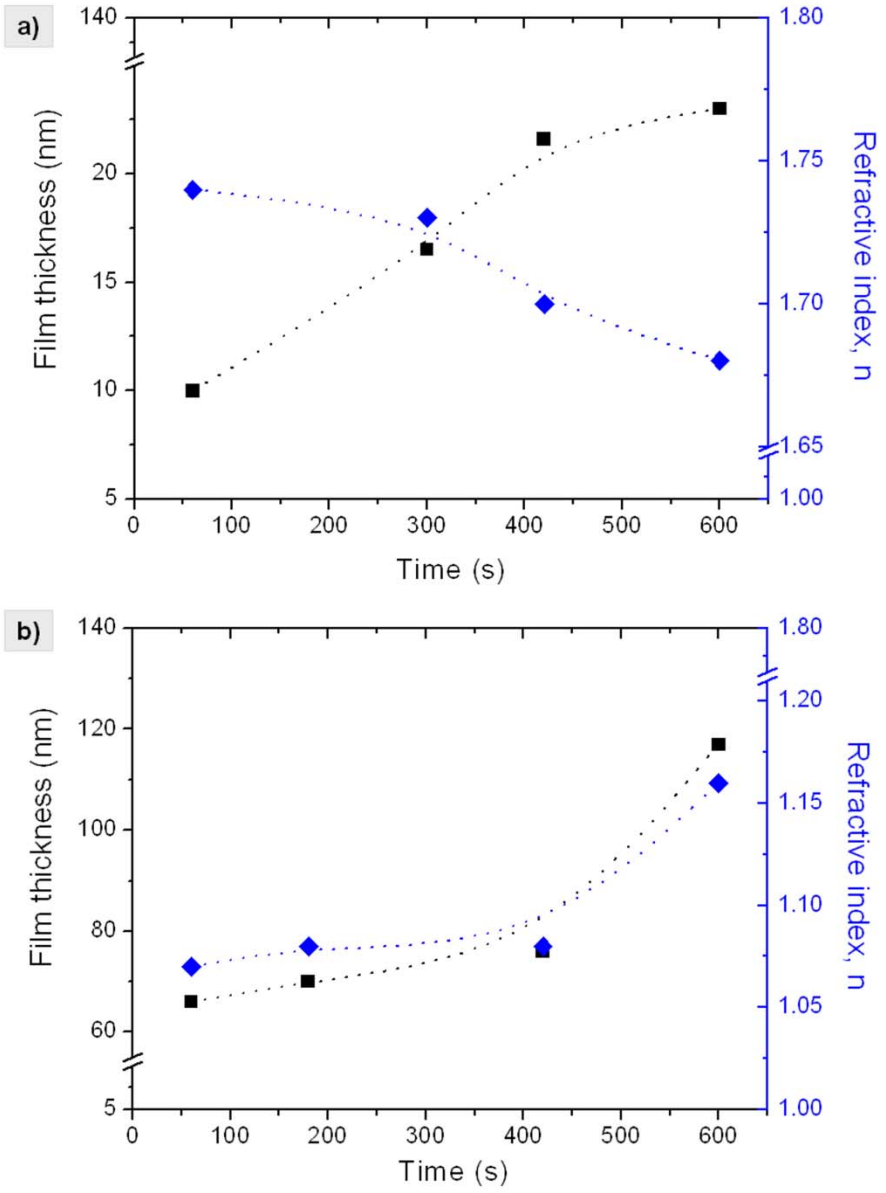

Figure 4.25: Values of films thickness and refractive indexes obtained from ellipsometry measurements of films deposited on ITO substrates from a) 0.1 g/L and b) 1 g/L ZnO-F suspensions.

From the results in Figure 4.25 it can be observed that for both solids contents the thicknesses of the films increase with deposition time. In addition, thickness of the films seems to increase noticeably with solids contents too, as the values obtained for films deposited from 1 g/L suspensions (60-120 nm) corresponded to six times those obtained from 0.1 g/L suspensions (10-20 nm). On the other hand, the refractive indexes, n, present very different behaviors for both solids contents: whereas for lower solid contents the obtained values are of about 1.75 and tend to decrease with time, with more concentrated suspensions these values of n are much lower, of about 1.08 and tend to increase with time. These lower values should be ascribed to the

translucent nature of the films, which absorb a significant fraction of the light and therefore directly affect the optical properties determined by ellipsometry [233].
From these data and according to the works by et al. [234, 235] the density of the films, *d*, can be calculated applying the following equation,

$$\frac{n_f^2-1}{n_f^2+2} = \frac{n_m^2-1}{n_m^2-1} \cdot d \qquad \text{(Eq. 4.9)}$$

in which n_f is the value of the refractive index obtained by ellipsometry and n_m is the theoretical refractive index of ZnO. In this case, however, the theoretical refractive index did not correspond to that of pure ZnO (n_{ZnO} = 2.0041) but to that of the ZnO-F powders. This latter was calculated by applying Eq 4.9, considering *d* as the relationship between the real and the theoretical densities of the powders (4.36 and 5.2 g/cm^{3,} respectively), and isolating n_f as the unknown variable in the equation. From this calculation the theoretical refractive index of ZnO-F turned out to be of 1.7821, and thus, the density of the films was calculated considering this as n_m. With this calculated density and the thickness of the films obtained by ellipsometry, and knowing the deposition area (in Table 4.3) and the density of the powders, the mass of the deposit was geometrically calculated. The values of the data obtained by the adjustment of the ellipsometry model and the subsequent density and mass calculations are summarized in Table 4.6.

Table 4.6: Results obtained from the analysis of the ellipsometry measurements.

Sample		Thickness (nm)	n	Film Density (%)	Mass (µg/cm^2)
0.1 g/L samples	FITO-01-1	10.2	1.74	95.9	4.4
	FITO-01-3	11.8*	1.55	73.5	4.2
	FITO-01-5	16.5	1.73	95.0	6.9
	FITO-01-7	21.6	1.7	91.9	8.2
	FITO-01-10	22.9	1.68	89.9	8.7
1 g/L samples	FITO-1-1	66	1.07	11.0	3.0
	FITO-1-3	70	1.08	12.5	3.3
	FITO-1-5	64*	1.14	21.6	3.3
	FITO-1-7	76	1.08	12.5	4.8
	FITO-1-10	117	1.16	24.6	12.7

* These samples showed a certain degree of inhomogeneity during the adjustment of the ellipsometry model, and thus are considered uncertain.

From the data in Table 4.6 it can be noted that the calculated deposited masses for 0.1 g/L suspensions are in range with those obtained by the other indirect method (Table 4.5). The masses obtained for films deposited from 1 g/L suspensions, in contrast, are approximately one order of magnitude smaller than those obtained by weighing. This decrease in the calculated deposited mass is due to the low values of density, which in turn, are due to the low refractive index of these films. However, this decrease in the calculated mass is not reflected on the thicknesses values, which, as for lower solid contents, seem to slowly grow with deposition times and solid contents. This increase in thickness and decrease in refractive index and density of the films point out to a decrease in the packing density of the particles with deposition time and solids content.

Table 4.7 summarizes results from 0.1 (a) and 1 g/L (b) suspensions. The deposited masses determined by weighing (M_W), UV-Vis ($M_{UV\text{-}Vis}$) and Ellipsometry (M_{Ellips}), the thickness determined by ellipsometry (e_{Ellips}) and their calculated densities (ρ_w, $\rho_{UV\text{-}Vis}$ and ρ_{Ellips}) are collected in this table. Film densities were calculated geometrically, i.e. dividing the deposited mass per area by the film thickness determined by ellipsometry, dividing the result by the density of the ZnO-F particles (4.4 g/cm^3), and thus are referred to a full dense film. From these results it can be inferred that the densities calculated in this way for the films deposited from 0.1 g/L suspensions were in agreement with those obtained directly from ellipsometry. For those deposited from more concentrated suspensions, however, some divergences appeared: even though the density calculated from the weighing data was “normal/logical”, those calculated considering the UV-Vis and ellipsometry data were excessively high and low, respectively. Thus it can be considered that the indirect methods were once more unreliable for depositions from high solid content suspensions.

Table 4.7a: Summary of the results obtained for 0.1 g/L suspensions.

0.1 g/L samples	**($M_{UV\text{-}Vis}$) ($\mu g/cm^2$)**	**(M_{Ellips}) ($\mu g/cm^2$)**	**(e_{Ellips}) (nm)**	**$\rho_{UV\text{-}Vis}$ (%)**	**$\rho_{Ellips.}$ (%)**
FITO-01-1	-	4.4	10.2	-	98.9
FITO-01-10	8.5	8.7	22.9	87.1	85.1

Table 4.7b: Summary of the results obtained for 1 g/L suspensions.

1 g/L samples	(M_W) ($\mu g/cm^2$)	(M_{UV-Vis}) ($\mu g/cm^2$)	(M_{Ellips}) ($\mu g/cm^2$)	(e_{Ellips}) (nm)	ρ_W (%)	ρ_{UV-Vis} (%)	$\rho_{Ellips.}$ (%)
FITO-1-1	9.7	113.7	3.0	66	33.7	394	10.4
FITO-1-10	31.6	198.1	12.7	117	61.9	388	25.9

Taking into account the results described in this section and summarized in Table 4.7, it can be concluded that for suspensions with low solid contents the two indirect methods gave similar and coherent results, and therefore can be considered as feasible ways of determining the mass deposited by EPD. On the other hand, these methods were not as reliable for the characterization of films deposited from suspensions with higher solids contents. In those cases, the deposited mass data determined by the indirect methods did not fit the data obtained by direct weighing. The divergence can be ascribed to different experimental impediments hampered the obtaining of correct measurements. For the UV-Vis method, although the experimental variability in the preparation of the suspensions decreased with increasing solid contents, their dilutions for the measurement before and after EPD diminished the accuracy of the obtained results. For the ellipsometry measurements, in contrast, the problem lied in the opacity of the films and in the assumptions made for the simulation of the model of the film, which were far from the reality and therefore gave place to results which were also inaccurate.

In any case the results obtained by all three methods pointed out several important trends of the studied system: (i) a very slow deposition and/or a low deposition yield for both solid contents, (ii) film thicknesses increased with time, whereas their packing degree decreased for both solid contents (iii) neither the deposit growth nor the packing density of the films reflected the increase of one order of magnitude in the solids contents.

The thicker films obtained from 0.1 g/L and 1 g/L suspensions (FITO-01-10 and FITO-1-10) were then characterized by SEM. SEM micrographs of the surface of the films (Figure 4.26) seemed to verify the above discussed statements: the deposited films were not homogeneous, but seemed to deposit as “islands” of agglomerates, under and in between which the surface of the substrate could be observed during the surface scanning.

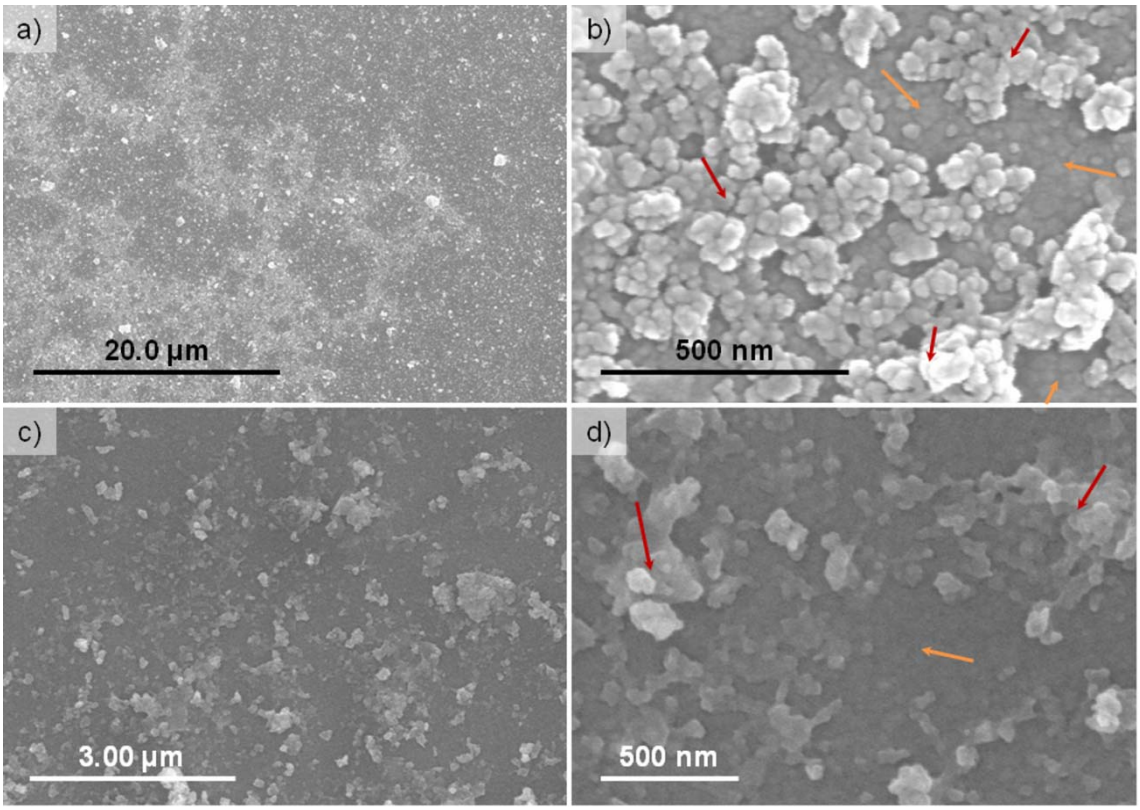

Figure 4.26: SEM micrographs of the surface of the a, b) FITO-01-10 and c, d) FITO-1-10 samples. The surface of the ITO substrates (signaled by orange arrows) can be observed underneath and in between the islands of ZnO-F deposits (signaled by red arrows).

Moreover, these micrographs evidenced a heterogeneous deposition and the lower density of the films deposited from higher solid content suspensions, already described by the different methods. The lack of homogeneity of these films can be ascribed to two factors related to each other: on the one hand the homogeneity of the surface, which does not provide points of charge accumulation [236] and on the other hand to the measured low conductivity of the ITO-coated substrate (see Section 4.2.2). These two factors together might hamper a homogeneous deposition by reducing the effective electric field in the surroundings of the substrate surface.

In this sense, with the aim of verifying the cause of the scarce deposition, a test was carried out in which 0.1 and 1 g/L suspensions were deposited directly on HRTEM copper grids. For this purpose the grids were attached to a Si wafer with a platinum wire, and similar conditions that those applied to obtain FITO-01-10 and FITO-1-10 (constant currents of 100 µA and times of 10 min) were fixed. The micrographs of films deposited from 0.1 g/L are shown in Figure 4.27.

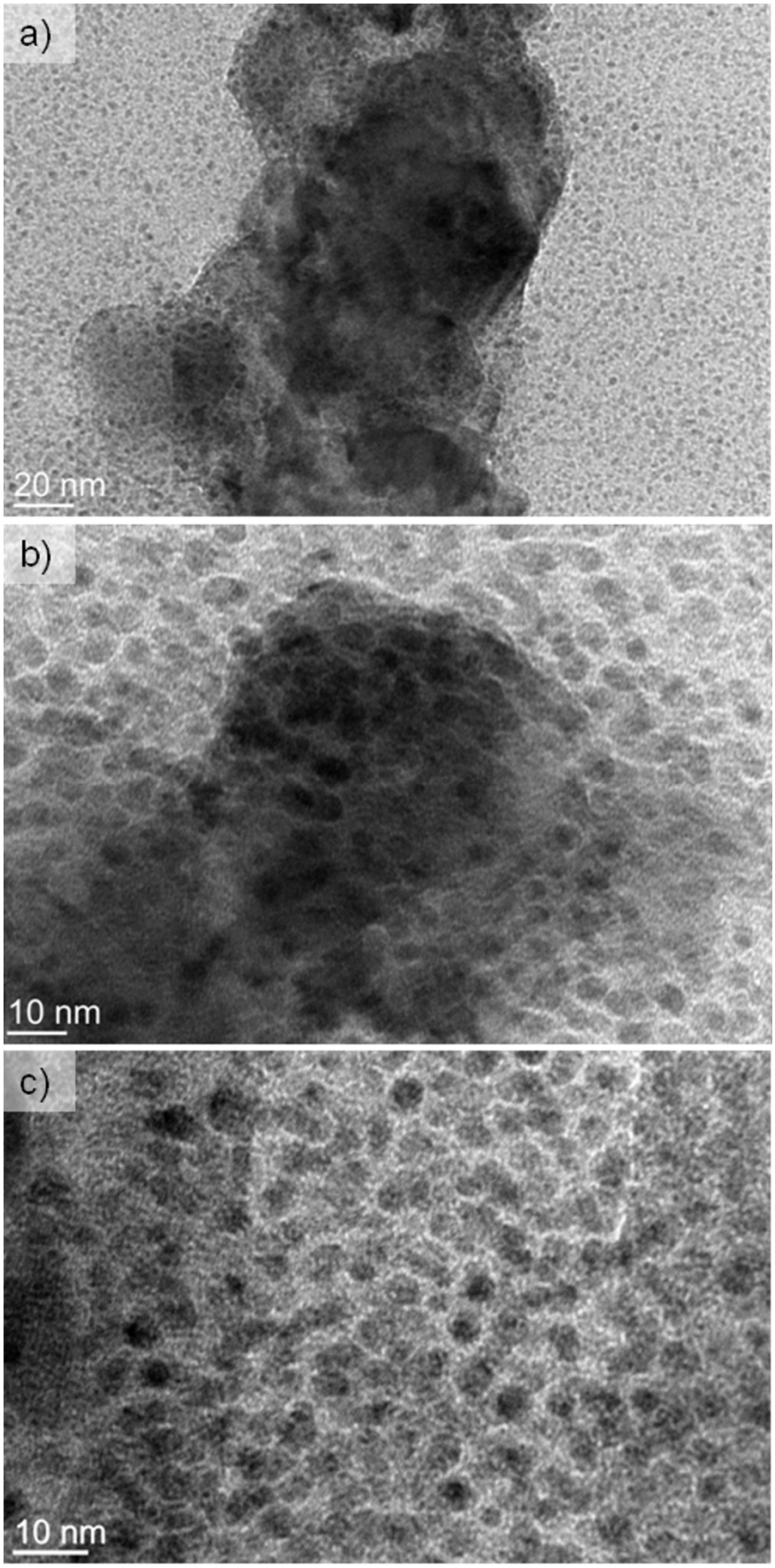
a)
20 nm
b)
10 nm
c)
10 nm

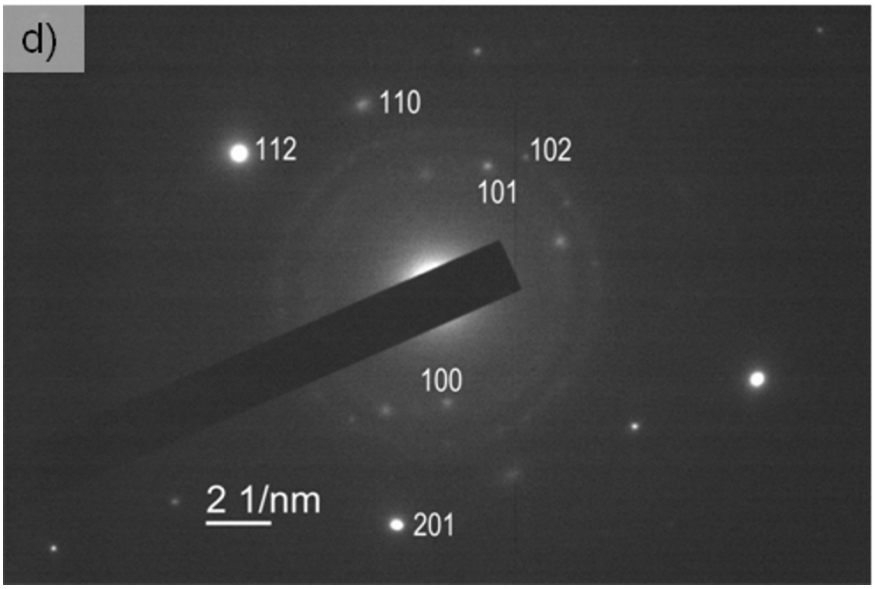

Fig. 4.27: a-c) HRTEM micrographs and d) SAED analysis of the ZnO-F films deposited from 0.1 g/L suspensions. The scale in d) corresponds to the reciprocal space used for the calculation of the d-spacing and assignment of the diffraction indexes.

In these micrographs the presence of the two populations of particles in the ZnO-F powder, the large hexagonal flakes and the smaller rounded particles, can be observed. The flake- like particles, of about 50 nm, arrange themselves in stacks, which are covered and surrounded by the smaller particles, which are very densely packed. Moreover, it can be postulated that the distance between the smaller particles, which seems to be constant, can be due to the presence of the polyelectrolyte, which is in a collapsed state due to the pH increase in the surroundings of the electrode [237]. The presence of this dense film formed by the smaller ZnO particles and not observable by the SEM might be the responsible for several of the phenomena or characteristics of the studied system. In the first place, the presence of this extremely thin and transparent layer of nano ZnO-F particles explains the high density measured by ellipsometry in FITO-01 films (up to 98.9% in Table 4.7). Moreover it can also be the cause of the low deposition yield: due to the dense packing of the ZnO-F particles in the film, the field is blocked and deposition stops.

SAED of these films showed bright spots which originated from the larger flakes and low intensity circles “produced” by the finer particles. This low intensity of the diffraction circles can be due to a low crystallinity of the particles or just to their small size. In any case, both types of contribution were indexed to zincite.

When the solids content was increased to 1 g/L the dispersion of the smaller particles in the film was decreased, as can be observed in the micrographs in Figure 4.28. In this case, the proportion of larger particles was higher, and the smaller

particles tended to agglomerate with them, forming “islands”. In addition, micrographs with higher magnification allowed the observation of lattice fringes which corresponded to a zincite structure in the smaller particles. This pointed out to a crystalline nature in these particles, which therefore allowed ascribing the low intensity of the diffraction spots in Figure 4.27c to their small size. These results are in good agreement with the poor density of thicker films shaped from 1g/L suspensions (Table 4.7b).

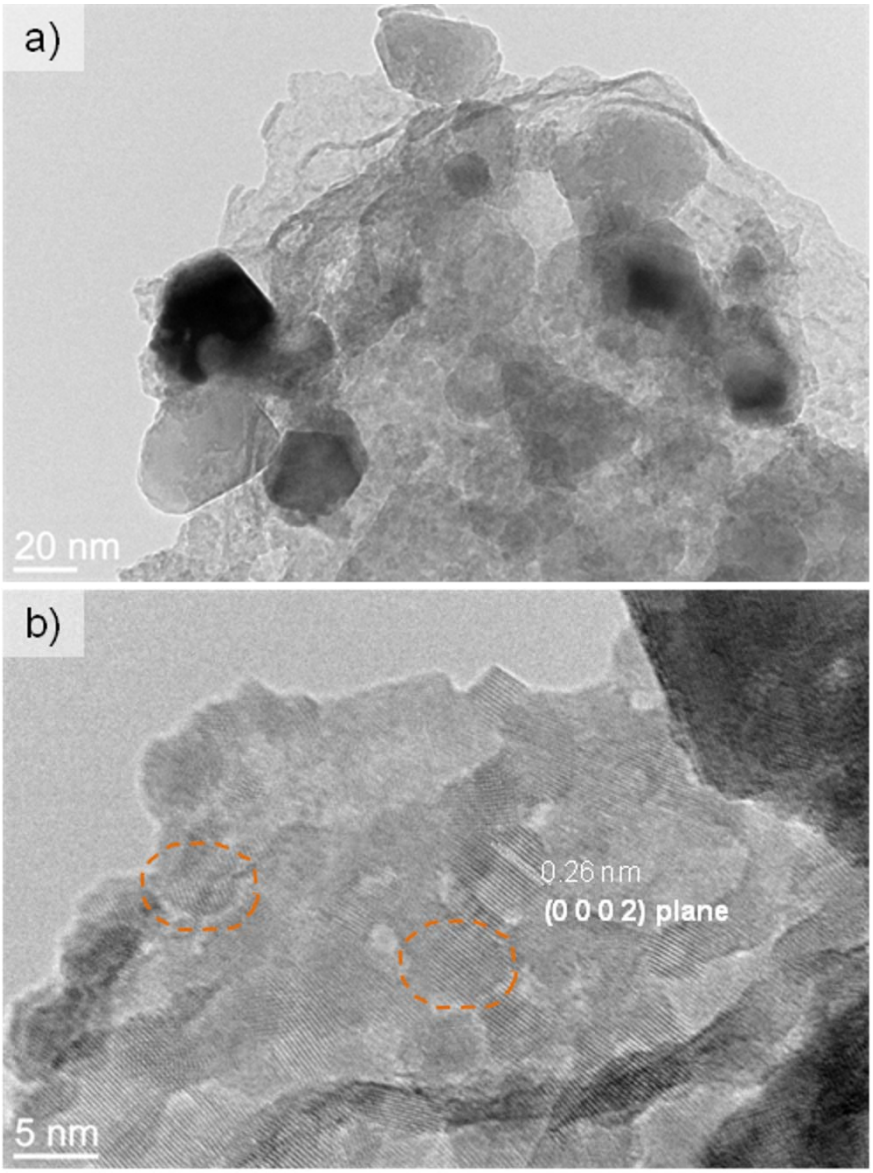

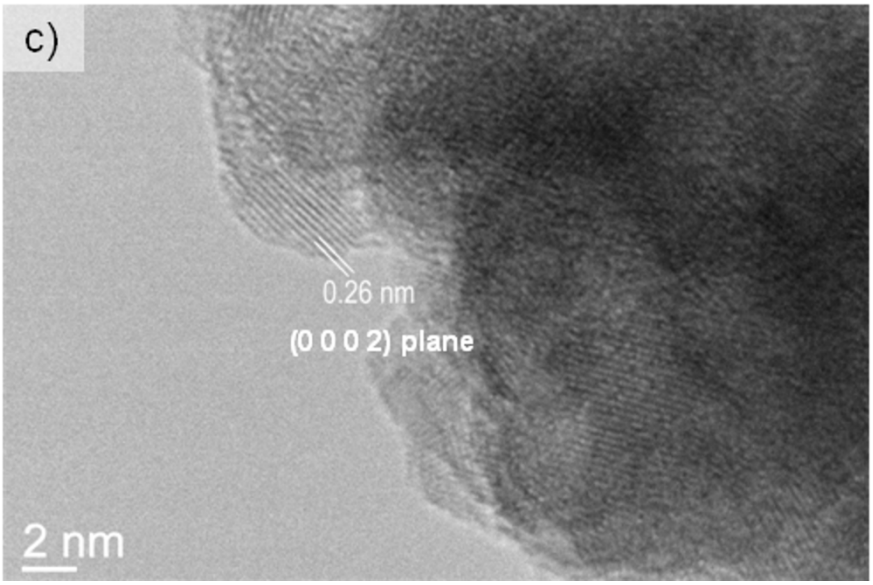

Fig. 4.28: HRTEM micrographs of ZnO-F films deposited from 1 g/L suspensions.

As this point, and considering its higher conductivity and roughness, stainless steel substrates (ESS) were used next so as to study the influence of the kind of substrate on the deposition. As in the previous case, films were deposited by EPD applying increasing deposition times, from 1 to 10 min to ZnO-F fresh suspensions. The parameters fixed for all depositions are the same as those summarized in Table 4.3, except for the deposition conduction areas, which were of 4.9 and 4.8 cm^2 for 0.1 and 1 g/L suspensions. The variation of the electric field with deposition time is shown in Figure 4.29.

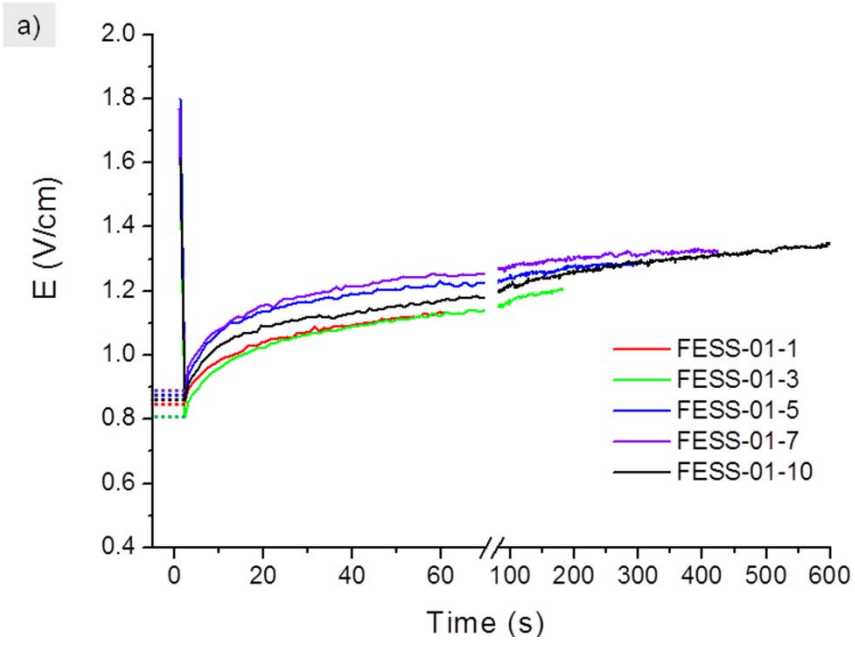

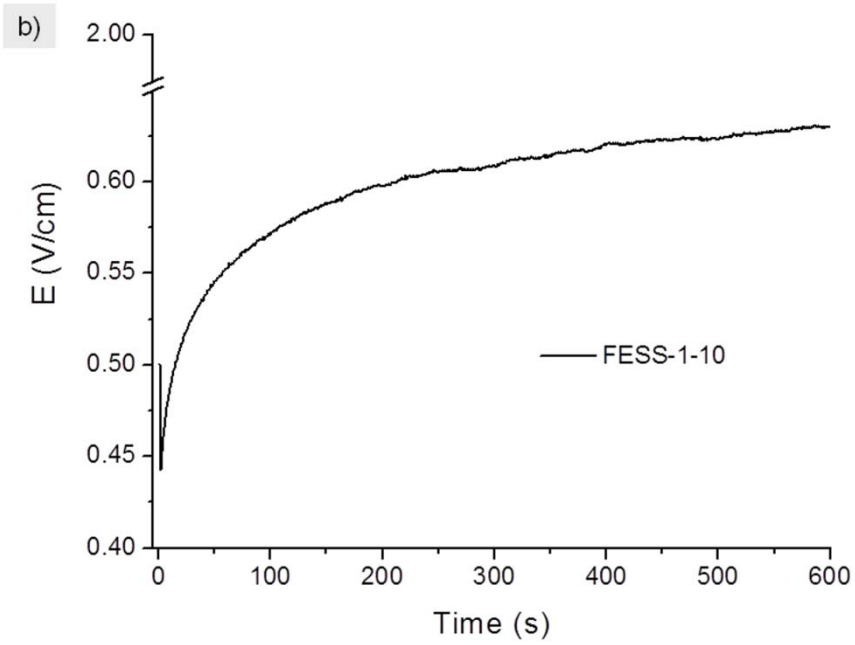

Figure 4.29: Electric field vs. deposition time curves for a) 0.1 and b) 1 g/L ZnO-F suspensions.

With comparative purposes, only times of 600 s were considered for high solid content suspensions. From Figure 4.29 it can be observed how the increase in solid contents decreased the effective field from average initial values of $E_{t=0}$ = 0.86 for 0.1 g/L suspensions to 0.44 V/cm for 1 g/L respectively. Moreover, it must be noted that these electric fields are much lower than those obtained for deposition on ITO substrates (1.41 and 0.76 V/cm for 0.1 and 1 g/L respectively). The reason for this decrease is found in the conduction area, which in this case is higher than that for the deposition on ITO substrates, as both sides of the stainless steel substrate are conducting, and this affects the electric field, which is inversely proportional to the area (see Eq. 4.8). It is important to note that in this case, within a similar range of values, the electric field slowly increased during EPD, oppositely to the deposition on ITO, in which constant values of E were registered for times above 60 s (see Figure 4.21).

As in the previous case, films deposited from 0.1 g/L suspensions were transparent and could not be detected by visual inspection. Films obtained from 1 g/L suspensions however, were translucent, i.e. visible to the naked eye, as can be observed in the photograph in Figure 4.30.

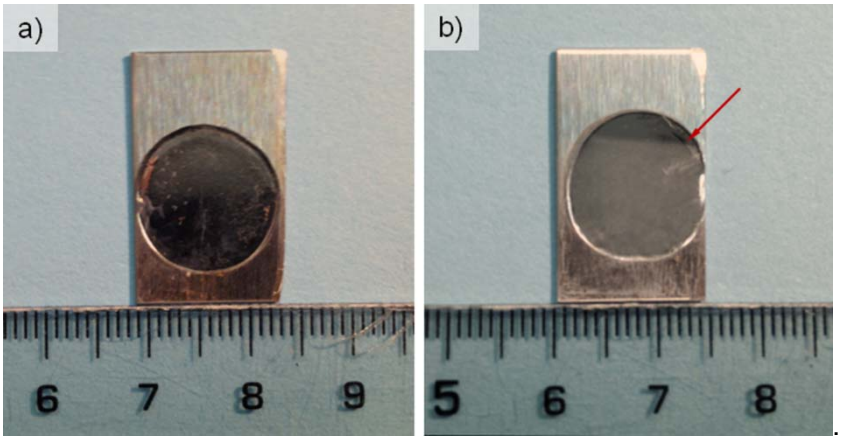

Figure 4.30: Photographs of an electropolished stainless steel substrate with a ZnO-F film deposited from a 1 g/L suspension and deposition conditions of 100 µA for of 10 min. The red arrow points to the upper limit of the ZnO-F film.

The different deposited films were therefore characterized by the methods validated above to study their deposited mass and structure, i.e. by weighing in the case of 1 g/L films and by UV-Vis for films deposited from 0.1 g/L suspensions. These latter could not be characterized by ellipsometry in this case, given the opaque and rough nature of the electropolished stainless steel substrates.

Therefore, in this case, the mass deposited from 0.1 g/L suspensions was estimated from the variation of intensity in the UV-Vis absorbance spectra measured previously and after the deposition process, applying Lamber-Beer's law (Eq.2.7). The absorbance spectra of the suspensions before and after EPD and their corresponding masses obtained by this calculation are shown in Figure 4.31 and Table 4.10, respectively. Table 4.10 also compiles the deposition mass of the film obtained from a 1 g/L suspension in an EPD test of 10 min.

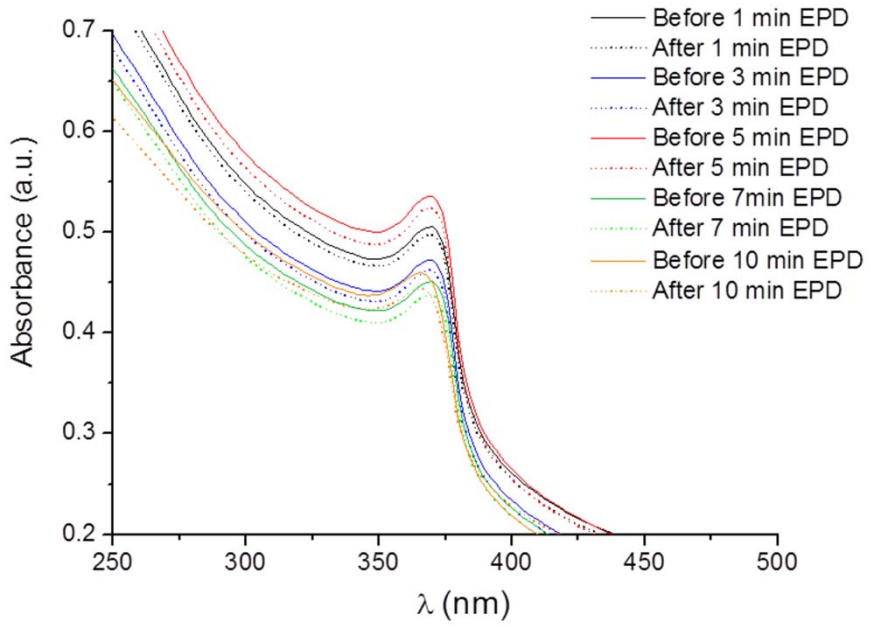

Figure 4.31.: UV-Vis absorbance spectra of the 0.1 g/L ZnO-F suspensions before and after EPD.

Table 4.10: results obtained from the analysis of the UV-spectra of 0.1 g/L suspensions before and after EPD and by weighing of the films deposited from 1 g/L suspensions.

0.1 g/L samples	Δ Abs. ($\cdot 10^{-3}$)	Calculated Mass (μg/cm^2)	1 g/L samples	Weighed Mass (μg/cm^2)
FESS-01-1	7.5	17.7	-	-
FESS-01-3	10.3	24.5	-	-
FESS-01-5	12.1	28.6	-	-
FESS-01-7	12.9	30.4	-	-
FESS-01-10	13.5	32	FESS-01-10	24.5

From the spectra in the figure and the data in the table it can be observed how, despite the variability in the preparation of the suspensions, which gave place to different absorbances, the variation of the latter increased with deposition time, as more mass was being removed from the suspensions. By comparing these results with those obtained on ITO substrates (Figure 4.23 and Table 4.5) it can be observed how, despite the decrease of the electric field, more mass was deposited on stainless steel substrates for 0.1 g/L suspensions. From the data in Table 4.9 it can also be noted that, similarly to what happened for the deposition on ITO substrates, the masses deposited from high solid contents suspensions were lower than those from 0.1 g/L

suspensions. Moreover, these masses were also lower than those deposited on ITO substrates.

Samples obtained for deposition times of 600 s (FESS-01-10 and FESS-1-10) were characterized. SEM micrographs of the FESS-01-10 ES sample (Figure 4.32) verified the presence of a homogeneous ZnO dense film with some agglomerates and disperse pores on its surface. However, this porosity did not affect the films transparency, as the pores size was below 50 nm.

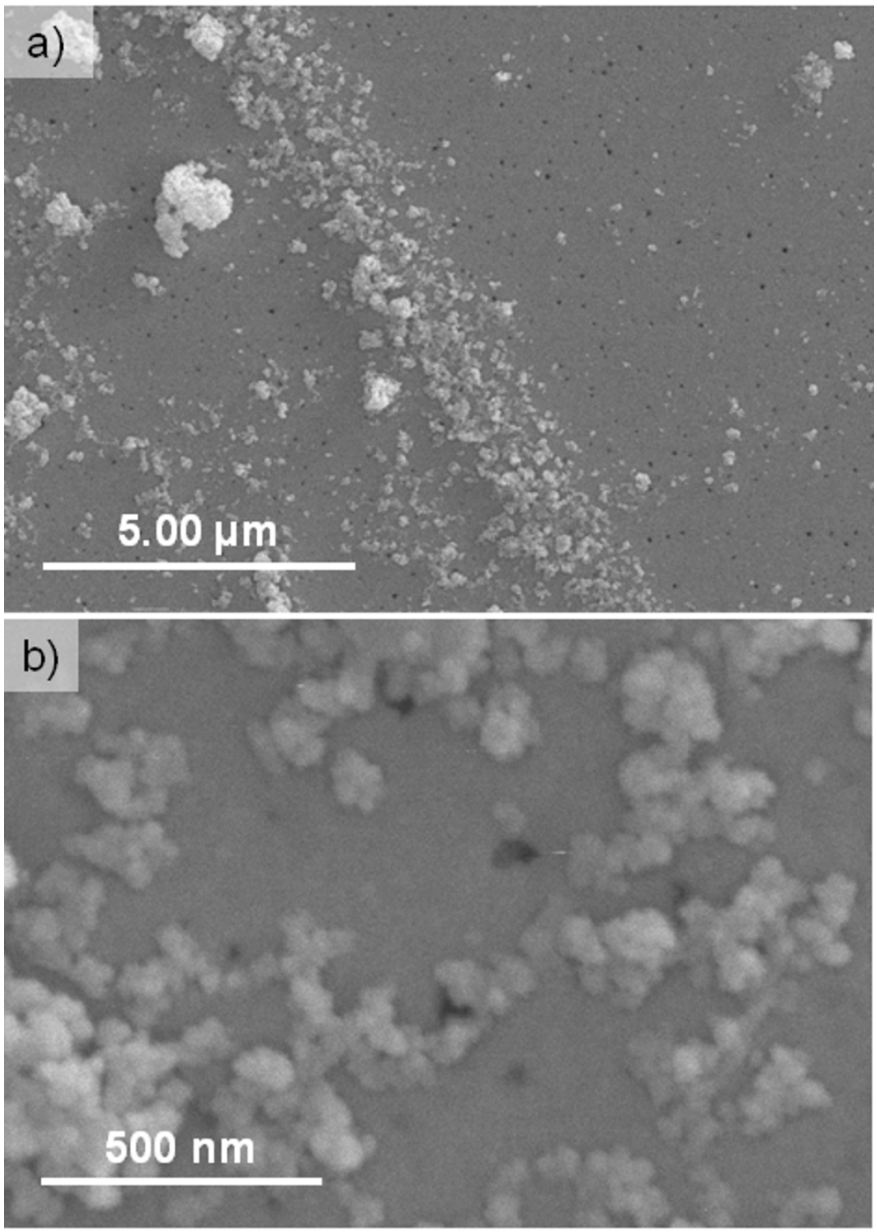

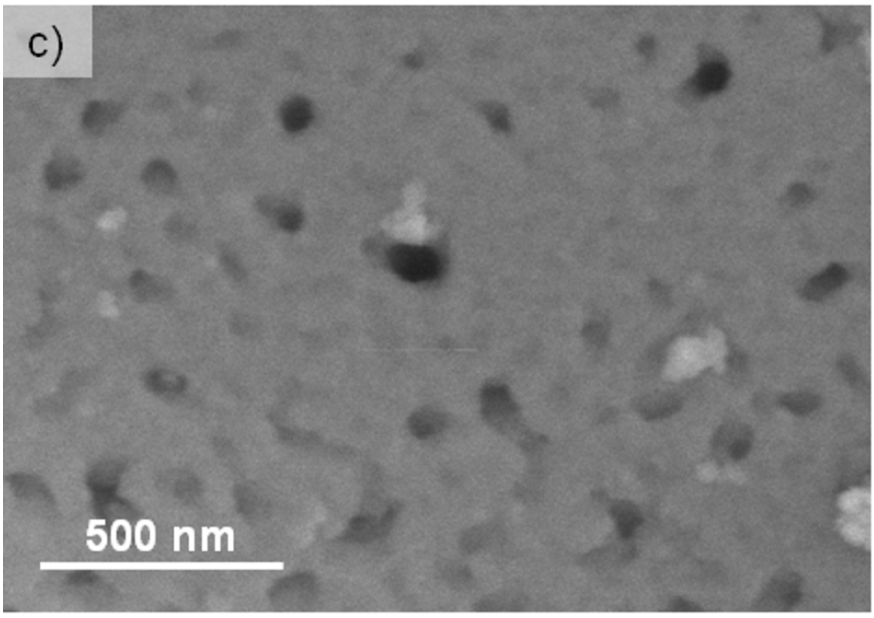

Figure 4.32: SEM micrographs of the FESS-01-10 sample. The micrograph in a) corresponds to the border of the ZnO film, where most powder is accumulated, as it corresponds to the suspension/air interface.

When magnification was increased it could be observed that the ZnO-F film presented a very high packing density of its particles (Figure 4.32 b and c). This high packing density of the small amount of mass deposited is responsible for the transparency of the film, and can be ascribed to the morphology and orientation of the ZnO-F particles: during the electrophoresis of the ZnO-F nanoparticles, and due to addition of PEI resulting in the jellyfish-like structure, orientation of the majority of the particles is opposite to that favored by hydrodynamics i.e. ZnO-F nanoparticles with PEI attached to their surface move with their basal plane parallel to the substrate (see scheme in Figure 4.33a). However, when reaching the substrates surface, PEI, which is a weak cationic polyelectrolyte, loses charge and reduces its electrostatic effect as dispersant due to the high pH increase near the cathode surface [237, 238]. Nevertheless, when the ZnO-F nanoparticles arrive to the substrates surface, the steric effect of PEI helps them organize in the same way they moved, aligning their principal dimension parallel to the substrate according to electro-hydrodynamics (Figure 4.33b) and forming clusters of 50-100 nm which appear to be the building-blocks of the structure.

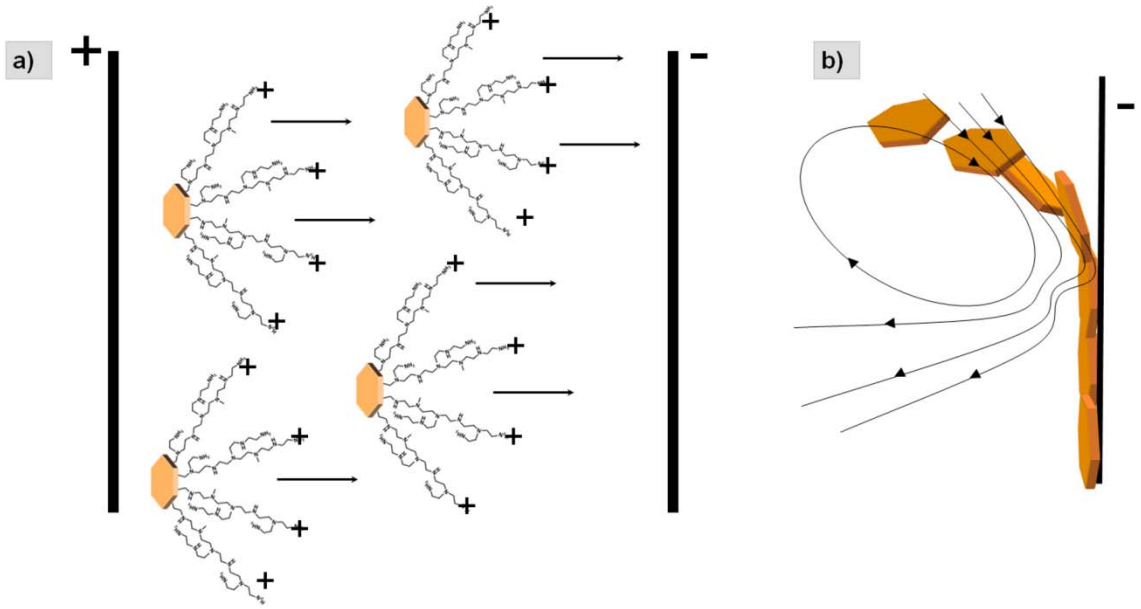

Figure 4.33: Scheme of a) the suggested movement of the ZnO-F particles with the attached PEI during electrophoresis and b) orientation of the flakes according to hydrodynamics in the area close to the electrodes surface.

FE-SEM micrographs of the films obtained for higher solid contents are shown in Figure 4.34. In this case, vast amounts of agglomerates on top of the film can be observed, which hampered a closer observation of the surface. This high number of agglomerates is responsible for the fact that these films were visible to the naked eye.

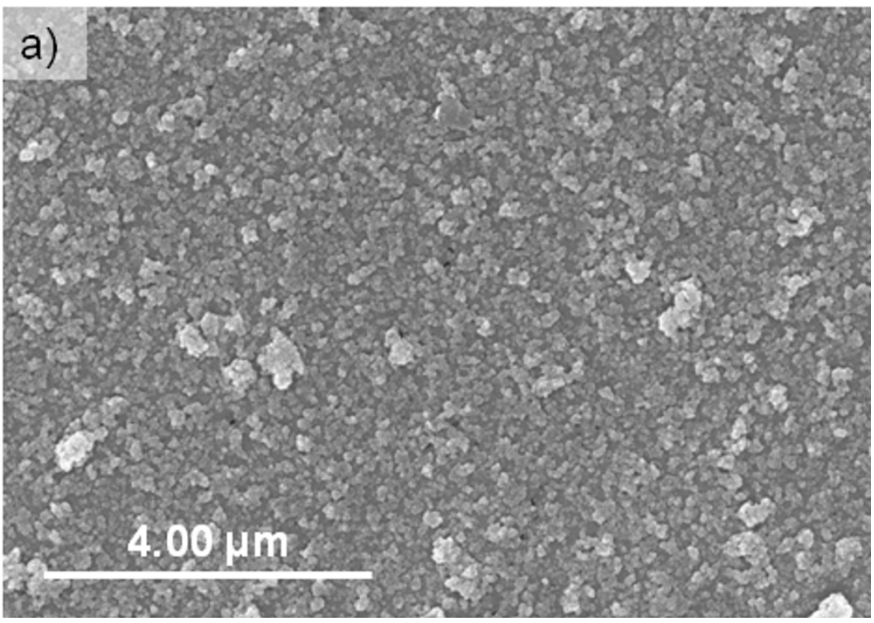

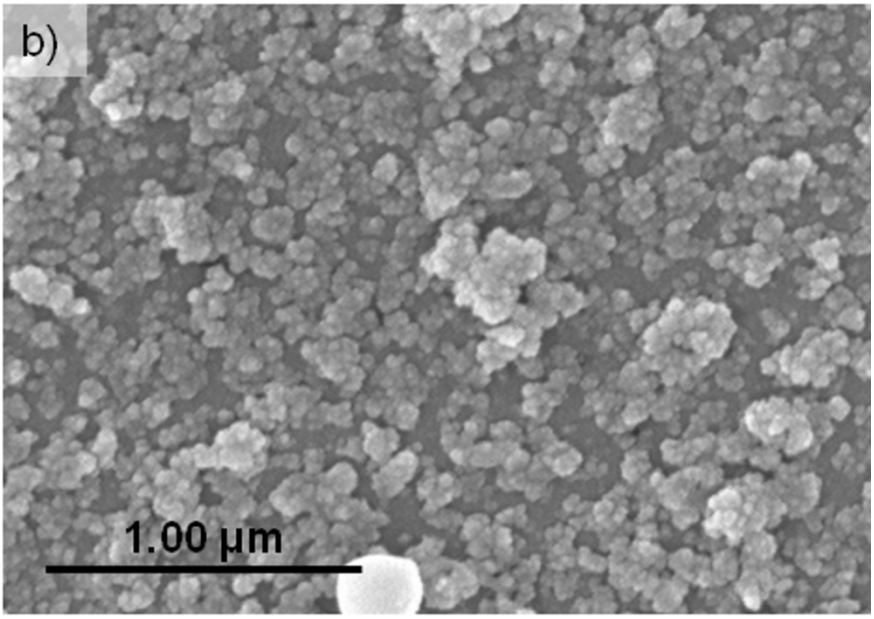

Figure 4.34: SEM micrographs of a ZnO-F film obtained after 10 min EPD on a stainless steel substrate from a 1 g/L suspension.

In any case, given the low deposition yields, very thin films should be expected. At this point, the rough nature of the surface of the electropolished stainless steel substrate hampered the use of cross-section SEM. Therefore, in order to try and observe the thickness of the films, the substrates were bent, as shown in the photograph in Figure 4.35.

Figure 4.35: Photograph of the bent stainless steel substrates.

SEM micrographs of the bent samples (Figure 4.36) showed several interesting features. The most noticeable of them was that the film did not break, but bent with the substrate. In this sense, the presence of the film could only be clearly observed in areas close to defects of the substrate, in which tension areas appear. This “flexibility” of the films was especially remarkable for films deposited for 1 g/L, for which no defects could be found. Hence, all the micrographs in the figure correspond to defective areas

found in films from 0.1 g/L suspensions. In these areas, some cracks appeared on the films due to induced tensions, but no complete fracture was observed. Moreover, in these micrographs it could also be observed that the pores in the films were in fact pores in the stainless steel substrate (already observed by AFM) some of which were too big to be covered by the ZnO-F nanoparticles.

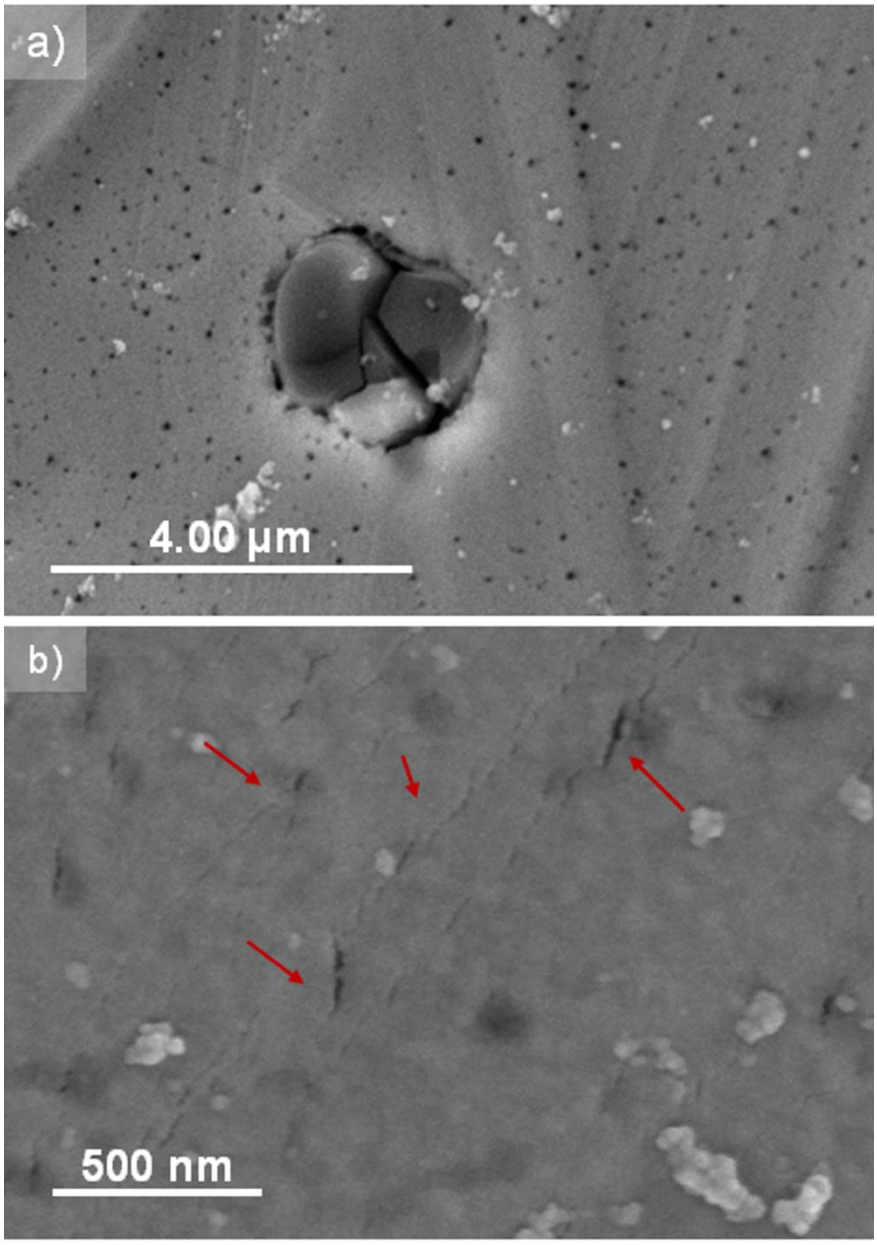

Figure 4.36: SEM micrographs of the bent FESS-01-10 sample. a) shows a defect in the substrate around which tensioned areas in the film appear (red arrows in b). The FESS-1-10 sample showed no defective areas and thus is not shown here.

Finally, the films deposited after 10 min (FESS-01-10) were also characterized by atomic force microscopy (AFM) in order to verify the topology of the surface and confirm the orientation observed by SEM. Figure 4.37a shows the 2D AFM topography

of one of these films, in which it can be observed that the diameter of the nanoparticles in the film is of 20 - 40 nm, in agreement with those observed by TEM (see Figure 3.22). This image also shows the defects produced in the substrate during electropolishing, and how the particles arranged around it but were not big enough to cover it. The amplitude map (Figure 4.37b) shows the organization of the platelets parallel to the substrate. Moreover, the profile of the topography in 4.37c shows a local roughness below 20 nm, which is in agreement with the suggested orientation of the particles parallel to the substrate, as it corresponds to approximately two or three times the thickness of the nano-flakes.

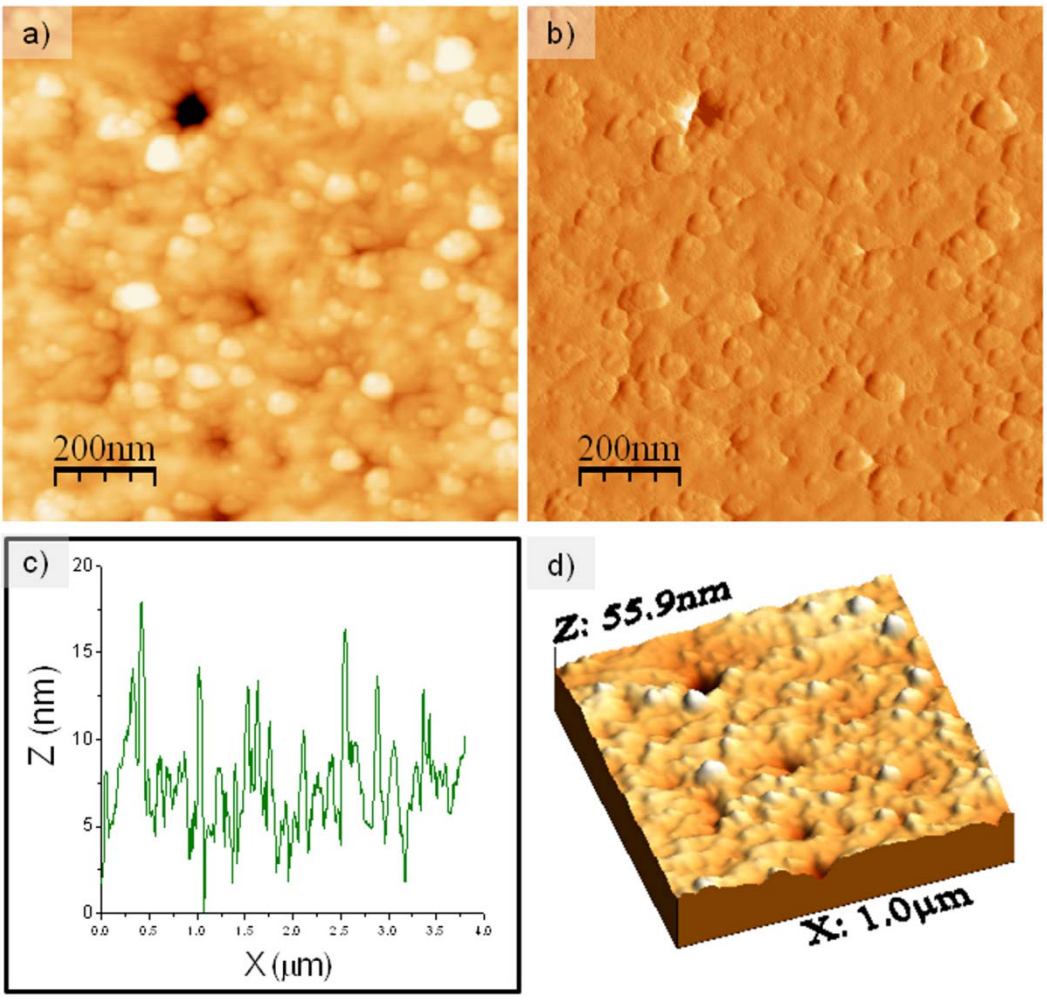

Figure 4.37: AFM a) topography image, b) amplitude map, c) profile and d) 3D image of a ZnO-F film deposited from 0.1g/L suspensions after 10 min EPD.

- Thermal treatments.

In order to densify and consolidate the ZnO-F films deposited from 0.1 g/L suspensions on electropolished stainless steel substrates, several thermal treatments

in air were studied: 180, 300 and 500 ºC for 2 hours. The resulting densified films were characterized by SEM. The micrographs in Figure 4.38 show the evolution of densification with increasing temperatures: the treatment at 180ºC/2h did not produce a significant increase on densification, as the samples treated at this temperature (Figure 4.38a-c) showed the same disperse porosity as the samples in green. On the other hand, the samples treated at 300ºC did show a slight decrease of this porosity and "rows" of aligned particles, evidencing the beginning of interparticle necks growth (Figures 4.38d-f). Finally, for the samples treated at 500 ºC no remaining porosity was detected, and complete densification was achieved, though the agglomerates in the surface of the films presented a remarkable coarsening (Figures 4.38g and h). Moreover, in the micrograph in Figure 4.38h the grain boundaries of the stainless steel substrate can be observed through the ZnO-F film, which is transparent to the electron beam.

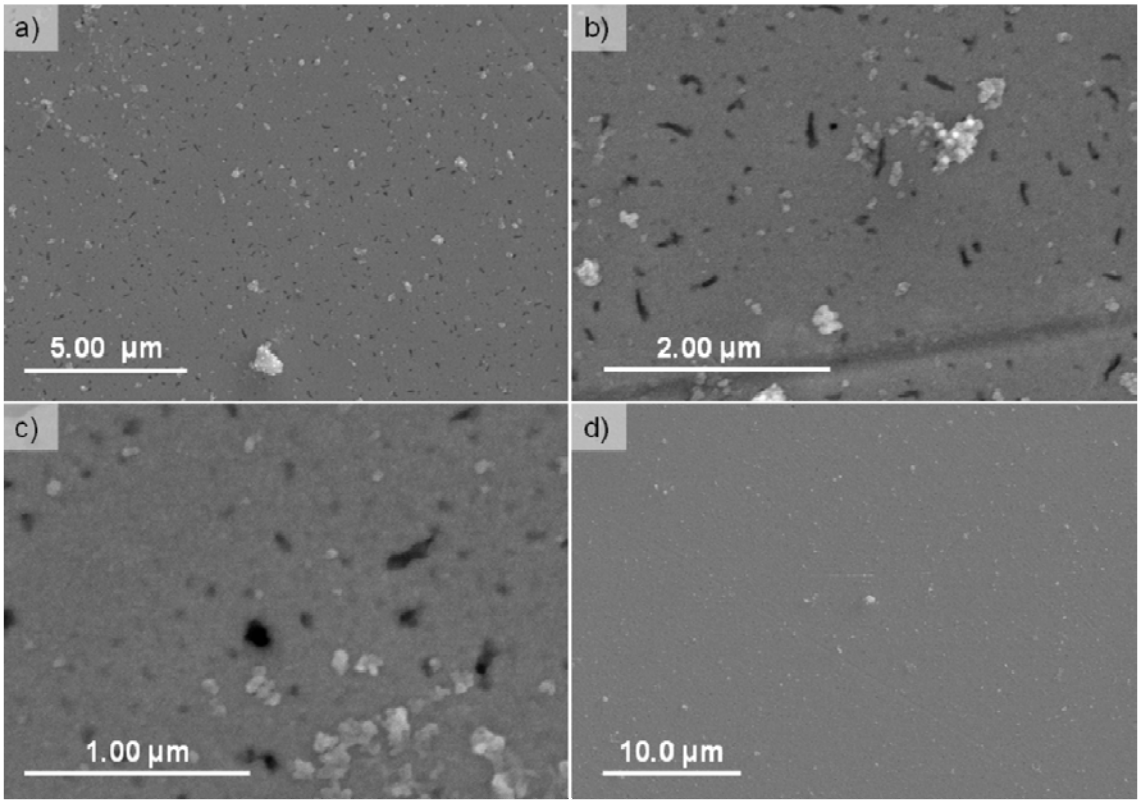

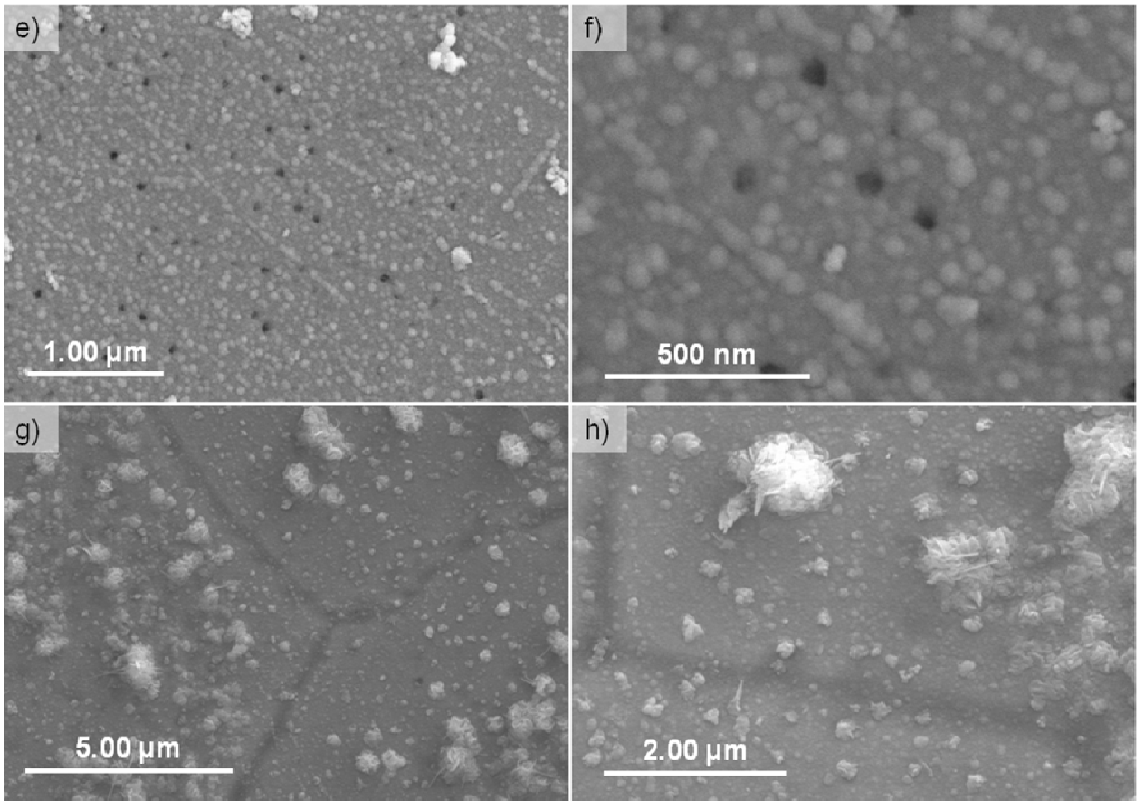

Figure 4.38: SEM micrographs of ZnO-F films obtained from 0.1g/L suspensions after 10 min of deposition treated at: a-c) 180 ºC/2h, d-f) 300 ºC/2h and g, h) 500ºC/2h.

From the micrographs in Figure 4.38, the chosen thermal treatment was that of 300 ºC, as it was considered that it allowed reaching a certain degree of densification without unwanted particle coarsening. In order to observe the thickness and densification of these layers the substrates were bent and characterized once more by FE-SEM (Figure 4.39). In the micrographs of the bent samples it can be observed how, in this case and due to densification, the films (which reproduce the defects of the substrate) fractured with the bending. In addition, in the fracture areas some of the pieces of the film “peeled-off” from the substrate, which can be seen underneath, and this allowed observing the thickness of the film, which was of about 25 nm in close agreement with the thickness determined by ellipsometry (see Table 4.7a), and seemed to correspond to a monolayer of particles.

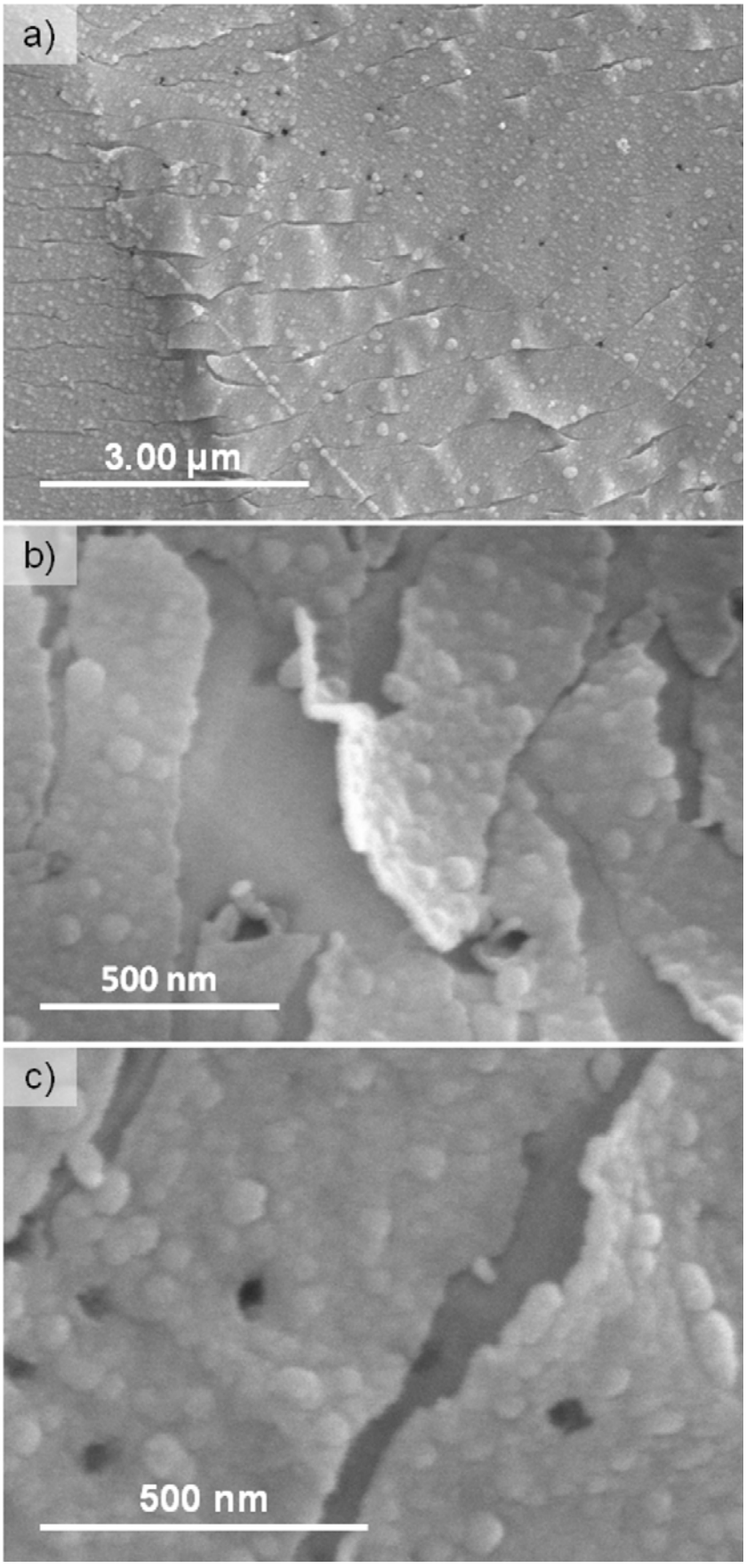

Figure 4.39: SEM micrographs of a ZnO-F film obtained from 0.1 g/L suspension after 10 min EPD and treated at 300 ºC for 2 hours. Orange arrows point to the surface of the substrate underneath the film.

Taking into account these results, the samples with higher solid contents were treated at 300 and 500 ºC for 2 hours, bent and observed in the SEM. The resulting SEM micrographs are shown in Figure 4.40.

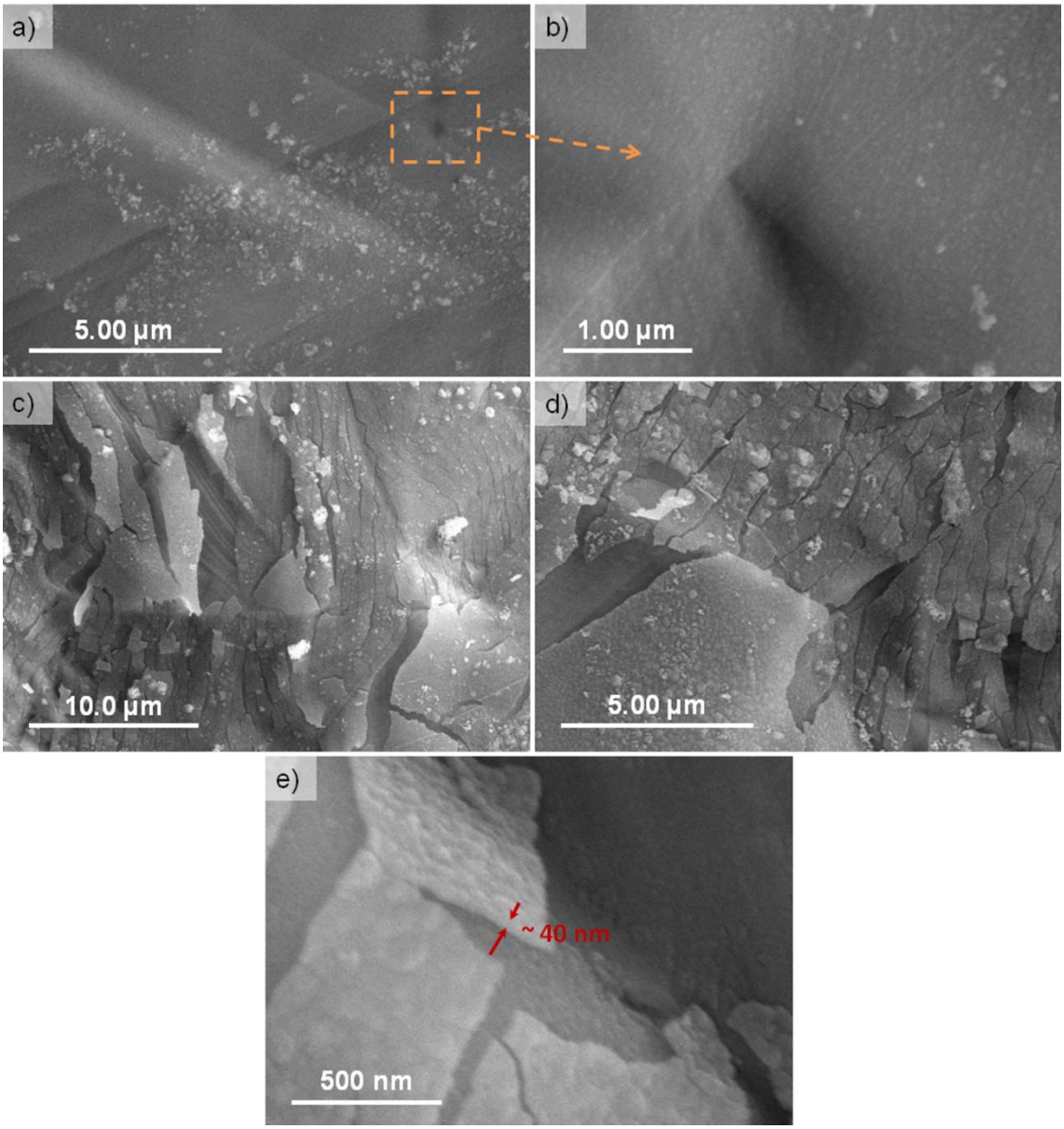

Figure 4.40: SEM micrographs of films obtained from 1 g/L suspensions after 10 min EPD treated at a,b) 300 ºC and c-e) 500 ºC for 2h.

From these micrographs it can be observed that these films still present a very high packing density, with low porosity in them. In contrast to the previous case of lower solid contents, films treated at 300 ºC bent with the substrate and did not break, not even in defective areas as the one shown in Figure 4.41b. In this sense, only films treated at the higher temperature of 500 ºC fractured, showing a film thickness of about 40 nm (well below the value obtained by ellipsometry –see table 4.7b). Even though

this thickness seems higher than that observed for 0.1 g/L suspensions (of about 25 nm), it must only be considered as an estimation, as there is not enough resolution in the micrographs, and no real increase in thickness with the solids content can be stated.

4.2.3.2. Influence of the Interface on ZnO thin films growth and ordering in aqueous EPD under mild conditions.

In order to clarify the reason for the low deposited masses, the theoretical approximation of the deposition kinetics was studied for F-ZnO powders. This study was carried out applying the approximation developed by Sarkar and Nicholson to the Hamaker equation,

$$m(t) = m_0(1 - e^{-t/\tau}) \qquad \text{(Eq. 4.10)}$$

where $m(t)$ is the mass deposited after a deposition time t, m_0 is the initial mass of the suspension, and τ, the characteristic time scale of the system, which is defined as

$$\tau = V / f\mu SE \qquad \text{(Eq. 4.11)}$$

where V is the volume of suspension, μ the electrophoretic mobility, S the deposition area and f the efficiency factor or “sticking parameter”. The reasons for choosing this equation amongst the different models for the kinetics of EPD were several: on the one hand, it was one of the first models to consider changes in particle concentration during EPD. Most important is the fact that under certain conditions, all subsequent models can be reduced to this one [136]. In addition, the characteristic time of the system, τ, is directly related to the kinetics, as its inverse value is the kinetics parameter, k. Thus, the higher the value of τ, the slower the deposition will be. In this sense, applying this equation and considering an efficiency factor of 1, the maximum theoretical mass that could be deposited under the applied electrical conditions was calculated. It must be noted that the electric field considered, E, was the average initial electric field, $E_{t=0}$, mentioned before. Figure 4.41a shows the graphical representations of the theoretical approximations to the kinetics of EPD from 0.1 g/L deposited on ITO and electropolished stainless steel (ESS) substrates, and of 1 g/L suspensions deposited on ITO-coated glass substrates. The experimental deposited masses, determined by UV-Vis and ellipsometry for 0.1 g/L suspensions and by direct weighing for 1 g/L suspensions, have also been represented (Figure 4.41b).

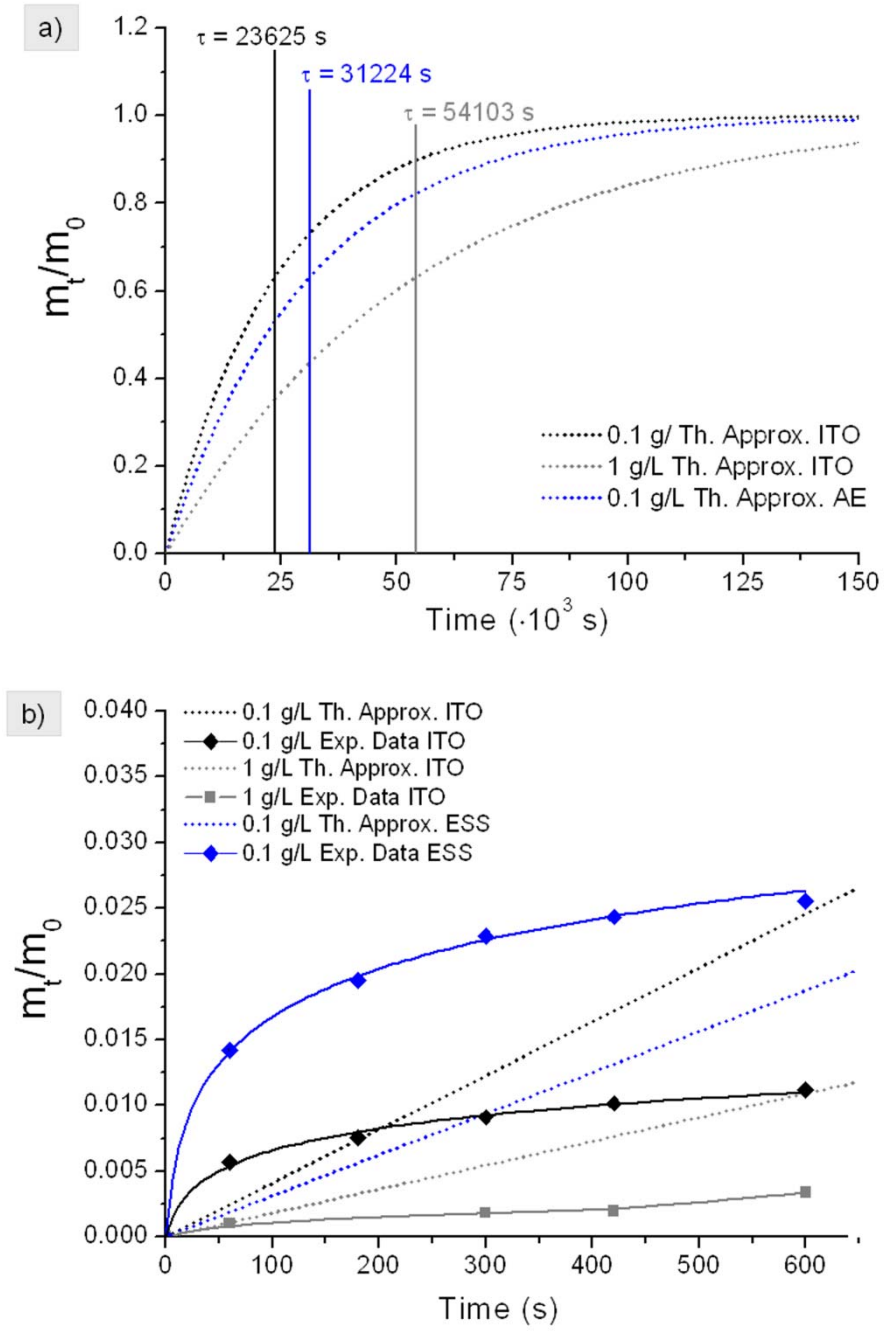

Figure 4.41: Theoretical and experimental approximation of the EPD kinetics of ZnO-F 0.1 and 1 g/L suspensions deposited on ITO and ESS substrates. The graph also shows the experimental masses normalized to the initial mass of powder in suspension.

Theoretical approximations were calculated considering the data summarized in Table 4.11, i.e the volume, V, the electrophoretic mobility, μ, and the surface of deposition, S, of each system (Table 4.3) and the electric field, $E_{t=0}$, registered for t=0 during the EPD tests (Figures 4.21 and 4.29). These data correspond to the starting conditions of the systems. Table 4.11 also collects relevant characteristics of the work electrode surface.

Table 4:11: Summary of the data used for the calculation of the theoretical approximations and of the characteristics of the electrode surface.

System Parameters	FITO-01	FITO-1	FESS-01
Parameters used to determine the time constant, τ			
Volume, V (mL)	30	30	30
Electrophoretic mobility, μ_e ($cm^2/V{\cdot}s$)	$2.28{\cdot}10^{-4}$	$2.28{\cdot}10^{-4}$	$2.28{\cdot}10^{-4}$
Electric Field (V/cm)	1.41	0.76	0.86
Geometric conduction area, (cm^2)	3.9	3.2	4.9
Calculated time constant, *τ*	23625	54103	31224
Parameters describing the electrochemical behavior			
Roughness R_c (nm)	5.2	5.2	11.6
Roughness R_a (nm)	1.1	1.1	2.7
Roughness R_{ku} (nm)	-	-	11.2
Substrate resistance (Ω·cm)	30	30	$1.5{\cdot}10^{-3}$

From the graphical representation in Figure 4.41 it can be observed that the set conditions gave place to very slow depositions, with very high time constants, τ (Fig. 4.41a). The figure shows how the increase in solid contents for ITO substrates slowed down the deposition, increasing the value of τ from 23625 (6.5 h) to 54103 s (15 h), and decreasing the calculated electrophoretic velocity, $v{=}\mu{\cdot}E$, from $3.2{\cdot}10^{-4}$ to $1.7{\cdot}10^{-4}$ cm/s. From a practical point of view, it can also be inferred from the figure that the maximum theoretical mass that could be deposited from 0.1 g/L suspensions considering the longest deposition times (600 s) corresponds to a 2.5 % of the total mass (Figure 4.41b). Similarly, the theoretical yield of suspensions with higher solid contents was only a 1.1 **%** of the total mass in suspension. In fact, the deposition yield was extremely slow because in 600 s particles were only able to cover distances of 1 - 2 mm.

Although the mild EPD electrical conditions were selected in order to promote the ZnO-F ordering during the film growth on ITO, in general the massive theoretical results were far for the experimental ones. Analyzing the representation of the experimental data (Fig. 4.41b) it can be observed that the experimental yields were below the theoretical ones for ITO coatings, except for the very first stage of deposition (t < 180 s) for 0.1g/L suspensions. Taking into consideration the data from 0.1 g/L suspensions (Table 4.7a), where the deposited mass for 600 s of deposition was of 8.5 - 8.7 μg/cm^2, the maximum deposited mass in this system corresponds to a 1 % of the total mass in suspension, that is approximately 40 % of the deposition expected

theoretically. For depositions from 1 g/L suspensions the experimental kinetics is even lower, being the maximum experimental deposited mass of 31.6 μg/cm^2 (Table 4.7b), i.e. a 0.3 % of the total mass in suspension and thus a ~30 % of the deposition expected theoretically.

For both solid contents, deposition seemed to take place very quickly for short times (< 70 s), with experimental values in range or even over the theoretical approximation. However, this behavior only lasts for deposition times up to 180 s and 60 s for 0.1 and 1 g/L solid contents, respectively, time after which the deposition rates seem to remain constant with increasing deposition time.

Plot in Figure 4.41 also shows how the theoretical predicted deposition of 0.1 g/L suspensions on ESS substrates was slower than that on ITO substrates, as the values of the time constants increased from 23625 s (6.5 h) on ITO, to 31224 s (8.7 h) on ESS. These high time constants are mainly due to the low electric fields applied. Variations in the conduction surface are the cause of the dissimilar electric fields applied when comparing deposition on ITO and ESS for a similar suspension (Figures 4.21 and 4.29). In fact, the conductive surface of the ESS substrates almost doubles geometrically of those used for ITO, whereas nano-roughness was also double (see Figure 4.19).

The slowing down of the deposition with the change of substrate was also patent in the calculated electrophoretic mobilities, which decreased from $3.2 \cdot 10^{-4}$ cm/s for ITO coatings to $1.9 \cdot 10^{-4}$ cm/s for the films grown on ESS. Thus, under the applied conditions, the maximum theoretical mass that could be deposited on ESS considering the longest deposition times (600 s) corresponded to a 1.9 % of the total mass in suspension. However, analyzing the experimental values it can be observed that experimental mass data was much higher than the theoretical values. In fact, the maximum experimental mass that was actually deposited corresponded to a 2.5 % of the total mass in suspension, i.e. 73 μg. These results point out to values of the efficiency or sticking factors, f, (see eq. 4.10) above 1.

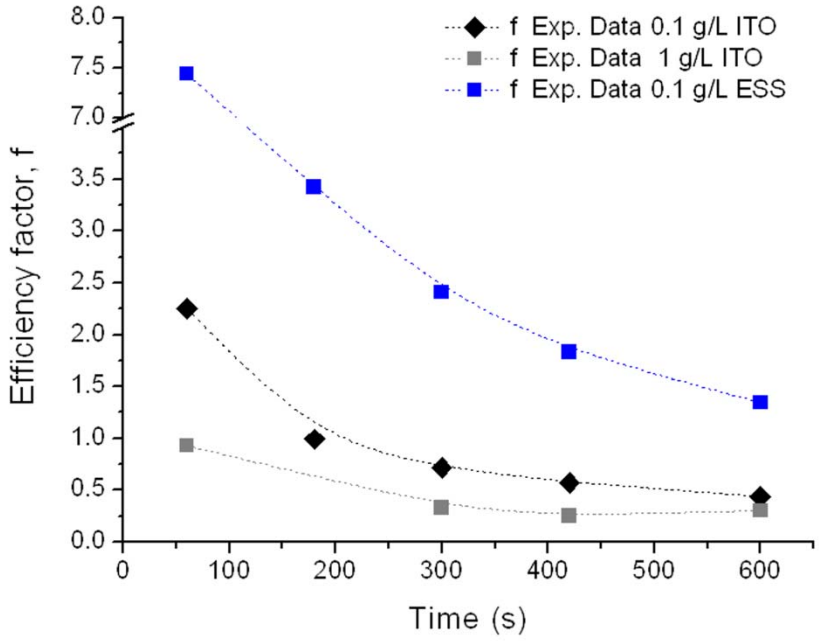

Figure 4.42: Evolution of the sticking factors, f, with deposition time.

Therefore, analyzing the sticking factors, whose evolution with time for the three systems is plotted in Figure 4.42, we can verify that their values were mainly over 1 for low solid loadings (0.1 g/L) and short deposition times for ITO-coatings, and over 1 for all deposition times on ESS. Moreover, a similar trend in the evolution of the sticking factor in all systems can also be observed, which decreased with time for both substrates. However the values decreased down to 1.5 for ESS substrates, whereas values as low as 0.2 were achieved on ITO for both ZnO concentrations.

Taking all these data into account, it can be noticed that with the change of substrate, deposition was enhanced for low solid content suspensions. Given the more conductive nature and the larger surface of conduction of the ESS substrates compared to ITO ones, deposition yield was improved. The decrease of the sticking factor can be ascribed to the dense film formed by the smaller particles of the ZnO-F powders (see Figure 4.28). Consequently, in all three systems the process seems to be blocked due to the formation of a dense ZnO-F film (with densities up to 98.9 %, Table 4.7a) which has been described by HR-TEM (Figure 4.27).

The formation of this dense ZnO-F film at the initial stage of deposition was verified by observing in the FE-SEM a sample deposited after 60 s (FESS-01-1) treated at 300 ºC for 2 hours and bent. As can be observed in the FE-SEM micrograph in Figure 4.43, the film in the sample showed the same “monolayer” appearance as the films obtained after longer deposition times (see Figure 4.39). It must be noted, though, that these

layer were much thicker than those deposited on ITO substrates (Figure 4.26), which were transparent to the electron beam, or to those observed in the HR-TEM (Figure 4.27).

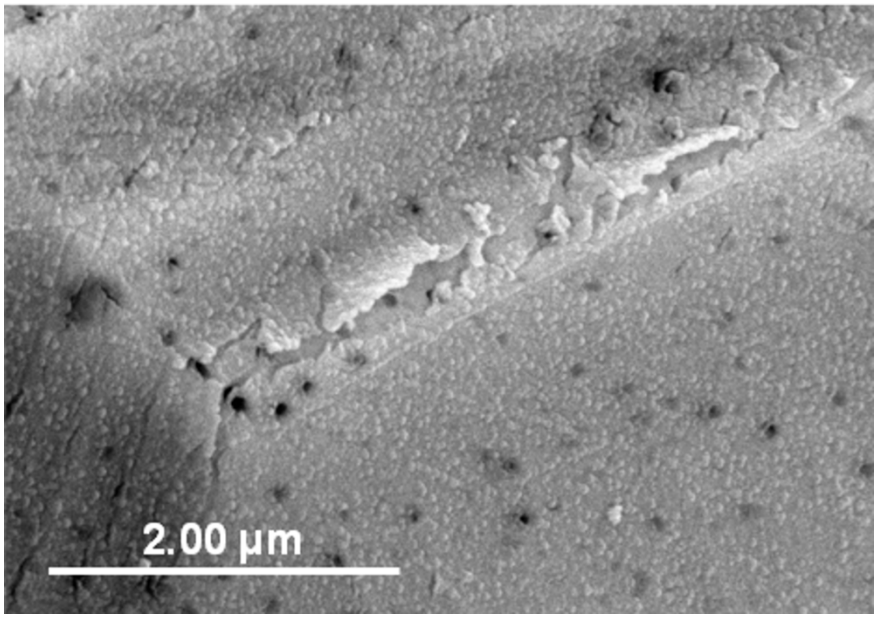

Figure 4.43: FE-SEM micrograph of the FESS-01-1 sample treated at 300 ºC/2h and bent.

Regarding the mismatch between the theoretical approximation and experimental results, it is important to note that equation 4.10 mainly considers parameters related with the electrophoresis of the particles (the volume of suspension, the electrophoretic mobility and the electric field) whereas the considered conduction area was calculated geometrically. Consequently, surface characteristics such as roughness and/or electrochemical affinity were neglected, and the effect of relevant phenomena such as the surface charge magnitude and distribution are not reflected in this approximation. On the other hand, the significance of the electrode surface characteristics predominates over other parameters at the nanoscale under mild electric conditions.

Considering the large differences in deposition for low solid contents (0.1 g/L suspensions) when different substrates were used, the effect of the increase in solid contents (1 g/L suspensions) was studied for ITO, ESS and as-received Ni substrates, in order to establish the extent of the effect of the electrode surface under mild electric conditions in aqueous media. As-received Ni foils were considered as substrates so as to evaluate a substrate with better electrochemical affinity (lower electrical conductance) and higher roughness. Table 4.12 summarizes the most relevant parameters for the deposition of 1 g/L suspensions onto different substrates, whereas

Table 4.13 summarizes those parameters used for the calculations of the theoretical approximations to the kinetics and the most relevant characteristics of the substrates.

Table 4.12: Summary of the parameters used for the deposition on different substrates.

System parameters	FITO-1	FESS-1	FNi-1
Parameters of the suspension			
Volume (mL)	30	30	30
Initial mass, m_0 (mg)	30	30	30
pH (t=0)	7.5	7.5	7.5
Electrophoretic mobility, μ_e ($cm^2/V{\cdot}s$)	$2.28 \cdot 10^{-4}$	$2.28 \cdot 10^{-4}$	$1.27 \cdot 10^{-4}$
Conduction Area (cm^2)	3.2	2.4	3.9
Intensity, I(μA)	100	100	250
Distance between electrodes, L (cm)	2	1	2

Table 4:13: Summary of the data used for the calculation of the theoretical approximations and of the characteristics of the electrode surface for 1 g/L suspensions.

System Parameters	FITO-1	FESS-1	FNi-1
Parameters used to determine the time constant, τ			
Volume, V (mL)	30	30	30
Electrophoretic mobility, μ_e ($cm^2/V{\cdot}s$)	$2.28 \cdot 10^{-4}$	$2.28 \cdot 10^{-4}$	$1.27 \cdot 10^{-4}$
Electric Field (V/cm)	0.76	0.82	0.90
Geometric conduction area, (cm^2)	3.2	4.8	7.8
Calculated time constant, *τ*	54103		
Parameters describing the electrochemical behaviour			
Roughness R_c (nm)	5.2	11.6	26.5
Roughness R_a (nm)	1.1	2.7	6.0
Roughness R_{ku} (nm)	-	11.2	2.8
Substrate resistance (Ω·cm)	30	$1.5 \cdot 10^{-3}$	$2.0 \cdot 10^{-4}$

Note that Ni substrate presented a lower resistivity ($2 \cdot 10^{-4}$ Ω/cm) than the previous substrates when measured by the four point probe method, and a higher roughness as can be observed in the AFM and FE-SEM micrographs in Figures 4.19 and 4.20: the topography of the Ni substrate showed a mean height of 26.5 nm and a R_a of 6.0 nm, more than twice that of the ESS substrate. In addition, the R_{ku} pointed out to a bumpy surface. All these data imply that the effective conduction area of the Ni substrate will

be much larger than those of the other substrates and larger than the geometric conduction area too.

Figure 4.44 shows the theoretical approximations to the kinetics (a) and the details of the early deposition (for times < 600 s).

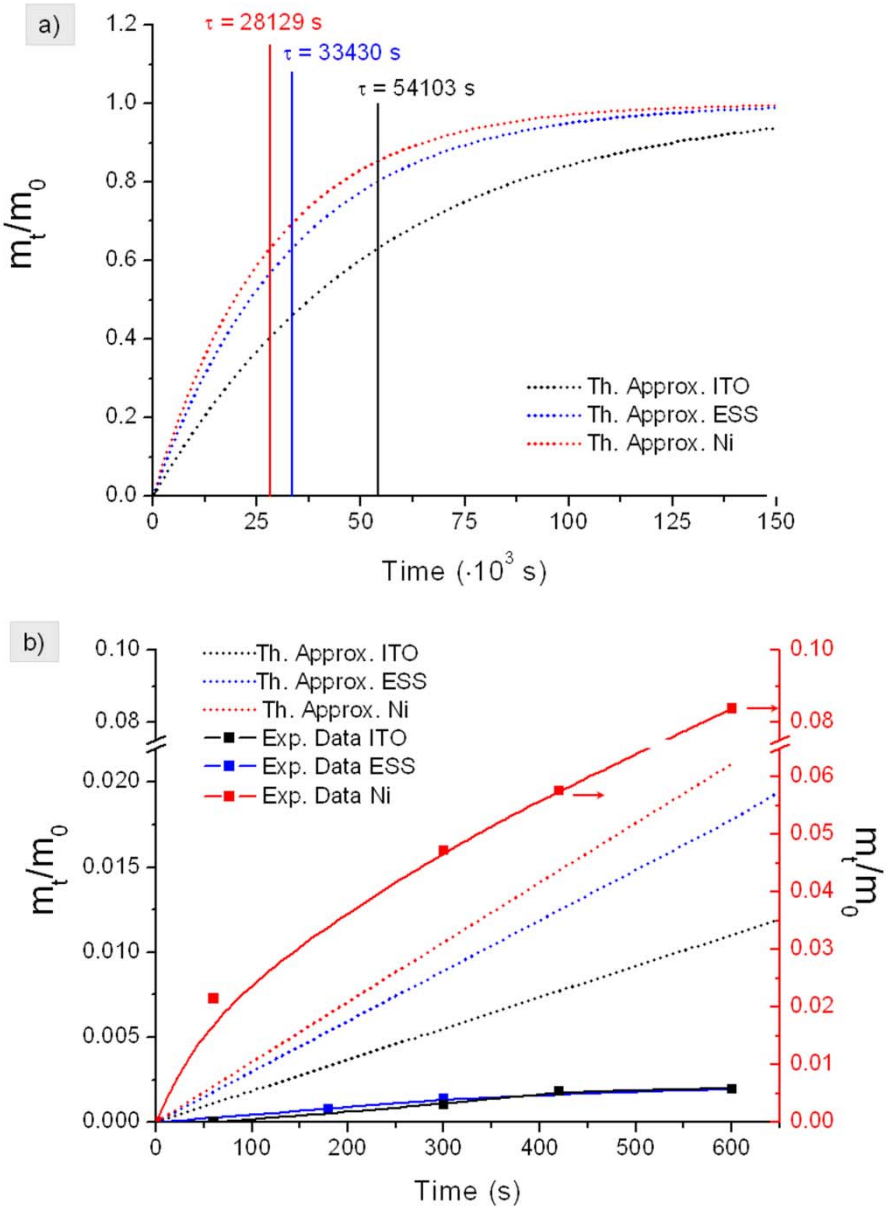

Figure 4.44: Theoretical and experimental approximation of the EPD kinetics of ZnO-F 1 g/L suspensions deposited on ITO, ESS and Ni substrates. The graph also shows the experimental masses normalized to the initial mass of powder in suspension. Note that in b), the experimental data for Ni is referred to the right axis, whereas the remaining data, both theoretical and experimental, are referred to the left axis.

Figure 4.44a shows how in agreement with the suspensions conditions, the deposition rate should be higher for deposition in metal substrates. However, experimental results in Figure 4.44b demonstrate that the coating growth dramatically

steps up on Ni substrates, largely surpassing the theoretical expectations. These results verified the relevance of the phenomena taking place of the interface, which govern the electrophoretic deposition of ZnO-F particles in this system.

The FE-SEM micrographs in Figure 4.45 show a highly dense nanostructured film of F-ZnO particles with ZnO clusters dispersed on top. The packing of the particles in the film was extremely high, with no detectable porosity, not even in the fractured pieces. Moreover, from the crack shown in the first micrograph it can be noted that the thickness of this film was higher than a monolayer. This increase in film thickness can be ascribed to both the increased conductivity and roughness of the substrate, which provided a vast number of points with field accumulation in which deposition was favored.

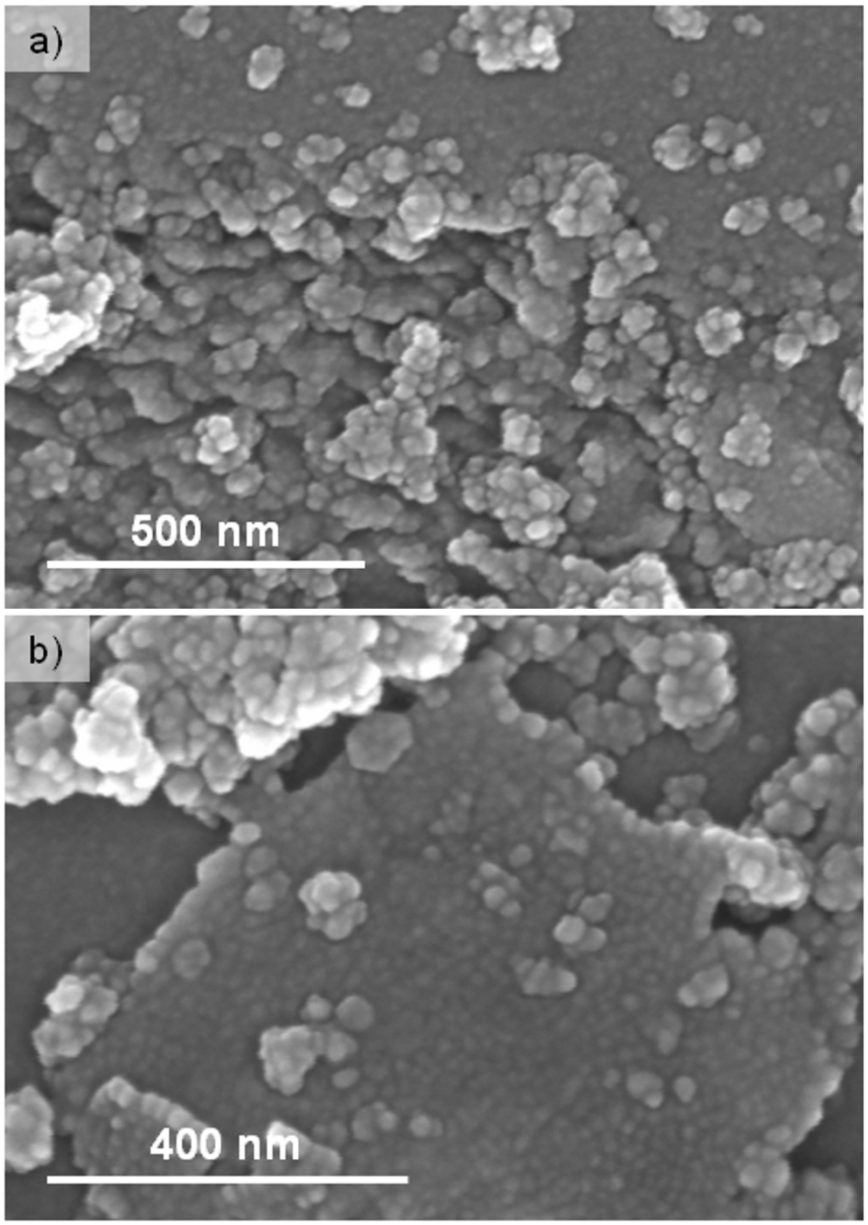

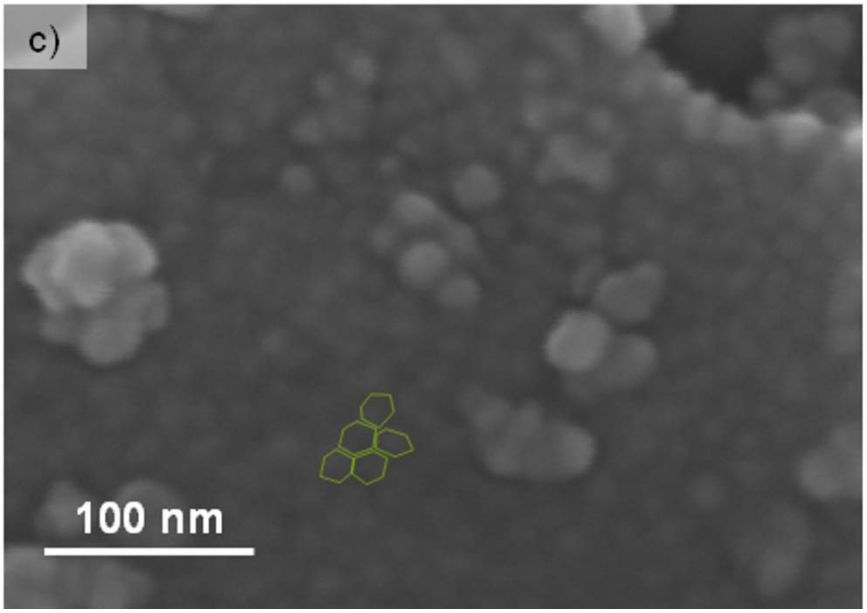

Figure 4.45: SEM micrographs of the film deposited from a 1 g/L suspension on a Ni substrate.

On the other hand, massive deposition of ZnO-F particles did not disturb ordering, as a clear, dense and well packed structure can be observed in the detail in micrograph 4.45c. In fact Figure 4.46 shows the macroscopical translucent coating of the Ni substrates.

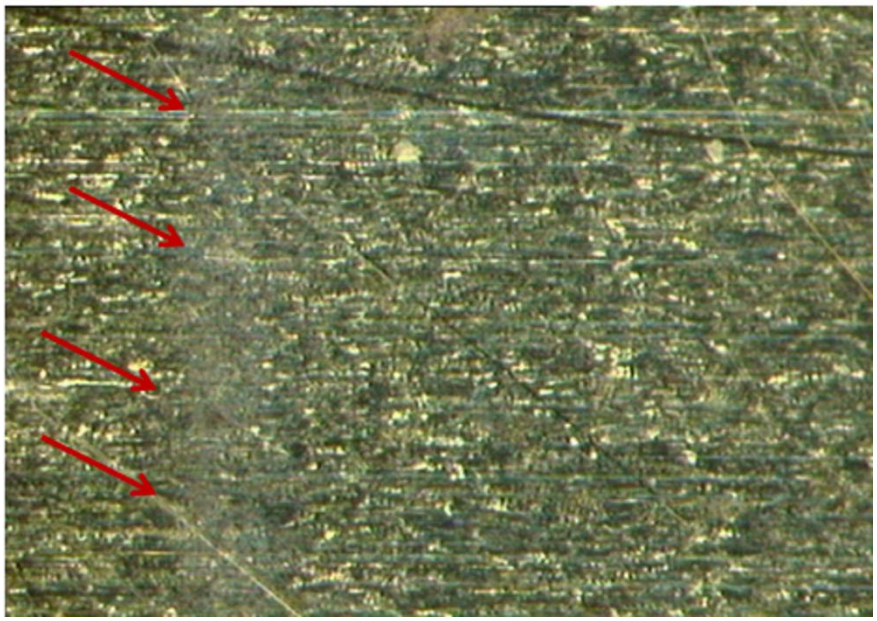

Figure 4.46: Optical micrograph of the Ni substrate coated with a ZnO-F film deposited from a 1 g/L suspension. The arrows point to the border of the ZnO film, which coats the area to the right.

4.2.4. Electrophoretic deposition of ZnO-NC powders.

ZnO-NC suspensions for EPD were prepared applying the optimized parameters for particles dispersion and stabilization described in section 4.1.1. The conditions of these suspensions are summarized in Table 4.14.

Table 4.14: ZnO-NC EPD suspensions conditions.

Powder / Medium	Cc (g/L)	Dispersant	pH	d_{V50}	μ_e ($cm^2/V{\cdot}s$)
ZnO-NC / H_2O	0.1-1	1.5 wt.%PEI (Mw = 25000)	6< pH<8	45 nm	$2.54{\cdot}10^{-4}$

EPD was carried out in the same conditions as those used for the ZnO-F powders and deposition times of 600 s, using ITO-coated glass and ESS substrates.

The conditions used for the deposition on ITO and ESS substrates were the same as those used for ZnO-F powders (see Tables 4.3 and 4.8), with the exception of the geometric conduction areas, which in this case were of 3.8 and 5 cm^2 respectively . The obtained E vs. time curves are shown in Figure 4.47.

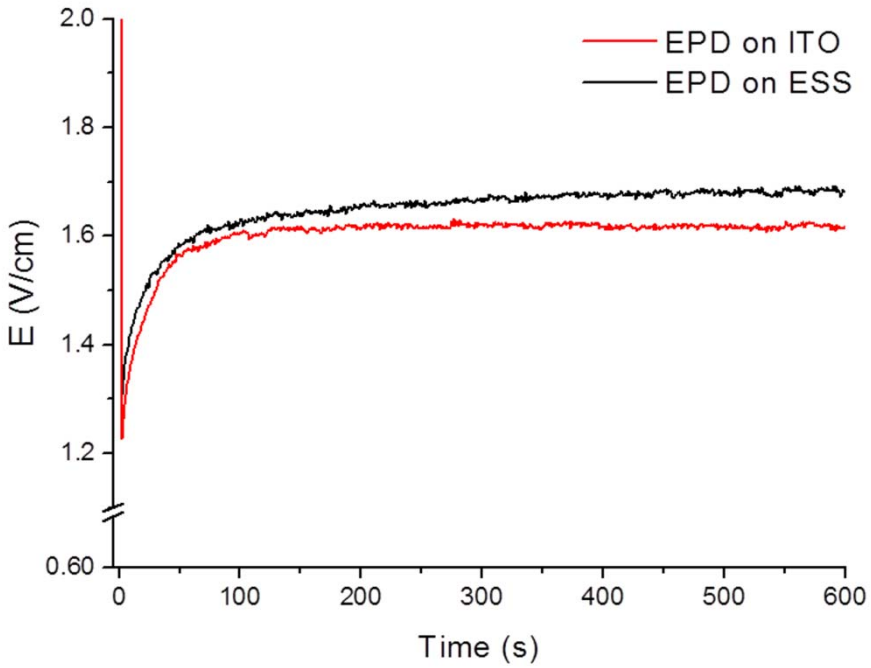

Figure 4.47: Electric field vs. deposition time curves recorded for the deposition of 0.1 g/L ZnO-NC suspensions on ITO and electropolished stainless steel (ESS) substrates.

From the curves in the figure it can be noted that the fields applied in this case are in range with those applied to ZnO-F suspensions (see Figures 4.21a and 4.29a). As observed in the case of ZnO-F powders, the electric field remained constant for times

above 60 s when depositing on ITO, whereas a slight increase of the field with deposition time could be observed for deposition on stainless steel substrates.

Films deposited on ITO substrates applying these conditions were characterized by ellipsometry. The obtained thicknesses varied between 58 and 65 nm, with refraction indexes of 1.60-1.65, which correspond to densities over 100 % (referred to the density of ZnO-NC powders: 3.3 g/cm^3). These results pointed out to a deposition comparable to those obtained in similar conditions from 0.1 g/L suspensions of ZnO-F powders (Table 4.7), which had densities ranging from 78.9 to 98.9 %. In this case, the films were observable to the naked eye (Figure 4.48), though not as clearly as those obtained from 1 g/L suspensions of ZnO-F powders (Figure 4.22).

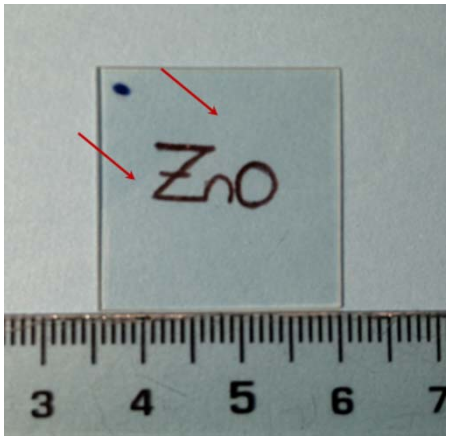

Figure 4.48: Photograph of a ZnO-NC film deposited on ITO from a 0.1 g/L suspensions and deposition conditions of 100 µA for of 10 min. The red arrows point to the limit of the ZnO-F film, which in this case is in diagonal.

In order to confirm the massive results, films were observed in the FE-SEM. Micrographs of the surface of the films (Figure 4.49) verified the deposition of ZnO-NC agglomerates on the surface of the ITO substrate.

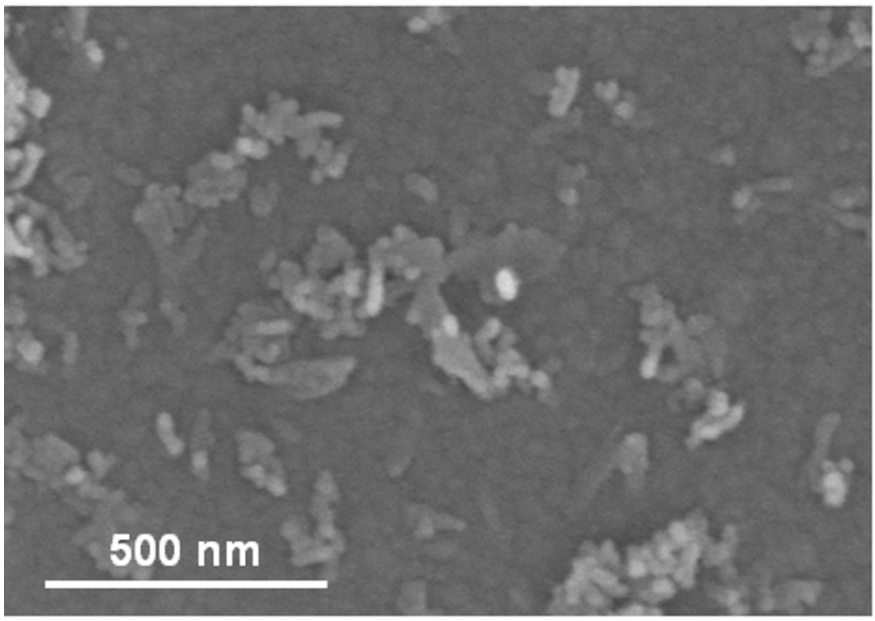

Figure 4.49: SEM micrograph of the ZnO-NC deposit on an ITO substrate.

Therefore, with the aim of verifying the cause of the apparently scarce deposition a test was carried out in which 0.1 and 1 g/L suspensions were deposited directly on HRTEM copper grids and characterized.

Films obtained from 0.1 g/L ZnO-NC suspensions had the appearance of weaved threads, as can be observed in the micrographs in Figure 4.50. In these micrographs it can also be observed how, in contrast to the results for the deposition of ZnO-F powders, in this case a continuous and homogeneous film was not obtained, as the ZnO-NC powders deposited forming “islands”.

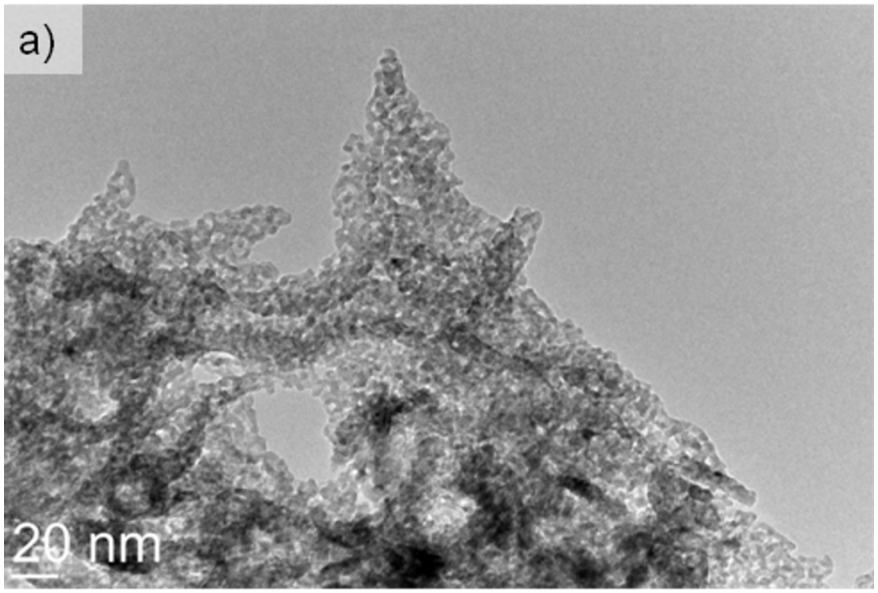

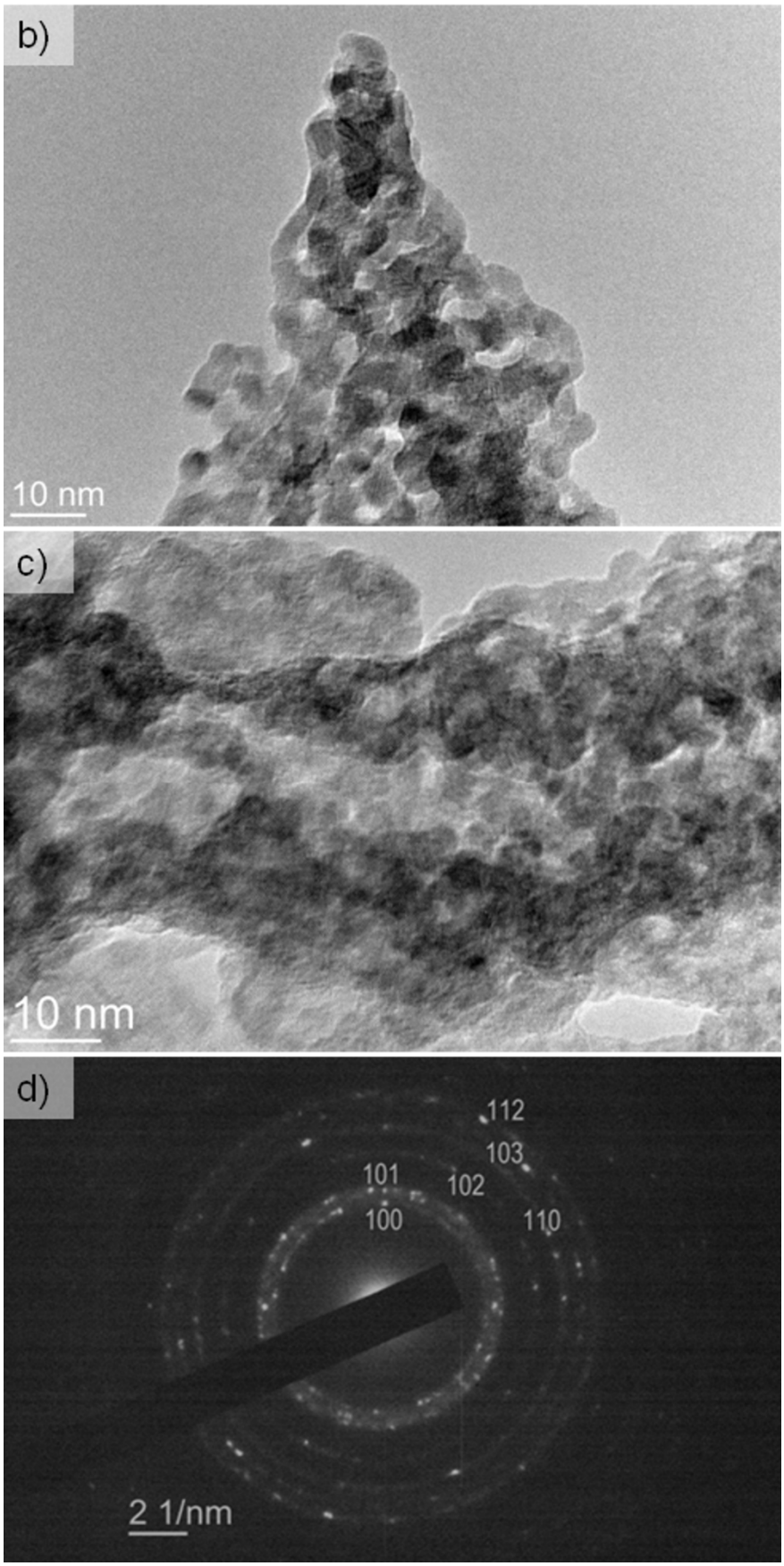

Figure 4.50: HRTEM micrographs and SAED analysis of ZnO-NC films deposited from 0.1 g/L suspensions.

Higher magnification of the films allowed observing that the thread-like structure was due to the presence of some rests of acetate (LBZA) species from the synthesis procedure, which acted as “glue”, sticking the small ZnO-NC particles together, forming agglomerates in the shape of threads. All this resulted in pieces of films which showed a much lower density and packing of the particles in it. The SAED diffractogram of these films however, showed no diffraction ascribed to these intermediate species (pointing out to their amorphous nature) and only low intensity diffraction rings and spots indexed to zincite were observed.

Increasing the solid contents to 1 g/L did not produce a notorious change in the structure of the films, which showed the same thread-like structure (Figure 4.51). In these films it could be clearly observed how the threads were composed of small, crystalline particles.

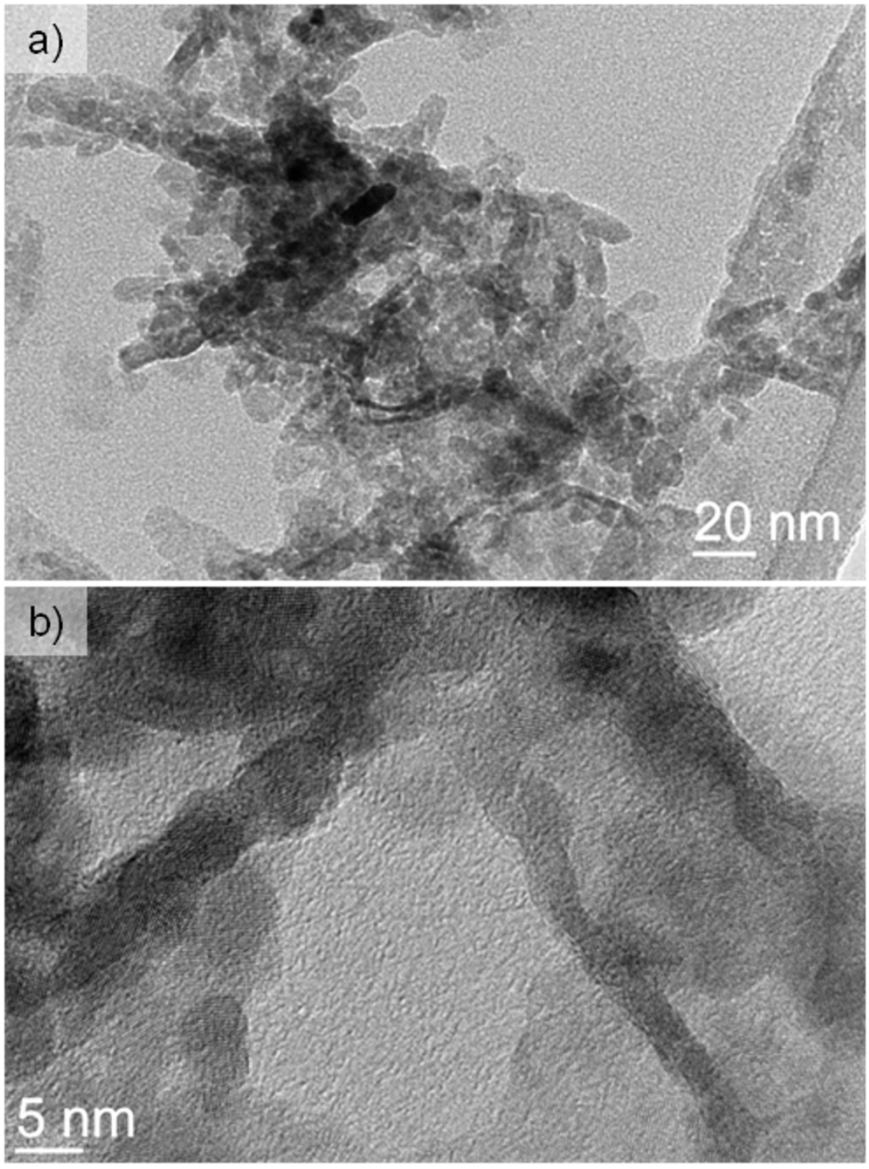

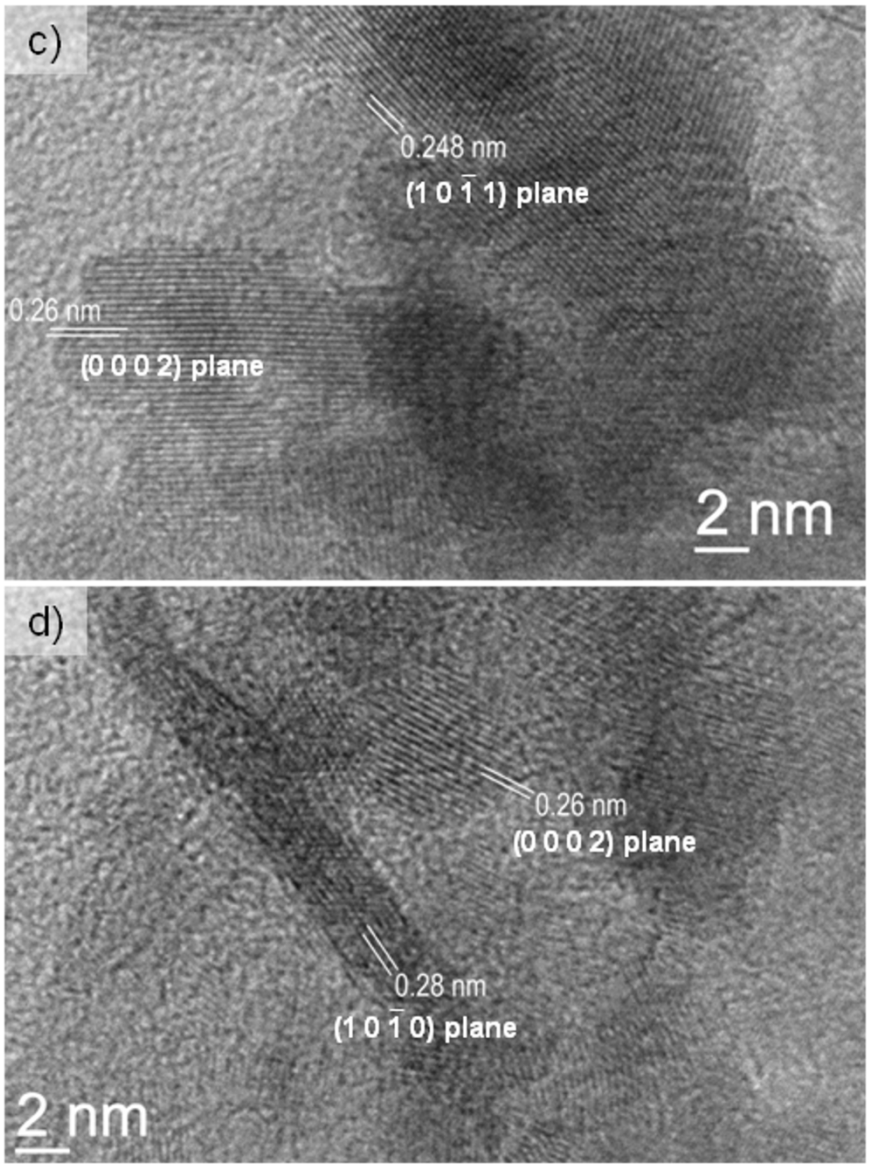

Figure 4.51: HRTEM micrographs of ZnO-NC films obtained from 1 g/L suspensions.

From these results it can be concluded that a homogeneous was not possible in this kind of substrates.

Thus, the films deposited on stainless steel substrates were characterized next. As for the films deposited on ITO substrates, these were visible to the naked eye, despite the low solid contents of the suspensions (Figure 4.52).

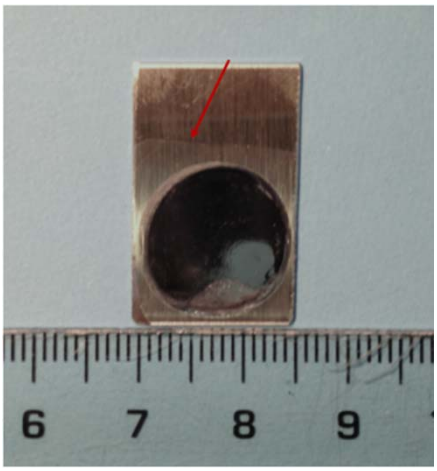

Figure 4.52: Photograph of a ZnO-NC film deposited on ESS from a 0.1 g/L suspensions and deposition conditions of 100 µA for of 10 min. The red arrow points to the limit of the ZnO-F film.

However, in contrast to the previous case, FE-SEM micrographs of these samples (Figure 4.53) showed very dense films of ZnO-NC particles with no porosity in them, and the presence of some larger agglomerates on the surface. Nevertheless, a closer observation of the packing of the particles in the films was hampered by the small size of the particles and the presence of the polyelectrolyte, which made the image blurry.

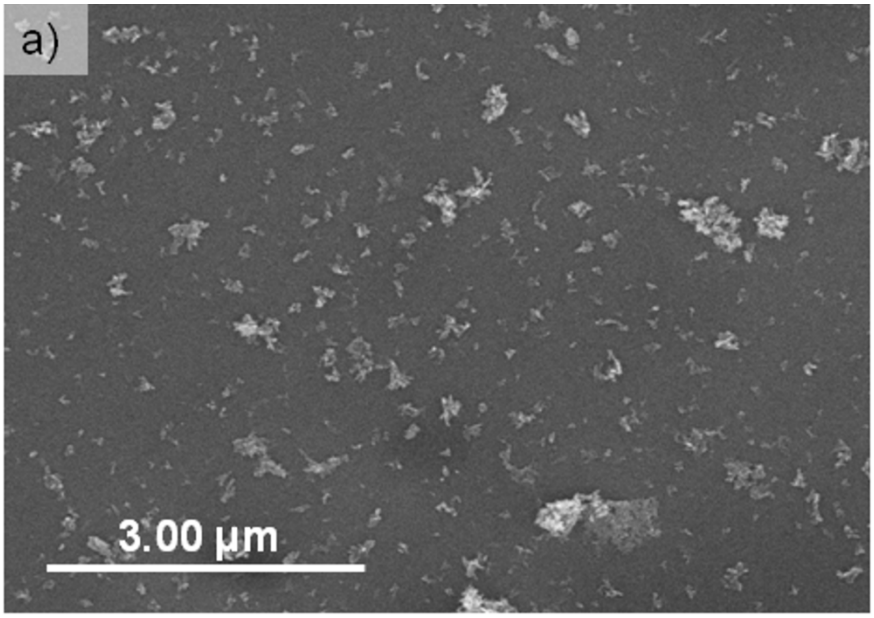

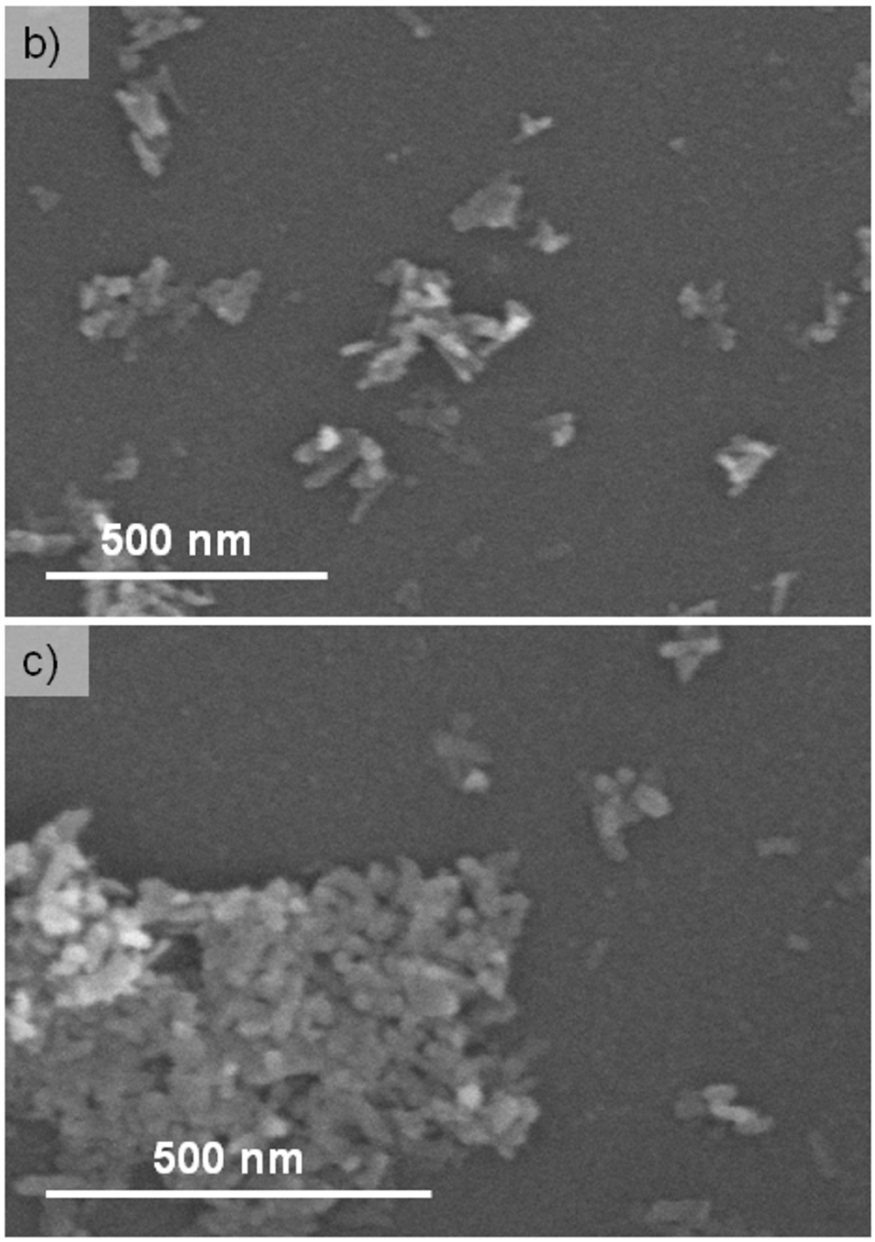

Figure 4.53: FE-SEM micrographs of ZnO-NC films obtained on electropolished stainless steel substrates after 10 min EPD at 100 μA.

These films were also characterized by AFM (Figure 4.54). In the AFM amplitude map it can be observed how these ZnO-NC films showed the same self-organized appearance as those obtained using ZnO-F powders (see Figure 4.37). Moreover, it can also be observed how the ZnO-NC particles maintained their identity in the densely packed film, showing very small particle sizes.

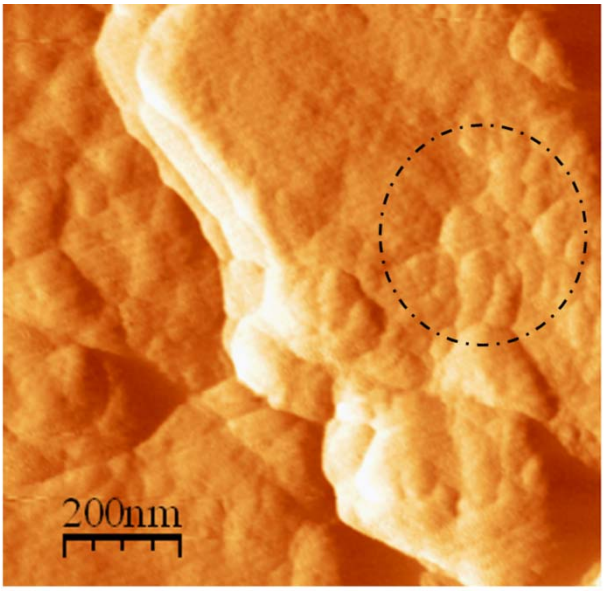

Figure 4.54: AFM amplitude map of a ZnO-NC film deposited on an electropolished stainless steel substrate after 10 min EPD at 100 µA.

In order to burn out some of the PEI which hampered a closer observation in the FE-SEM, the samples were treated at 300 ºC for 2 hours. The FE-SEM micrographs of the thermally treated films are shown in Figure 4.55. In these micrographs it can be observed how the films reproduce the defects in the substrate surface, such as lines and scratches. In this sense, the thermal treatment made the films more easily detectable, as it not only burnt part of the polyelectrolyte, but produced a slight coarsening of the particles. In any case, it must be noted, that, despite the coarsening the particle size of the ZnO-NC powders is well below 50 nm.

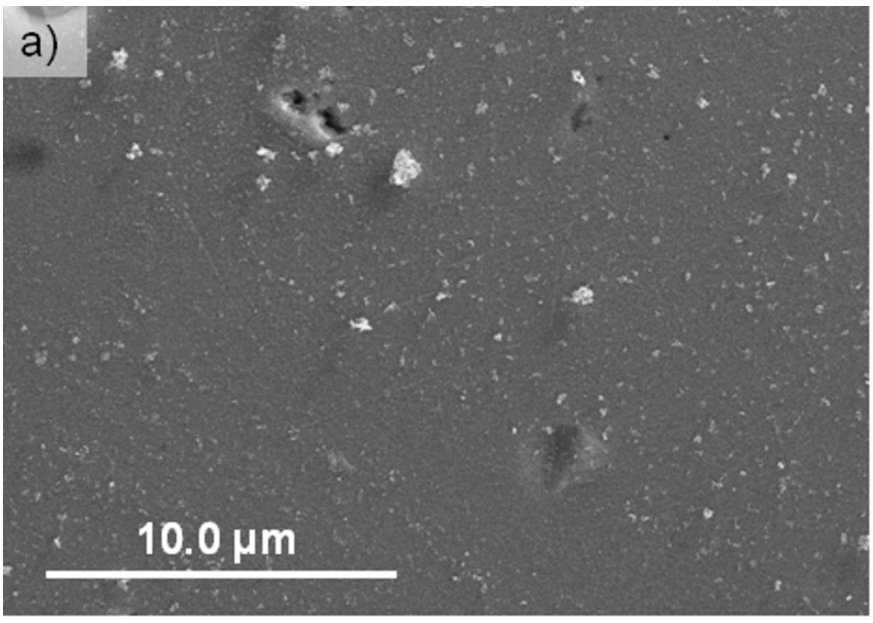

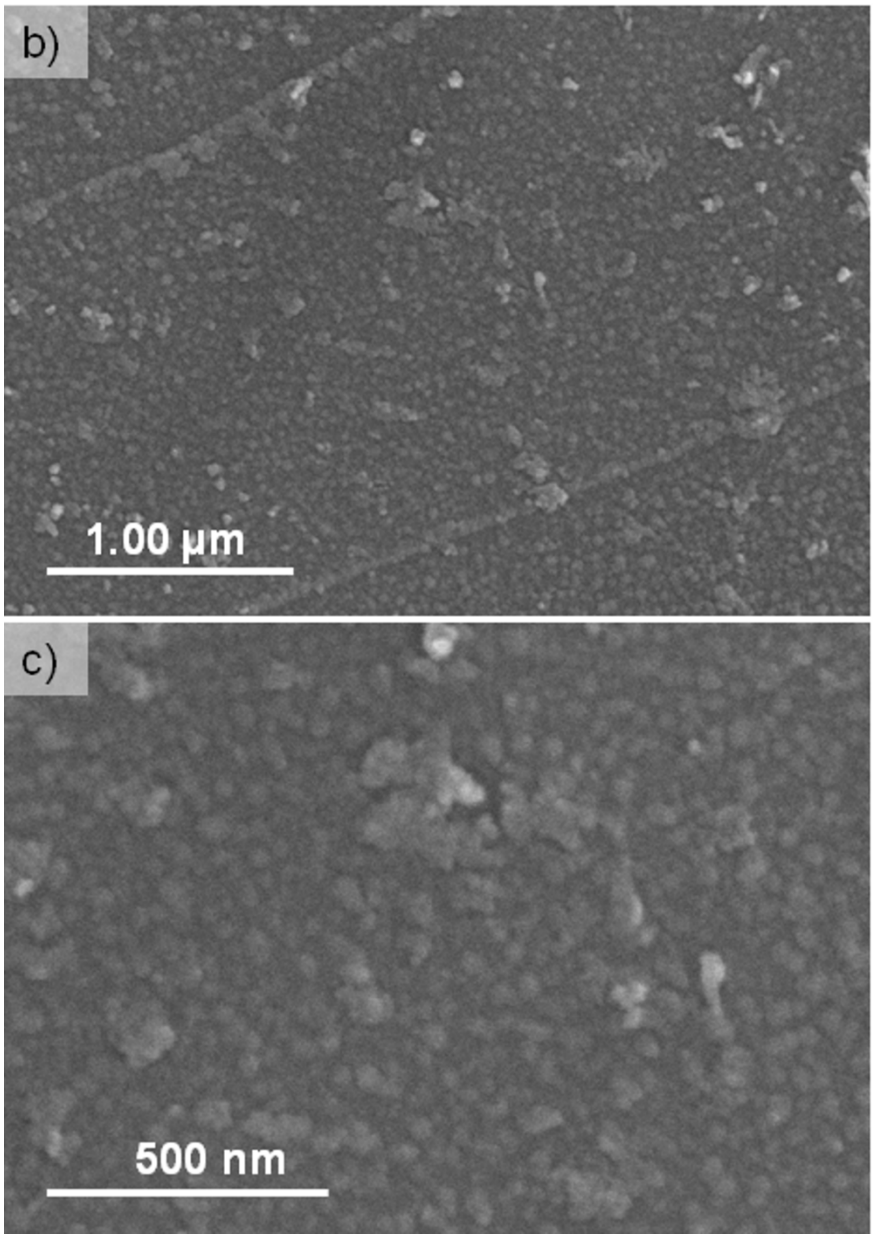

Fig. 4.55: FE-SEM micrographs of films obtained from 0.1 g/L ZnO-NC suspensions after a thermal treatment of 300 ºC for 2h.

Taking into account these results, it might be postulated that, as in the case of ZnO-F powders, a dense ZnO-NC film is formed for both substrates at the initial stage of the deposition, which is transparent to the electron beam, (and thus could not be observed until after the thermal treatment) and hampers further deposition.

4.3. Summary and Conclusions

In this chapter the colloidal chemistry and stabilization of the synthesized ZnO powders in aqueous suspensions and their shaping by EPD has been described.

For this purpose, in the first place the behavior of the powders surfaces was characterized by means of zeta potential and particle size measurements, observing that the different nature of the powders (described in Chapter 3) had an effect on both their behavior (with different isoelectric points) and their size (larger agglomerates were obtained for the better crystallized ZnO-F powders). Therefore surface modification with a cationic polyelectrolyte, PEI, was studied so as to extend and improve the stabilization and dispersion of the suspensions, necessary for their electrophoretic deposition. In this sense, it was found that a large PEI chain provided a better stabilization due to larger electrosteric effects.

EPD was carried out on several substrates with different conductivities and roughnesses, (ITO-coated glass, electropolished stainless steel and nickel substrates) and it was found that the conduction area of the substrates (dependent on their roughness) played a major role on the effective electric field, and thus on the deposition.

The use of ellipsometry and UV-Vis spectroscopy as indirect methods for the estimation of the deposited mass has been validated for films with thicknesses < 70 nm and masses < 35 μg/cm^2.

It was observed that a first layer of nanoparticles, which constituted a film with a remarkable packing density and transparency, was formed at the initial stage of deposition blocking its evolution, and hampering the obtaining of films thicker than 50 nm. A mechanism based on the preferential adsorption of PEI onto negatively charged ZnO-F facets, resulting in a jellyfish-like and its orientation due to the intrinsic polarity of ZnO and hydrodynamics near the electrodes surfaces was suggested as the cause for the formation of this dense layer. The remarkable density of the films was confirmed by the fact that they showed certain flexibility, as they could be bent without breaking, and that when they did break, after their consolidation (at temperatures up to 500 ºC) they broke in a “solidary” fracture.

The blocking of the electric field was not observed when using nickel foils, with higher conductivity and roughness, as substrates, and thicker films were deposited. These films, however, showed a larger amount of agglomerates on their surface.

The same blocking of the applied electric field was observed during the deposition of ZnO-NC suspensions. In this case, even though the formation of the dense film could not be observed in the HRTEM due to the presence of remaining acetates, it could be observed by FE-SEM after consolidation.

Chapter 5

Chapter 5: Obtaining of ZnO thick films

Up to now the synthesis of powders by (co)precipitation and their shaping by electrophoretic deposition have been studied. As seen in the previous chapter, the use of electrophoretic deposition as shaping procedure allowed a high microstructural control of the final films, which were remarkably dense, even in green (i.e. before sintering), and thin, with thicknesses of about 40 nm.

In this chapter, the obtaining of thicker films is addressed by several methodologies. In the first place by modifiying the EPD conditions, applying pulsed fields and using non-aqueous systems, and second by hydrothermal growth. In this second method the aim is not only to enlarge the films, but also to control their morphology by using seeded substrates.

5.1 Pulsed Electrophoretic Deposition.

In the previous chapter the obtaining of dense ZnO films was described. In it, the deposition was blocked soon after it began, due to the formation of very dense films. Therefore, in order to try and reactivate the deposition process, pulsed EPD from ZnO-F suspensions was carried out, as it has been reported that application of pulse current in a specific pulse condition permits higher current densities for longer times than the limiting direct current density, thus enabling deposits of fine-grained microstructure [132]. Ammam et al [239] reported that the advantages of pulsed direct current (PDC) over continuous direct current (CDC) included reduction of the coalescence between gas bubbles, reduction of the aggregation between nanometer sized and generation of a lower pH change near the electrode. These advantages arise from the fact that PDC modifies the conditions of the suspension-electrode interface, therefore affecting the different phenomena that take place in the surroundings of the electrodes surface. In this sense, the aim of applying PDC is to try to avoid the blocking of the deposition observed in the previous chapter due to the formation of a dense ZnO film at the initial stage of deposition, which acted as a capacitor, accumulating the electric field. The application of PDC might produce the “discharging” of the ZnO film during the times of zero current (i.e. off times) thus resetting the electrical conditions of the system and resuming the deposition process.

5.1.1 Pulsed Current EPD.

In order to carry out the pulsed EPD, ZnO-F suspensions with 1 g/L solid contents were prepared in the conditions described in Table 4.2. Pulse EPD was conducted on electropolished stainless steel substrates, applying a series of 10 one min pulses of dc current (of 100 μA) separated by periods of 1 or 10 seconds of off time. These two times were tested so as to try give time for the ZnO film to discharge.

The current and voltage vs. time curves obtained for each off time are shown in Figure 5.1.

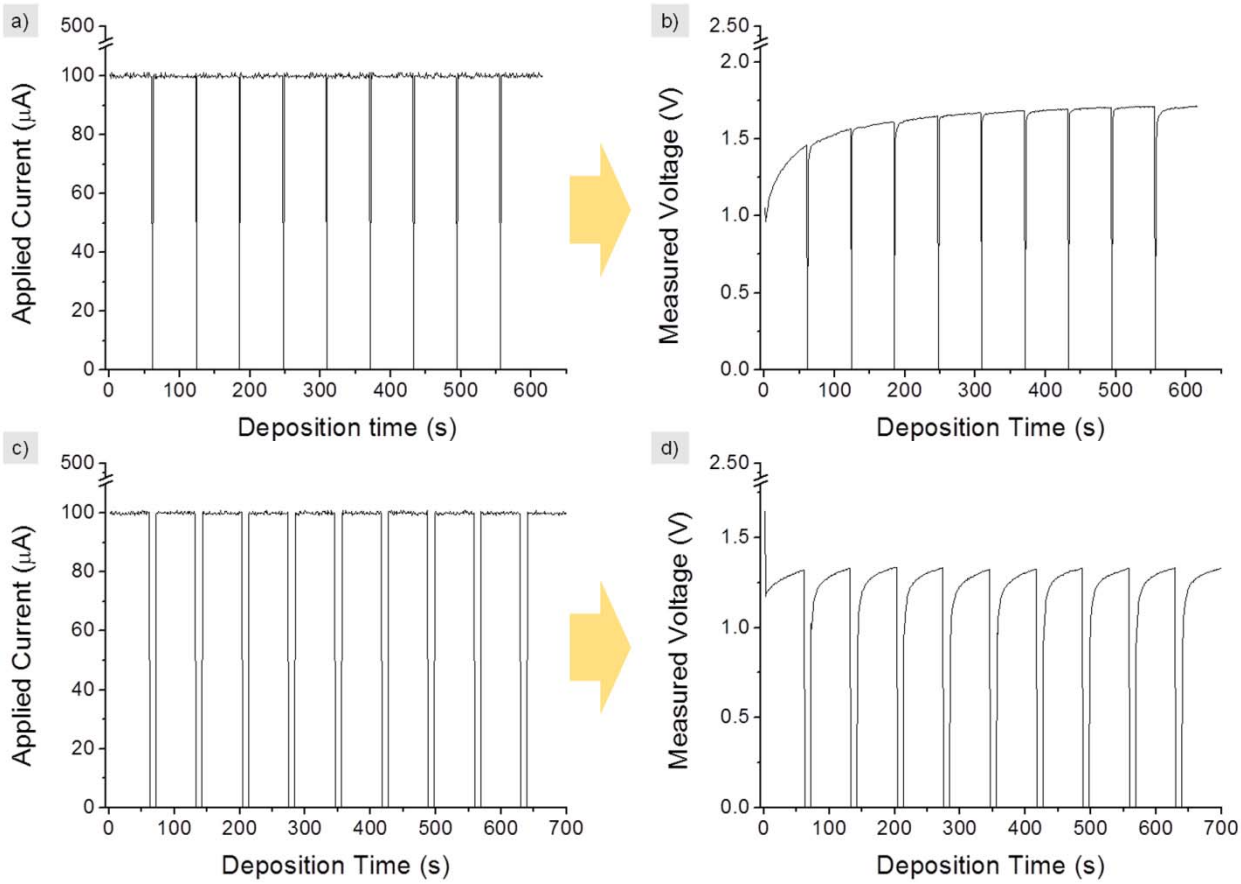

Figure 5.1: I-t curves showing the applied current pulses with off time =1 s (a) and t=10 s (c) and their corresponding V-t curves (b and d respectively).

In the graphs in the figure it can be observed how as in the previous case, the deposition is blocked after a short deposition time, as the measured voltage rapidly becomes constant and stops evolving. This effect is most notorious in the case of longer off times, where the evolution of the voltage is very small (barely 0.2V). From these graphs it can be inferred that the aim of “discharging” the ZnO film so as to resume the deposition was not achieved.

The deposited films were thermally treated at 500ºC for 2 hours in air and subsequently bent to facilitate their characterization by SEM. The micrographs in Figure 5.2 confirm the fact that films thicknesses remained in the same range, of about 40-50 nm, and particularly dense. Moreover, for those obtained with longer off times the ordered organization of the ZnO-F particles suggested in the previous chapter (see Figure 4.36) and observed in the films obtained with 1 s off times seems to be lost (Figure 5.2c and d). This loss might be ascribed to the agglomeration of the particles during the off-time and to the loss of the hydrodynamics due to the “intermittences” of the electric field.

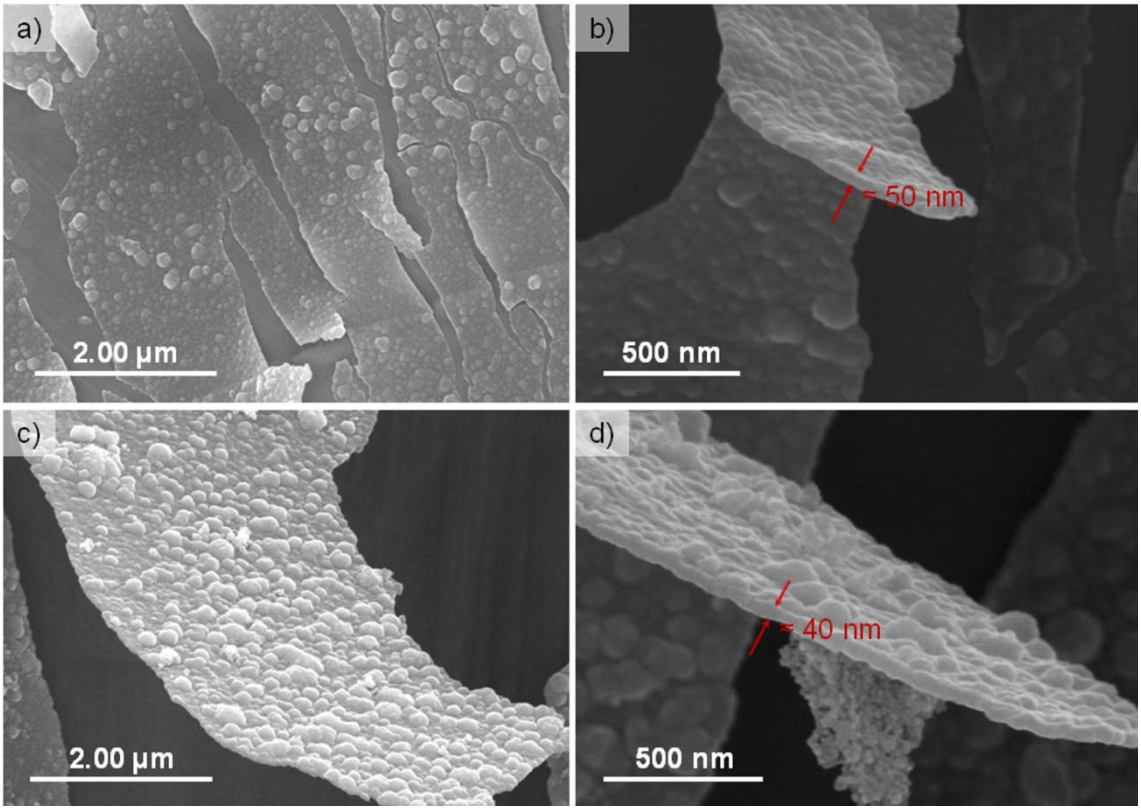

Figure 5.2: SEM micrographs of the films obtained applying pulsed current EPD with off times of a,b) 1s and c,d) 10 s. The films were thermally treated at 500 ºC for 2 hours and bent for their observation.

Taking into account these results, the same test was repeated, this time applying voltage pulses in order to verify if thicker films could be grown.

5.1.2 Pulsed Voltage EPD.

As in the previous case, series of 10 one min pulses, in this case of dc voltage (2 V) were applied, separated by periods of 1 or 10 seconds of zero voltage (Figure 5.3). From the graphical representations in Figure 5.3 it is clear that the field is blocked after

a short deposition time, as the measured current rapidly decreases and the application of new pulses do not seem to have an effect on it.

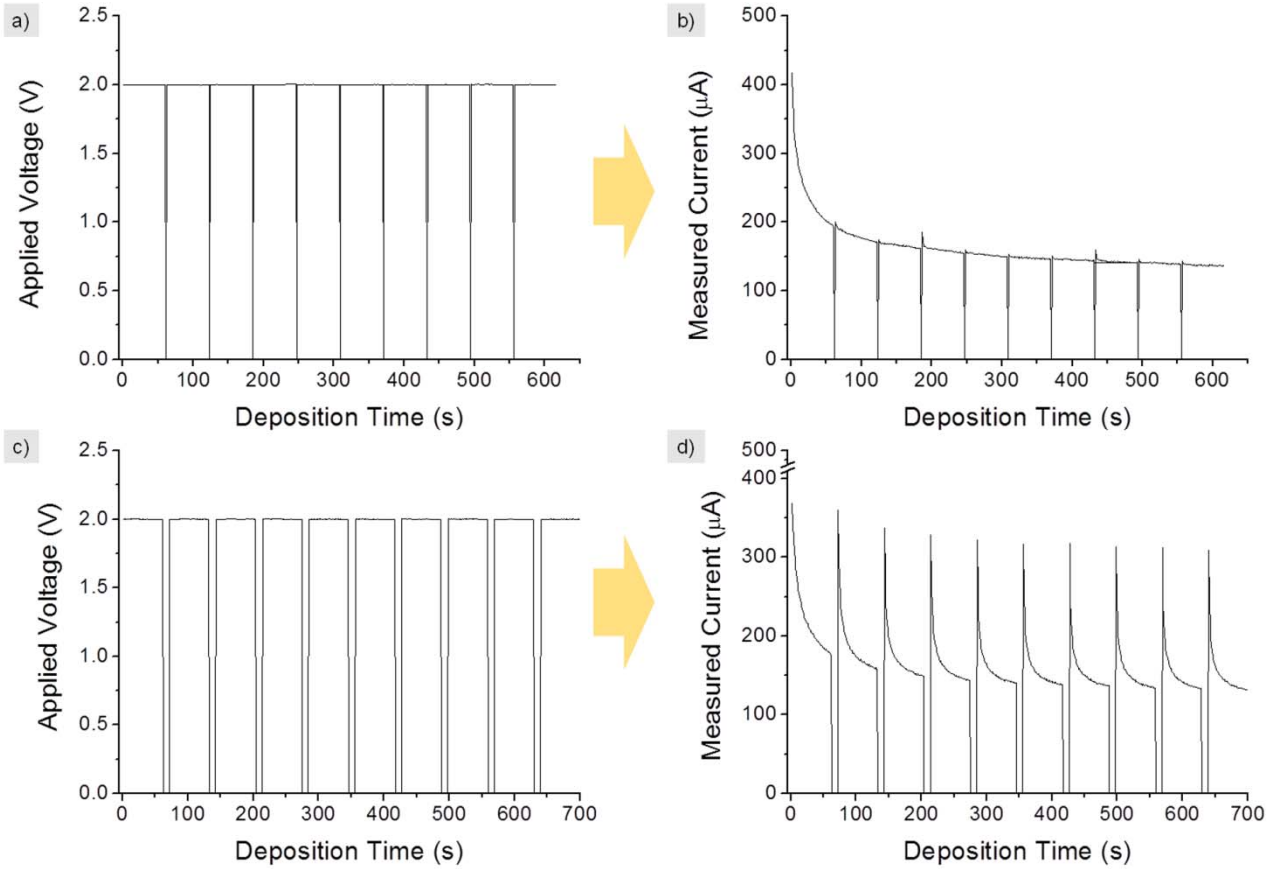

Figure 5.3: V-t curves showing the applied voltage pulses with off time =1 s (a) and t=10 s (c) and their corresponding I-t curves (b and d respectively).

The SEM micrographs of the thermally treated films confirm these results, showing thicknesses of about 50 nm (Figure 5.4). Moreover, it seemed that the application of pulses with slightly higher voltages than those obtained in galvanostatic conditions resulted in the obtaining of more homogeneous films, with a smoother texture.

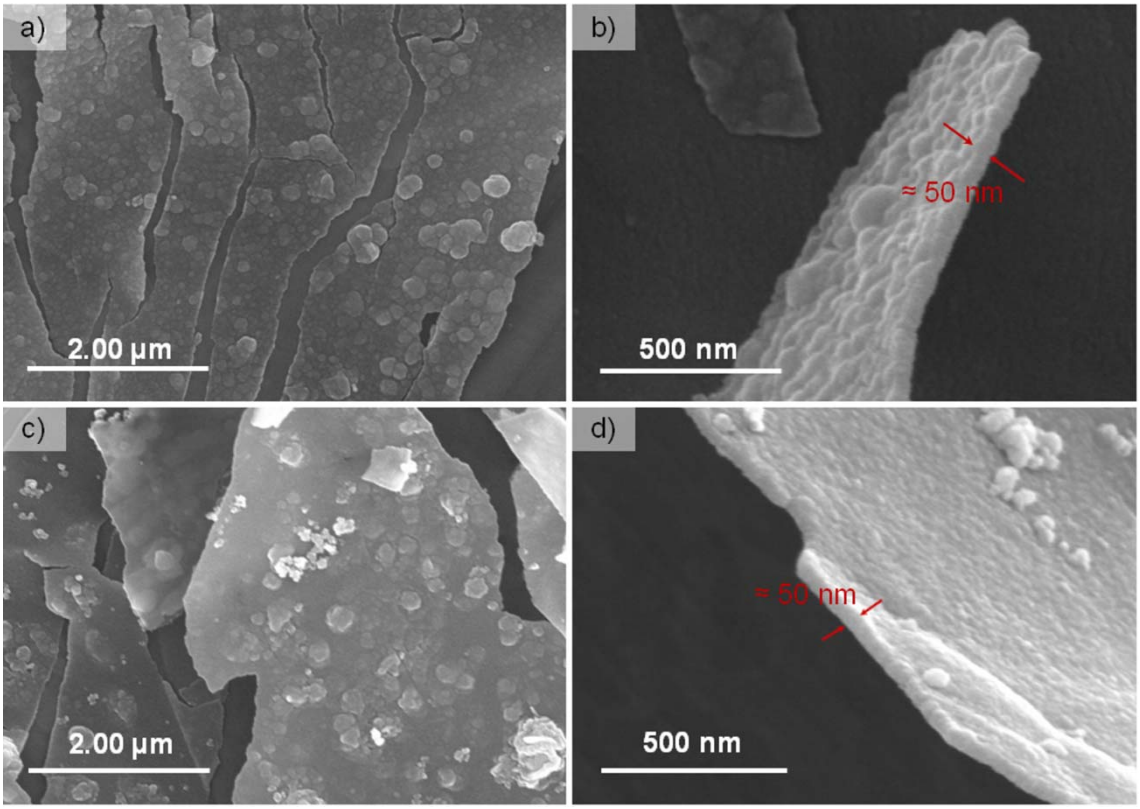

Figure 5.4: SEM micrographs of the films obtained applying pulsed voltage EPD with off times of a,b) 1s and c,d) 10 s. The films were thermally treated at 500 ºC for 2 hours and bent for their observation.

5.2 Non-aqueous Electrophoretic Deposition.

In order to verify whether the blocking of the electric field during deposition was due to the system or inherent to the EPD process, EPD of ZnO-NC suspensions was carried out using ethanol as solvent. This system allowed the application of higher voltages without producing unwanted reactions, as it belongs to the high field–low current regime [240].

For this purpose, the suspensions were prepared following the protocols described in Chapter 2, and their colloidal stability was determined by means of zeta potential and particle size measurements. The results obtained by these measurements are shown in Figure 5.5.

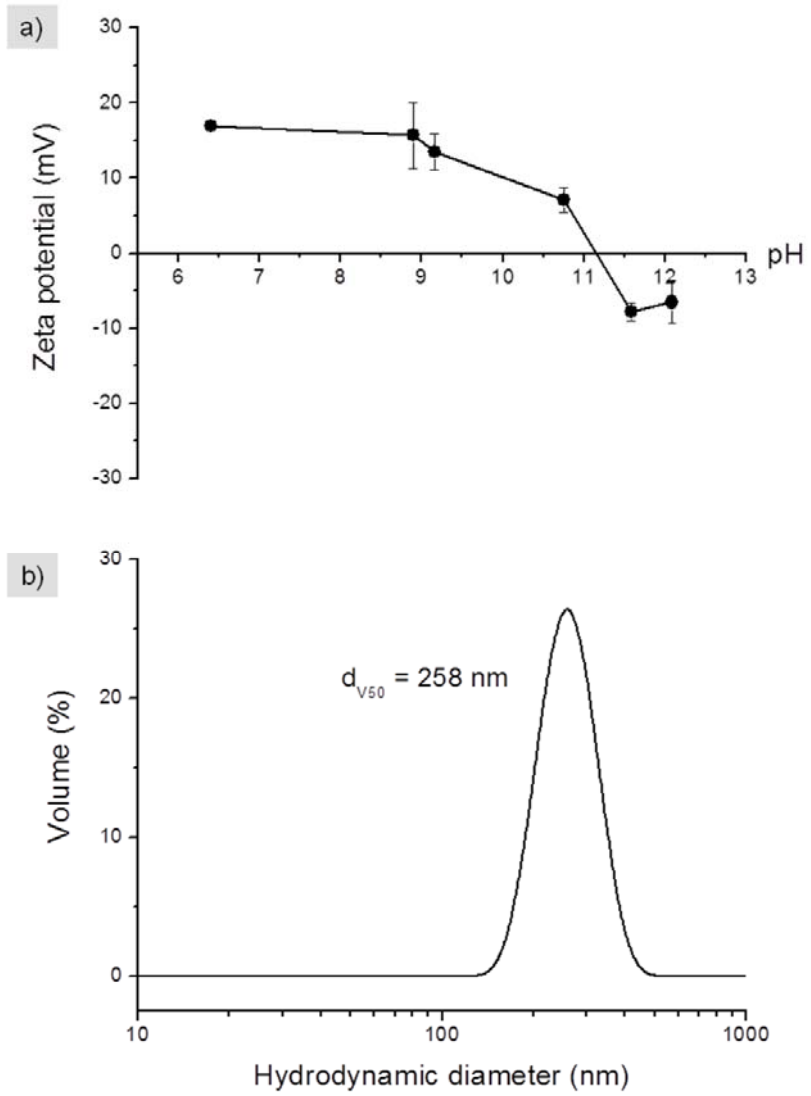

Figure 5.5: a) Zeta potential as a function of pH and b) particle size distribution of ZnO-NC powders in ethanol.

In the figure 5.5a it can be observed how the zeta potential of the suspensions in ethanol was lower than those in aqueous media (see Figure 4.5). This is due to the fact that the electrophoretic mobility of the powders (and thus their zeta potential) depends on the dielectric constant of the medium, which is higher for water (ε_r= 80.1 at 20ºC) than for ethanol (ε_r= 25 at 20ºC). However the suspensions in ethanol were still stable in a wide range of pH, as their zeta potential was around 20 mV. Moreover, it must be noted that the isoelectric point of the alcoholic suspensions coincided with that of aqueous suspensions with the presence of 1.5 % wt PEI (in Figure 4.5), thus allowing a wide pH range in which to work (according to the requirements of 6 < pH < IEP to avoid ZnO dissolution and have positively charged surfaces).

On the other hand, the results of the particle size measurement presented a wide size distribution curve, with a medium agglomerate size, $d_{V50,}$ of 258 nm, much higher than that obtained in aqueous suspensions (see Figure 4.6). Thus, from these results it can be inferred that, even though ethanol allowed the obtaining of stable ZnO-NC suspensions, this could not be well dispersed.

The next step consisted in the use of these suspensions whose characteristics are summarized in Table 5.1 for the EPD of ZnO-NC films.

Table 5.1: Characteristics of the ZnO suspensions used for EPD

Powder/Medium	Cc (g/L)	Dispersant	pH	d_{V50}	μ_e ($cm^2/V{\cdot}s$)
ZnO-NC / EtOH	1	-	7-8	258 nm	$4.06{\cdot}10^{-5}$

The applied electric conditions were of 500 V/cm for deposition times between 600 and 6000 s, using ITO substrates. The application of such high voltages is due to the non polar nature of the suspension medium, which strongly controls the deposition current: higher voltages are necessary for the deposition from non-aqueous suspensions, as the electrophoretic mobility of the particles in them is slower. The experimental results of deposited mass per unit area (determined by direct weighing) are shown in Figure 5.6.

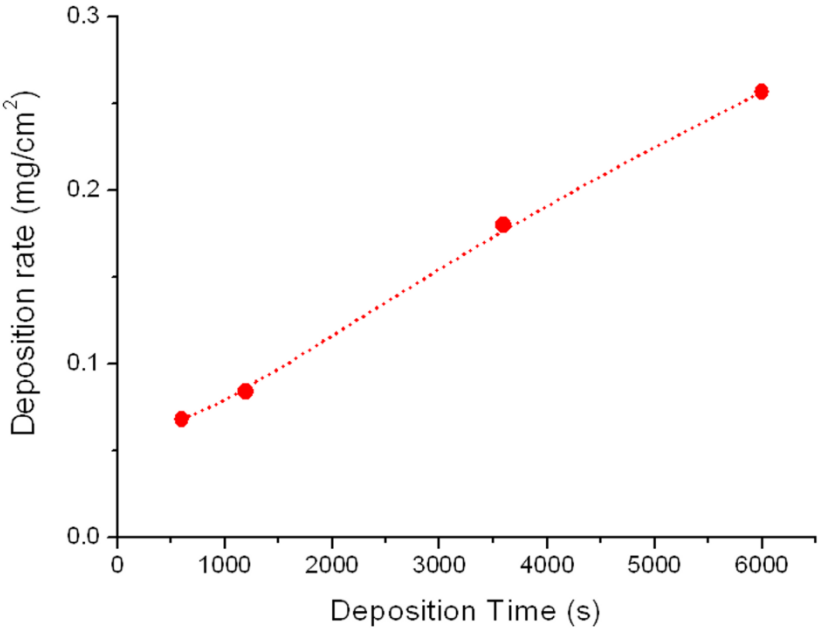

Figure 5.6: Deposition rates (deposited mass per unit area as a function of the deposition time) for the two systems studied.

Finally, films deposited after deposition times of 600 s were characterized. In the FE- SEM micrographs in Figure 5.7, it can be observed how in this case thicker films of about 10 µm were grown. The obtaining of such thick films can be ascribed to the decrease in the density of the films, due to both the absence of dispersant and the formation of large agglomerates which showed what is known as a “house of cards” arrangement (Figure 5.7b and d). The formation of this arrangement , in turn, might be due to the presence of LBZA rests from the synthesis procedure (Figure 5.7b), which did not dissolve in the ethanolic medium, and acted as glue, forming the large agglomerates observed in the DLS measurement (Figure 5.4). The rapid evaporation of the solvent during drying results in cracking of the film (Figure 5.7c), which hampered further characterization.

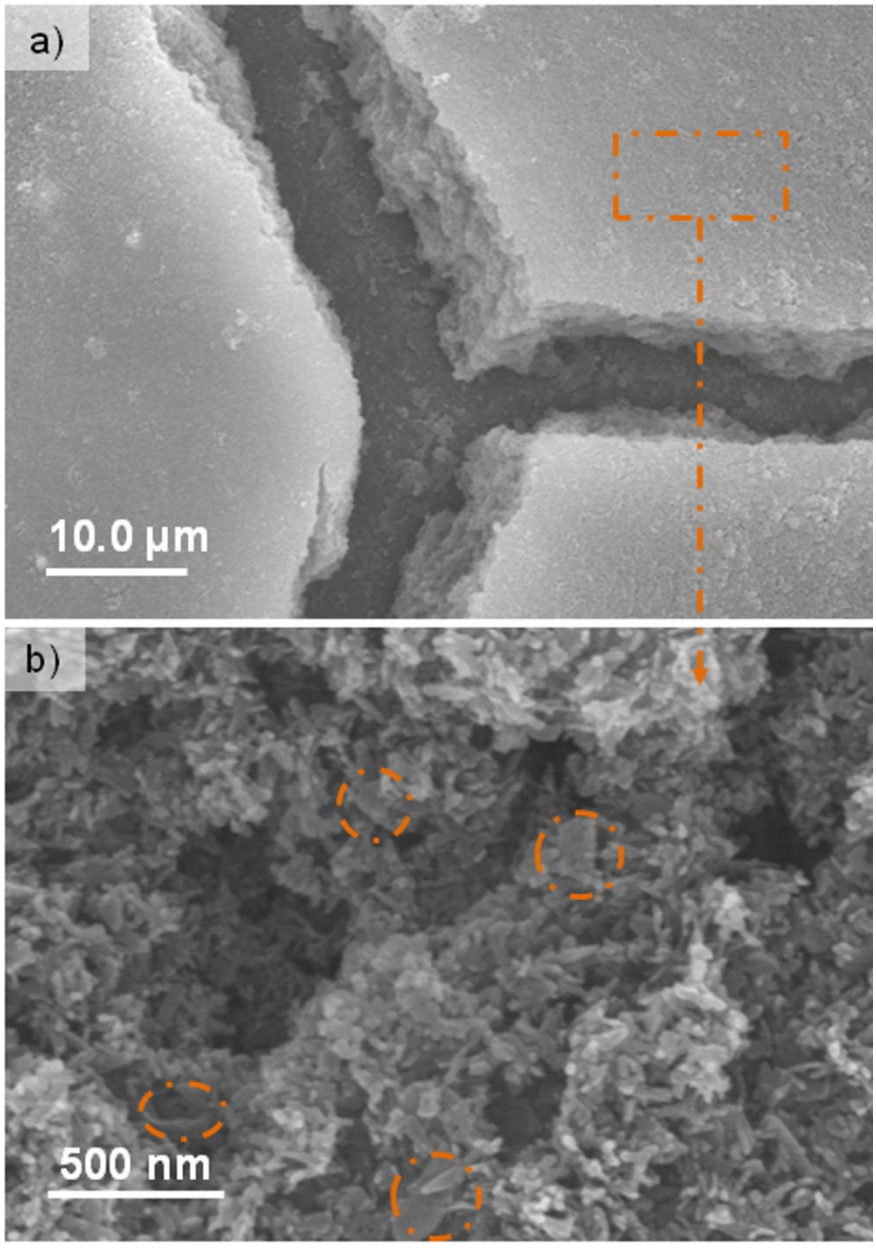

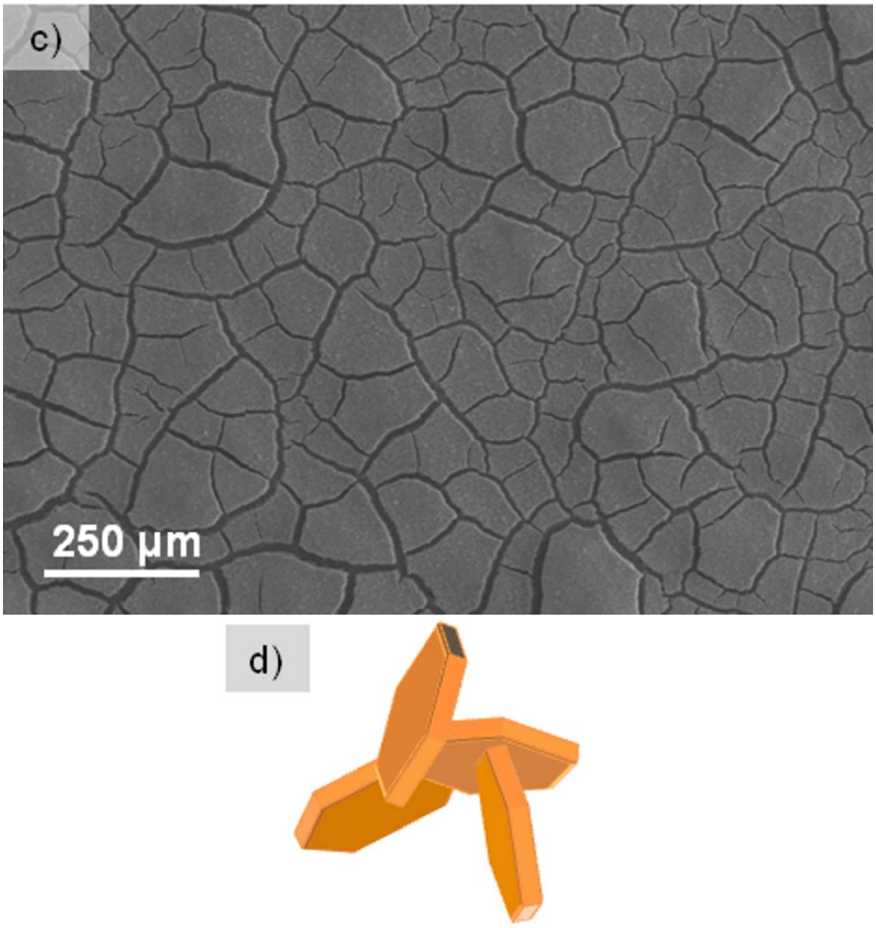

Figure 5.7: a-c)SEM micrographs of ZnO-NC films deposited from suspensions in EtOH and d) scheme of the house of cards arrangement of the particles. The circles in b) indicate rests of LBZA from the synthesis.

5.3 Hydrothermal growth of ZnO nanostructures.

The films deposited by EPD described in Chapter 4 were evaluated as seeds for the hydrothermal growth of one and two dimensional (1D and 2D) ZnO nanoarrays.

Hydrothermal growth was chosen among the wide variety of methods available for the preparation of these nanostructures due to the fact that its characteristics (its easy and low-cost procedure, low growth temperature, easy upward scaling and great control over experimental parameters) make it a powerful low-energy consumption route to successfully control the crystallization engineering of ZnO [52, 241, 242]. Moreover, as described in Chapter 1, the use of EPD-seeded substrates might represent a feasible sustainable, low cost and low energy consuming procedure to control the morphology, texture and orientation of the ZnO structures during hydrothermal growth.

Thus, in the present section the combination of EPD and hydrothermal processes is studied. For this purpose, several different cases of hydrothermal growth of ZnO nanostructures will be studied: in the absence of substrates, with presence of unseeded stainless steel substrates, and in presence of ZnO films prepared by EPD that will act as seed layers. In this last case, the ZnO-F and ZnO-NC films obtained by EPD described in the previous chapter were used.

5.3.1. Hydrothermal growth of ZnO powders without substrate.

The hydrothermal growth of ZnO nanostructures was studied in order to have a reference to which compare the subsequent results in the presence of untreated and seeded substrates. For this purpose, a 0.14 M aqueous solution of zinc acetate dihydrate ($Zn(CH_3COO)2{\cdot}2H_2O$) was prepared, and transferred to a teflon-lined stainless steel autoclave as the one shown in Figure 2.2 of the experimental section (Chapter 2). Subsequently, 40 ml of 1 M KOH were added dropwise to the solution under vigorous magnetic stirring at room temperature [184], forming a white precipitate (identified in the literature as aggregates of semi-crystalline hydrated ZnO [42]). Once all the corresponding reactants were introduced in the autoclave, this was sealed tightly, heated up to 200 ºC and maintained at this temperature for 4 h. Autogenous pressure gradually increased as the temperature rose during the hydrothermal procedure, after which the system was allowed to cool down naturally to room temperature. The resulting precipitate powder was retrieved from the solution by filtration, washed twice with ethanol and distilled water in sequence and finally dried in air at 60 ºC.

The resulting powders were characterized by XRD diffraction. The diffractogram in Figure 5.1 shows how the hydrothermal conditions were enough to decompose all rests of the starting products: all diffraction peaks were in good agreement with the ICDD card no. 36-1451 for a typical wurtzite-type ZnO crystal and no evidence of secondary phases or impurities was detected. Moreover the estimated lattice parameters calculated and refined using the least square method in the FullProf 2k program, a = 3.250 $\pm$ 0.005 Å and c = 5.209 $\pm$ 0.005 Å, closely match those of the ZnO wurtzite pattern (a = 3.2498 Å and c = 5.2066 Å).

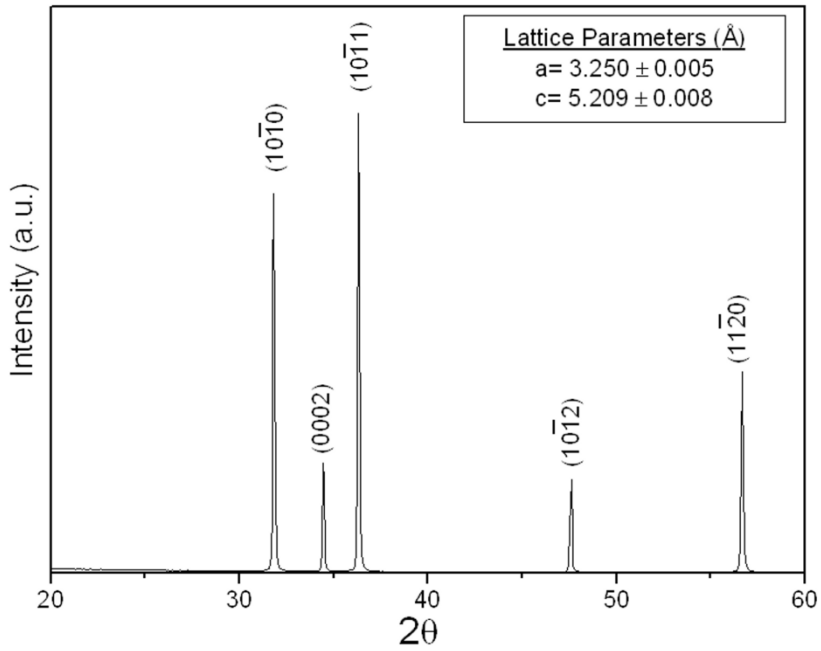

Figure 5.1: XRD pattern of the synthesized powder, ZnO (ICDD nº 36-1451). Calculated lattice parameters are shown in the inset.

The microstructure of the obtained ZnO powders was then examined by FE-SEM. The micrographs in Figure 5.8 show a vast number of microrods with a hexagonal dumbbell-like bipod morphology, in which each bipod is divided in its half by the presence of a planar defect.

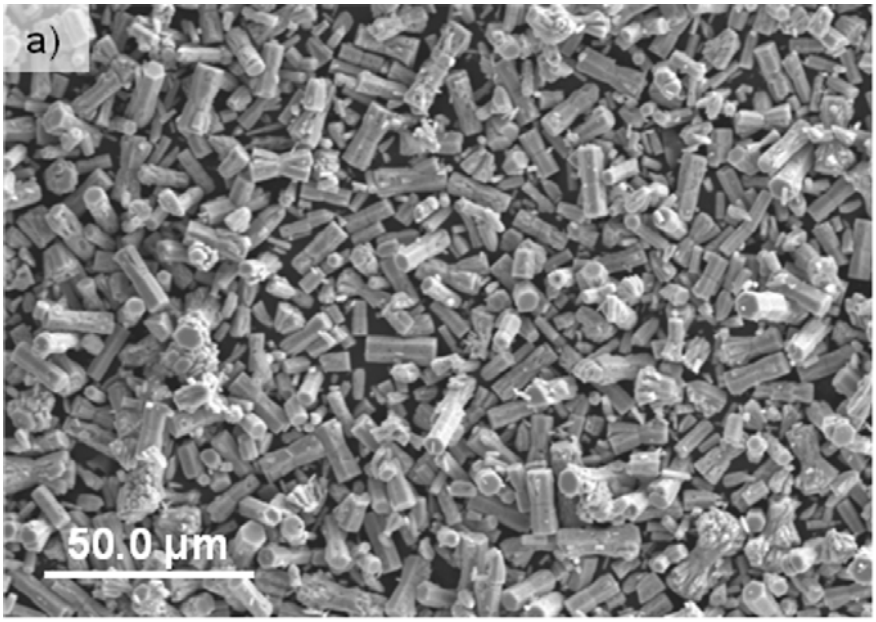

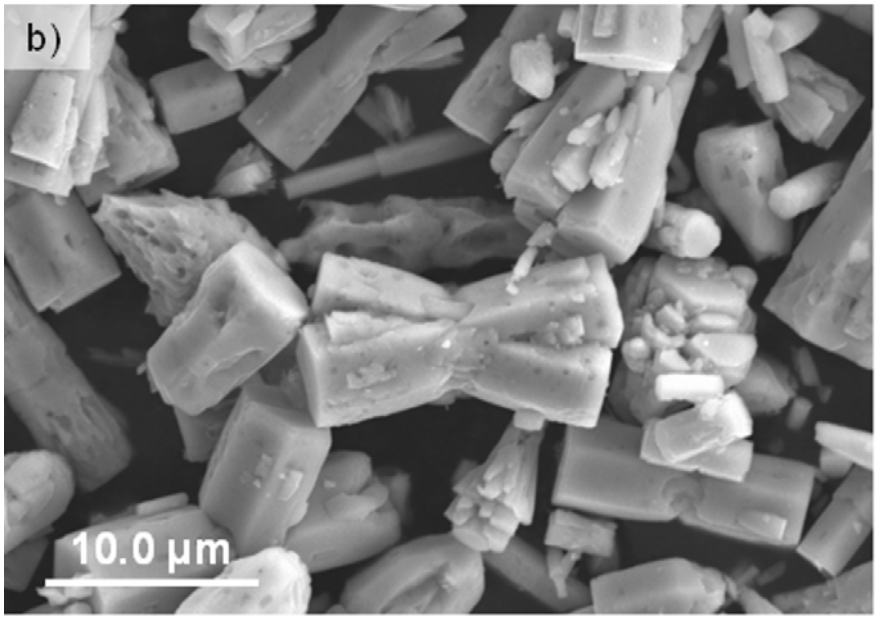

Figure 5.8: FE-SEM micrographs of the hydrothermally synthesized powders. The powder is mainly constituted by hexagonal bipods with a dumbbell-like morphology.

Bitenc *et al.* [243] identified these basal-plane defects as inversion domain boundaries (IDBs) that result from the high proneness of ZnO crystals to twinning. In essence, the formation of these IDBs and the overall growth mechanism of the observed rods are consistent with the intrinsic polar structure of hexagonal ZnO and the trend of the system towards decreasing its energy: as the system tends to reduce the facets with higher surface energy, i.e, the polar ones, the growth rate is faster along this ± [0 0 0 1] direction and the rod-like morphology develops [29, 244]. Moreover, the lack of centrosymmetry of the wurtzite crystal makes the growth in the [0 0 0 1] direction perceptibly faster than in the [0 0 0] direction [18, 245], thus inversion boundaries are likely to be formed in which the (0 0 0 1) planes will be pointing towards each other (*head to head configuration*) leading to the observed dumbbell-like morphology [246-248].

5.3.2. Influence of the presence of substrates in hydrothermal growth.

As mentioned previously, the incorporation of seeded substrates to the hydrothermal growth might open way of controlling the morphology, texture and orientation of the grown ZnO structures. This is due to the intrinsic competition between homogeneous and heterogeneous nucleation that takes place in solution processes: the interfacial energy between crystals and substrates is typically lower than that between crystals and solution [92], and this, together with the fact that heterogeneous nucleation

generally has a lower activation energy barrier than homogeneous nucleation, favors that the first one will occur more readily onto a foreign surface [52, 249]. In other words, the presence of energetically favorable sites on the rough surface of the substrate may enable heterogeneous nucleation, and this could lead, under certain specific conditions, to the creation of a hierarchical structure. Pursuing this goal several experiments were carried out, in which different substrates were introduced in the autoclave to run the hydrothermal synthesis: an unseeded stainless steel foil, a stainless steel foil with a ZnO-F seed layer deposited by EPD, a stainless steel foil with a ZnO-NC seed layer deposited by EPD and an ITO substrate with a ZnO-NC seed layer deposited by EPD.

5.3.2.1. Hydrothermal growth in the presence of unseeded stainless steel substrates.

The influence of the presence of a bare stainless steel substrate on the morphology of hydrothermally grown ZnO nanostructures was first studied. For this purpose, the substrate was introduced in the autoclave prior to the transferring of the $Zn(Ac)_2$ solution. After the hydrothermal procedure the resulting film on the substrate was rinsed with distilled water to remove the residual reactants or products from the surface, and dried at room temperature. These samples were then characterized by scanning electron microscopy (Figure 5.9).

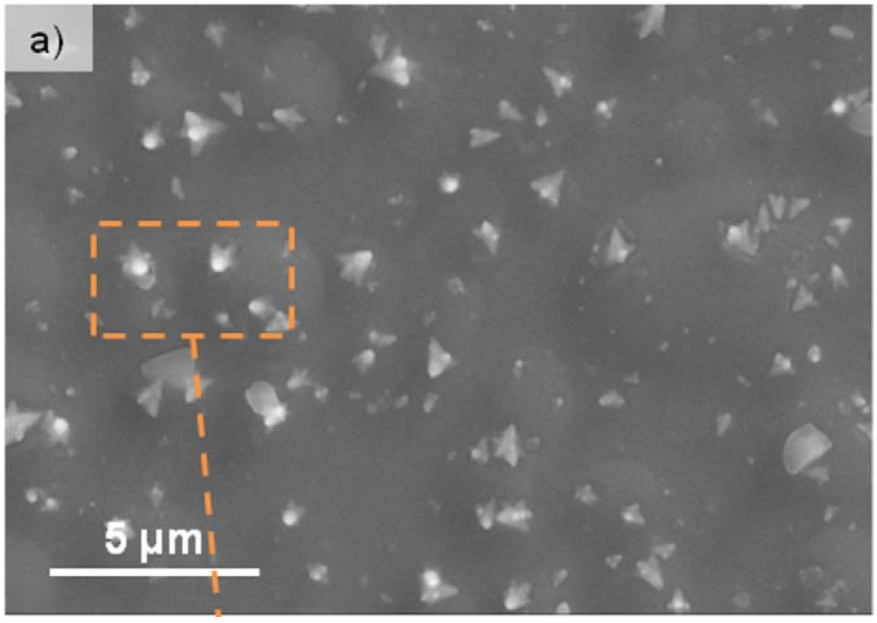

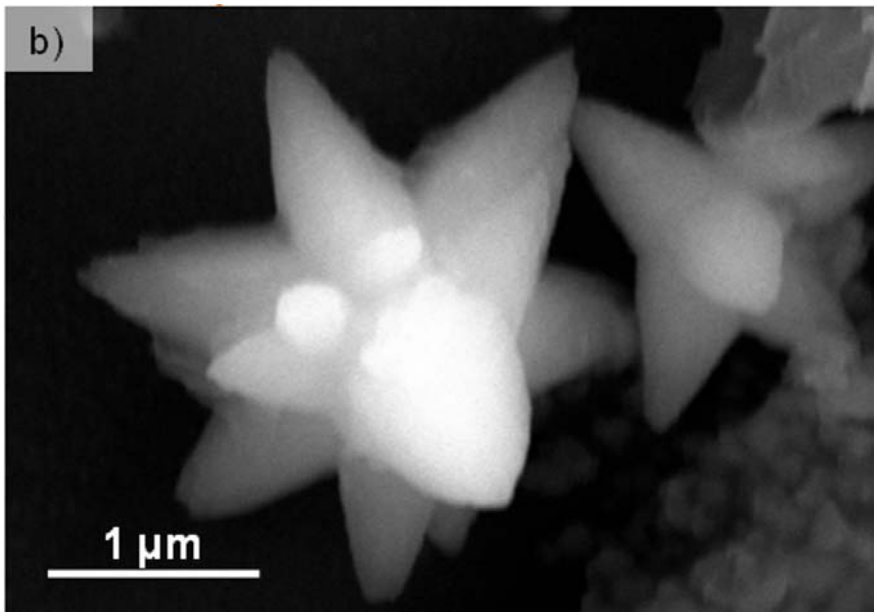

Figure 5.9: FE-SEM micrographos of the ZnO nanostructures grown onto the surface of an unseeded stainless steel substrate.

As can be observed in the FE-SEM micrographs, the surface of the substrate appeared poorly populated by ZnO structures with a completely different morphology of that observed in Figure 5.8. A closer look at higher magnification (Figure 5.9b) showed that in this case, the morphology of the hydrothermally grow ZnO particles was of micron-sized multipods. This scarce population of multipod-like structures can be explained by crystal nucleation and growth theories. In the first place, taking into account the random and complex nature of the nuclei forming on a foreign surface, it has been reported that only those nuclei which occupy the most favorable energy sites and are beyond the critical nuclear size can survive [93, 250]. Therefore, on the surface of unmodified substrates the number of forming nuclei is limited, and this leads to a slow consumption rate of the precursors. As the concentration of the precursor solution remains at a relatively high saturation level, the crystal growth rate of the already formed nuclei is favored versus the nucleation of new ones, and consequently large and scattered crystals like those observed in Figure 5.9 are obtained. On the other hand, the multipod morphology is in agreement with what has been described in the literature as kinetic growth morphology, which consists, again, in the rearrangement of the thermodynamically less stable polar facets of ZnO in order to decrease the energy of the system [29, 244]. In this sense, Peiteado et al. [184] reported how under certain conditions ZnO twinned crystals can accumulate, forming octahedral nuclei and/or polyhedral cores from which new rods germinate and grow along the [0 0 0 1] direction, giving place to the formation of multipods.

From the analysis of these results it can be concluded that in order to obtain a dense array of ZnO (nano)structures, a pre-coating of the substrate with seeds of ZnO would help to have nucleation sites.

5.3.2.2. Hydrothermal growth in the presence of EPD- seeded substrates

In order to study the influence of the seeding and the nature of the powder used for it, the ZnO-F and ZnO-NC films shaped by EPD described in the previous chapter were used as seed layers. In particular, the films used corresponded to samples deposited from 0.1 g/L suspensions applying intensities of 100 μA for 10 min.

- Growth in the presence of ZnO-F films deposited on stainless steel substrates.

In the first place, the hydrothermal procedure was carried out using ZnO-F films deposited on electropolished stainless steel substrates, i.e. sample FESS-01-10 in the previous chapter, as seed layers.

The results of the hydrothermal growth onto these seeded samples are shown in the FE-SEM micrographs in Figure 5.10. As can be clearly observed, the seeding with the ZnO-F powder affected the number and size of the ZnO structures, as in this case a vast population of ZnO nanostructures covering the substrates surface was obtained. However, the seeding did not seem to influence the morphology during hydrothermal growth, provided that the same multipod structures observed when using unseeded substrates were obtained, and only their size was affected, decreasing the average diameter to the nanoscale.

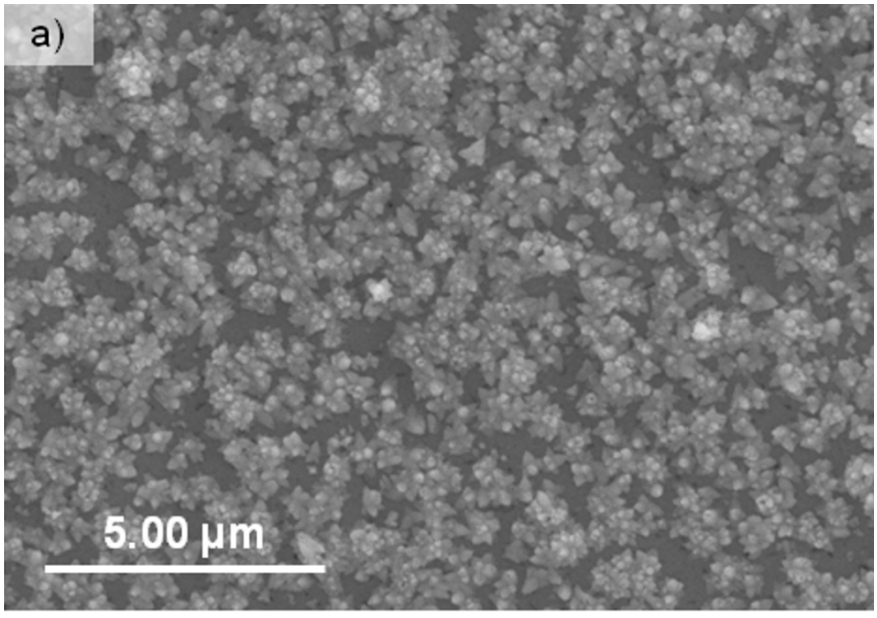

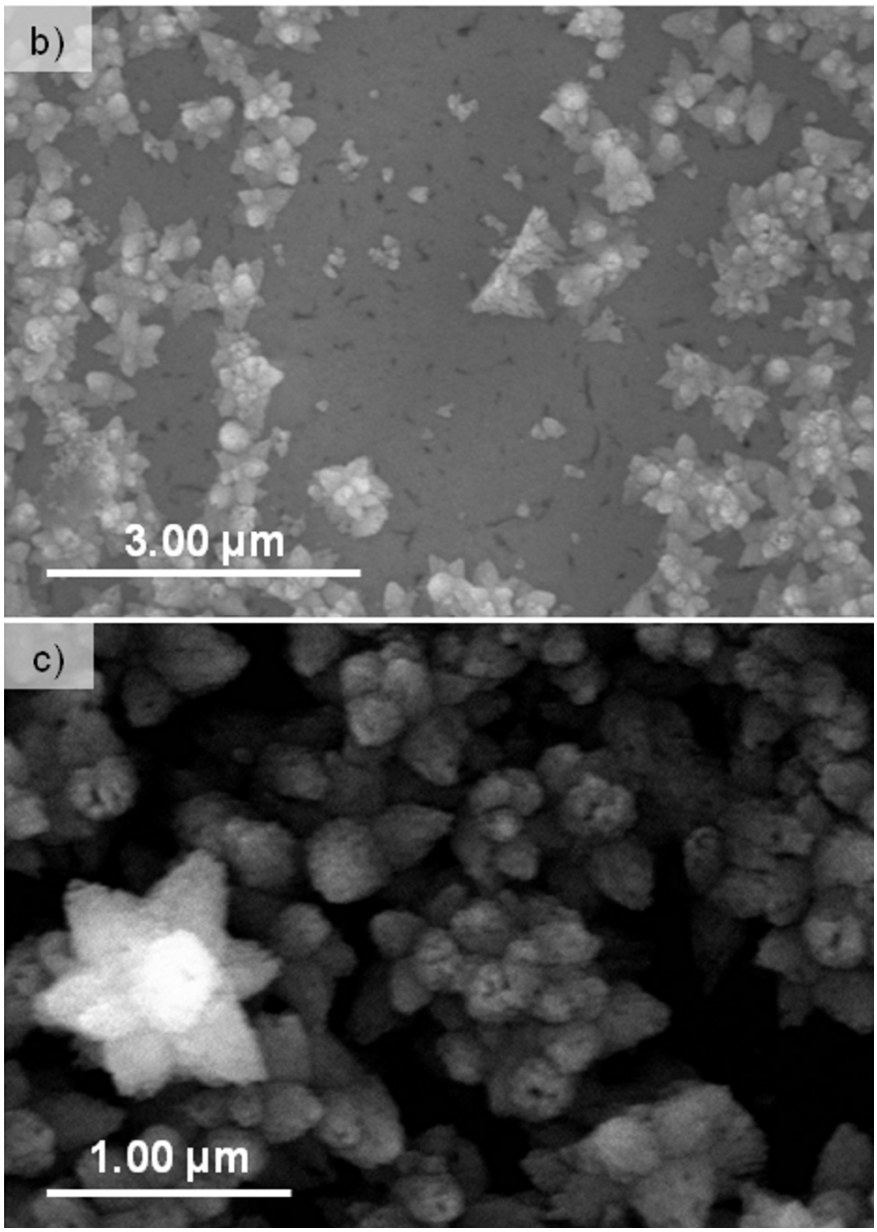

Figure 5.10: FE-SEM micrographs of the ZnO nanostructures hydrothermally grown onto a ZnO-F film prepared by EPD. b) is a magnification of an area in a) in which the ZnO-F seed layer can be observed.

The increase in the number of multipods and their decrease in size can be explained taking into account the competition between crystal nucleation and crystal growth [91, 93, 251]. In this case, the large number of ZnO crystals deposited on the seed layer serve as nucleation sites, thus lowering the supersaturation level of the precursor solution and reducing the crystal growth rate: nucleation is now favored versus growth, resulting in a larger number of smaller multipods (nano-sized).

At this point it is clear that the seeding procedure rendered an energetically favorable region for the ZnO crystals to nucleate under hydrothermal conditions. However it somehow seemed that, as opposed to what happens with other seeding methods, the species in the starting solution did not perceive the electrophoretically

deposited particles as proper seeds from which a patterned array with defined morphology, texture and orientation could develop. Furthermore, dense arrays covering the whole substrate foil were still not feasibly grown, since as shown in Figure 5.10b the structure of the EPD-seeded layer can still be seen underneath the vast amount of hydrothermally grown multipods.

- Growth in the presence of ZnO-NC films deposited on stainless steel substrates.

In order to verify if the limitations observed in the seeding with the ZnO-F powder were inherent to the EPD process itself experiments were repeated using ZnO-NC films.

FE-SEM micrographs of the samples obtained after the hydrothermal procedure, shown in Figure 5.11, show a dramatic change in the morphology of the hydrothermally grown nanostructures. In this case, a dense array of hexagonal nanorods was obtained which completely covered the surface of the stainless steel substrate.

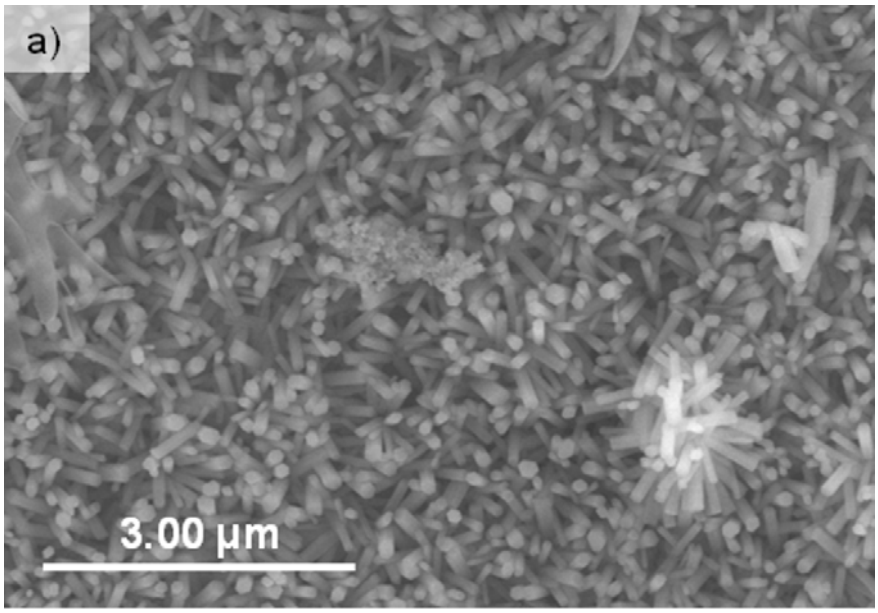

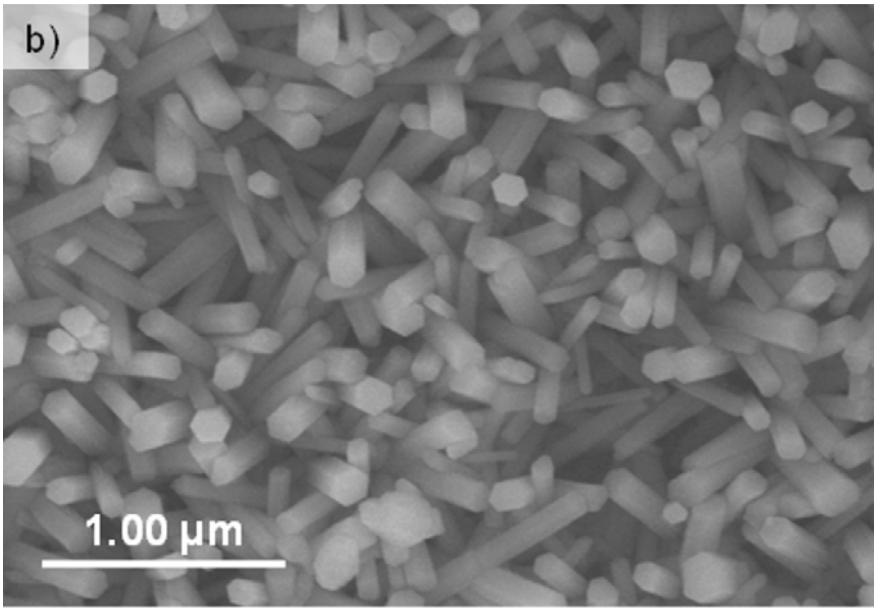

Figure 5.11: SEM micrographs of the ZnO nanorods obtained after hydrothermal growth on a stainless steel substrate coated with a ZnO-NC seed layer.

The reason for this different morphology should be found on the nature of the powders. As described in Chapter 3, despite their similar synthesis, both powders showed very different characteristics: whereas ZnO-F was a well crystallized powder, with a relatively high density (4.4 g/cm^3) and flake-like particles of 50 nm, ZnO-NC powders had a low crystallinity, presence of impurities (acetates) , low density (3.3 g/cm^3) and particle sizes of about 5 nm. The fact that ZnO-NC powders are less crystalline and almost one order of magnitude smaller than the ZnO-F powders imply that the first will have a higher reactivity. Therefore, in this case the ZnO-NC seed layer not only yielded high energy sites for nucleation, but also provided seeds with a much higher reactivity. As a consequence, the precursor species in the solution growed up following the habit drawn by these seeds, i.e. along the c-axis of wurtzite, leading to the observed rod-like units. On the other hand, the apparent lack of vertical orientation in the obtained array of ZnO nanorods is directly related to the roughness of the steel substrates, as schematized in Figure 5.12.

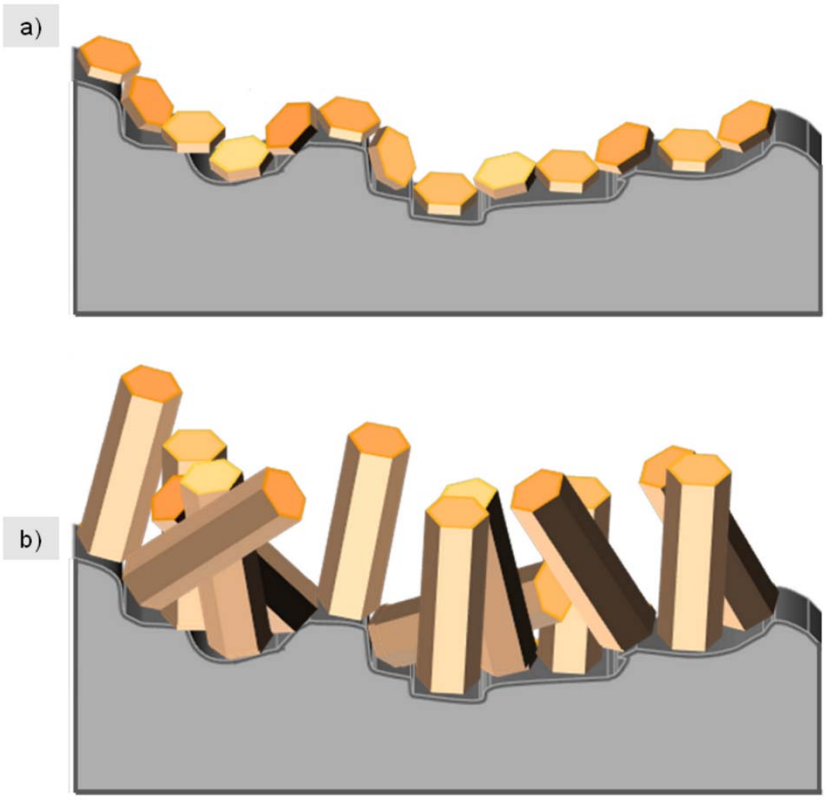

Figure 5.12: Scheme of the particles orientation a) after EPD (seed layer) and b) of the nanorods after hydrothermal growth.

In spite of the electropolishing treatment, the substrate roughness is still too high for the small ZnO-NC particles to overcome. Therefore, even though the particles in the film showed a good self-organized appearance and high packing density, as confirmed in the AFM micrographs in Fig. 4.54, the seeds were actually randomly oriented in the substrate, thus impeding a uniform orientation of the array, as it has been reported that the orientation of the ZnO seeds directly determines the orientation of the nanorods [89, 197]. In order to observe this lack of orientation due to substrates roughness, the steel substrates were bent (as shown in Figure 4.35) for their characterization by SEM. The FE-SEM micrographs of this “cross-section” shown in Figure 5.13 confirmed how the roughness and corrugation of the substrate affected the orientation of the rods. However, when observed at lower magnifications it could be noticed that this apparent lack of vertical orientation was not as remarkable.

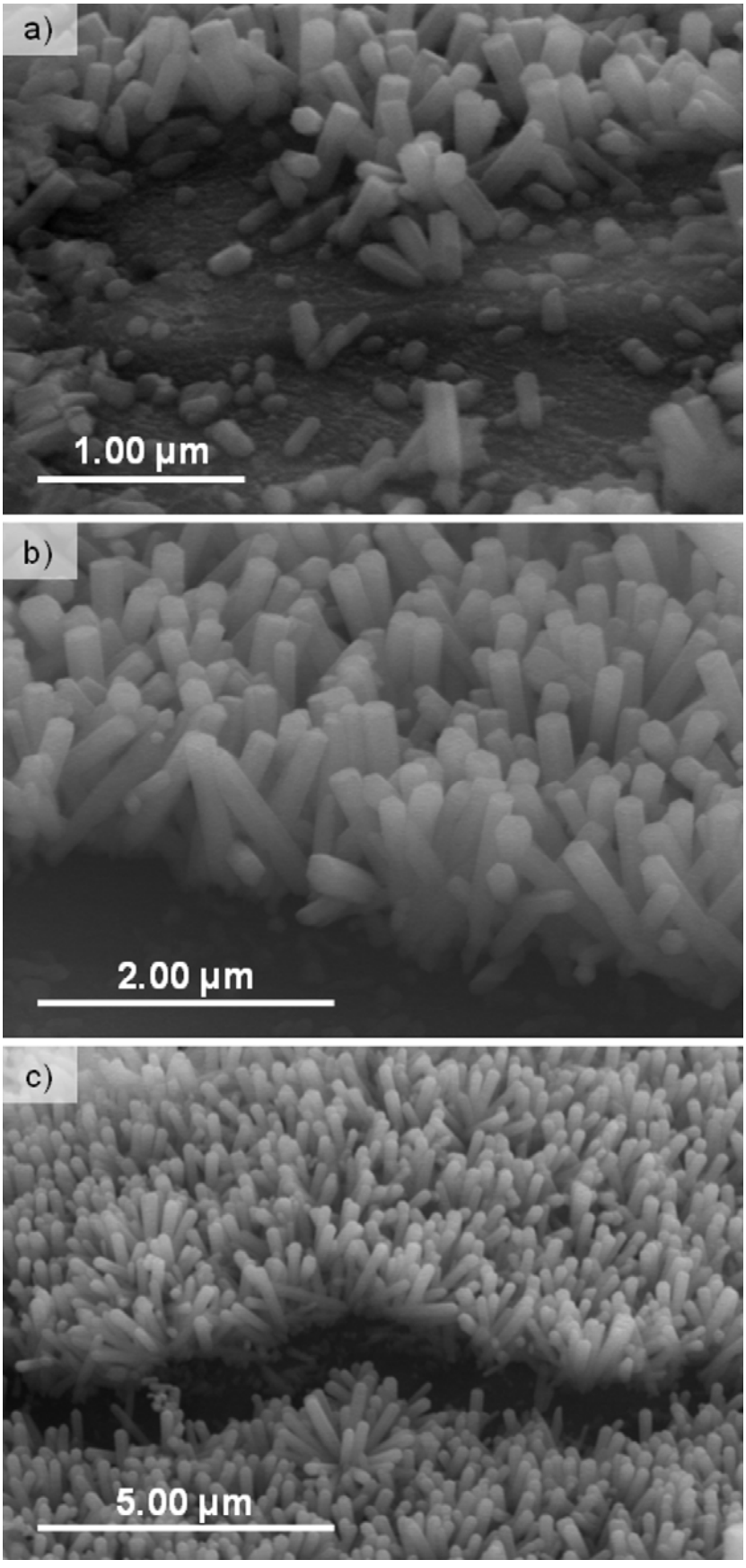

Figure 5.13: FE-SEM micrographs of the “cross-section” of the ZnO nanorods obtained after hydrothermal growth on a stainless steel substrate coated with a ZnO-NC seed layer. Roughness of the substrate is clearly observed.

- Growth in the presence of ZnO-NC films deposited on ITO substrates.

Finally, in order to verify if the orientation of the ZnO nanorods obtained by hydrothermal growth could be improved, ZnO-NC films deposited on ITO substrates were introduced in the autoclave since, as shown in the previous chapter, the roughness of this kind of substrates was much lower than that of stainless steel substrates. The films used in this case corresponded to those in Figure 4.49.

The obtained results are shown in the FE-SEM micrographs in Figure 5.14. In these micrographs it can be clearly observed how the ZnO nanostructures densely covered the area of the ITO substrate which had been previously coated by EPD, whereas growth on the uncoated area was quite scarce. Moreover, the obtained ZnO nanostructures presented a new morphology, which in this case consisted of petal or plate-like particles with thicknesses of about 50 nm, as observed in Fig. 5.14c.

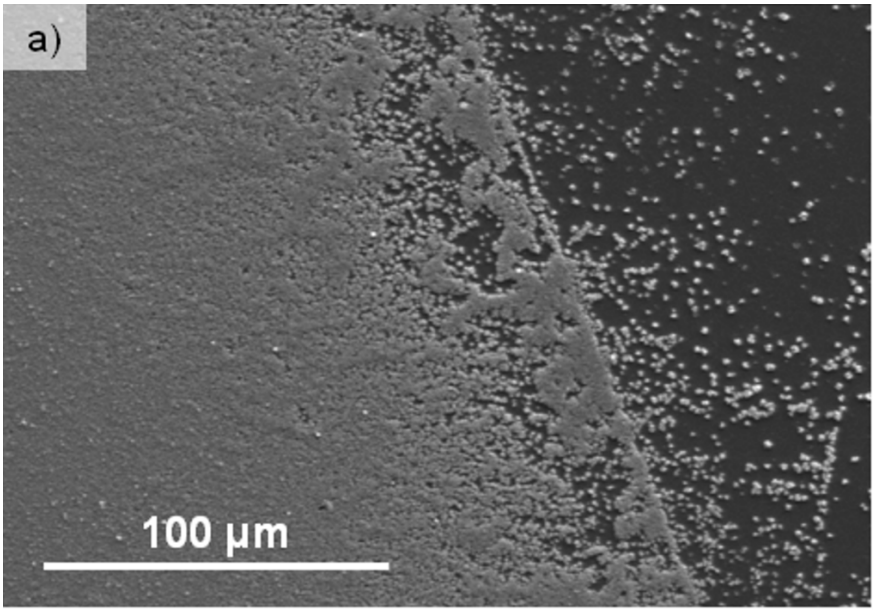

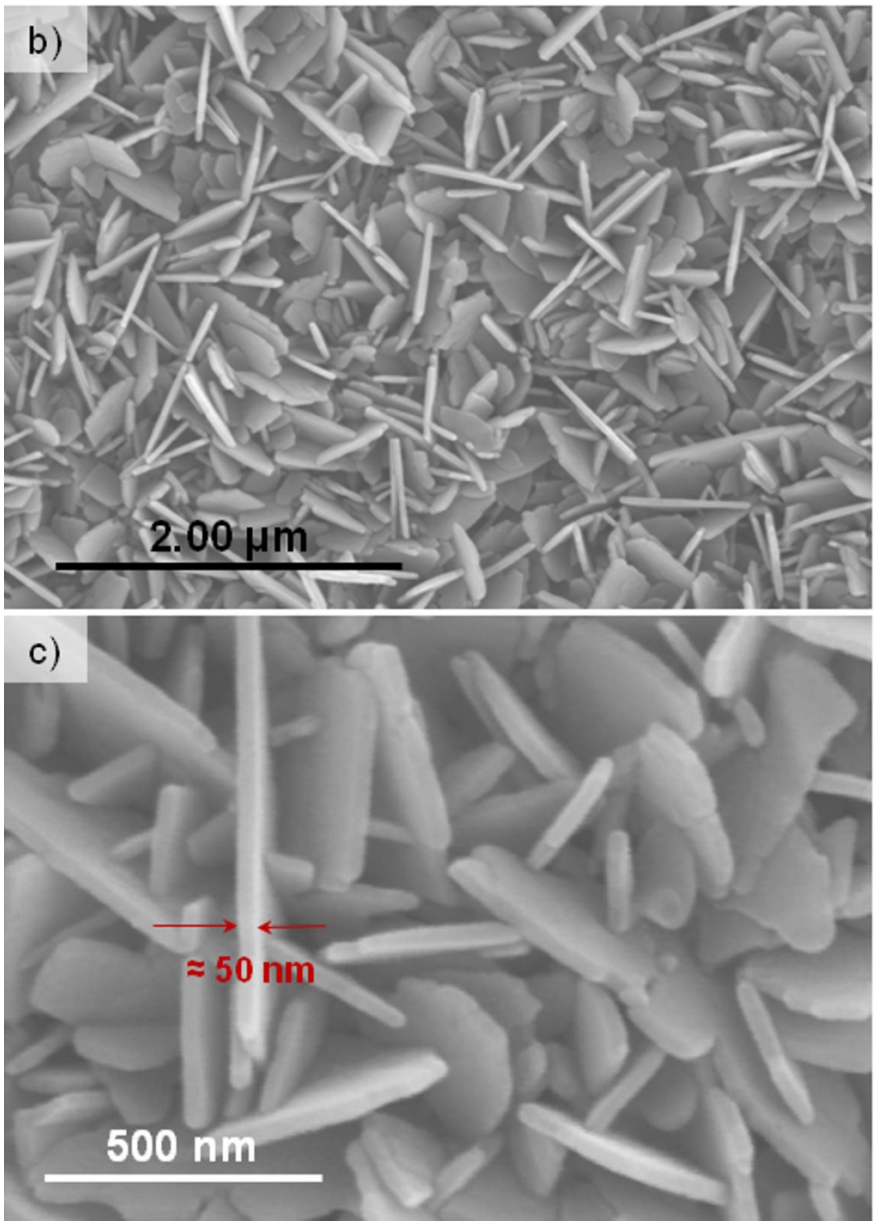

Figure 5.14: FE-SEM micrographs of the ZnO petals obtained after hydrothermal growth on an ITO substrate coated with a ZnO-NC seed layer.

This morphology has been reported in the literature as the product obtained using capping agents that hampered ZnO growth in the (0001) direction and/or using extremely basic conditions (OH^-/Zn^{2+} ratio between 4 and 10) [91, 252-255]. In this case, however, none of these conditions were applied and the plate-like morphology is ascribed mainly to the inhomogeneous nature of the films deposited on ITO substrates, i.e. as the seed layer forms “islands”, the lateral growth of the ZnO nanostructures is less confined/constricted, giving place to larger structures.

5.4. Summary and Conclusions

The controlled growth of ZnO films has been addressed by several methods, so as to "enlarge" the thicknesses obtained by EPD in the previous chapter.

First, the use of pulsed-EPD was tried as a way to reset the electrical conditions of the system and avoid the blocking of the electric field previously observed. For this purpose, both current and voltage pulses with different off times were applied to ZnO-F suspensions. However, the results showed that, as in the case of constant conditions, deposition took place very rapidly, forming remarkably dense films with thicknesses of about 40-50 nm, and then stopped. Moreover, it seemed that the application of further pulses only resulted in the agglomeration of the particles that due to the "intermittences" could not become oriented by the hydrodynamic forces.

The use of non- aqueous systems was considered next. In this case, ZnO-NC suspensions were prepared using ethanol as solvent, so as to allow the application of high electric fields without bubbling. In this way, the application of 500 V resulted in the formation of ZnO-NC films with thickness in the order of microns. However, the apparent density of the films (by FE-SEM) seemed to be low, probably due to the presence of acetate species that did not dissolve in ethanol and gave place to a "house of cards" arrangement of the particles. This, together with the fast evaporation of the solvent, gave place to cracking of the films.

Finally, the combination of EPD and hydrothermal processes was studied as a way to tailor the morphology of ZnO structures during hydrothermal growth. In this sense it was found that the use of both unseeded and EPD-seeded substrates had a strong influence on the morphology of the ZnO structures obtained by hydrothermal growth: micron-sized ZnO multipods were grown when using unseeded substrates which provided a limited number of nucleation sites, whereas their size decreased to the nanoscale when using EPD-seeded substrates. In addition it was observed that when seeding with a smaller, more reactive powder (ZnO-NC powder instead of ZnO-F) the morphology changed. Moreover, depending on the nature of the substrate (electropolished stainless steel or ITO coated glass), and thus (as described in the previous chapter) on the homogeneity of the seed layer, homogeneous populations of either randomly oriented ZnO nanorods of ZnO or submicron sized nanopetals were attained after the hydrothermal reaction.

Conclusiones generales

Las conclusiones generales que se han obtenido en este trabajo tesis pueden agruparse de la siguiente manera:

Con respecto a la obtención de nanopartículas de ZnO:

- ✓ Mediante un proceso de precipitación en medio acuoso se han sintetizado nanopartículas de ZnO con tamaño y morfología controlados. Se ha usado acetato de Zinc como precursor y NaOH como precipitante. El uso de acetato de Zn propicia la formación de precipitados laminares, basados en acetatos con diferentes grados de hidratación, que se constituyen en precursores de la morfología de las nanopartículas.
- ✓ El proceso de lavado del precipitado se ha mostrado crítico para el control del tamaño de las nanopartículas. Durante los sucesivos ciclos de lavado, las láminas del precursor se descomponen y van formando estructuras en forma de copos (0D) o placas (2D). Cuando el lavado se prolonga estas placas crecen a lo largo del plano basal de la wurtzita y, tras el tratamiento térmico, las partículas en forma de placa de ZnO pierden la dimensión nanométrica de su diámetro, pero no de su espesor.
- ✓ Controlando el proceso de lavado y mediante tratamientos térmicos de calentamiento y enfriamiento brusco entre 200 y 300 ºC, ciclos frio-frio de 10 minutos, se pueden obtener partículas en el rango 10 - 100 nm con forma de copo o placa. Al aumentar el tamaño de la partícula aumenta igualmente el factor de forma y la cristalinidad. Los planos basales son preferencialmente perpendiculares al eje c de la estructura wurtzita del ZnO y por tanto las caras pueden presentar carga eléctrica diferente.
- ✓ En el caso de la obtención de materiales dopados con Co^{2+} el proceso de síntesis utilizado se ha mostrado igualmente útil para obtener nanopartículas de ZnO dopadas en el rango 10 - 100 nm. Se ha podido verificar la incorporación del Cobalto en la red wurtzita con un tratamiento térmico tan bajo como 300 ºC.

Con respecto al proceso de EPD de las nanopartículas

- ✓ Se han determinado las condiciones óptimas para la preparación de las suspensiones para EPD. Se ha encontrado que la utilización de un polielectrolito de cadena larga (PEI Mw = 25000 a.u.) permite estabilizar las

suspensiones mediante un mecanismo electroestérico. Frente a los polímeros de cadena corta, el PEI 25000 permite incrementar el rango de estabilidad coloidal, e igualarlo al de estabilidad química. Al modificar la superficie de la partícula por adsorción, la dota de carga positiva y por tanto propicia la deposición catódica.

- ✓ El PEI se adsorbe preferencialmente en las superficies de las nanopartículas con carga neta negativa y configuran un conjunto partícula-polielectrolito que asemeja la geometría de una medusa bajo ciertos valores de pH. Esta geometría resulta esencial para el movimiento de las partículas en el seno del líquido y para la deposición ordenada sobre el sustrato, en la que sus planos basales se alinean paralelos al mismo.
- ✓ Se ha validado el uso de la Espectroscopía de Ultravioleta-Visible para la determinación de forma indirecta del crecimiento de capas con espesores < 70 nm y masa < 35 μg/cm^2.
- ✓ Durante el proceso de EPD, para tiempos muy cortos se forma una primera capa de nanoparticulas ordenadas que constituyen una lámina con una anormalmente elevada densidad de empaquetamiento que le permite ser transparente y flexible directamente tras el proceso de secado sin necesidad de un tratamiento térmico de consolidación posterior.
- ✓ Tanto sobre sustratos de ITO como de acero AISI 304 electropulido y para suspensiones con concentraciones de sólidos entre 0.1 y 1 g/L, el proceso de EPD conforma esta lámina en un tiempo muy corto, tras el cual se para la deposición. La elevada densidad de esta primera capa es el origen del bloqueo de la deposición en estas condiciones de trabajo.
- ✓ La diferente rugosidad y conductividad eléctrica de los sustratos de ITO y acero afecta a la homogeneidad de la capa depositada. El espesor de lámina sobre el acero está en el entorno de 50 nm mientras que sobre el ITO se forma una monocapa de nanopartículas sobre la que aparecen islas o pequeños aglomerados.
- ✓ Mediante el empleo de suspensiones con concentraciones de 1 g/L y sustratos de Ni con mayor rugosidad y conductividad eléctrica pueden obtenerse capas gruesas evitando el bloqueo del proceso. En este tipo de capas, si bien se mantiene el orden estructural de corto alcance, la deposición de los aglomerados es aleatoria, lo que reduce la densidad de las mismas. Las capas de ZnO se vuelven traslucidas.

Con respecto al crecimiento de las láminas con morfología controlada

- ✓ En el caso de la aplicación de un proceso de EPD pulsada, tanto en el caso de la aplicación de una densidad de corriente como de un campo eléctrico, se genera una lámina densa ordenada de un espesor similar, alrededor de 50 nm, al que se obtiene mediante EPD en condiciones dc. La aplicación de pulsos de voltajes algo superiores a los que se alcanzan en las condiciones de EPD galvanostática empleada conduce a láminas más homogéneas.
- ✓ La aplicación de pulsos con diferentes frecuencias no conduce a un proceso de crecimiento capa a capa, registrándose un bloqueo del proceso de deposición idéntico al observado en condiciones dc.
- ✓ En sistemas no acuosos, con suspensiones preparadas en etanol y sin PEI, utilizando altos voltajes para la deposición se crecieron capas de espesores superiores a la micra. La razón para que la deposición no se bloquee parece relacionarse con la pérdida de la nanoestructura ordenada de la capa, y por tanto con la no formación de una capa densa inicial. El origen de este desordenamiento de las partículas se debe tanto al voltaje como a la ausencia de PEI y por tanto a la ausencia del conjunto “con forma de medusa” que posibilita la ordenación de las nanopartículas al llegar al sustrato.
- ✓ El uso de sustratos semillados por EPD para el crecimiento hidrotermal permitió obtener morfologías diferenciadas en función de la homogeneidad de la capa y de la cristalinidad de las partículas.
- ✓ Cuando el semillado conforma una capa densa obtenida con las nanopartículas de 50nm, se favorece la nucleación frente al crecimiento y crecen nanoestructuras sobre el semillado con forma de estrella, en una estructura conocida como “multipod”.
- ✓ Cuando el semillado conforma una capa compacta pero se realiza con las nanopartículas de 5 - 8 nm, con menor cristalinidad, se favorece el crecimiento apareciendo una estructura prismas ordenados alineados verticalmente.
- ✓ El origen de esta diferencia reside en que las partículas de la capa semillada recristalizan y se constituyen en núcleos que crecen en la dirección libre, ya que el crecimiento lateral esta constreñido por el ordenamiento de las partículas que conforman la lámina con su plano basal paralelo al sustrato y perpendicular al eje c de la wurtzita.
- ✓ Cuando el semillado conforma una capa heterogenea en la que existe un estructura de pequeñas islas o aglomerados se obtiene un crecimiento en forma de pétalos agrupados a modo de flores. Esto sucede porque en estas

islas el crecimiento lateral está permitido y no existe un ordenamiento tan acusado de las partículas.

- ✓ La combinación de sustratos semillados por EPD con procesos de crecimiento hidrotermal constituye una aproximación al control morfológico de las láminas de ZnO con un tremendo potencial de aplicación en un entorno de sostenibilidad y bajo impacto medioambiental.

References

[1] H. E. Brown, *Zinc oxide rediscovered*, The New Jersey Zinc Company, New York, 1957.

[2] C. Klingshirn and H. Haug, *Phys. Rep.*, **70, (**1981), 315-398.

[3] B. Hönerlage, R. Lévy, J. B. Grun, et al., *Phys. Rep.*, **124, (**1985), 161-253.

[4] W. Hirschwald, P. Bonasewicz, L. Ernst, et al., *Curr. Topics Mat. Sci.*, **7, (**1981), 143-482.

[5] U. Özgur, D. Hofstetter and H. Morkoç, *Proc. IEEE*, **98, (**2010), 1255-1268.

[6] Y.-B. Hahn, *Korean J. Chem. Eng.*, **28, (**2011), 1797-1813.

[7] A. Moezzi, A. M. McDonagh and M. B. Cortie, *Chem. Eng. J.*, **185-186, (**2012), 1-22.

[8] C. Klingshirn, J. Fallert, H. Zhou, et al., *Phys. Status Solidi B*, **247, (**2010), 1424-1447.

[9] C. Barry Carter and M. Grant Norton, *Ceramic Materials: Science and Engineering*, Springer,New York, 2007.

[10] *Database of Ionic Radii*, Atomistic Simulation Group, Department of Materials at Imperial College London, http://abulafia.mt.ic.ac.uk/shannon/ptable.php.

[11] U. Özgur, *J. Appl. Phys.*, **98, (**2005), 1-103.

[12] R. R. Reeber, *J. Appl.Phys.*, **41, (**1970), 5063-5066.

[13] C. Wöll, *Prog. Surf. Sci.*, **82, (**2007), 55-120.

[14] A.-L. Joudrier, F. Levy, N. Simon, et al., *ECS Trans.*, **25, (**2010), 21-27.

[15] Y. Dong, Z.-Q. Fang, D. C. Look, et al., *Appl. Phys. Lett.*, **93, (**2008), 072111-3.

[16] P. W. Tasker, *J. Phys. C: Sol. State Phys.*, **12, (**1979), 49-77.

[17] A. Wander, F. Schedin, P. Steadman, et al., *Phys. Rev. Lett.*, **86, (**2001), 3811-3814.

[18] U. Diebold, S.-C. Li and M. Schmid, *Annu. Rev. Phys. Chem.*, **61, (**2010), 129-148.

[19] M. H. Huang, Y. Wu, H. Feick, et al., *Adv. Mater.*, **13, (**2001), 113-116.

[20] A. Umar, S. H. Kim, Y.-S. Lee, et al., *J. Cryst. Growth.*, **282, (**2005), 131-136.

[21] G. Zhu, Y. Zhou, S. Wang, et al., *Nanotechnology*, **23, (**2012),

[22] J. S. Jeong, J. Y. Lee, J. H. Cho, et al., *Chem. Mater.*, **17, (**2005), 2752-2756.

[23] Z. W. Pan, Z. R. Dai and Z. L. Wang, *Science*, **291, (**2001), 1947-1949.

[24] X. Y. Kong, Y. Ding, R. Yang, et al., *Science*, **303, (**2004), 1348-1351.

[25] A. Umar and Y. B. Hahn, *Appl. Phys. Lett.*, **88, (**2006), 173120-3.

[26] A. Umar, S. Lee, Y. S. Lee, et al., *J. Cryst. Growth*, **277, (**2005), 479-484.

[27] A. Umar, S. Lee, Y. H. Im, et al., *Nanotechnology*, **16, (**2005), 2462.

[28] D. Zhang, X. Wu, N. Han, et al., *J. Nanopart. Res.*, **15, (**2013), 1-10.

[29] Z. L. Wang, *J. Phys. Condens. Matter*, **16, (**2004), R829-R858.

[30] Z. L. Wang, *Mater. Today*, **7, (**2004), 26-33.

[31] M. Yoshimura, *J. Soc. Mater.Sci. Jap.*, **45, (**1996), 829-830.

[32] M. Yoshimura and W. Suchanek, *Solid State Ionics*, **98, (**1997), 197-208.

[33] C. Chen, P. Liu and C. Lu, *Chem. Eng. J.*, **144, (**2008), 509-513.

[34] G. Cao, *Nanostructures and Nanomaterials: Synthesis, Properties, and Applications*, Imperial College Press, London, 2004.

[35] M. Campanati, G. Fornasari and A. Vaccari, *Catal. Today*, **77, (**2003), 299-314.

[36] J. J. De Yoreo and P. G. Vekilov, *Rev. Mineral. Geochem.*, **54, (**2003), 57-93.

[37] M. Haruta and B. Delrnon, *J. Chim. Phys.*, **83, (**1986), 859.

[38] R. Williams, P. N. Yocom and F. S. Stofko, *J. Colloid Interf. Sci.*, **106, (**1985), 388-398.

[39] A. P. A. Oliveira, J.-F. Hochepied, F. Grillon, et al., *Chem. Mater.*, **15, (**2003), 3202-3207.

[40] Q. Yu, C. Yu, H. Yang, et al., *Inorg. Chem.*, **46, (**2007), 6204-6210.

[41] Z. Zhang, M. Lu, H. Xu, et al., *Chem. Eur. J.*, **13, (**2007), 632-638.

[42] R. A. McBride, J. M. Kelly and D. E. McCormack, *J. Mater. Chem.*, **13, (**2003), 1196-1201.

[43] L. Vayssieres, *Adv. Mater.*, **15, (**2003), 464-466.

[44] B. Liu and H. C. Zeng, *Langmuir*, **20, (**2004), 4196-4204.

[45] J. E. Rodriguez-Paez, A. C. Caballero, M. Villegas, et al., *J. Eur. Ceram. Soc.*, **21, (**2001), 925-930.

[46] A. Moezzi, M. Cortie and A. McDonagh, *Dalton Trans.*, **40, (**2011), 4871-4878.

[47] W. Huang, J. Jia, X. Zhou, et al., *Mater. Chem. Phys.*, **123, (**2010), 104-108.

[48] S. Xu and Z. L. Wang, *Nano Res.*, **4, (**2011), 1013-1098.

[49] A. Chittofrati and E. Matijevic, *Coll. .Surf.*, **48, (**1990), 65-78.

[50] C. K. Srikanth and P. Jeevanandam, *J. Alloy. Compd.*, **486, (**2009), 677-684.

[51] T. R. Giraldi, G. V. F. Santos, V. R. De Mendonca, et al., *Mater. Chem. Phys.*, **136, (**2012), 505-511.

[52] K. Govender, D. S. Boyle, P. B. Kenway, et al., *J. Mater. Chem.*, **14, (**2004), 2575-2591.

[53] T. R. Giraldi, G. V. Santos, V. R. Mendonca, et al., *J. Nanosci. Nanotechnol.*, **11, (**2011), 3635-3640.

[54] M. Distaso, R. N. Klupp Taylor, N. Taccardi, et al., *Chem. Eur. J.*, **17, (**2011), 2923-2930.

[55] H. Bahadur, A. Srivastava, R. Sharma, et al., *Nanoscale Res. Lett.*, **2, (**2007), 469-475.

[56] E. Hosono, S. Fujihara, T. Kimura, et al., *J. Coll. Interf. Sci.*, **272, (**2004), 391-398.

[57] L. Poul, N. Jouini and F. Fievet, *Chem. Mater.*, **12, (**2000), 3123-3132.

[58] H. Morioka, H. Tagaya, J.-I. Kadokawa, et al., *J. Mater. Sci. Lett.*, **18, (**1999), 995-998.

[59] I. Golgotiu, *Bul. Inst. Politeh*, **15, (**1969), 1.

[60] A. C. Cakir and S. Erten-Ela, *Adv. Powd. Tech.*, **23, (**2012), 655-660.

[61] N. Uekawa, R. Yamashita, Y. Jun Wu, et al., *Phys. Chem. Chem. Phys.*, **6, (**2004), 442-446.

[62] R. Viswanatha, H. Amenitsch and D. D. Sarma, *J. Am. Chem. Soc.*, **129, (**2007), 4470-4475.

[63] W. Guo, T. Liu, L. Huang, et al., *Phys. E*, **(**2011), 680 - 685.

[64] Y. Zhou, W. Wu, G. Hu, et al., *Mater. Res. Bull.*, **43, (**2008), 2113-2118.

[65] M. S. Akhtar, M. A. Khan, M. S. Jeon, et al., *Electrochim. Acta*, **53, (**2008), 7869-7874.

[66] X. M. Sun, X. Chen, Z. X. Deng, et al., *Mater. Chem. Phys.*, **78, (**2003), 99-104.

[67] P. Li, Y. Wei, H. Liu, et al., *J. Sol. State Chem.*, **178, (**2005), 855-860.

[68] H. Zhang, D. Yang, D. Li, et al., *Cryst. Growth Des.*, **5, (**2005), 547-550.

[69] J. Wu and D. Xue, *Mater. Res. Bull.*, **45, (**2010), 300-304.

[70] X. Gao, X. Li and W. Yu, *J. Phys. Chem. B*, **109, (**2005), 1155-1161.

[71] Z. Hu, G. Oskam and P. C. Searson, *J. Coll. Interf. Sci.*, **263, (**2003), 454-460.

[72] Q. Zhong and E. Matijevic, *J. Mater. Chem.*, **6, (**1996), 443-447.

[73] B. Claflin, D. C. Look, S. J. Park, et al., *J. Cryst. Growth*, **287, (**2006), 16-22.

[74] A. B. Djurisic, A. M. C. Ng and X. Y. Chen, *Prog. Quant. Electron.*, **34, (**2010), 151-259.

[75] S. J. Pearton, D. P. Norton, K. Ip, et al., *Superlattices Microstruct.*, **34, (**2003), 3-32.

[76] S. Wang, P. Li, H. Liu, et al., *J. Alloy. Compd.*, **505, (**2010), 362-366.

[77] T. Dietl, *Nat. Mater.*, **9, (**2010), 965-974.

[78] K. Ueda, H. Tabata and T. Kawai, *Appl. Phys. Lett.*, **79, (**2001), 988-990.

[79] S. B. Ogale, *Adv. Mater.*, **22, (**2010), 3125-3155.

[80] N. Zhang, R. Yi, R. Shi, et al., *Mater. Lett.*, **63, (**2009), 496-499.

[81] M.-Y. Choi, H.-K. Park, M.-J. Jin, et al., *J. Cryst. Growth*, **311, (**2009), 504-507.

[82] P. Gao, Y. Chen, Y. Wang, et al., *Chem. Comm.*, **(**2009), 2762-2764.

[83] J. H. Yang, J. H. Zheng, H. J. Zhai, et al., *J. Alloy. Compd.*, **475, (**2009), 741-744.

[84] I. M. Kolthoff, *Am. Chem. Soc.*, **36, (**1931), 860-881.

[85] M. Yoshimura and K. Byrappa, *J. Mater. Sci*, **43, (**2008), 2085-2103.

[86] W. Jia, S. Dang, H. Liu, et al., *Mater. Lett.*, **82, (**2012), 99-101.

[87] N. J. Nicholas, G. V. Franks and W. A. Ducker, *CrystEngComm*, **14, (**2012), 1232-1240.

[88] M. Wang, Y. Zhou, Y. Zhang, et al., *CrystEngComm*, **13, (**2011), 6024-6026.

[89] L. E. Greene, M. Law, D. H. Tan, et al., *Nano Lett.*, **5, (**2005), 1231-1236.

[90] Y. Tao, M. Fu, A. Zhao, et al., *J. Alloy. Compd.*, **489, (**2010), 99-102.

[91] J. H. Yang, J. H. Zheng, H. J. Zhai, et al., *J. Alloy. Compd.*, **481, (**2009), 628-631.

[92] X. Y. Liu, *J. Chem. Phys.*, **111, (**1999), 1628-1635.

[93] M. Guo, P. Diao and S. Cai, *J. Solid. State Chem.*, **178, (**2005), 1864-1873.

[94] W. Weng, Q. Li, H. Sun, et al., *J. Alloy. Compd.*, **503, (**2010), 514-518.

[95] J. Yang, J. Zheng, H. Zhai, et al., *J. Alloy. Compd.*, **489, (**2010), 51-55.

[96] R. K. Kumar, M. Husain and Z. H. Khan, *Dig. J. Nanomater. Biostr.*, **6, (**2011), 1317-1323.

[97] R. Hong, J. Shao, H. He, et al., *Appl. Surf. Sci.*, **252, (**2006), 2888-2893.

[98] R. Swapna and M. C. Santhosh Kumar, *Ceram. Int.*, **38, (**2012), 3875-3883.

[99] N. Nishimoto, O. Senthilkumar, T. Yamamae, et al., *J. Korean Phys. Soc.*, **53, (**2008), 2951-2954.

[100] B. J. Jin, S. Im and S. Y. Lee, *Thin Solid Films*, **366, (**2000), 107-110.

[101] J. W. Goodwin, *Colloids and Interfaces with Surfactants and Polymers - An Introduction.*, John Wiley & Sons, London, 2004.

[102] O. O. Van Der Biest and L. J. Vandeperre, *Annu. Rev. Mater. Sci.*, **(**1999), 327-352.

[103] D. J. Shaw, *Introduction to colloid and surface chemistry*, Butterworth-Heinemann, Oxford, 1992.

[104] A. Degen and M. Kosec, *J. Eur. Ceram. Soc.*, **20, (**2000), 667-673.

[105] R. A. Reichle, K. G. McCurdy and L. G. Hepler, *Can. J. Chem.*, **53, (**1975), 3841-3845.

[106] J. S. Reed, *Introduction to the Principles of Ceramic Processing.*, John Wiley & Sons, New York, 1986.

[107] G. A. Parks, *Chem. Rev.*, **65, (**1965), 177-198.

[108] F. Tang, Y. Sakka and T. Uchikoshi, *Mater. Res. Bull.*, **38, (**2003), 207-212.

[109] V. Osipov and E. Sergeev, *B. Eng. Geol. Environ.*, **5, (**1972), 9-15.

[110] S. L. Swartzen-Allen and E. Matijevic, *J. Coll. Interf. Sci*, **50, (**1975), 143-153.

[111] S. L. Swartzen-Allen and E. Matijevic, *J. Coll. Interf. Sci.*, **56, (**1976), 159-167.

[112] B. K. Schroth and G. Sposito, *Materials Research Society Symposium - Proceedings*, **432, (**1997), 87-92.

[113] G. Sposito, N. T. Skipper, R. Sutton, et al., *Proceedings of the National Academy of Sciences*, **96, (**1999), 3358-3364.

[114] J. A. Lewis, *J. Am. Ceram. Soc.*, **83, (**2000), 2341-2359.

[115] J. F. Kelso and T. A. Ferrazzoli, *J. Am. Ceram. Soc.*, **72, (**1989), 625-627.

[116] G. V. Franks and Y. Gan, *J. Am. Ceram. Soc.*, **90, (**2007), 3373-3388.

[117] M. Valtiner, X. Torrelles, A. Pareek, et al., *J. Phys. Chem. C*, **114, (**2010), 15440-15447.

[118] R. Moreno, *Reología de suspensiones cerámicas*, CSIC, Madrid, 2005.

[119] P. Sarkar and P. S. Nicholson, *J. Am. Ceram. Soc.*, **79, (**1996), 1987-2002.

[120] F. Caruso, *Colloids and Colloid Assemblies: Synthesis, Modification, Organization and Utilization of Colloid Particles*, Wiley-VCH Verlag GmbH & Co KgaA,Weinheim, 2006.

[121] I. Zhitomirsky, *Adv. Colloid Interface Sci.*, **97, (**2002), 277-315.

[122] R. Meszaros, L. Thompson, M. Bos, et al., *Langmuir*, **18, (**2002), 6164-6169.

[123] P. C. Griffiths, A. Paul, P. Stilbs, et al., *Macromolecules*, **38, (**2005), 3539-3542.

[124] L. Avadiar and Y. K. Leong, *Colloid Polym. Sci.*, **289, (**2011), 237-245.

[125] M. Verde, M. Peiteado, A. C. Caballero, et al., *J. Colloid Interf. Sci.*, **373, (**2011), 27-33.

[126] L. Stappers, L. Zhang, O. Van der Biest, et al., *J. Colloid Interf. Sci.*, **328, (**2008), 436-446.

[127] B. Ferrari and R. Moreno, *J. Eur. Ceram. Soc.*, **17, (**1997), 549-556.

[128] M. Trau, D. A. Saville and I. A. Aksay, *Science*, **272, (**1996), 706-709.

[129] A. R. Boccaccini and I. Zhitomirsky, *Curr. Opin. Solid State Mat. Sci.*, **6, (**2002), 251-260.

[130] M. Ammam, *RSC Adv.*, **2, (**2012), 7633-7646.

[131] A. Chávez-Valdez and A. R. Boccaccini, *Electrochim. Acta*, **65, (**2012), 70-89.

[132] L. Besra, T. Uchikoshi, T. S. Suzuki, et al., *J. Am. Ceram. Soc.*, **91, (**2008), 3154-3159.

[133] H. C. Hamaker, *Trans. Faraday Soc.*, **35, (**1940), 279-287.

[134] Y. Hirata, A. Nishimoto and Y. Ishihara, *J. Ceram. Soc. Jpn.,Int. Ed.*, **99, (**1991), 105-109.

[135] Z. Zhang, Y. Huang and Z. Jiang, *J. Am. Ceram. Soc.*, **77, (**1994), 1946-1949.

[136] B. Ferrari and R. Moreno, *J. Eur. Ceram. Soc.*, **30, (**2010), 1069-1078.

[137] D. De and P. S. Nicholson, *J. Am. Ceram. Soc.*, **82, (**1999), 3031-3036.

[138] P. Richetti, J. Prost and P. Barois, *J. Physique Lett.*, **45, (**1984), 1137-1143.

[139] M. Böhmer, *Langmuir*, **12, (**1996), X-5750.

[140] Y. Solomentsev, M. Bahmer and J. L. Anderson, *Langmuir*, **13, (**1997), 6058-6061.

[141] W. D. Ristenpart, I. A. Aksay and D. A. Saville, *Phys. Rev. E J1 - PRE*, **69, (**2004), 021405.

[142] W. D. Ristenpart, I. A. Aksay and D. A. Saville, *Langmuir*, **23, (**2007), 4071-4080.

[143] W. D. Ristenpart, P. Jiang, M. A. Slowik, et al., *Langmuir*, **24, (**2008), 12172-12180.

[144] D. C. Prieve, P. J. Sides and C. L. Wirth, *Curr. Op. Coll. Interf. Sci.*, **15, (**2010), 160-174.

[145] P. J. Sides, *Langmuir*, **17, (**2001), 5791-5800.

[146] P. J. Sides, *Langmuir*, **19, (**2003), 2745-2751.

[147] Y. Solomentsev and J. L. Anderson, *J. Fluid. Mech.*, **279, (**1994), 197-215.

[148] S. Yamamoto and T. Matsuoka, *J. Chem. Phys.*, **107, (**1997), 3300-3308.

[149] E. Yariv, *Phys. Fluids*, **17, (**2005), 1-4.

[150] L. Zhang, A. K. Kanjarla, J. Vleugels, et al., *Key Eng. Mater.*, **412, (**2009), 261-266.

[151] N. A. Mody, O. Lomakin, T. A. Doggett, et al., *Biophys. J.*, **88, (**2005), 1432-1443.

[152] L. Harnau and S. Dietrich, *Phys. Rev. E*, **65, (**2002), 021505.

[153] F. Tang, T. Uchikoshi, Y. Sakka, *J. Am. Ceram. Soc.*, **85, (**2002), 2161-2165.

[154] M. Verde, A. C. Caballero, Y. Iglesias, et al., *J. Electrochem. Soc.*, **157, (**2010), H55-H59.

[155] E. M. Wong and P. C. Searson, *Chem. Mater.*, **11, (**1999), 1959-1961.

[156] Y. Wang, I. C. Leu, M.H. Hon, *J. Am. Ceram. Soc.*, **87, (**2004), 84-88.

[157] P. Lommens, D. Van Thourhout, P. F. Smet, et al., *Nanotechnology*, **19, (**2008), 245-301.

[158] J. Balaji, S. Boominathasellarajan, N. T. Sasikala, et al., *Int. J. Nanosci.*, **10, (**2011), 787-792.

[159] L. Miao, S. Cai and Z. Xiao, *J. Alloy Compd.*, **490, (**2010), 422-426.

[160] J.-H. Lee, I.-C. Leu, Y.-W. Chung, et al., *Nanotechnology*, **17, (**2006), 4445-4450.

[161] Y. C. Wang, I. C. Leu and M. H. Hon, *J. Mater. Chem.*, **12, (**2002), 2439-2444.

[162] Y. C. Wang, I. C. Leu and M. H. Hon, *J. Cryst. Growth*, **237-239, (**2002), 564-568.

[163] Y. C. Wang, I. C. Leu and M. H. Hon, *J. Appl. Phys.*, **95, (**2004), 1444-1449.

[164] Y.-C. Wang, I.-C. Leu and M.-H. Hon, *Electrochem. Sol. State Lett.*, **5, (**2002),

[165] Y.-C. Wang, I.-C. Leu and M.-H. Hon, *Electrochem. Sol. State Lett.*, **7, (**2004),

[166] Y.-W. Chung, I.-C. Leu, J.-H. Lee, et al., *J. Electrochem. Soc.*, **156, (**2009), E91-E95.

[167] Y.-W. Chung, I.-C. Leu, J.-H. Lee, et al., *Electrochim. Acta*, **54, (**2009), 3677-3682.

[168] C. S. Rout, S. Hari Krishna, S. R. C. Vivekchand, et al., *Chem. Phys. Lett.*, **418, (**2006), 586-590.

[169] C. S. Rout, A. R. Raju, A. Govindaraj, et al., *J. Nanosci. Nanotechnol.*, **7, (**2007), 1923-1929.

[170] N. Dougami and T. Takada, *Sens. Act. B*, **93, (**2003), 316-320.

[171] F. Hossein-Babaei and F. Taghibakhsh, *Electron. Lett.*, **36, (**2000), 1815-1816.

[172] A. Dogan, E. Suvaci, G. Gunkaya, et al., *Key Eng. Mater.*, **(**2004), 269-272.

[173] H. Zhang, Y. Cui, Y. Men, et al., *J. Lumin.*, **121, (**2006), 601-605.

[174] E. M. Wong and P. C. Searson, *Appl Phys Lett*, **74, (**1999), 2939-2941.

[175] B.-S. Jeon, J. S. Yoo and J. D. Lee, *J. Electrochem. Soc.*, **143, (**1996), 3923-3927.

[176] R. Nedyalkova, A. Casanovas, J. Llorca, et al., *Int. J. Hydrog. Energy*, **34, (**2009), 2591-2599.

[177] Y. Hara, M. I. Tejedor-Tejedor, K. Lara, et al., *Electrochim. Acta*, **56, (**2011), 8873-8879.

[178] Y. Hara, J. R. S. Brownson and M. A. Anderson, *Int. J. Appl. Ceram. Technol.*, **9, (**2012), 115-123.

[179] Y. Hara, M. I. Tejedor-Tejedor, L. J. Brzozowski, et al., *J. Electrochem. Soc.*, **158, (**2011), B1417-B1422.

[180] K. Keis, C. Bauer, G. Boschloo, et al., *J. Photochem.Photobio. A*, **148, (**2002), 57-64.

[181] H.-W. Chen, C.-Y. Lin, Y.-H. Lai, et al., *J. Power Sources*, **196, (**2011), 4859-4864.

[182] X. Yin, X. Liu, L. Wang, et al., *Electrochem. Commun.*, **12, (**2010), 1241-1244.

[183] *Test & Precision Measurement tools*, Keithley Instruments Inc., http://www.keithley.com/.

[184] M. Peiteado, T. Jardiel, F. Rubio, et al., *Mater. Res. Bull.*, **45, (**2010), 1586-1592.

[185] Berghof GmbH, www.berghof.com.

[186] *Laboratorio de Difracción de Rayos X Policristal*, Servicio Interdepartamental de Investigación, UAM, http://www.uam.es/investigacion/servicios/sidi/.

[187] *FullProf Suite*, http://www.ill.eu/sites/fullprof/.

[188] *Thermal Analysis Consumables & Accessories*, Perkin Elmer, www.perkinelmer.com/.

[189] *ASAP 2020 - Physisorption Analyzer*, Micromeritics Inc., http://www.micromeritics.com/.

[190] *Microscopios electrónicos de barrido*, Instituto de Cerámica y Vidrio-CSIC., http://www.icv.csic.es//node/25.

[191] *Microscopios electrónicos de transmisión*, Instituto de Cerámica y Vidrio-CSIC, http://www.icv.csic.es//node/26.

[192] *Microscopía Electrónica de Transmisión*, Instituto de Catálisis y Petroleoquímica-CSIC, http://www.icp.csic.es/microscopia.php.

[193] *Centre for Electron Microscopy*, Jozef Stefan Institute, http://brukit.ijs.si/cem.htm.

[194] M. Staiger, R. J. Flatt, P. Bowen and H. Hofman, *Colloidal Processing of Nanosized Ceramic Dispersions: Particle Size Distributions and their Effect on Colloid Stability. Calculation and Rheological Behaviour.*, The American Ceramic Society, Ohio, USA, 2001.

[195] R. M. German, *Int. J. Powder Metall.*, **32, (**1996), 365-373.

[196] *Zetasizer Nano Zs*, Malvern Instruments, www.malvern.com.

[197] R. Moreno and B. Ferrari, *Electrophoretic Deposition of Nanomaterials*, J. H. Dickerson and A. R. Boccaccini,Springer, New York, 2012.

[198] *Conductivity Measurements*, WTW, a Xylem brand, http://www.wtw.de/.

[199] D. Segets, J. Gradl, R. K. Taylor, et al., *ACS Nano*, **3, (**2009), 1703-1710.

[200] D. Segets, J. M. Lucas, R. N. Klupp Taylor, et al., *ACS Nano*, **6, (**2012), 9021-9032.

[201] *LAMBDA 950 UV/Vis/NIR Spectrophotometer*, Perkin Elmer, http://www.perkinelmer.com/Catalog/Product/ID/L950.

[202] *Surtronic 3+ Operation Instructions*, Taylor Hobson Precision, http://www.taylor-hobson.com/uploads/files/SUR3+%20Operators%20Handbook.pdf.

[203] *Nanotec Cervantes FullMode AFM*, Nanotec Electrónica SL., http://www.nanotec.es/.

[204] Z. Hu, G. Oskam, R. L. Penn, et al., *J. Phys. Chem. B*, **107, (**2003), 3124-3130.

[205] *McGraw-Hill Dictionary of Scientific and Technical Terms, 6th edition*, McGraw-Hill Professional Publishing, 2002.

[206] A. Moezzi, A. McDonagh, A. Dowd, et al., *Inorg. Chem.*, **52, (**2012), 95-102.

[207] H. P. Klug and L. E. Alexander, *X Ray Diffraction Procedures for Polycrystalline and Amorphous Materials*, Wiley Interscience, Canada, 1974.

[208] *Gaussian Function from Wolfram MathWorld*, http://mathworld.wolfram.com/GaussianFunction.html.

[209] L. Poul, S. Ammar, N. Jouini, et al., *Solid State Sci.*, **3, (**2001), 31-42.

[210] M. Peiteado, D. Makovec, M. Villegas, et al., *J. Solid State Chem.*, **181, (**2008), 2456-2461.

[211] N. N. Greenwood and A. Earnshaw, *Chemistry of the Elements*, Elsevier, Oxford, 2003.

[212] T. P. J. Han, M. Villegas, M. Peiteado, et al., *Chem. Phys. Lett.*, **488, (**2010), 173-176.

[213] G. L. Mar, P. Y. Timbrell and R. N. Lamb, *Chem. Mater.*, **7, (**1995), 1890-1896.

[214] M. Wei, D. Zhi and J. L. MacManus-Driscoll, *Nanotechnology*, **16, (**2005), 1364-1368.

[215] D. Paraguay, F., L. Estrada, W., N. Acosta, D.R., et al., *Thin Solid Films*, **350, (**1999), 192-202.

[216] R. Kitsomboonloha, S. Baruah, M. T. Z. Myint, et al., *J. Cryst. Growth*, **311, (**2009), 2352-2358.

[217] O. W. Perez-Lopez, A. C. Farias, N. R. Marcilio, et al., *Mater. Res. Bull.*, **40, (**2005), 2089-2099.

[218] J. Goniakowski and C. Noguera, *Phys.Rev. B.*, **83, (**2011),

[219] I. Gonzalo-Juan, B. Ferrari and M. T. Colomer, *J. Eur. Ceram. Soc.*, **29, (**2009), 3185-3195.

[220] C. Tallon, R. Moreno and M. I. Nieto, *Int. J. Appl. Ceram. Technol.*, **6, (**2009), 324-334.

[221] F. Burriel, F. Lucena, S. Arribas, et al., *Química Analítica Cualitativa*, Paraninfo,Madrid, 1983.

[222] E. M. Kosacheva, D. B. Kudryavtsev, R. F. Bakeeva, et al., *Colloid J.*, **68, (**2006), 713-720.

[223] F. Crea, P. Crea, A. De Robertis, et al., *J. Chem. Eng. Data*, **52, (**2007), 279-285.

[224] M. E. Helgeson, T. K. Hodgdon, E. W. Kaler, et al., *Langmuir*, **26, (**2010), 8049-8060.

[225] P. M. Biesheuvel and H. Verweij, *J. Am. Ceram. Soc.*, **82, (**1999), 1451-1455.

[226] R. Moreno and B. Ferrari, *Am. Ceram. Soc. Bull.*, **79, (**2000), 44-48.

[227] R. Desai, V. Mankad, S. K. Gupta, et al., *Nanosci. Nanotech. Lett.*, **4, (**2012), 30-34.

[228] H. Kato, A. Nakamura, K. Takahashi, et al., *Phys. Chem. Chem. Phys.*, **11, (**2009), 4946-4948.

[229] Z. F. Li, G. H. Luo, W. P. Zhou, et al., *Nanotechnology*, **17, (**2006), 3692-3698.

[230] Z. Zhang and Y. Wu, *Langmuir*, **26, (**2010), 9214-9223.

[231] J. Ma and W. Cheng, *J. Am. Ceram. Soc.*, **85, (**2002), 1735-1737.

[232] G. Anne, K. Vanmeensel, J. Vleugels, et al., *Coll. Surf. A: Physicochem. Eng. Asp.*, **245, (**2004), 35-39.
[233] A. Lizana, M. Foldyna, M. Stchakovsky, et al., *J. Phys. D: Appl .Phys.*, **46, (**2013),
[234] M. Ohyama, H. Kouzuka and T. Yoko, *Thin Solid Films*, **306, (**1997), 78-85.
[235] B. E. Yoldas and D. P. Partlow, *Thin Solid Films*, **129, (**1985), 1-14.
[236] J. C. Maxwell, *A Treatise on Electricity and Magnetism*, Clarendon Press, Oxford, 1873.
[237] L. Besra, T. Uchikoshi, T. S. Suzuki, et al., *J. Eur. Ceram. Soc.*, **30, (**2010), 1187-1193.
[238] M. Mishra, S. Bhattacharjee, L. Besra, et al., *J. Eur. Ceram. Soc.*, **30, (**2010), 2467-2473.
[239] M. Ammam, *RSC Adv.*, **(**2012),
[240] S. V. Mahajan, S. A. Hasan, J. Cho, et al., *Nanotechnology*, **19, (**2008),
[241] S. Baruah and J. Dutta, *Sci. Technol. Adv. Mat.*, **10, (**2009), 013001.
[242] M. Guo, P. Diao and S. Cai, *Appl. Surf. Sci.*, **249, (**2005), 71-75.
[243] M. Bitenc, G. Drazic and Z. C. Orel, *Cryst. Growth Des.*, **10, (**2009), 830-837.
[244] Z. Yang, Y.-Y. Shi, X.-L. Sun, et al., *Mater. Res. Bull.*, **45, (**2010), 474-480.
[245] R. W. Nosker, P. Mark and J. D. Levine, *Surf. Sci.*, **19, (**1970), 291-317.
[246] J. C. Kim and E. Goo, *J. Am. Ceram. Soc.*, **73, (**1990), 877-884.
[247] Y. Liu, H. Lv, S. Li, et al., *Adv. Powder Technol.*, **22, (**2011), 784-788.
[248] E.-S. Jang, J.-H. Won, S.-J. Hwang, et al., *Adv. Mater.*, **18, (**2006), 3309-3312.
[249] Y.-F. Gao, H.-Y. Miao, H.-J. Luo, et al., *J. Phys. Chem. C*, **112, (**2008), 1498-1506.
[250] A. W. Adamson and A. P. Gast, *Physical Chemistry of Surfaces, 6th Ed.*, Interscience Publishers,Wiley, New York, 1997.
[251] J. A. Venables, G. D. T. Spiller and M. Hanbucken, *Rep. Prog. Phys.*, **47, (**1984), 399-459.
[252] R. Zhang, X. Yang, D. Zhang, et al., *Cryst. Res. Technol.*, **46, (**2011), 1189-1194.
[253] Y. Ni, G. Wu, X. Zhang, et al., *Mat. Res. Bull.*, **43, (**2008), 2919-2928.
[254] Y. Lu, L. Wang, D. Wang, et al., *Mater. Chem. Phys.*, **129, (**2011), 281-287.
[255] M. Ma, J. P. Tu, Y. F. Yuan, et al., *J. Power Sources*, **179, (**2008), 395-400.